



**Electrodeposition of Cu, Sn and Cu-Sn Alloy from  
Choline Chloride Ionic Liquid**

A Thesis submitted by

**Swatilekha Ghosh**

For the Degree of Doctor of Philosophy

**September 2013**

**School of Chemical Engineering and Advanced Materials  
Newcastle University  
United Kingdom**

## **Abstract**

Copper, tin and their alloy deposits are popular for its various applications in industrial aspects like enhance corrosion resistance and provide decorative finish. This work concentrated on the fabrication of these coatings, accomplished by electrodeposition technique which allows the control of thickness and microstructure of the films. Previously these metals and alloy were electrodeposited from different aqueous electrolytes. However these baths suffer from various environmental issues and deposits suffers from H<sub>2</sub> evolution and metal oxide formation. As a result solution ionic liquid (IL) was proposed as an alternative. ILs are categorized as salts liquid at room temperature and consist only of cations and anions. Presently Choline chloride based IL was used due to its advantages of low cost, low melting point, low toxicity, low viscosity and high conductivity than other ILs.

Physical properties of the ILs like density, viscosity and conductivity were measured with variation of temperature and concentration of added metallic salts. To determine the electrochemical properties of individual metals and alloy, voltammetry scans were carried out using various scan rates and agitation rates. For all these measurements the concentration of Cu and Sn were varied in a range of 0.01 to 0.2 M and 0.01 to 0.1 M respectively at temperature range of 25 to 55 °C using a platinum rotating disk electrode (RDE). Deposition experiments were then carried out under potentiostatic and galvanostatic conditions using a stainless steel RDE. Material properties of the deposits like crystalline structure, grain size, strain, deposit morphology and chemical composition were analyzed using x-ray diffraction (XRD), optical microscope and scanning electron microscopy (SEM).

The measurement showed that density and viscosity decreases and conductivity increases with rise in operation temperature for the electrolyte with and without metal ions. The reduction of both the metal was found to be mass transfer control and limiting current for metal deposition was found. The diffusion co-efficient obtained for Cu and Sn in the IL system was  $1.22 \times 10^{-7}$  cm<sup>2</sup>/s and  $1.96 \times 10^{-7}$  cm<sup>2</sup>/s respectively. For individual metal Cu and Sn, best deposits were obtained at  $4.7 \times 10^{-3}$  A/cm<sup>2</sup> and  $1.6 \times 10^{-3}$  A/cm<sup>2</sup> respectively using RDE speed of 700 rpm at 25 °C. The Cu deposit showed face centered cubic structure of  $66 \pm 10$  nm grain size and that of Sn was  $62 \pm 10$  nm with tetragonal crystalline structure. The smooth and bright Cu-Sn alloy deposit was obtained by applying potential in the range of 0.35 to 0.36 V vs. Ag wire or  $0.8$  to  $0.9 \times 10^{-3}$  A/cm<sup>2</sup> of RDE speed is 220 rpm at 25 °C. The obtained deposits showed orthorhombic Cu<sub>3</sub>Sn structure with a grain size of  $21 \pm 10$  nm. On annealing the crystalline structure changed to hexagonal Cu<sub>10</sub>Sn<sub>3</sub> structure and the crystalline size was obtained as  $77 \pm 50$  nm.

## TABLE OF CONTENTS

	Page no.
Acknowledgments .....	vii
<u>List of symbols</u> .....	viii
<u>List of figures</u> .....	xii
<u>List of tables</u> .....	xvii

### **Chapter 1: INTRODUCTION**

1.1. Background .....	1
1.2. Fabrication techniques and their limitation .....	5
1.2.1. <i>Coating processes</i> .....	5
1.3. Industrial aqueous electrolytes for deposition of individual metals and alloys .....	6
1.3.1. <i>Copper deposition</i> .....	7
1.3.2. <i>Tin deposition</i> .....	8
1.3.3. <i>Copper-Tin alloy deposition</i> .....	8
1.4. Ionic liquids .....	10
1.4.1. <i>Background</i> .....	11
1.4.2. <i>Synthesis and classification of Ionic liquids</i> .....	15
1.4.3. <i>Eutectic based Ionic liquids</i> .....	17
1.4.4. <i>Important parameters for deposition from Ionic liquids</i> .....	22
1.4.5. <i>Summary of electrochemical study and electrodeposition of         Copper, Tin and its alloy from various Ionic liquids</i> .....	28
1.5. Aims and objective of the present work .....	32
Reference .....	33

### **Chapter 2: FUNDAMENTAL ASPECTS**

2.1. Fundamentals of electrochemical deposition .....	43
2.1.1. <i>Electrochemical thermodynamics</i> .....	46
2.1.2. <i>Electrochemical kinetics</i> .....	49
2.1.3. <i>Electrochemical mass transport conditions</i> .....	51
2.1.4. <i>Faraday's law of electrolysis</i> .....	54
2.2. Alloy classification .....	55
2.3. Material crystalline structure at solid state .....	58
Reference .....	61

### **Chapter 3 : EXPERIMENTAL**

3.1.	Electrolyte preparation	64
3.2.	Electrolyte characterization	66
3.2.1.	<i>Density measurements</i>	66
3.2.2.	<i>Conductivity measurements</i>	67
3.2.3.	<i>Viscosity measurements</i>	68
3.3.	Electrochemical characterization of the electrolytes	69
3.3.1.	<i>Formal potential determination experiments</i>	73
3.3.2.	<i>Voltammetry experiments</i>	74
3.3.3.	<i>Anodic stripping voltammetry experiments</i>	76
3.4.	Electrodeposition experiments	77
3.4.1.	<i>Individual metal deposition</i>	77
3.4.2.	<i>Alloy deposition</i>	79
3.5.	Annealing experiments	82
3.6.	Deposit characterization	83
3.6.1.	<i>Optical microscope</i>	83
3.6.2.	<i>Scanning electron microscope</i>	84
3.6.3.	<i>X-ray crystallography</i>	85
Reference		87

### **Chapter 4: PHYSICAL PROPERTY MEASUREMENTS**

4.1.	Introduction	89
4.2.	Ethaline melt	91
4.2.1.	<i>Density measurement</i>	91
4.2.2.	<i>Viscosity and conductivity measurement</i>	91
4.3.	Ethaline melt with individual metal ions	94
4.3.1.	<i>Density measurement</i>	94
4.3.2.	<i>Viscosity and conductivity measurement</i>	95
4.4.	Ethaline melt with both metal ions	99
4.4.1.	<i>Density measurement</i>	99
4.4.2.	<i>Conductivity measurement</i>	100
4.5.	Discussion	100
4.6.	Conclusion	102
Reference		103

## **Chapter 5: ELECTROCHEMICAL CHARACTERIZATION**

### **OF INDIVIDUAL METALS**

5.1.	Introduction	105
5.2.	Voltammetry of the Ethaline melt	106
5.3.	Electrochemical characterization of copper in Ethaline melt	106
5.3.1.	<i>Formal potential measurements</i>	106
5.3.2.	<i>Voltammetry of Ethaline melt containing copper ions</i>	108
5.4.	Electrochemical characterization of tin in Ethaline melt	117
5.4.1.	<i>Formal potential measurements</i>	117
5.4.2.	<i>Voltammetry of Ethaline melt containing tin ions</i>	119
5.5.	Mass transfer co-relation of individual metals	121
5.6.	Current efficiency calculation of individual metals	123
5.7.	Discussion	125
5.8.	Conclusion	126
	Reference	128

## **Chapter 6: ELECTRODEPOSITION OF INDIVIDUAL METALS**

6.1.	Introduction	130
6.2.	Electrodeposition of Copper	131
6.2.1.	<i>Potentiostatic deposition</i>	131
6.2.2.	<i>Galvanostatic deposition</i>	133
6.2.3.	<i>Long term deposition experiments</i>	134
6.2.4.	<i>SEM, EDAX and XRD measurements on deposited copper</i>	136
6.3.	Electrodeposition of Sn	140
6.3.1.	<i>Potentiostatic deposition</i>	140
6.3.2.	<i>Galvanostatic deposition</i>	141
6.3.3.	<i>Long term deposition experiments</i>	144
6.3.4.	<i>SEM, EDAX and XRD measurements on deposited tin</i>	145
6.4.	Discussion	149
6.5.	Conclusion	150
	Reference	151

## **Chapter 7: ELECTRODEPOSITION OF ALLOYS**

7.1.	Introduction	154
7.2.	Preliminary experiments	154

7.3.	Electrochemical characterization	158
7.3.1.	<i>Voltammetry experiments</i>	158
7.3.2.	<i>Anodic stripping voltammetry experiments</i>	160
7.4.	Deposition experiments	162
7.4.1.	<i>Potentiostatic deposition</i>	162
7.4.2.	<i>Galvanostatic deposition</i>	162
7.5.	Material property analysis of the deposited alloy	163
7.5.1.	<i>SEM analysis of the as-deposited and annealed alloy</i>	163
7.5.2.	<i>EDAX analysis of the as-deposited and annealed alloy</i>	164
7.5.3.	<i>XRD analysis of the as-deposited and annealed alloy</i>	165
7.6.	Bath stability for long term deposition	170
7.6.1.	<i>Bath stability without any deposition process</i>	170
7.6.2.	<i>Bath stability after several deposition processes</i>	171
7.7.	Discussion	173
7.8.	Conclusion	177
	Reference	178
	<b><u>Chapter 8: CONCLUSION</u></b>	180
	<b>AVENUE FOR THE FUTURE WORKS</b>	182
	<b>APPENDIX</b>	184

## **Acknowledgements**

From the very day of my admission to this University and throughout the duration of my working on this thesis, I owe many people a great deal of gratitude for supporting my studies financially, scientifically and also by personal friendships. First of all, I would like to give my most sincere gratitude to my supervisor Professor (Dr.) Sudipta Roy for giving me the opportunity to join the Electrochemical group, sharing her knowledge, encouraging me to grow as an independent researcher over the years, and provide valuable direction and advice on the research methodologies. Her words were not only thought provoking within the academic arena but also supportive in both my public and private lives.

I sincerely thank Dr Andrew Cobley, Coventry University and Prof. Paul Christensen, Newcastle University for providing useful feedback that helped in improving this thesis significantly.

I wish to express my deep thanks to the head of the School of Chemical Engineering and Advanced Materials (CEAM), Newcastle University for offering me admission in the PhD program and supporting me with NUPIS and ORSAS scholarship for carrying out my studies.

I would like to thank the entire staff of School of CEAM for their every help in many aspects during my studies here. I am personally grateful to my colleagues and co-workers for providing friendly, helpful and endless discussions. Special thanks to Pauline and Maggie for carrying out study using Scanning Electron Microscope (SEM) and XRD.

I would like to thank my friends and family for their continuous support during the research. Particularly I am grateful to my present and former colleagues from room C402 for their endless support and encouragement during the research.

## List of symbols

- $A$  = Area of the electrode,  $\text{cm}^2$   
 $A_s$  = Plated surface area,  $\text{cm}^2$   
 $A_{wt}$  = Atomic weight of the deposited metal in the cathode, gm/mole  
 $A^{VTF}$  = Constant in Vogel-Tamman-Fulcher equation  
 $a, b, c$  = Length of the each side in a unit cell  
 $a_{Mi}$  = Activity of the ion  
 $C$  = Concentration of the reacting species,  $\text{mol}/\text{cm}^3$   
 $c'$  = Constant  
 $D$  = Diffusion coefficient,  $\text{cm}^2/\text{s}$   
 $D_s$  = Strain free lattice spacing or crystallite size  
 $D_s'$  = Strained lattice spacing or crystallite size  
 $d$  = Rotating cylinder electrode diameter,  $\text{cm}$   
 $d_{hkl}$  = Separation of the  $hkl$  plane of an unit cell  
 $E$  = Applied potential,  $\text{V}$   
 $E^0$  = Standard electrode potential,  $\text{V}$   
 $E^o$  = Formal potential,  $\text{V}$   
 $E_e$  = Open circuit potential or equilibrium potential,  $\text{V}$   
 $E_\mu$  = Activation energy of the viscous flow,  $\text{kJ}/\text{mol}$   
 $e$  = Charge of a single electron,  $1.6021 \times 10^{-19}$  Coulomb  
 $F$  = Faradays constant,  $96485$  Coulomb/mol  
 $f$  = Linear frequency of rotation, revolution per second  
 $\Delta H_D$  = Activation energy for diffusion,  $\text{kJ}/\text{mol}$   
 $hkl$  = Notation for the individual plane / Miller indices  
 $\Delta G$  = Gibbs free energy  
 $\Delta G^0$  = Standard state Gibbs free energy  
 $i_a, i_c$  = Anodic and cathodic current density,  $\text{A}/\text{cm}^2$   
 $i_0$  = Exchange current density,  $\text{A}/\text{cm}^2$   
 $i_T$  = Total current in a system,  $\text{A}/\text{cm}^2$   
 $i_L$  = Limiting current density,  $\text{A}/\text{cm}^2$   
 $i_{avg}$  = Average current density to the system,  $\text{A}/\text{cm}^2$   
 $i_p$  = Peak current,  $\text{A}$   
 $i$  = Current density,  $\text{A}/\text{cm}^2$   
 $K_c$  = Constant  
 $k$  = Boltzmann's constant,  $1.38 \times 10^{-23}$   $\text{J}/\text{K}$   
 $K$  = Heterogeneous rate constant,  $\text{cm}/\text{s}$   
 $k_f, k_b$  = Rate constant for forward and backward reaction,  $\text{cm}/\text{s}$



$k_m$  = Mass transport coefficient =  $i_L / nFC$ , m/s  
 $k_p$  = Constant in Vogel-Tamman-Fulcher equation  
 $L$  = Total length of the cathode, cm  
 $M$  = Molecular weight of the deposited metal in the cathode  
 $M^{n+}$  = Ions of metal M in aqueous electrolyte  
 $m$  = An integer in Bragg's law  
 $N_A$  = Avogadro constant,  $6.02 \times 10^{23} \text{ mol}^{-1}$   
 $N_{M^{n+}}$  = Flux of the species at the electrode surface,  $\text{mol/m}^2\text{s}$   
 $n$  = Number of electrons  
 $n'$  = no. of carrier ions  
 $Q$  = Electric charge passed through an electrochemical cell, Coulomb  
 $R$  = Gas constant, 8.3144 joule / mol-K  
 $r'$  = Stokes radius, nm  
 $s$  = Scan rate, V/s  
 $T$  = Absolute temperature, K  
 $T_g$  = Glass transition temperature, K  
 $t$  = Time, s  
 $U_0$  = limiting velocity at the RCE, cm/s  
 $U$  = Velocity, cm/s  
 $u$  = mobility of an ion  
 $V_y, V_r$  = Velocity profile near and away to the RDE, cm/s  
 $V$  = Volume of the deposit,  $\text{cm}^3$   
 $W$  = Weight of the a product of electrolysis, g  
 $x$  = Distance along the rotating cylinder cathode, cm  
 $Z$  = Electrochemical equivalent

**Greek letter:**

$\alpha, \beta, \gamma$  = Angle between a, b, c  
 $\alpha_a, \alpha_c$  = Transfer coefficient  
 $\beta'$  = Peak broadening in a XRD scan  
 $\eta$  = Overpotential, V  
 $\eta_Q$  = Current efficiency  
 $\Delta$  = Deposit thickness, cm  
 $\rho$  = Fluid density,  $\text{g/cm}^3$   
 $\mu$  = Dynamic viscosity, cP or Pa-s  
 $\mu_\infty$  = Viscosity at infinite temperature, Pa-s or g/cm-s  
 $\nu$  = Kinematic viscosity =  $\mu/\rho$ ,  $\text{cm}^2/\text{sec}$   
 $\omega$  = Rotation speed of the RCE or RDE, revolution per minute

$\delta$  = Diffusion layer thickness, cm

$\lambda$  = Wavelength, Å

$\theta$  = Angle between the incident ray and scattering planes, degree

$\varepsilon$  = Inhomogenous strain within the material

$\sigma$  = Ionic conductivity, mS/cm

$\tau$  = Shear stress, Pa

$\gamma_s$  = Shear rate, s<sup>-1</sup>

$\gamma_i'$  = Activity coefficient

### Dimensionless groups:

$Sh = (k_m d)/D$  : Sherwood number

$Re = (U d)/\nu$  : Reynolds number

$Sc = \nu / D$  : Schmidt number

### Abbreviated anion, cations and ILs :

[AlCl<sub>3</sub>-MeEtimCl] : Aluminium chloride-1-methyl-3-ethylimidazolium chloride

[AlCl<sub>3</sub>-BuPyCl]: Aluminium chloride-N-(n-butyl)pyridinium chloride

[AlCl<sub>3</sub>-MePyCl] : Aluminium chloride-N-methylpyridinium chloride

BPCI : 1-butylpyridinium chloride

BMICI : 1-butyl-3-methylimidazolium chloride

BP : N-Butylpyridinium

BuPyCl : N-(n-butyl)pyridinium chloride

[BMP-Tf<sub>2</sub>N] : 1-butyl-1-methylpyrrolidinium bis(trifluoromethylsulfonyl)amide

[BMI-PF<sub>6</sub>] : 1-butyl-1-methylimidazolium hexafluorophosphate

[BMI-Tf<sub>2</sub>N] : 1-butyl-1-methylimidazolium bis(trifluoromethylsulfonyl)imide

[BMP-Tf<sub>2</sub>N] : 1-butyl-1-methylpyrrolidinium-bis(trifluoromethylsulfonyl) imide

CF<sub>3</sub>SO<sub>3</sub><sup>-</sup> : Tri fluoromethane sulfonic acid

(CF<sub>3</sub>SO<sub>2</sub>)<sub>2</sub>N<sup>-</sup> or Tf<sub>2</sub>N : Bis trifluoromethylsulfonyl imide

[EMI-Tf<sub>2</sub>N] : 1-ethyl-3-methylimidazolium bis(trifluoromethylsulonyl)imide (bistriflimide)

[Cu(MeCN)<sub>4</sub>-Tf<sub>2</sub>N] : Tetrakis(acetonitrile) copper(I) bis(trifluoromethylsulonyl)imide (bistriflimide)

[Cu(PhCN)<sub>2</sub>-Tf<sub>2</sub>N] : bis(benzonitrile) copper(I) bis(trifluoromethylsulonyl)imide (bistriflimide)

[Cu(CH<sub>3</sub>CN)<sub>2</sub>-Tf<sub>2</sub>N] : bis(aminonitrile) copper(I) bis(trifluoromethylsulonyl)imide (bistriflimide)

[C<sub>4</sub>mpyrr-DCA] : N-butyl-N-methyl-pyrrolidinium dicyanamide

[C<sub>4</sub>mpyrr-Tf<sub>2</sub>N] : N-butyl-N-methyl-pyrrolidinium bis(trifluoromethylsulfonyl)imide

EMI : 1-ethyl-3-methylimidazolium

EMICl : 1-ethyl-3-methylimidazolium chloride  
EtPyBr : Ethylpyridinium bromide  
[EMI-Tf<sub>2</sub>N] : 1-ethyl-3-methylimidazolium bis[(trifluoromethyl)sulfonyl]amide  
[EMI-DCA] : 1-ethyl-3-methylimidazolium dicyanide  
[EMI-BF<sub>4</sub>] : 1-ethyl-3-methylimidazolium tetrafluoroborate  
[Et<sub>3</sub>BuN-Tf<sub>2</sub>N] : Triethylbutylammonium bis(trifluoromethylsulfonyl)imide)  
[FcC<sub>1</sub>MIm-Tf<sub>2</sub>N] : 1-ferrocenylmethyl-3-methylimidazolium  
bis(trifluoromethylsulfonyl)imide (bistriflimide)  
MeCN : acetonitrile  
MePyCl : N-methylpyridinium chloride  
MeEtImCl : 1-methyl-3-ethylimidazolium chloride  
MP : Methylpyridinium  
PhCN : Benzonitrile  
[TMHA-Tf<sub>2</sub>N] : Trimethyl-n-hexylammonium bis((trifluoro-methyl)sulfonyl)amide  
[TOMAC-ChCl<sub>3</sub>] : Tri-n-octylmethylammonium chloride/chloroform  
[ZnCl<sub>2</sub>-EMIC] : Zinc chloride-1-ethyl-3-methyl-imidazolium chloride

## List of figures

Page no.

### Chapter 1

Figure 1-1 : Worldwide Cu consumption change in a time period of twenty years, data for 2008 is estimated (e) from three quarters of the year .....	2
Figure 1-2 : Phase diagram of Cu-Sn binary system showing different phases with varying temperature .....	4
Figure 1-3 : Formation of IL from the available anions and cations .....	12
Figure 1-4 : A range of cations which were used for ILs preparation electrodeposition was carried out from these ILs .....	12
Figure 1-5 : Schematic representation of eutectic point on a two component phase diagram .....	18

### Chapter 2

Figure 2-1 : General electrochemical cell .....	44
Figure 2-2 : Structure of the electrochemical double layer showing the inner and outer Helmholtz plane and diffusion layer after outer Helmholtz plane (OHP) .....	45
Figure 2-3 : The configuration and orientation of different anions and cation in bulk of the electrolyte and near a strongly charged interface .....	46
Figure 2-4 : Tafel plots for anodic and cathodic process .....	51
Figure 2-5 : Variation of concentration and formation of diffusion layer .....	52
Figure 2-6 : Current-potential relationship during deposition of $M_1$ alloy where parent metals are $M_2$ and $M_3$ .....	56
Figure 2-7 : Alloy deposition under different conditions .....	57
Figure 2-8 : Crystalline plan and crystalline structure .....	59
Figure 2-9 : Diffracted x-ray pattern for a metal and determination of $\beta'$ from FWHM .....	60

### Chapter 3

Figure 3-1 : Re-crystallization of the prepared IL at 15 °C .....	65
Figure 3-2 : Conductivity probe along with bench meter .....	67
Figure 3-3 : The viscosity measurement setup .....	68

Figure 3-4 : Side view of the three electrode jacketed cell used for electrochemical characterization showing the position of working electrode, counter electrode and reference electrode .....	70
Figure 3-5 : Rotating disc electrode .....	71
Figure 3-6 : Tip of the rotating disk electrode .....	72
Figure 3-7 : The potential to the system as a function time .....	74
Figure 3-8 : Arrangement for potentiostatic/galvanostatic deposition experiments showing the connection between different instrument and three electrode .....	77
Figure 3-9 : Schematic diagram of a Rota Hull cell .....	79
Figure 3-10 : Metal deposition along the cathode length in a Rota hull cell .....	81
Figure 3-11 : Furnace for heat treatments showing the thermocouple to note the temperature increase and the glass tube for sample insertion in the furnace and the rubber tube for N <sub>2</sub> flow was connected to the both ends of this glass tube .....	82
Figure 3-12 : Schematic diagram of scanning electron microscope (SEM) .....	85
Figure 3-13 : Details of the XRD tube along with position of the substrate surface for XRD analysis .....	86

#### **Chapter 4**

Figure 4-1 : A typical variation of density measurements for ethaline melt as a function of temperature .....	91
Figure 4-2 : Conductivity and viscosity measurements as a function of temperature for ethaline melt .....	92
Figure 4-3 : Conductivity and viscosity measurements as a function of temperature according to Arrhenius model for ethaline melt .....	93
Figure 4-4 : Density measurements for ethaline melt with and without metal salts as a function of temperature .....	95
Figure 4-5 : Viscosity measurements for ethaline melt with and without metal salts as a function of temperature .....	96
Figure 4-6 : Conductivity measurements for ethaline melt with and without metal salts as a function of temperature .....	97
Figure 4-7 : Viscosity measurements for ethaline melt with and without metal salts as a function of temperature for Arrhenius model comparison .....	98
Figure 4-8 : Conductivity measurements for ethaline melt with and without metal salts as a function of temperature for Arrhenius model comparison .....	98

Figure 4-9 : Density measurements for ethaline melt with two metal salts as a function of temperature .....	99
Figure 4-10 : Conductivity measurements for ethaline melt with two metal salts as a function of temperature .....	100
Figure 4-11 : Conductivity and viscosity measurements as a function of temperature according to VTF model for ethaline melt .....	101
 <b><u>Chapter 5</u></b>	
Figure 5-1 : Voltammetry on ethaline melt using different RDE speeds and a range of temperatures .....	106
Figure 5-2 : The formal potential plot with concentration change of $\text{CuCl}_2 \cdot 2\text{H}_2\text{O}$ for $\text{Cu}^{2+}/\text{Cu}^+$ couple .....	107
Figure 5-3 : Voltammetry for ethaline melt with Cu ion on static Pt RDE at 25 °C using various scan rates .....	108
Figure 5-4 : The relationship between the peak current and scan rate to determine diffusion co-efficient of $\text{Cu}^{2+}$ in ethaline melt .....	110
Figure 5-5: The relationship between the peak current and scan rate to determine diffusion co-efficient of $\text{Cu}^+$ in ethaline melt .....	111
Figure 5-6: Voltammetry for ethaline melt with Cu ion at various RDE speeds at 25 °C .....	112
Figure 5-7 : The relationship between the two reduction steps during Cu studies .....	113
Figure 5-8 : Verification of Levich equation by limiting current vs. concentration of Cu ions at various RDE sppeds .....	114
Figure 5-9 : Verification of Levich equation for each temperature .....	116
Figure 5-10 : The formal potential plot with concentration change of $\text{SnCl}_2 \cdot 2\text{H}_2\text{O}$ for $\text{Sn}^{2+}/\text{Sn}^0$ couple .....	118
Figure 5-11 : Voltammetry at various scan rates using a static Pt RDE at 25 °C for ethaline melt containing 0.05 M $\text{SnCl}_2 \cdot 2\text{H}_2\text{O}$ .....	119
Figure 5-12 : The relationship between the peak current and scan rate to determine diffusion co-efficient of $\text{Sn}^{2+}$ in ethaline melt .....	120
Figure 5-13 : Voltammetry for ethaline melt containing 0.01 M $\text{SnCl}_2 \cdot 2\text{H}_2\text{O}$ at 35 °C using various RDE speeds .....	121
Figure 5-14 : Mass transfer correlation for individual metal system using various dimensionless numbers .....	123
Figure 5-15 : The cathodic and anodic potential range from voltammetry Scans at agitated condition used for current efficiency calculation .....	124

Figure 5-16 : Mass transfer correlation for individual metal system using various dimensionless numbers, for Levich system .....	126
--	-----

## **Chapter 6**

Figure 6-1 : Cu deposit obtained by potentiostatic method at various concentrations .....	131
Figure 6-2 : Cu deposit obtained by potentiostatic method at various RDE speed .....	132
Figure 6-3 : Cu deposit obtained at higher temperature .....	132
Figure 6-4 : Cu deposit obtained by galvanostatic method at various concentrations .....	133
Figure 6-5 : Monitoring the variation in colour of the ethaline melt during several electrodeposition experiment to test the stability of the bath .....	136
Figure 6-6 : Cross sectional view of the deposited Cu .....	137
Figure 6-7 : EDAX spectra of the deposited Cu .....	137
Figure 6-8 : XRD pattern of the Cu deposit .....	138
Figure 6-9 : Zoomed peaks from XRD pattern which were used for grain size calculation for the Cu deposit .....	139
Figure 6-10 : Sn deposit obtained by potentiostatic method at various duration .....	141
Figure 6-11 : Sn deposit obtained by galvanostatic method at various current density .....	142
Figure 6-12 : Cross sectional view of the deposited Sn .....	145
Figure 6-13 : EDAX spectra of the deposited Sn .....	146
Figure 6-14 : XRD pattern of the Sn deposit .....	147
Figure 6-15 : Zoomed peaks from XRD pattern which were used for grain size calculation for the Sn deposit .....	148

## **Chapter 7**

Figure 7-1 : Deposit obtained from the electrolytes with different concentrations of Cu-Sn in electrolyte using Rota-Hull cell .....	156
Figure 7-2 : Voltammetry on ethaline melt containing various concentration of Cu salt with constant concentration of Sn salt .....	159
Figure 7-3 : Voltammetry on 0.1 M Sn salt .....	159
Figure 7-4 : Anodic stripping voltammetry on 0.04 M Cu salt-0.1 M Sn salt .....	160
Figure 7-5 : Cu-Sn alloy deposition by potentiostatic and galvanostatic method .....	163

Figure 7-6 : Cross sectional view of the as-deposited and annealed Cu-Sn alloy deposit .....	164
Figure 7-7: EDAX of as-deposited and annealed Cu-Sn alloy .....	165
Figure 7-8 : XRD pattern of the as-deposited Cu-Sn alloy .....	166
Figure 7-9 : Zoomed peaks from XRD pattern which were used for grain size calculation for the as-deposited Cu-Sn alloy .....	167
Figure 7-10 : XRD pattern of the annealed Cu-Sn alloy .....	168
Figure 7-11 : Zoomed peaks from XRD pattern which were used for grain size calculation for the annealed Cu-Sn alloy .....	169
Figure 7-12 : The colour change in a time span of 2month, for ethaline melt containing various concentration of hydrated Cu and Sn metals .....	170
Figure 7-13 : Voltammetry for stability test on ethaline melt containing Cu-Sn salts without any deposition experiments .....	171
Figure 7-14 : Voltammetry for stability test on ethaline melt containing Cu-Sn salts after several deposition experiments .....	172
Figure 7-15 : Formed complex in mixed system containing Cu and Sn in ChCl IL electrolyte .....	174



## List of tables

Page no.

### Chapter 1

Table 1.1: Operating parameters for Cu plating from various aqueous baths .....	7
Table 1.2 : Operating parameters for tin plating from various acidic and alkaline baths .....	9
Table 1.3 : Operating parameters for copper-tin alloy plating from various acidic and alkaline baths .....	10
Table 1.4 : A range of anions which were used for ILs preparation, these ILs are used for electrodeposition .....	13
Table 1.5 : Cations used for Cu, Sn and their alloys deposition .....	14
Table 1.6 : Eutectic based ILs used for various metal deposition .....	19
Table 1.7 : Choline chloride based ILs used for various metal deposition, including Cu and Sn .....	21
Table 1.8 : Assessment of electrolytes for price and bulk supply comparison ...	22

### Chapter 2

Table 2.1: Formal potential values Cu & Sn interaction in chloroaluminate IL electrolyte at 40 °C .....	49
---	----

### Chapter 3

Table 3.1: Electrolytes used for different studies on metal and alloy system .....	65
Table 3.2: Electrolytes used for density measurement .....	66
Table 3.3: Electrolytes used for conductivity measurement .....	67
Table 3.4: Electrolytes used for viscosity measurement .....	69
Table 3.5: Voltammetry experiments in IL electrolytes with and without metallic salts .....	75
Table 3.6: Anodic Stripping Voltammetry experiments in IL electrolytes .....	76
Table 3.7: Potentiostatic deposition of Cu, Sn and Cu-Sn alloy .....	78
Table 3.8: Galvanostatic deposition of Cu, Sn and Cu-Sn alloy .....	78

### Chapter 4

Table 4.1 : Formation of different Cu and Sn complexes in various ILs .....	90
Table 4.2 : The variation in the value of different physical parameters with change in metal ion concentrations and temperature .....	94
Table 4.3 : Reactions and Speciation in Ethaline with and without metal salts ...	96

## **Chapter 6**

Table 6.1 : Long term experiments for Cu deposition .....	135
Table 6.2 : Deposition as obtained by varying current density and RDE speed for galvanostatic Sn deposition .....	143
Table 6.3 : Long term experiments for Sn deposition .....	144

## **Chapter 7**

Table 7.1 : Comparison of the charge ratios obtained from voltammetry scans and EDAX analysis .....	161
Table 7.2 : Comparative study of various parameters of individual metal and alloy deposition process .....	176

# Chapter 1- INTRODUCTION

## 1.1. Background

In human history, the first metal ever extracted and used was copper (Cu) which had important contributions in improving the society since 8000 B.C. During the time of 8000 to 5000 B.C., Cu was used to produce ornaments, coins and tools <sup>[1]</sup>. With time Cu became material of choice for various domestic, industrial and high-technological applications.

The use of Cu became popular due to its properties like corrosion resistance, good conductor of heat and electricity. The physical properties like malleability and softness make it more useful in many other applications. Now-a-days Cu is found in many systems like building construction, power generation and transmission, electronic components, industrial machines and vehicles <sup>[1]</sup>. In daily life, use of Cu is found in wiring and plumbing systems, heating and cooling gadgets and telecommunication links. In automobile industries, Cu is used in motors components, wiring, radiators, connectors, brakes and bearings <sup>[1]</sup>. Moreover due to the antimicrobial properties of Cu, this metal is applied on frequently touched surfaces <sup>[1]</sup>.

In nature Cu is found in various ores and 90% of primary Cu is mainly produced from sulphide ores such as chalcopyrite ( $\text{CuFeS}_2$ ), chalcocite ( $\text{Cu}_2\text{S}$ ) and bornite ( $\text{Cu}_5\text{FeS}_4$ ) <sup>[2]</sup>. Remaining 10% is produced from oxides, silicates and sulphate ores <sup>[2]</sup>. From these ores Cu is extracted and refined through several metallurgical steps. At first ores are finely ground, then concentrated by floatation and later on smelted at high temperature and finally refined of impurities. This Cu is used to produce wires, cables, sheets, strips, plates, foils, rods, bars, tubing, extrusion, casting and powdery shapes <sup>[2]</sup> which are usually known as mill or foundry products.

According to archaeological evidence, tin (Sn) had been used by mankind from past 3500 years <sup>[3]</sup>. However, in the earliest period this metal was not used in the elemental form <sup>[3]</sup>. Tin became an important metal as this metal can be used to fabricate tools, weapons and jewellery <sup>[4]</sup>. It is a good corrosion resistant, soft and malleable metal. This metal is used as protective coating on other metals due to its corrosion resistance properties <sup>[5]</sup>. This metal is mainly used as coating for steel sheet which offers non-toxic corrosion protection <sup>[3]</sup>. In addition to this it is also widely used for decorative purpose and to produce solders <sup>[3]</sup>.

In nature Sn was found in cassiterite mineral an oxide ore ( $\text{SnO}_2$ ) of Sn <sup>[3]</sup>. This mineral is one of the denser mineral among all mineral extracted in world. The density of this ore helps in extracting the ores from the layers by mining <sup>[3]</sup>. For metal extraction

the ore is smelted in the blast or reverberatory furnace with carbon. For various other ores like limestone, silica and salt are used during extraction of Sn. It was found that below temperature of 13.2 °C, the colour of Sn is appeared as grey while at elevated temperature white Sn is obtained due to its allotropic nature <sup>[5]</sup>. For industrial applications these white tin is used.

The picture of worldwide supply and demand for Cu has changed lots in last 25 years. This is due to the increase in demand in the developing countries. The United States Geological Survey (USGS) studied during the period of 1980 to 2008 and their studies indicated an increase in trend for Cu consumption both in China and India <sup>[1]</sup>. The Cu consumption worldwide in this time frame is shown in the figure 1-1. South America is known for highest Cu producer in the world and total 53% of Cu is produced from here <sup>[1]</sup>. Interestingly, Cu can be recycled for further use without disturbing the chemical or physical properties and one third of the consumed Cu is recycled metal <sup>[1,2]</sup>. The global mine production of Cu in 2010 and 2011 (estimated) was in range of 15,900 to 16,100 metric tons <sup>[6]</sup>.

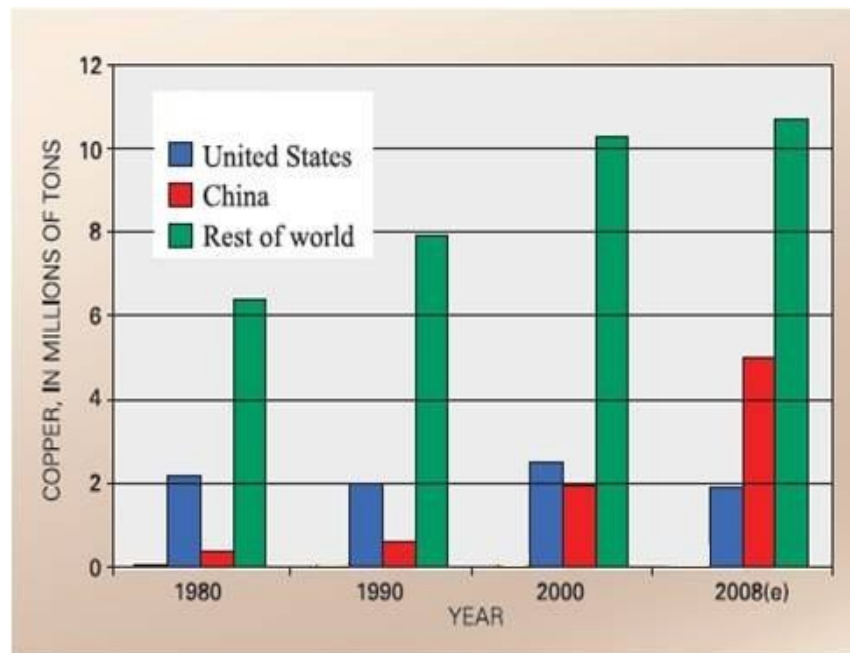


Figure 1-1 : Worldwide Cu consumption change in a time period of twenty years, data for 2008 is estimated (e) from three quarters of the year, adapted from ref. <sup>[1]</sup>

Compared to Cu, Sn production is very small and the availability of this mineral is 0.001% of earth's crust <sup>[5]</sup>. South East Asia mainly Malaysia, Indonesia and Thailand and then Bolivia, Brazil and Nigeria together produces 93% of the Sn in 20<sup>th</sup> century <sup>[3]</sup>. Currently China, Peru and Indonesia produce 99% of the Sn <sup>[3]</sup>. Another source of Sn is refinement of the metal from scrap materials <sup>[7]</sup>. The annual consumptions of Sn are highest in USA, Japan and EU countries <sup>[3]</sup>. The global Sn consumption is reported as 370,000 tonnes in 2007 and it is expected that consumption of Sn will reach to 400,000

tonnes by 2015 <sup>[4]</sup>. In 2011, the global mine production of Sn was 275,029 tonnes and through recycling of various forms of Sn above 139,000 tonnes of metals was achieved.

Official price for Cu and Sn is reported by London Metal Exchange in July 2011 as 9606 US\$/metric ton and 27260 US\$/metric ton respectively. The reservation of mine production for Cu and Sn was reported as 690,000 metric tons and 4,800,000 metric tons respectively <sup>[6]</sup>. To reduce the usage of the individual metals, their alloy was proposed to be more economic than their individual usage.

Pure Cu with impurity of one or more metals showed superior physical properties compared to the purer one. By varying the composition of these impurities the characteristics of the alloys can be controlled and are used for specified applications.

Bronze, an alloy of Cu and Sn which generated the Bronze Age at about 3000 B.C <sup>[1,8]</sup>, is harder than Cu and has a lower melting point which leads to many advantages including easy melting and casting <sup>[8]</sup>. During Bronze Age, this alloy was used to manufacture tools and weapons. This alloy was preferable over stones due to the strength and hardness of the product <sup>[8]</sup>. This was fabricated by smelting process carried out in crucibles or furnaces where ore is converted in to alloy through heating process <sup>[8-9]</sup>.

Bronze has wide range of applications in arts such as casting, engraving and forgings. This is also used in casting of gun barrels, bells, piston rings, pump bodies, valves, gear, coins, medals and ornaments <sup>[10-11]</sup>. It has wide range of applications in mechanical engineering for its properties like antifriction and corrosion resistance <sup>[11-12]</sup>. Recently this is also used in electronics industries to develop lead free solder and also producing smart materials. Shape memory alloy is one of such smart materials which showed its potential applications in many fields. In a sense bronze has many of the advantages over Cu, whilst having better mechanical properties.

To understand the Cu-Sn binary system more deeply a phase diagram of this binary system is essential. The phase diagram for Cu-Sn binary system <sup>[13-14]</sup> is presented in fig. 1-2 below. The phase diagram will help to determine various phases of the alloy system within a range of temperatures. Generally  $Cu_6Sn_5$  formed from the interfacial reaction between Cu and Sn at room temperature (as shown by yellow highlight in fig. 1-2). With increase in deposit thickness the growth of this intermediate phase changed to diffusion controlled from reaction controlled. For thicker layer the atomic flux across the layers was reduced and rate of the reaction was controlled by diffusion <sup>[13]</sup>. When annealed at 100 °C, no change in intermetallic compound was found. Annealing at a temperature 150 °C,  $Cu_3Sn$  phase (as shown by orange highlight

in fig. 1-2) was appeared. This phase was formed by the interfacial reaction between  $\text{Cu}_6\text{Sn}_5$  and Cu [13]. With increase in annealing temperature these intermetallic phases converted into phases like  $\text{Cu}_{10}\text{Sn}_3$  and  $\text{Cu}_{41}\text{Sn}_{11}$ . Different physical properties and crystalline structure, lattice parameters of the obtained alloy was determined using the phase diagram. From this phase diagram the composition of the parent metals, the nature and the applications of the obtained deposits could be determined.

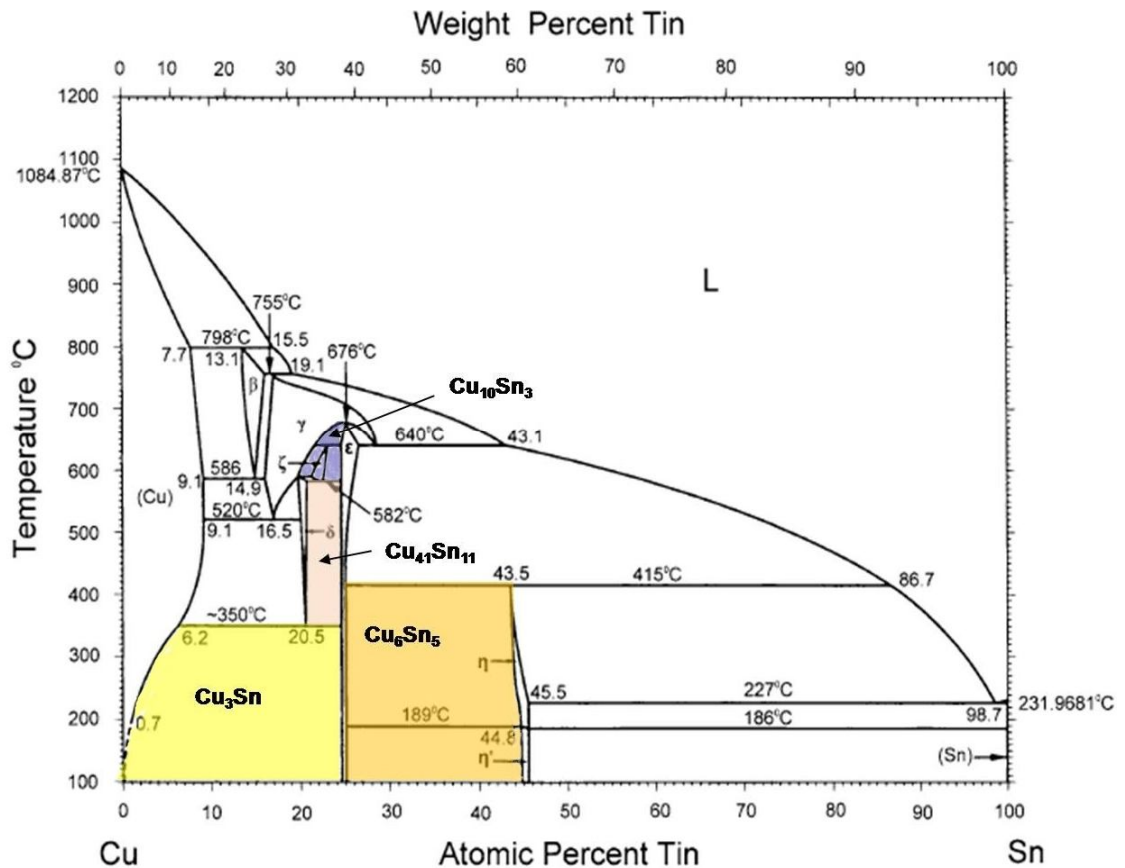


Figure 1-2 : The phase diagram of Cu-Sn binary system [13-14] showing different phases with varying temperature

To develop appropriate alloy for specific applications exact atomic percent of individual elements is very important. The desired phase of the alloy depends on the elemental composition and temperature which is found in the phase diagram of the system. Normally alloys are fabricated using metallurgical and coating processes. In large scale metallurgical process percentage of the individual elements sometime differs, as a result yield for the product get hampered. However, in coating processes the approximate percentage of individual element could be controlled very precisely which helps in obtaining the exact alloy composition.

Again metallurgical process is carried out in very high temperature, thus the obtained alloy suffers from rapid grain growth and poorer fatigue properties [15]. Other drawbacks of metallurgical process are contamination from crucible and oxygen and requirement of multiple re-melts for desired homogeneity in the mixture of materials. In

addition the structures with smaller dimension are difficult to manufacture at commercial scale using this technique <sup>[16]</sup>. As this process cannot be performed in the normal atmospheric ambient it became an expensive fabrication process. Using coating process all these limitations can be resolved, so the coating process is much more preferable for obtaining an alloy film.

## 1.2. Fabrication techniques and their limitations

### 1.2.1. Coating processes

Coating processes are very popular for fabrication of metallic layers and their alloys. Usually films are fabricated using coating processes. These metallic films are achieved by vapour deposition process or chemical reduction process. Depending on the involvement of water in the fabrication process, these methods are termed as either dry process or wet process.

#### 1.2.1.1. Vapour deposition processes

Vapour deposition processes is divided into two categories, physical vapour deposition (PVD) process and chemical vapour deposition (CVD) process <sup>[17]</sup>. The physical deposition process can also be identified as vacuum deposition process and the films are deposited by condensation of vapour form of material over various substrate surface. The PVD process is classified as evaporation of materials by resistive heating or electron beam heating and sputtering from target materials <sup>[17]</sup>. In CVD process, the substrate is exposed to volatile precursors that reacts and decompose on to the substrate surface to generate the desired deposit. In this fabrication process the films are obtained without involving any water. As a result all of these are dry process.

Fabrication of individual metals and their alloys by coating processes was carried out to improve the properties of the materials <sup>[16,18-19]</sup>. However, the deposit obtained by coating process suffers from porosity, carbon, hydrogen and oxygen contaminations <sup>[20]</sup>. During the fabrication process it is necessary to maintain vacuum or inert atmosphere which increases the cost of the process. In addition this process consumes lot of time and power throughout its processing period due to stabilize the system to reach in its operative mode <sup>[17, 21]</sup>.

#### 1.2.1.2. Reduction processes

Reduction process is one of the important coating process, where metal deposition is achieved by using electrodeposition or electroless deposition process. In the case of electroless deposition process no electricity is applied externally and the

deposition is initiated through auto catalytic process by sensitizing and activating the substrate surface <sup>[17,22]</sup>. Thus, in this process the substrate simultaneously acts as anode and cathode. Again for deposition of metal like Ni using this process it requires high temperature for successful operation <sup>[23]</sup>. As the deposition is initiated by auto catalytic process, control on deposition is very difficult. Thus, alloys with the desired proportions of the parent metals are very hard to achieve using this process.

In electroplating process, electricity is applied from external source to initiate the reduction process to achieve the desired metal or alloy deposition. It is a well established technology from long time. This technique is popular for its simplicity of operation that involves simple equipment and is appropriate for mass production, such as the plating of steel sheets or barrel plating of small objects. Another advantage of this process is that the deposition on complex shapes can also be achieved by using the electrolytic systems with high throwing power. Throwing power is the ability of the electrolyte to deposit as nearly as possible a uniform deposit across the electrode surface irrespective of the electrode shape <sup>[3,24-25]</sup>. Electrolytes with high throwing power produce a uniform deposit on the outer plane of the substrate or at the base of valleys or cracks <sup>[25]</sup>. The throwing power (TP) is calculated <sup>[24]</sup> using eqn. 1.1,

$$TP = \frac{R-M}{R-1} \times 100 (\%) \quad (1.1)$$

Where, R= ratio of the distances between a central anode and two equipotential cathodes at unequal distances, M= measured deposit thickness or mass ratio.

The deposit thickness can be varied from the scale range of nanometres to centimetres. Moreover, electrodeposition process is very useful in fabrication of uniform single layer or multilayered coatings of metals, alloys and metal matrix composites. This process can be scaled up to deposit on large parts and deposits can be achieved at room temperature also <sup>[22]</sup>. Thus, electrodeposition seems to be a good choice for an economic and commercial stand point. As the deposition is obtained by involving a liquid medium, the coating process is called as wet process.

### 1.3. Industrial aqueous electrolyte for deposition of individual metals and alloy

Electrodeposition of Cu, Sn and Cu-Sn alloy was carried out from various acidic and alkaline baths for many years <sup>[22]</sup>. These electrolytes are well established due to high throwing power and operation at high cathode current density. It was further reported by the researchers that the cathode current efficiency of these systems ranges in between 25-100 % <sup>[22]</sup>. Most of these bath components were reported in the literature and are easily available in market at comparatively cheap rate. Detail studies on these various popular acidic and alkaline baths for individual metal and alloy deposition is presented below.



## 1.3.1. Copper deposition

The electrodeposited Cu is used in printing wiring boards, microelectronics, electroforming, diamond turning, heat exchangers, items for military and aerospace engineering [22]. Cu was deposited successfully on various substrates like steel, zinc and aluminium. Mainly four types of aqueous electrolytes such as acid bath, cyanide bath, alkaline non-cyanide bath, pyrophosphate bath are used for deposition. The details of the bath composition and plating performances are presented shown in the table 1.1.

Table 1.1: Operating parameters for Cu plating from various aqueous baths [22]

Operating parameters	Acid bath	Cyanide bath	Alkaline noncyanide bath	Pyrophosphate bath
Anode used	soluble (copper sheets)	soluble (copper sheets)	Soluble [(oxygen free high conductivity (OFHC) copper)]	Soluble (OFHC copper, electrolytic sheet, rolled electrolytic copper, cast anodes of good purity)
Temperature (°C)	32-43	40-75	38-65	50-60
Additives	Benzotriazole [26-29], cadmium [30], Gelatine [31], thiourea [26-27, 32-33]	Organic amines, inorganic compounds containing metals, unsaturated alcohols, saccharin	-	Casein [35], glycocoll [35], glycerol [36-37], triethanolamine [36-37], sodium selenite [38]
pH	1.7	10-12	9-10.5	8-9
Cathode current density (A/cm <sup>2</sup> )	(16-22)x10 <sup>-2</sup>	(1-11)x10 <sup>-2</sup>	(0.5-3)x10 <sup>-2</sup>	(1-8)x10 <sup>-2</sup>
Applications	Electroforming, electrorefining, and electroplating [Plating of printed wiring board, semiconductor interconnect technology ]	Protect basis metal or promote adhesion, decorative plating, surface improvement	Heat treat masking barrier prior to carburizing, nitriding, through hardening	Selecting hardening operation like nitriding and carburizing, roll plating, minimizing hydrogen embrittlement
Plating performance	Fine grain structure, less stress, surface roughness, porosity, improved hardness and throwing power	Excellent adhesion, very bright deposits, good electrical conductivity and throwing power	Good mechanical properties with higher ductility, outstanding metal distribution, very good tolerance to common impurities	Excellent mechanical property

The plating electrolytic baths, especially cyanide and alkaline suffers from environmental, health and safety aspects [22]. All these aspects appeared from the chance of accidental acid spill out to the cyanide bath or cyanide bath spill out to the sewer system. Thus the waste treatment of cyanide bath is very important which is carried out in a tank under specific conditions [39]. The disposal of cyanide bath requires many other treatments like oxidation of cyanide, precipitation of heavy metals as an outcome the process becomes extremely expensive [40]. Moreover deposits obtained from cyanide bath were thin and not suitable for application like electroforming [22]. The alkaline bath suffers from other difficulties like sensitivity to impurity, difficult chemistry to control and high operating costs [22]. In addition to these, the use of different types of additives leads to very complex process. The obtained deposits often suffer from H<sub>2</sub> evolution and oxide formation during the deposition process [22].

### 1.3.2. Tin deposition

Electrodeposited Sn is widely used in food processing, shipping equipment, containers, pump parts, automotive pistons, electrical components, printed wiring boards and decorative purposes [22]. Deposition was carried out from acid baths based on fluoboric acid, sulfuric acid, phenolsulfonic acid (PSA), hydrochloric or hydrofluoric acid and methane sulfonic acid (MSA). Similarly popular alkaline baths are based on sodium stannate and potassium stannate. The operating parameters and plating performance from this acid and alkali based bath are listed in the table 1.2.

These baths suffer from number of limitations. The fluoboric and sulfuric acid bath suffer from their corrosive nature [22,41-42]. Other problems associated with sulfuric acid bath is reported as anode passivation at high current densities and oxidation of Sn(II) to Sn(IV) [22,41]. The PSA and halogen acid bath undergo sludge formation which results to tin loss and decrease in current efficiency [22]. As an outcome poor quality of the deposits were obtained. In case of alkaline baths hydrolysis of Sn(IV) occurs very often, thus deposition process suffers from SnO<sub>2</sub> and Sn(OH)<sub>6</sub> formation [22,43]. Moreover most of these baths require expensive waste treatment due to the use of various additives, reactant and formation of other toxic end products [22].

### 1.3.3. Copper-tin alloy deposition

The Cu-Sn alloy was also electrodeposited from various aqueous electrolytic baths. Electrodeposited Cu-Sn alloy from aqueous electrolytes are smooth, fine grained and the colour of deposit can be varied from silver white to yellow and red. The Cu content in the deposit was varied in the range of 12% - 95% [44]. The deposit

obtained are used as an under layer coating for variety of items like parts of automobiles, electric applications, radio and television equipment and to replace the white brass for Ni coating [44]. This alloy also have applications for decorative and corrosion resistance purposes [44]. The three types of aqueous electrolytes like acid bath, cyanide bath, and alkaline bath are used to deposit Cu-Sn alloy. The details of the bath composition and plating performances are shown in the table 1.3.

Table 1.2 : Operating parameters for tin plating from various acidic and alkaline baths

[22, 41-43,45-49]

Operating parameters	Fluoboric acid	Sulfuric acid	Phenolsulfonic acid	Hydrochloric or hydrofluoric acid	Methane sulfonic acid	Alkaline bath
Anode used	soluble (Pure tin)	soluble (Pure tin)	soluble/ insoluble	soluble	insoluble	soluble/ insoluble
Temperature (°C)	30-55	25-28	30-40	55-65	30-60	65-90
Additives	organic compound (peptone, gelatine)	organic compound (imidazoline , heterocyclic aldehydes)	ethoylated $\beta$ -naphthol-sulfonic acid	Naphthol sulfonic acid and polyalkylene	hydroquinone, organic compound	not required
pH	< 1	< 1	< 1	3-4	< 1	> 8
Cathode current density (A/cm <sup>2</sup> )	(1.08-324) x10 <sup>-2</sup>	(1.08-27) x10 <sup>-2</sup>	(216-540) x10 <sup>-2</sup>		(27-756) x10 <sup>-2</sup>	(0.54-43) x10 <sup>-2</sup>
Metal solubility	very soluble	less soluble with respect to other acid and alkaline baths	soluble		very soluble	soluble
Applications	high speed plating (rack and barrel, reel to reel plating)	reel to reel plating	pure tin in the continuous steel strip plating industry		high speed reel-to-reel and wire application	-
Plating performance	smooth, fine-grain deposits	matt, semi-bright to bright deposit	smooth deposits		satin, semi-bright and bright deposit	smooth deposits

Table 1.3 : Operating parameters for copper-tin alloy plating from various acidic and alkaline baths <sup>[44,50-54]</sup>

Operating parameters	Cyanide bath	Acid bath (oxalate, fluoroborate and sulphate)	Alkaline bath (tartarate, pyrophosphate,)
Anode used	Bimetallic anode system	Dual anode system	-
Temperature (°C)	40-65	23-70	60
Additives	Glycerine, sodium chloride, hydrogen peroxide, diethylenetriamine	Beta-naphthol, naphthalene sulfonic acid, thymol, gelatin	-
pH	9-14	-	9
Cathode current density (A/cm <sup>2</sup> )	$(2 - 10) \times 10^{-2}$	$(0.3 - 1.5) \times 10^{-2}$	$(0.4 - 1.1) \times 10^{-2}$
Applications	Suitable substitute for nickel plating compared to white brass, also used underneath chromium for different appliances like parts of automobiles, motorcycles, electronic uses, and radio and television equipment. As stop-offs in the nitriding of steel, for decorative applications for indoor use, for example bathroom fixtures, ashtrays, and tableware.		
Plating performance	Good in quality, bright hard, ductile, pore free and excellent corrosion resistant (10 to 84 % tin content )	Thin, fine grained deposits with 10-80% tin content	Smooth and fine grained, ranged in colour from yellow and red to silvery white (12 to 95 % of tin content)

One of the limitations of these baths was to obtain deposits on various substrate surfaces. In case of acidic oxalate bath, the electrolyte suffers from low solubility of the metal salts with less stability of the bath in the air. Moreover it is hard to maintain the composition of the bath with far apart deposition potential of the metals <sup>[44]</sup>. In addition to this the toxicity of the cyanide bath put constraints on successful applications <sup>[44]</sup>. These baths also require additives to obtain desired quality of deposits. As a result waste treatment for these electrolytes is essential which are expensive in nature.

To overcome the environmental impact along with health and safety issues the choice of the aqueous electrolytes for electroplating is not suitable in the present time. In order to overcome these complications from aqueous electrolytes a non-aqueous electrolyte such as ionic liquid (IL) is proposed for electrodeposition of Cu, Sn and Cu-Sn alloys.

#### 1.4. Ionic liquids

It was mentioned that in electroplating the most important factor is the choice of electrolyte. A suitable electrolyte should enclose properties like high solubility of metal

ions, high conductivity, high current efficiency and high throwing power, wide potential window, high rate of mass transfer, good electrochemical stability, non flammability and low cost <sup>[55]</sup>. After aqueous electrolytes, ionic liquids (ILs) have fulfilled most of these requirements for electroplating.

#### 1.4.1. Background

Studies on Room Temperature ionic liquids (RTILs) started long time ago. Walden <sup>[56]</sup> first reported about the room temperature molten salt in 1914. According to his report, ethylammonium nitrate  $[C_2H_5NH_3]NO_3$  melt was prepared from chemical reaction between the ethylamine and concentrated nitric acid. The melting point of this melt was obtained as 12 °C. Other RTILs were prepared by mixing the warm 1-ethyl pyridinium chloride with aluminium chloride as reported by Hurley and Weir <sup>[57]</sup>. In 1970s and 1980s, a detail research on RTILs from organic chloride-aluminium chloride ( $AlCl_3$ ) was carried out by Osteryoung et al. <sup>[58-59]</sup> and Hussey et al. <sup>[60-62]</sup>. With time a range of RTILs was developed for various applications.

RTILs became popular in the last decade due to its expanded range of applications in different fields <sup>[63-65]</sup>. For electrochemical applications RTILs are popular as electrolytes of lithium ion rechargeable batteries, fuel cells, capacitors, solar cells, actuators <sup>[63]</sup>. In metal finishing industries, a range of important metal such as Li, Na, Ti, Al studies were difficult or even impossible using aqueous electrolyte which was resolved using RTILs <sup>[66]</sup>. The range of electrodeposited metals and alloys from IL electrolytes is available from the reference <sup>[66]</sup>. Other than metals, semiconductors like GaAs, InSb, ZnTe, Ge <sup>[67]</sup> was studied using RTILs.

In general ILs are the salts having melting point below boiling point of water. An IL is defined as 'a liquid consisting solely of cations and anions with a melting point of 100 °C and below' <sup>[68]</sup>. A range of anions and cations were used for IL preparation. IL formation is described in fig. 1-3. It was further reported that with compared to classical molten salt electrolytes, ILs are less corrosive and easy to handle <sup>[69]</sup>.

Cations and anions are the main components for ILs and these influences different parameters of ILs. The physical properties of ILs are controlled by the cations. The stability and chemical reactivity of ILs are influenced by the anions <sup>[70]</sup>. Some of these anions and cations are shown in the table 1.4 and fig. 1-4. Anions and cations are specified by the application of the IL, for electrodeposition a specified range of anions and cations were used.

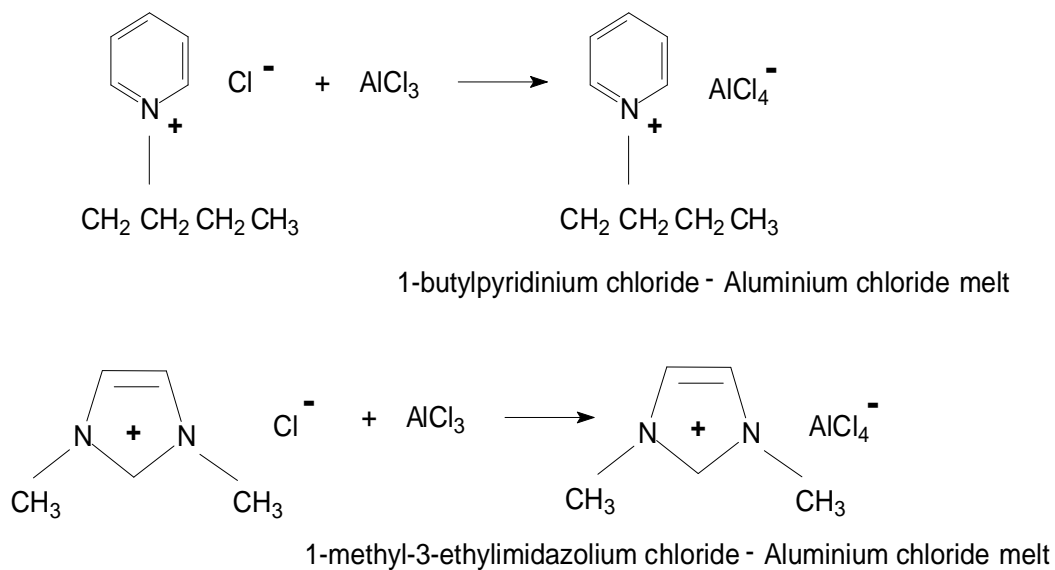


Figure 1-3 : Formation of IL from the available anions and cations, adapted from ref [71-72]

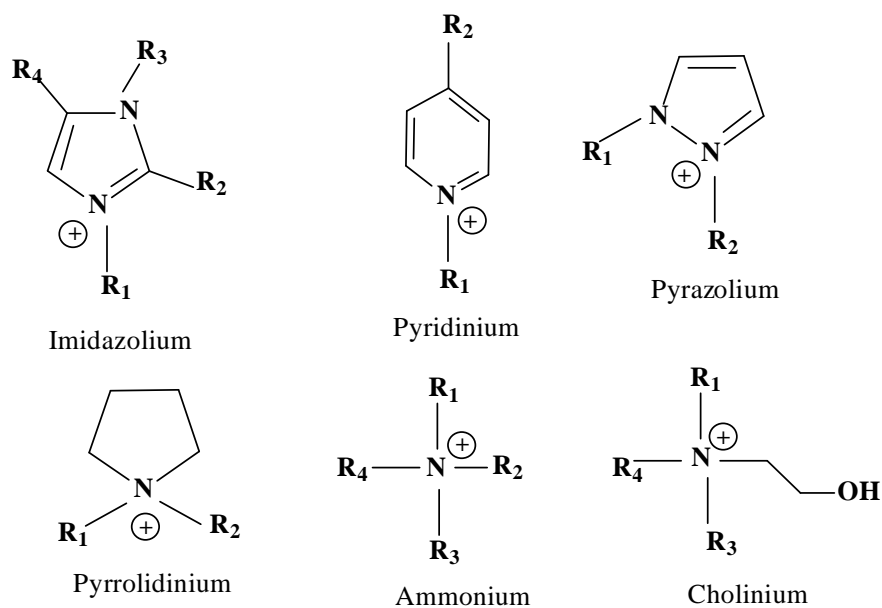


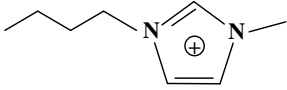
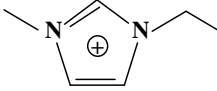
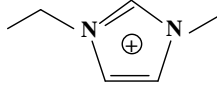
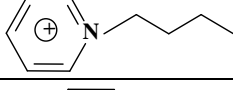
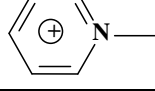
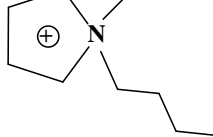
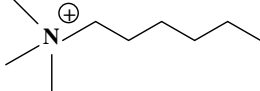
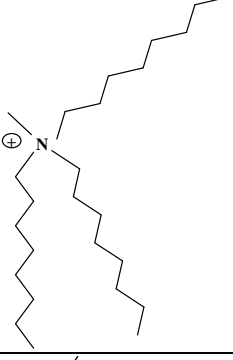
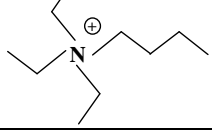
Figure 1-4 : A range of cations which were used for ILs preparation and electrodeposition was carried out from these ILs [65, 73-78]

Table 1.4 : A range of anions which were used for ILs preparation, these ILs are used for electrodeposition <sup>[64-65,70]</sup>

Anion	Chemical formula	Structure
Tetrafluoroborate	$\text{BF}_4^-$	
Hexafluorophosphate	$\text{PF}_6^-$	
Nitrate	$\text{NO}_3^-$	
Chloride	$\text{Cl}^-$	$\text{Cl}^\ominus$
Bromide	$\text{Br}^-$	$\text{Br}^\ominus$
Copper chloride	$\text{CuCl}_2^-$	
Hepta chlorodialuminate	$\text{Al}_2\text{Cl}_7^-$	
Trifluoromethane sulfonate	$\text{CF}_3\text{SO}_3^-$	
Bis(trifluoromethyl sulfonyl)imide	$(\text{CF}_3\text{SO}_2)_2\text{N}^-$ or $\text{TF}_2\text{N}$	
Dicyanamide	DCA	

For electrochemical studies on metals mainly chloroaluminate ( $\text{AlCl}_3$ ) melt was used from long time <sup>[66]</sup>. Other than  $\text{AlCl}_4^-$  anion,  $\text{SnCl}_2$ ,  $\text{BF}_4$ ,  $\text{PF}_6$ ,  $\text{Tf}_2\text{N}$ ,  $\text{ZnBr}_2$ ,  $\text{ZnCl}_2$ ,  $\text{NiCl}_2$ ,  $\text{NbCl}_5$ , DCA <sup>[66]</sup> anions were used for electrochemical study of metals. Using ILs based on chloroaluminate melt, the investigated metals were some first, second and third row transition-metal chloride complexes and metal ions <sup>[79-81]</sup>. The cations used by previous researchers for Cu, Sn and their alloy study are shown in the table 1.5.

Table 1.5 : Cations of the ILs which used for Cu, Sn and their alloys deposition [82-99]

Cation	Abbreviation	Structure
1-butyl-3-methylimidazolium	BMI	
1-methyl-3-ethylimidazolium	MeEtim	
1-ethyl-3-methylimidazolium	EMI	
1-butylpyridinium	BuPy	
N-methylpyridinium	MePy	
1-butyl-1-methylpyrrolidinium	BMP	
Trimethyl-n-hexylammonium	TMHA	
Tri-n-octylmethylammonium	TOMA	
Triethylbutylammonium	Et <sub>3</sub> BuN	

The anions and cations for metal study were chosen according to the nature of the IL required for the particular metal deposition. These anions and cations influences the physical properties like viscosity, conductivity of the electrolyte [70]. Generally cations are of bigger in size than the anions. The cations from organic species with low symmetry resulted ILs with low melting point. The chain length of the cation also influences the melting point of the IL. With increase in carbon atom numbers from 3 to



5 in the chain, decrease in melting point of the IL was observed. The radii of the cations vary in a wide range which influences viscosity of an IL and as a result this influences the mass transport of the metal ions [70]. At the time of deposition the cations are absorbed at the electrode surface as a result it influences the structure of the double layer and thickness of the helmholtz layer [70].

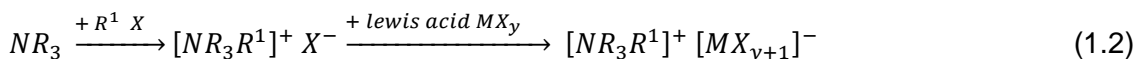
For electrodeposition the ILs with small and less symmetric anions are favourable which leads to low viscosity. If the negative charge of the anion do not participate on the hydrogen bonding then that also helps in achieving ILs with low viscosity. In addition to this by controlling the proportion of the anion, reduction potential and nucleation process of the metal ions also can be controlled [62]. Depending on the acidic, basic or neutral nature of the IL, it is likely to predict the possibility of the reduction of a particular metal [62]. This nature of the IL depends on the proportion of anion and cation used. The ILs used for electrodeposition purpose can be classified in several groups depending on the nature and behaviour of the ILs. Various classifications in the wide range of IL can be found in the literature by several authors [64-65, 69-70].

#### 1.4.2. *Synthesis and classification of Ionic liquids*

##### 1.4.2.1. Group I Ionic liquids

Group I ILs are based on aluminium halide (mainly chloride) and a halide salt of an organic cation. The mixture of halide salt  $Q^+X^-$  with a lewis acid  $MX_n$  forms a salt as  $Q^+MX_{n+1}^-$  [66]. In order to obtain a eutectic mixture involving  $AlCl_3$  various inorganic and organic compounds are used [57,59,100--107].

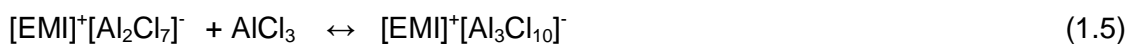
The haloaluminate-based ILs were produced by mixing halide salts with Al based lewis acids ( $AlX_3$ ,  $X=Cl, Br$ ) in two steps. Here preparation of the cation is the first step. The desired cation is achieved by reaction between imidazole or amine with haloalkane followed by addition of Al halide or lewis acid to the cation [66]. This reaction scheme [66] is shown in eqn. 1.2 below :



The above reaction is an exothermic reaction and the temperatures of the mixtures have to be monitored very carefully. An excessive amount of heat can cause the decomposition of the organic materials in electrolyte [66,108]. It is preferable to add the ingredient in small amounts for efficient stirring and heat dissipation. Purification is required for all starting materials and specifically oxygen and water content was

excluded before the synthesis process. The preparation should be carried out in a dry and inert atmosphere. Thus this IL suffers from handling issues under normal atmospheric condition <sup>[108]</sup>.

The produced ILs was divided in three types such as acidic ILs, neutral ILs and basic ILs. These categories are based on the nature of the ILs which is controlled by the ratio of anion and cation used for electrolyte preparation as mentioned earlier. When AlCl<sub>3</sub> concentration is more than 50%, the electrolyte became acidic <sup>[66,108]</sup>. With decrease in concentration the electrolyte turned to neutral and then basic <sup>[66,108]</sup>. This acidic-neutral-basic nature of the electrolyte is likely to be due to the formation of different species and bonding between Al and Cl<sup>-</sup>. Formation of different species can be explained through the reaction scheme <sup>[66]</sup> shown below.

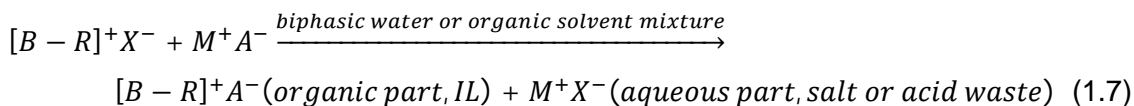


With increase in mole fraction of X(AlCl<sub>3</sub>), the produced ILs changes from alkaline to acidic. At lower concentration Cl<sup>-</sup> is not bound to Al, as a result basic IL was obtained. With increase in X(AlCl<sub>3</sub>) mole fraction, the available Cl<sup>-</sup> starts to bound to Al. At 0.5 mol fraction all Cl<sup>-</sup> is bound to Al now and as a result neutral IL was obtained. The only available complex in the electrolyte is AlCl<sub>4</sub><sup>-</sup> <sup>[66,108]</sup>. Based on the complexes formed and its ability to withdraw the chloride ion from the metal chloride, metal reduction properties can be predicted. Moreover depending on the reduction potential of the cationic species of the metal and complex of AlCl<sub>3</sub>, deposition of many metals is possible <sup>[63]</sup>.

#### 1.4.2.2. Group II Ionic liquids

Group II ILs are Lewis neutral ILs <sup>[109]</sup>. In these ILs, cations are based on weak acids and anions are achieved from weak bases <sup>[109]</sup>. The anions are BF<sub>4</sub><sup>-</sup>, PF<sub>6</sub><sup>-</sup>, SCN<sup>-</sup> and SbF<sub>6</sub><sup>-</sup> and the cations are based on imidazolium, pyridinium and quaternary ammonium salts <sup>[67,109]</sup>. These ILs are also known as air and water stable ILs <sup>[68]</sup>. However, long time exposure to water can have some serious effect on the properties of these ILs <sup>[68-69]</sup>.

For preparation of these ILs, removal of impurity is a common step. The preparation of these ionic liquids also takes place in two steps, alkylation of the organic base and anion exchange <sup>[66]</sup>. This reaction scheme is shown in eqn. (1.6) and (1.7) below :



Here B = pyridinium, N-methylimidazole, N = methylpyrrolidine etc, R = methyl, ethyl, propyl etc, X = chloride, bromide, iodide etc, M = H+ / an alkali metal (Li, Na etc), A = [BF<sub>4</sub>], [PF<sub>6</sub>] etc.

The extraction of the IL is carried out through washing with water and with appropriate acid or metal salt. This IL preparation is possible at room temperature but application is possible only at elevated temperature <sup>[66]</sup>. Due to choice of cations like ethyl and methyl imidazolium, the formed ILs have low viscosity and high conductivity <sup>[67]</sup>. These ILs are very expensive and cannot be used under normal atmospheric condition due to the purity issues <sup>[67]</sup>.

#### 1.4.2.3. Group III Ionic liquids

Group III ILs are prepared from same organic cations used in the previous group of ILs and anions like CF<sub>3</sub>SO<sub>3</sub><sup>-</sup>, (CF<sub>3</sub>SO<sub>2</sub>)<sub>2</sub>N<sup>-</sup> <sup>[109]</sup>. These ILs are stable under ambient conditions with only low water uptake <sup>[109]</sup>. This stability is assumed to be due to the strong bond of fluoride and oxide. Electrodeposition of elements like Si, Ge, Ti, Al was carried out using these ILs <sup>[109]</sup>.

#### 1.4.3. Eutectic based Ionic liquids

The melting point of a mixture can be predicted from the nature of the interaction between the components of the mixture. Freezing point varies linearly with mole fraction when the components of the mixture do not interact with each other <sup>[66]</sup>. When this interaction is strong, large negative deviation in freezing point vs. mole fraction plot is expected <sup>[66]</sup>. The eutectic point of a mixture is shown in fig. 1-5. The eutectic point of a melt is known by the composition of minimum freezing point. It can also be defined as the phase transformation temperature from molten state to solidification or crystallization <sup>[66]</sup>.

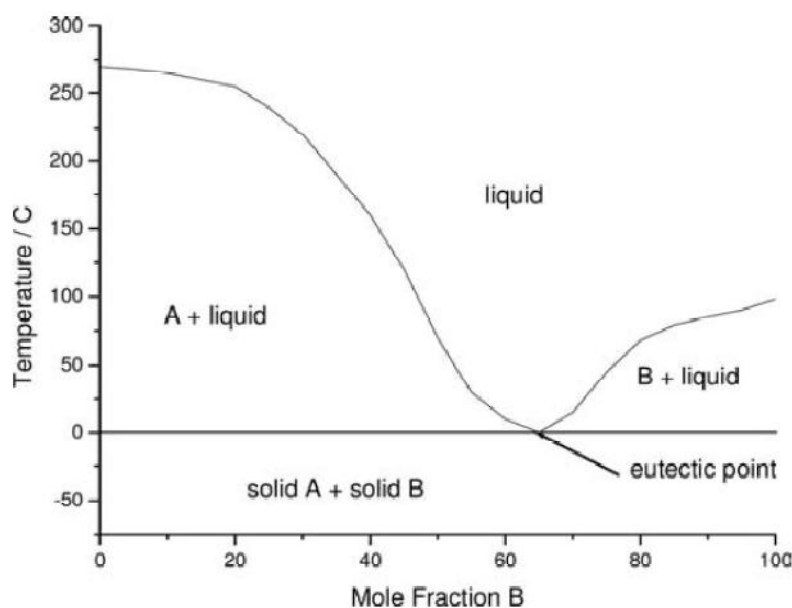


Figure 1-5 : Schematic representation of eutectic point on a two component phase diagram <sup>[66]</sup>

Eutectic based IL are presented by general formula as  $R_1R_2R_3R_4N^+ X.z.Y$  <sup>[66]</sup>. The cation  $R_1R_2R_3R_4N^+$  is a quaternary ammonium salt like choline, ammonium, phosphonium, sulphonium. X is a halide anion (mainly Cl<sup>-</sup>) <sup>[110-111]</sup>. Y is a complexing agent and z represents the number of molecules required. Some examples of the eutectic based ILs is shown in Table 1.6.

Eutectic based ILs can be subcategorised into three types according to the nature of complexing agent,

Type 1.  $Y = MCl_x$ , where M = Zn, Sn, Al, Fe, Ge

Type 2.  $Y = MCl_x \cdot yH_2O$  where M = Cr, Co, Cu, Ni, Fe

Type 3.  $Y = RZ$ , where Z = CONH<sub>2</sub>, COOH, OH

The preparation of this type of ILs is easiest among all categories of ILs. For these ILs, preparation involves simple mixing of two components with gentle heating and reaction during preparation is mild endothermic <sup>[66,110]</sup>.

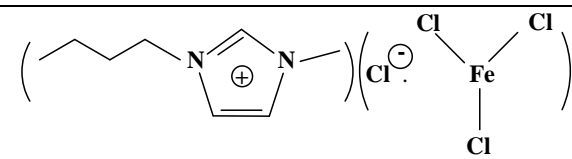
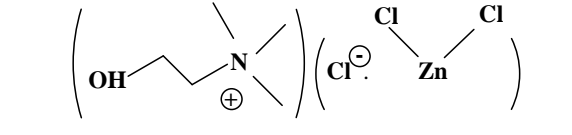
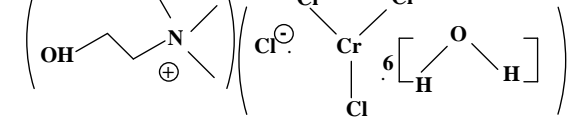
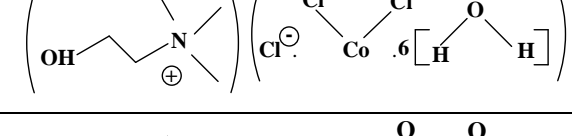
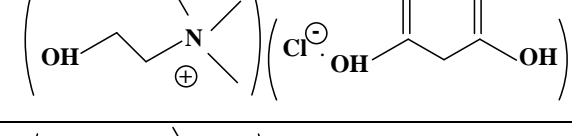
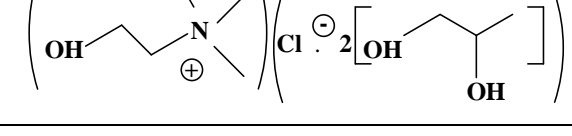
#### 1.4.3.1. Type 1 eutectics

The type 1 eutectic ILs are based on metal halides. A wide range of metal studies were carried out to produce these ILs <sup>[110]</sup>. However, few metal salts like FeCl<sub>3</sub>, SnCl<sub>2</sub>, ZnCl<sub>2</sub>, CuCl<sub>2</sub> <sup>[113]</sup>, InCl<sub>3</sub> <sup>[114]</sup> and AuCl<sub>3</sub> <sup>[115-116]</sup> form IL with pyridinium, imidazolium and quaternary ammonium halide. For eutectic mixtures composition of anions and cations are very important. This composition depends on the amount of  $MCl_x$  used in the electrolyte <sup>[66]</sup>. It was observed as the speciation in IL varies with the composition of the IL. With increase in molar ratio of ZnCl<sub>2</sub> more than half percent, several Lewis

acidic chlorozincate cluster ( $\text{ZnCl}_3^-$ ,  $\text{Zn}_2\text{Cl}_5^-$ ,  $\text{Zn}_3\text{Cl}_7^-$ )<sup>[110-112,117-123]</sup> was formed and similar trend was observed for  $\text{SnCl}_2$ <sup>[124]</sup>. A variety of halometallate species was found in this eutectic mixture when Fast Atom Bombardment and Extended x-ray absorption fine structure spectroscopy was carried out.  $\text{ZnCl}_4^{2-}$  and  $\text{CuCl}_4^{2-}$  species was found for metal salt  $\text{ZnCl}_2$  and  $\text{CuCl}_2$  and assumed to be dimers of  $\text{Zn}_2\text{Cl}_6^{2-}$  and  $\text{Cu}_2\text{Cl}_6^{2-}$ <sup>[125-126]</sup>.

Again the freezing point of these ILs is also influenced by size of cation used<sup>[88]</sup>. Among the range of this eutectic ILs, imidazolium based ILs have lower viscosities and higher conductivities with respect to pyridinium and quaternary ammonium eutectics<sup>[88]</sup>. This is due to lower symmetry of imidazolium cation and the lowest melting point chloride is ethyl methyl-imidazolium chloride.

Table 1.6 : Eutectic based ILs used for various metal deposition<sup>[66]</sup>

Ionic liquid (IL)	Structure
[(BMI)Cl-FeCl <sub>3</sub> ]	
[(Ch)Cl-ZnCl <sub>2</sub> ]	
[(Ch)Cl-CrCl <sub>3</sub> .6H <sub>2</sub> O] (Chromeline)	
[(Ch)Cl-CoCl <sub>2</sub> .6H <sub>2</sub> O]	
[(Ch)Cl-malonic acid] (Maline)	
[(Ch)Cl-2propanediol]	

ChCl → choline chloride

#### 1.4.3.2. Type 2 eutectics

The type 2 eutectic ILs were produced to expand the range of metals which can be used to produce eutectic based ILs. With the presence of water a decrease in the

melting point of the metal salt was observed. This water of hydration helps in decreasing lattice energy as a result low melting point was achieved<sup>[66]</sup>. These ILs are mostly prepared with quaternary ammonium salts and hydrous metal salt. Most of them are made from choline chloride and chromium chloride<sup>[66]</sup>. Electrodeposition of Cr, Co was carried out from these electrolytes<sup>[66,127]</sup>.

#### 1.4.3.3. Type 3 eutectics

The type 3 eutectic ILs were created by complexing halide salts. The notable properties of these ILs are like wide variety of solutes, high solubility of metal salts and extremely large depression of freezing point in the range of 170 to 280 °C. Due to this property they are called as deep eutectic ILs<sup>[66]</sup>. Synthesis of this IL is possible by mixing quaternary ammonium salts with a range of amides<sup>[111,117]</sup>. The hydrogen bonding between the halide anions with an amide, carboxylic acid and alcohol helps in the delocalization of charge. For these mixtures mostly used cations were EMI and choline<sup>[66]</sup>.

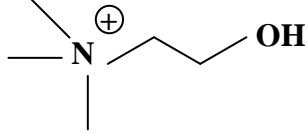
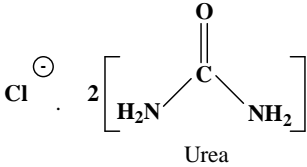
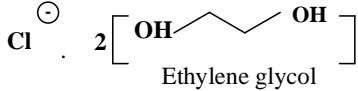
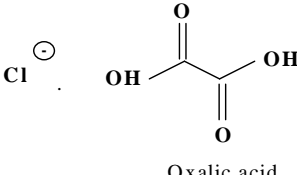
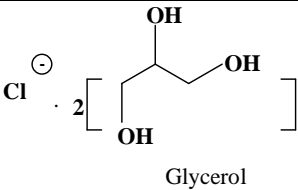
The lattice energy of the salt is an important factor for the freezing point of the IL. For quaternary ammonium salts the reaction between anion and hydrogen donor bond (HBD) controls the lattice energy of the HBD. The freezing point is also related to molecular weight and mass fraction of the HBD<sup>[66]</sup>. The ILs from diol-based HBD group showed lowest viscosities and highest conductivity of the mixture. It can be due to weak alcohol and chloride interaction<sup>[66]</sup>. This ILs are favourable for electrodeposition for certain advantages from health and safety viewpoint. Again these ILs have favourable physical properties suitable for electrodeposition process.

This deep eutectic ILs can also be described as choline chloride based Ionic liquids (ChCl based ILs). The most attractive aspect of these ILs is the preparation method and availability of the components in the market. The main component is choline chloride, a quaternary ammonium salt. The chemical name is ethanaminium, 2-hydroxy-N,N,N-trimethyl-chloride and trade name is (2-hydroxyethyl) trimethyl ammonium chloride [ $C_5H_{14}NOCl$ ] and choline is the cationic part of the IL. The anionic part is a hydrogen bond donor (HBD) such as  $CH_4N_2O$  (urea),  $C_2H_2O_4$  (oxalic acid),  $C_3H_8O_3$  (glycerol),  $CH_2(COOH)_2$  (malonic acid), or  $C_2H_6O_2$  (ethylene glycol). The cationic and anionic part<sup>[112-113,119]</sup> for some of these ILs is shown in the table 1.7.

The eutectic point of the solvent depends on the mol% of the HBD<sup>[66]</sup>. This mol% varies from 33 to 67 % range depending on the type of the anion used. The simple preparation method is mechanical mixing of two different components with no emission and mass efficiency<sup>[66,70]</sup> loss. The impurity control measurements are not

necessary and toxicological properties are well characterized for this type of eutectic based ILs [66,70].

Table 1.7 : Choline chloride based ILs used for various metal deposition, including Cu and Sn [66]

Cationic part	Anionic part	ChCl based IL
 <p>Choline</p>	 <p>Urea</p>	Reline (1ChCl : 2urea)
	 <p>Ethylene glycol</p>	Ethaline (1ChCl : 2EG)
	 <p>Oxalic acid</p>	Oxaline (1ChCl : oxalic acid)
	 <p>Glycerol</p>	Glyceline (1ChCl : 2glycerol)

The decomposition of these ILs is also an important economic issue. The stability of the bath for a longer period of time was examined by the electrolysis process. In the decomposition of the electrolyte, several products were found, such as 2-methyl-1,3-dioxolane and chlorinated products like chloromethane, dichloromethane, and chloroform [126]. However, chlorine gas was not detected during the decomposition process. It has been observed that the addition of water reduces the formation of chlorinated products, as ethylene glycol and water were oxidized. As a result, other organic components were detected [128].

It should be mentioned that ChCl based ILs are cheaper than any other type of IL electrolyte present in the market. The price comparison with other ILs is shown in Table 1.8. Moreover, during electrodeposition from these ILs, dehydrated salts are not required for electrodeposition studies. Dehydrated salts are available in 4 to 20 times smaller amounts and 9 to 12 times more expensive when compared to hydrated salts [129]. However, when compared to aqueous MSA electrolyte (£ 8/lt) ChCl based IL

especially ethaline [1ChCl:2EG] (£ 26/lt) is 3.25 times higher, which were used for Cu-Sn alloy deposition <sup>[130]</sup>.

Table 1.8 : Assessment of electrolytes for price and bulk supply comparison <sup>[129]</sup>

	BMI based ILs	EMI based ILs	BMP based ILs	ChCl based IL [1ChCl:2EG]
Cost /100 g	£ 357	£ 180.50	£ 532	£ 2.16
Bulk delivery amount	50 g	1 kg	50 g	20 kg

#### 1.4.4. Important parameters for deposition from Ionic liquids

It is evident from above discussion that ILs are different than that of the aqueous electroplating bath. This is due to high concentration of ions and different ligand formation with metal cation in IL electrolyte. The influential parameters for metal deposition are classified in terms of physical and electrochemical properties.

For electrodeposition the important physical properties are melting point, thermal decomposition temperature, viscosity, density, solubility of metal salts and electrochemical properties are ionic conductivity, potential window and diffusion coefficient of the component ions. Other important properties or issues like handling, availability and various environmental aspects should be considered for pre and post treatment. In the following section details on these properties are presented.

The environmental and handling aspects of the ILs needed to be described as they play an important role during and after electrodeposition process for the health and safety purpose. The anion stability towards hydrolysis is an important factor to handle the IL <sup>[131]</sup>. It becomes very difficult to handle chloroaluminate melt due to the presence of traces of water. It is also difficult to assess the stability which leads to handling issues of IL and the nature of the anion which control this property of the IL. Now a day the “green chemistry” and the “clean processes” uses IL as the potential solvent <sup>[132-133]</sup>. Volatile organic solvent causes some environmental and safety problems and this was resolved by using non-volatile ionic reaction medium. ILs are better alternatives for the environmental and safety issues <sup>[131]</sup>. However, the toxicity and disposal method of the ILs have not fully investigated yet which is another environmental issue for future work.



#### 1.4.4.1. Thermal properties

The thermal properties are considered as an interesting characteristic for any IL. The thermal properties like melting point, glass transition temperature, thermal decomposition temperature, liquid crystallinity-solid-solid transitions, thermal conductivity and vapour pressure are the important factor in using it. Melting point and thermal decomposition temperature are discussed here as these are important properties for electrodeposition process. Thus details on these properties are presented in the following section. The melting point of IL is expected to be below 100 °C [108,134-137].

- Melting point

Melting point is an important property for any ionic liquid, as the use and flexibility of the liquid is controlled by this property. The melting point of any IL is influenced by ion radius, cation and anion structure [66]. The variation in melting point was observed with change in cation and anion structure. With increase in ion radius decrease in electrostatic interactions and surface charge density was observed. As a result separation between the ions increases too. Thus to achieve ILs with low melting point anions or cations with bigger ionic radius is required [66].

Due to the presence of delocalized positive charge in aromatic salts, they show relatively low melting point [138-141]. The melting point can also be decreased by involving unsymmetric cation structure [141], for lower symmetric structure ions are not well organised in the crystalline structure [142]. However in case of anions, most of the room temperature ILs were formed using symmetric structure. Anions originating from halogen atoms mainly used to produce RTILs because of delocalized negative charge [66].

- Thermal decomposition temperature

Thermal decomposition temperature directs the thermal stability of an IL. The thermal stable up temperature for ionic liquids is up to 450 °C whereas the thermal degradation temperature is reported to be 500 °C [66].

Maximum operating temperature of ChCl based ILs is in the range of 150 to 300 °C, this temperature is lower than the degradation temperature. The mixture shows a large depression in freezing temperature for anions with low molecular weight. The mass fraction of the anionic part is also important for depression point of the ILs.

#### 1.4.4.2. Density

ILs are consists of anions and cations i.e. only of ions, so the density of ILs are higher than aqueous electrolytes. The density value varies in the range of 1 to 1.6

g/cm<sup>3</sup> depending on the anion and cation structure [66]. The density of the electrolyte increases with increase in formula weight of the ions. As the length of the alkyl chain in the cation increases the density of IL decreases [143]. Increase in bulkiness of the organic cation causes decrease in density of IL [131]. The density of the IL has been modelled as a function of temperature. It has been observed that with increase in temperature density of the electrolyte decreases following a linear relationship [144-146]. In case of ChCl based ILs density value reported to be in the range of 1.12 to 1.25 g/cm<sup>3</sup> [146]. For this IL the density value is directed by the density of HBD of the IL [146].

#### 1.4.4.3. Solubility of metal salts

The choice of the cations and anions control the solubility property of an IL. When a metal salt were dissolved in an electrolyte, the electrostatic interaction between the ions or metal atoms in metal salts were broken. For many ILs, the coordinating properties and solvation energy between the anions and cations are weak. As a result solubility performance for metals or metal salts is low for many ILs [66]. To improve the solubility property, ILs were prepared involving ions containing ether or hydroxyl group and introducing thioether or thiourea groups into the side chain of the cation [66,147]. The solubility property can also be improved by varying the alkyl group on the cation. The solubility in the melt increases with the increase of non polar characteristics of the cation [148]. With compared to different ILs available in the market, ChCl based ILs showed high solubility for wide range of solutes [111].

#### 1.4.4.4. Viscosity

For an electrochemical study the mass transport within an electrolyte is strongly influenced by the viscosity of the electrolyte. The hydrogen bonding and the strength of the Van der Waals interaction influences the viscosity of the ionic liquid [149]. The variation in viscosity value can be due to the impurities, synthetic route, starting materials and measurement method [66]. ILs are 10-100 times viscous than water or organic solvents which resulted from the strong electrostatic and other interactive forces [150-152]. The viscosity of the IL varies in the range of 10 to 1110 cP at room temperature [65,68]. The viscosity variation is explained with the help of hole theory [153-156]. The higher viscosity value may be due to large radii ( $\approx 3-4 \text{ \AA}$ ) of the solvent species compared to the average radius of the voids ( $\approx 2 \text{ \AA}$ ) [156]. The availability of free volume and probability of finding holes of suitable dimensions for the solvent molecules are also responsible for the higher or lower viscosity value. The mobility of the ions

depends on the size of the migrating species, the radii of the cations and complexed anions.

With increase in temperature, the viscosity value decreases in a non linear fashion. The relationship can be fitted to Arrhenius model. For viscosity change, the Arrhenius relationship <sup>[157]</sup> with temperature is shown in the eqn. 1.8.

$$\ln\mu = \ln\mu_{\infty} + \frac{E_{\mu}}{RT} \quad (1.8)$$

Here,  $\mu$ = viscosity,  $\mu_{\infty}$ = viscosity at infinite temperature,  $T$ = temperature,  $E_{\mu}$ = activation energy of the viscous flow. The activation energy for viscous flow and the viscosity at infinite temperature can be determined from the slope and intercept of the Arrhenius plot. With decrease in activation energy for viscous flow implies the presence of more mobile ions within the melt <sup>[157]</sup>. At infinite temperature the geometry of the ILs illustrates the viscosity of the electrolyte. Thus the value of  $\mu_{\infty}$  represents the structural contribution of the ions to the viscosity <sup>[157]</sup>.

For glass forming ILs,  $\ln \mu$  shows a non-linear relationship with  $1/T$  <sup>[158]</sup>. Thus Vogel-Tamman-Fulcher (VTF) model is much more appropriate as for these ILs and the VTF equation <sup>[157]</sup> is,

$$\ln\mu = \ln (A_{\mu}^{VTF} \sqrt{T}) - \frac{k_{\mu}}{T-T_g} \quad (1.9)$$

Where  $A_{\mu}^{VTF}$ ,  $k_{\mu}$  = constant,  $T_g$ = glass transition temperature

Arrhenius law was found to be valid for IL electrolyte contained asymmetric cations without functional groups in the alkyl chains <sup>[159]</sup>. The ILs containing small, symmetrical cations with low molar mass was found to follow the VTF equation <sup>[157,159]</sup>. RTILs containing higher molar mass cations and additional hydrogen bonding were expected to have a high viscosity <sup>[157]</sup>. It also has been observed for various RTILs which contains less symmetric cations with functional groups as C=O and OH, both models fit poorly <sup>[157]</sup>. For ChCl based ILs viscosity varies from 10 cP to 500 cP <sup>[66]</sup>. The diol-based ILs have lowest viscosity and highest conductivity. The weak interaction between alcohol and chloride enhanced the movement of some free glycol <sup>[66]</sup>. This movement helps in decreasing the viscosity of the liquid.

#### 1.4.4.5. Ionic conductivity

Ionic conductivity of any electrolyte can be defined using the eqn 1.10 <sup>[66]</sup> below,

$$\sigma = \sum n_i e_i u_i \quad (1.10)$$

where  $n_i$  = number of  $i^{\text{th}}$  ions,  $e_i$  = the charge of an electron and  $u_i$  = mobility of the  $i^{\text{th}}$  ion. The conductivity of an IL is lower than the concentrated aqueous electrolyte at room temperature. With comparison to other organic solvents or electrolytic system, IL is more conductive despite of the same viscosity value as other electrolytes <sup>[150]</sup>. The conductivity of the IL varies in the range of 0.1 to 20 mS/cm at room temperature <sup>[149,160-161]</sup>.

The conductivity of an IL is influenced by many factors like viscosity, density, ion size, anionic large delocalization, aggregation and ionic motion <sup>[159]</sup>. The conductivity of an electrolyte increases due to the presence of larger number of carrier ions. Again the mobility of the carrier ions depends on the size of the ions. Thus the ionic mobility is reduced when large component ions of IL are present, which leads to lower conductivity <sup>[68]</sup>. Moreover, the lower conductivity may be due to strong ion-pair formation. The ionic concentration was diluted by the neutral ion collection as an outcome of ion-pair formation. As a result decrease in coulombic interaction within the IL was observed <sup>[159]</sup>. Conductivity can be increased by increasing alkyl chain length and size of the anion <sup>[162-163]</sup>. The conductivity can also be increased by addition of small cations <sup>[159]</sup>.

The conductivity and viscosity relationship can be represented by Walden rule <sup>[68,162,164-166]</sup> and shown in the eqn. 1.11 below,

$$\sigma\mu = \text{constant} \quad (1.11)$$

With variation of temperature, the conductivity change follows Arrhenius or VTF relationship similar to viscosity change <sup>[66]</sup>. For ChCl based ILs the conductivity varies from 0.02 mS/cm to 7.6 mS/cm <sup>[66]</sup>. As the diol-based ILs have lowest viscosity so they are expected to have highest conductivity.

#### 1.4.4.6. Diffusion co-efficient of component ions

The transportation of desired metallic ions or protons depends on many factors, these can be very different in IL media. The diffusion coefficient value reported to be in the range of  $10^{-8}$  cm<sup>2</sup>/s at room temperature for maximum IL systems <sup>[167]</sup>. This value is 100-1000 times lower than aqueous electrolyte <sup>[168]</sup>. This difference is due to the strong electrostatic interaction forces of component ions in IL media. The electrostatic forces are weak in IL containing fluorinated anion as a result larger diffusion coefficient was observed <sup>[169]</sup>.

This parameter is also influenced by other physical properties like viscosity, ionic conductivity and temperature. The ionic conductivity relates to diffusion co-efficient by Nernst-Einstein equation <sup>[66]</sup> and show in the equation below,

$$\sigma = \frac{Dn'Q^2F^2}{RT} \quad (1.12)$$

Here,  $\sigma$  = ionic conductivity,  $D$  = diffusion coefficient,  $n'$  = no. of carrier ions,  $Q$  = electric charge,  $F$  = Faraday constant,  $T$  = temperature in K,  $R$  = gas constant

The viscosity relates to diffusion co-efficient by Stokes-Einstein equation<sup>[63]</sup> and show in the equation below,

$$D = \frac{kT}{c'\pi\mu r'} \quad (1.13)$$

Here,  $k$  = Boltzmann's constant,  $c'$  = constant,  $r'$  = stokes radius,  $\mu$  = viscosity. The self-diffusion coefficient for anion and cation follows an Arrhenius or VTF relationship<sup>[63]</sup> with temperature variation. ILs with low viscosity and high conductivity results in larger diffusion coefficient. With compare to anions, cations have larger diffusion coefficient values. As a result it was observed that cation diffuses more easily than the anion. By adding the value of diffusion coefficient of ions and ion pairs, the diffusion coefficient value of an IL was estimated. Thus the carrier ion number turns to be a smaller value than the value based on molar concentration calculation<sup>[66]</sup>. In addition of inorganic salts in IL system the viscosity increases with decrease in ionic conductivity. So with increase in inorganic salt concentration in IL system, the diffusion coefficient of the component ions tends to be smaller<sup>[170]</sup>. The self diffusion co-efficient for ChCl based ILs was found to be in the range of 0.064 to 2.62 x10<sup>-7</sup> cm<sup>2</sup>/s for the cationic part<sup>[146]</sup> and 0.06 to 4.77 x10<sup>-7</sup> cm<sup>2</sup>/s for HBD part<sup>[146]</sup>.

#### 1.4.4.7. Potential window

Electrochemical window of an IL conveys the information on the electrochemical stability of the electrolyte based on a particular electrode. The electrochemical window is the electrochemical potential range where any electrochemical reaction does not took place. In this potential range the electrolyte neither reduced nor oxidised at an electrode surface. The electrochemical window for the chloroaluminate ILs varies in the range of 2 to 4.5 V<sup>[69]</sup>. For air-water stable ILs, the wide electrochemical window is in the order of 4 V or more depending on the electrode substrate<sup>[69,171]</sup>. In group III, ILs the electrochemical window is very wide more than 4 V, as a result electrodeposition studies of many elements were possible<sup>[149]</sup>. This wide range of electrochemical window gives IL an opportunity to become superior to that of the high-temperature molten salts and aqueous electrolytic media. The quaternary ammonium and pyrrolidinium salts showed higher stability towards the reduction side. This was due to

the improved cathodic stability of these salts with respect to imidazolium salts [149,161,172-173].

This parameter is influenced by many factors like chemical structure of the anion and cation, the purity of the IL, nature of the electrode metal, temperature, atmosphere and the reference electrode used for measurement [63,66,159]. For this measurement various types of reference electrodes like ferrocene(Fc)/ferrocenium( $\text{Fc}^+$ ), Ag/AgCl (aq), Ag/Ag<sup>+</sup> (organic solvents) and pseudo-metal electrodes like Ag wire and Pt wire [88] were used. To determine potential window cyclic voltametry (CV) or linear sweep voltametry was used [63,66]. Determination of the potential window at the cathodic side was possible by the reduction of the cations and at the anodic side by oxidation of the anions. For some IL electrolytes when the cathodic stability of the cations are poor then potential window was determined using the anionic part of the IL. When the oxidation at the anodic side is independent on anions, then cation of the IL will help in potential window determination [63]. The electrodeposition of different metals from aqueous solvents becomes limited due to the small potential window of the solvent. Due to the wider potential window of IL various metals like Al, Mg, Si, Ge and rare earth materials can be electrodeposited from room temperature ionic liquid [68]. In case of ChCl based ILs the potential window varies in the range of 0.5 to 2.5 V [112,118]. For ChCl based ILs containing urea this window value is reported as - 1.2 to + 1.25 V vs. Ag [174]. It is also reported that a comparatively large potential window is obtained for glycol based ILs [66].

#### *1.4.5. Summary of electrochemical study and electrodeposition of Copper, Tin and its alloy from various Ionic liquids*

Metal deposition from these electrolytes have been carried out over the past 7 to 10 yrs. There are 33 companies, academic institutions and trade associations working to scale up and commercialise electroplating and electropolishing processes using this new ILs [67]. Deposition of several metals had been carried out using ChCl based ILs. To commercialize these ILs in metal finishing industry, the important parameters for process scale-up should be investigated. These parameters are temperature, cation, anion, electrolytes, metal salts, complexing agents, diluents, anode materials, brighteners and pre-treatment protocol. A range of transition and main group metal has been successfully deposited using IL electrolyte [67]. In the following section various electrochemical characterization and electrodeposition studies on Cu, Sn and their alloys are presented from range of electrolytes.

## 1.4.5.1. Copper studies in various ILs

Electrochemical studies of Cu have previously been carried out in all groups of ILs [82-88,100-101,175-177]. These ILs are [AlCl<sub>3</sub>-NaCl-KCl] [100-101], [AlCl<sub>3</sub>-MePyCl] [82], [AlCl<sub>3</sub>-BuPyCl] [83], [TMHA-Tf<sub>2</sub>N] [84], [BMP-Tf<sub>2</sub>N] [85], [TOMACl-ChCl<sub>3</sub>] [86], [EMI-BF<sub>4</sub>] [87], [BMI-PF<sub>6</sub>] [88], Cu(MeCN)<sub>4</sub>-Tf<sub>2</sub>N], [Cu(PhCN)<sub>2</sub>-Tf<sub>2</sub>N] and [Cu(CH<sub>3</sub>CN)<sub>2</sub>-Tf<sub>2</sub>N] [175-177]. The experimental temperature range for inorganic melts was 135 °C to 175 °C [100-101] and organic melts was 30°C to 60°C [82-83]. As these electrolytes contained AlCl<sub>3</sub> salt as a main component for IL formation, the influence of Al was observed and unavoidable during metal studies using these electrolytes [82]. The solubility of Cu salt in these electrolytes is very slow. The solubility factor is controlled by the proportion of anion and cation present in the electrolytes [100-101]. The operating temperatures for ILs like [TMHA-Tf<sub>2</sub>N] [84], [BMP-Tf<sub>2</sub>N] [85], [TOMACl-ChCl<sub>3</sub>] [86], [EMI-BF<sub>4</sub>] [87], [BMI-PF<sub>6</sub>] [88] were varied from room temperature to 90 °C [84-88,175-177].

All the studies in different IL electrolytes highlighted the presence of the redox couples Cu(I)/Cu(0) and Cu(II)/Cu(I) in the electrolyte. Additionally these studies were also reported about Cu(II) reduction procedure. In every case reduction took place in two steps, Cu(II) reduced to Cu(I) then Cu(I) to Cu(0) [82-88,100-101]. The Cu(II)/Cu(I) redox couple was diffusion controlled reversible electrode process in the most electrolytes mentioned previously. It must be mentioned that the variation of the acidity of the melt leads to different changes such as nature of the redox process [83].

Studies in ChCl based ILs also showed the Cu(II) reduction in two steps, Cu(II) reduced to Cu(0) via Cu(I) [178-181]. Reline was mostly used for these studies and most of the study is related to kinetic study [55,70,179-184]. These studies indicated a reversible nature for the Cu(II)/Cu(I) redox couple in most electrolytes [178]. The voltammogram also showed large increase in anodic current at a potential range beyond 1 V which is predicted as an outcome of irreversible oxidation of Cl<sup>-</sup> to Cl<sub>2</sub> [179]. The value of diffusion coefficient was determined in the range of 0.13 to 3 x10<sup>-7</sup> cm<sup>2</sup>/s in reline and ethaline [178-181]. The value of diffusion coefficient was determined to be 10<sup>-2</sup> times lower than in aqueous electrolyte and similar in magnitude to the value determined from all IL electrolytes mentioned above [178-181,184]. While using the glycine electrolyte, it was evident that the process is diffusion controlled. Analysis on the complex formation and speciation studies was carried out by UV-VIS spectroscopy analysis. This showed the speciation of Cu(I) as CuCl<sub>3</sub><sup>-2</sup> and Cu(II) as CuCl<sub>4</sub><sup>-2</sup> [180].

The current efficiency of the process was calculated from deposition and dissolution experiments in [TMHA-Tf<sub>2</sub>N] electrolyte [84]. The obtained efficiency was determined as 97% [84]. The current efficiency of the process in ChCl based IL was

close to 100% as determined using electrochemical quartz crystal microbalance (EQCM) by calculating the charge-mass balance of the deposit <sup>[178]</sup>.

Dense, nodular and compact Cu deposits were obtained using Cu(I) oxide in reline electrolyte on a Ni substrate <sup>[182]</sup>. The studies on Cu electrodeposition from ethaline melt with ethylene diamine additive showed Cu deposits of smooth, compact surface with finer grain <sup>[185]</sup>. Previously the use of additive like ethylene diamine and EDTA showed improve powdery deposits to lustrous deposits <sup>[70]</sup>. It is also has been reported that stability of the ethaline melt for long term Cu deposition purpose can be improved by adding ethylene diamine additive <sup>[185]</sup>.

#### 1.4.5.2. Tin studies in various ILs

Electrochemical studies and the electrodeposition of Sn had been carried out in both group I and group II ILs. From group I ILs, studies were carried out from [AlCl<sub>3</sub>-MeEtimCl] <sup>[91]</sup>. From group II ILs, studies were carried out from [BMP-TFSI] <sup>[93]</sup>, [ZnCl<sub>2</sub>-EMIC] <sup>[90]</sup>, [EMI-DCA] <sup>[92,186-187]</sup>, [EMI-BF<sub>4</sub>] <sup>[188]</sup>, [EMI-BF<sub>4</sub>Cl] <sup>[189]</sup>, [C<sub>4</sub>mpyrr-DCA] <sup>[190]</sup> and [C<sub>4</sub>mpyrr-Tf<sub>2</sub>N] <sup>[190]</sup>. The CV studies in all above mentioned IL electrolytes showed reduction of Sn(II) to Sn(0) by one single step <sup>[90-92,188-190]</sup>. This redox couple was obtained to be a quasi-reversible process in [AlCl<sub>3</sub>-MeEtimCl] <sup>[91]</sup> and irreversible electrode process in [EMI-BF<sub>4</sub>] <sup>[188]</sup> when studied by Pt electrode. During these studies reported Sn species are [SnCl<sub>3</sub>]<sup>-</sup> <sup>[91]</sup>, [SnCl<sub>4</sub>]<sup>2-</sup> <sup>[90,188]</sup>, [SnCl<sub>2</sub>(DCA)<sub>y</sub>]<sup>(y-2)-</sup> <sup>[92]</sup> and [Sn(DCA)<sub>x</sub>Cl<sub>z</sub>]<sup>(x+z-2)-</sup> <sup>[92]</sup>.

The study on diffusion co-efficient of Sn(II) was carried out with most of these ILs electrolytes mentioned above. The values were in the range of 0.18 to 9.8 x10<sup>-7</sup> cm<sup>2</sup>/s using a range of methods <sup>[90-92,190]</sup> in a temperature range of 25 to 90 °C. The obtained Sn deposits from these electrolytes showed dendrites or uniform sponge nature <sup>[186]</sup>. Improved smooth and adhesive electrodeposit was obtained from [BMP-TFSI] electrolyte <sup>[93]</sup>. The crystalline structure analysis of these deposits showed tetragonal crystalline structure <sup>[93,186-187]</sup>. The current efficiency of the deposition process varies in the range of 27% to 100% <sup>[90,92,190]</sup>. This variation was due to change in anions and cations of ILs and the electrode material.

The electrochemical study and electrodeposition of Sn from ChCl based ILs is not well reported yet. The voltammetry studies on Sn(II) in ethaline and reline electrolyte, were carried out using 0.05 M SnCl<sub>2</sub> in Pt microdisc electrode to compare the reduction potential in two different electrolyte <sup>[110]</sup>. This also gives an estimation of the solubility limit of the metal <sup>[110]</sup>. Dendritic clusters of simple cubic crystals of Sn were attained from reline electrolyte at an applied current density of 0.01 A/cm<sup>2</sup> <sup>[110]</sup>. The reported Sn complex in SnCl<sub>2</sub>-ChCl mixture and reline system is [SnCl<sub>3</sub>]<sup>-</sup> with ChCl



ligand <sup>[191]</sup>. The presence of another additional Sn complex like  $[\text{Sn}_2\text{Cl}_5]^-$  is reported <sup>[127]</sup> in  $\text{SnCl}_2\text{-ChCl}$  mixture. The voltammetry study of  $\text{SnCl}_2$  in reline system showed the reduction of Sn is diffusion controlled reversible electrode process <sup>[191]</sup>.

#### 1.4.5.3. Copper-Tin alloy studies in various ILs

There were few studies of Cu-Sn alloy deposition from ILs. The ILs involved in this study were  $[\text{EMI-DCA}]$  <sup>[94-95]</sup>,  $[\text{TMHA-Tf}_2\text{N}]$  <sup>[96-97]</sup>,  $[\text{EMI-Tf}_2\text{N}]$  <sup>[98]</sup>. The alloy was plated in a range of substrates like non-conductive epoxy substrate and Cu substrate. It was reported that a thin Cu layer of thickness  $0.5\mu\text{m}$  was deposited on non-conductive epoxy substrate by electroless method from conventional aqueous electroless plating bath before Cu-Sn deposition <sup>[98]</sup>. For alloy deposition, "contact" deposition of Sn onto a copper electrode was carried out. The deposition temperature was maintained in the range of 100 to 150 °C where Sn diffusion into the Cu was possible <sup>[96-97]</sup>.

The reported study concentrated on the deposition potential and applied current, time, intermetallic phases and temperature. The CV scan in  $[\text{EMI-DCA}]$  electrolyte showed two anodic stripping peaks, attributed to the dissolution of two different metals <sup>[94-95]</sup>. It was also assumed that the electrodeposition occurs under the charge transfer limited conditions. The deposition process was carried out at applied current of 100 to  $160\mu\text{A}/\text{cm}^2$  <sup>[97]</sup>. The deposited alloy thickness was in range of  $1\mu\text{m}$ . The obtained deposits were uniform with metallic gloss <sup>[97]</sup>. The Sn composition in the obtained alloy was in the range of 40 to 60 wt% <sup>[96]</sup>. Many intermetallic phases were found in the deposited alloys which were not found in the deposits from aqueous electrolyte. These intermetallic phases were  $\text{Cu}_6\text{Sn}_5$ ,  $\text{Cu}_3\text{Sn}$  and  $\text{Cu}_{10}\text{Sn}_3$  <sup>[96-97]</sup> depending on the applied potential, composition of the metal and deposition time <sup>[94,96,98]</sup>. The obtained intermetallic phases which depended on the composition of the metals in the electrolyte <sup>[94]</sup>. This is due to kinetically slower deposition of tin with respect to copper.

In case of investigation on Cu-Sn co-deposition from ChCl based ILs, CV scans were presented varying Cu and Sn ratio in the electrolyte <sup>[55]</sup>. Previously voltammetry studies on individual metal in ChCl based ILs showed that deposition of alloy is possible as the reduction potential of these individual metals in this melt is very near to each other. Cu-Sn co-deposition was also carried out using ethaline and reline melt at room temperature <sup>[174]</sup>. It was further reported that the composition of the Cu and Sn in Cu-Sn alloy is influenced by Cu concentration in the electrolyte. Deposits having the rough deposit morphologies were obtained in Sn rich alloy films <sup>[174]</sup>. With the addition of brighteners improved Cu-Sn alloy morphology was obtained <sup>[174]</sup>.

### 1.5. Aims and objective of this work

As mentioned earlier, the use of electrodeposition technique can be assumed to be a good alternative to other commercially used techniques for achieving individual metal and alloy films. This technique appeared to have less limitations and more cost effective. However, the choice of electrolyte is an important factor to implement this technique.

The electrodeposition process of Cu and Sn and its alloys from aqueous electrolytes is discussed with the limitations of the baths. As an alternative of the aqueous baths, the ChCl based IL is proposed for the deposition of Cu and Sn and its alloys. It is evident that desirable qualities of individual metal deposition along with their alloy deposition are possible from this IL baths. Based on the prior discussion it is evident that there are major gaps in knowledge about Cu, Sn, Cu-Sn alloy electrodeposition from ChCl based ILs. In order to fill up these gaps a systematic method to electrodeposit Cu-Sn alloy need to be followed. This work is focused on :

- Analysis of transport and electrochemical properties of the electrolytes.
- Voltammetry studies to determine electrochemical parameters of Cu, Sn and Cu-Sn alloy in IL electrolytic system. This can helps in understanding the behaviour of the individual metals in the electrolyte and electrodeposition process of Cu, Sn and their alloy from the electrolyte.
- Cu, Sn and Cu-Sn co-deposition experiments using potentiostatic (constant potential) and galvanostatic (constant current) methods with variation of different parameters to achieve good quality deposit suitable for various applications.
- Material property analysis of the individual metals and their alloy deposits.
- Characterisation the different intermetallic phases of Cu-Sn alloy films, before and after heat treatment.

## Reference:

1. USGS science for a changing world, USGS mineral resources programme, available from <<http://pubs.usgs.gov/fs/2009/3031/FS2009-3031.pdf>> [accessed date 25/4/2013 ].
2. J. R. Davis, Copper and Copper Alloys, ASM International (2001) : 10-13.
3. M. Jordan, The electrodeposition of tin and its alloys (1995) Eugen G. Leuze Publishers D-88348, Saulgau/Württ, Germany.
4. Tin for tomorrow, contributing to global sustainable development, available from <[https://www.itri.co.uk/index.php?option=com\\_mtree&task=att\\_download&link\\_id=53329&cf\\_id=24](https://www.itri.co.uk/index.php?option=com_mtree&task=att_download&link_id=53329&cf_id=24)> [accessed date 25/4/2013 ].
5. Jafferson lab report, available from <<http://education.jlab.org/itselemental/ele050.html>> [accessed date 25/4/2013].
6. U. S. Geological Survey, Mineral Commodity Summaries, 2012, available from < <http://minerals.usgs.gov/minerals/pubs/mcs/2012/mcs2012.pdf> > [accessed date 25/4/2013 ].
7. Jr. James F. Carlin, U. S. Geological Survey Minerals Yearbook, 2004 : 77.1-77.11.
8. The bronze age, available from <<http://mygeologypage.ucdavis.edu/cowen/~GEL115/115CH4.html>> [accessed date 25/4/2013 ].
9. N. Amzallag (2009) American Journal of Archaeology, 113 : 497-519.
10. Tin Bronze, available from <<http://www.hkramer.com/3KramerAlloyProperties.pdf> >[accessed date 25/4/2013].
11. Bronze, available from <<http://www.copperinfo.co.uk/alloys/bronze/>> [accessed date 25/4/2013].
12. High Tin Bronze, available from <[http://www.greenalloys.com/green\\_alloys\\_products\\_high\\_tin.asp](http://www.greenalloys.com/green_alloys_products_high_tin.asp)> [accessed date 25/4/2013].
13. T. Wen-ming, H. An-qiang, L. Qui and D. G. Ivey (2010) Trans. Nonferrous Met. Soc. China, 20 : 90-96.
14. N. Saunders and A. P. Miodownik (1990) Bulletin of Alloy Phase Diagrams, 11(3) : 278.
15. M. Igharo and J. V. Wood (1985) Powder Metall., 28 : 131.
16. M. H. Wu (2001) Proceedings, International Conference on Shape Memory and Superelastic Technologies, Kunming, China : 285-292.

17. D. M. Mattox and W. Andrew (1998) Handbook of physical vapor deposition (PVD) processing : film formation, adhesion, surface preparation and contamination control, New Jersey, Noyes publication : 31-38.
18. Z. G. Wei, C. Y. Tang and W. B. Lee (1997) Journal of Materials Processing Technology, 69 : 68-74.
19. G. Julien (2001) Post Processing For Nitinol Coated Articles, United State Patent 6,254,458.
20. Y. Tanaka, K. Oikawa, Y. Sutou, T. Omori, R. Kainuma and K. Ishida (2006) Materials Science and Engineering, A438-440 : 1054-1063.
21. Thin Films-CCVD Process (internet), available from  
<<http://www.ngimat.com/technology/ccvd.html>> [accessed date 6/11/2010]
22. M. Schlesinger and M. Paunovic (eds.) (2000) Modern Electroplating, 4<sup>th</sup> ed. John Wiley and Sons, Inc. : 24-25, 36-39, 258-260.
23. G. O. Mallory and J. B. Hajdu (ed.) Electroless Plating Fundamentals and Applications, 1990, Noyes Publications/William Andrew Publication, New York.
24. C. Madore, D. Landolt, C. Haßenpflug and J. A. Hermann (1995) Plating and Surface Finishing, August issue : 36-41.
25. H. H. Lou and Y. Huang (2006) Encyclopedia of Chemical Processing, DOI : 10.1081/E-ECHP-120007747 : 1-10.
26. S. Yoon, M. Schwartz and K. Nobe (1994) Plating Surf. Finish., 81: 65.
27. S. Yoon, M. Schwartz and K. Nobe (1995) Plating Surf. Finish., 82: 64.
28. E.E. Farndon, F.C. Walsh and S.A. Campbell (1995) J. Appl. Electrochem., 25 : 574.
29. M.J. Armstrong and R.H. Muller (1991) J. Electrochem. Soc., 138 : 2303.
30. R. Weil and J.-W. Chang (1988) Plating Surf. Finish., 75 : 60.
31. N. Koura, A. Tsutsumi and K. Watanabe (1990) Plating Surf. Finish., 77 : 58.
32. J. B. Mohler (1987) Met. Finish., 85 : 121.
33. G. Fabricius and G. Sundholm (1985) J. Appl. Electrochem., 15 : 797.
34. R.E. Gana, M.G. Figueroa and R.J. Larrain (1979) J. Appl. Electrochem., 9 : 465.
35. I. Hampel, G. Stumpf and H. Zeng (1963) Elektr. 17(8) : 269 ; (1963) Met. Finish. Abstr., 5 : 181.
36. T. L. Rama Char (1957) Electroplating, 10 : 347.
37. S. K. Panikkar and T. L. Rama Char (1960) J. Sci. Ind. Res., 19A.
38. O. S. Kogyo, Ltd. (1968) Japanese Patent 24,285/68; Met. Finish. Abstr. (1969) 11 : 14.
39. D. L. Snyder (1991) Met. Finish., 89 : 37.

40. L.M. Weisenberger and B.J. Durkin, "Copper Plating", in ASM Handlook, vol. 5, Surface Engineering, ASM international, 1994.
41. C. C. Roth and H. Leidheiser Jr. (1953) J. Electrochem. Soc., 100 : 553.
42. S. Hirsch, "Tin-Lead, Lead and Tin Plating," (1994) in metal finishing, Guidebook and Dictionary issue : 282.
43. F. A. Lowenheim (ed.) (1978) "Alkaline Tin Plating," in Modern Electroplating, McGraw-Hill, New York : 310.
44. A. Brenner (1963) Electrodeposition of alloys principles and Practice, vol.1, New York, Academic Press. : 75-78, 497-498.
45. K. Obata, N. Dohi, Y. Okuhama, S. Masaki, Y. Okada, M. Yoshimoto, U.S.patent 4459185.
46. F. I. Nobel, B. D. Ostrow and D. N. Schram, U.S.patent 4565609.
47. F. I. Nobel, B. D. Ostrow and D. N. Schram, U.S.patent 4717460.
48. G. A. Karustis and E. P. Leahy, U.S.patent 3850765.
49. J. C. Jonkind (1970) Plating, 901.
50. G. Schmerling (1952) Modified bronze plating as a substitute for nickel electroplating, 5 : 115-118.
51. H. M. Batten and C.J. Welcome (1934) U.S. patents 1, 970, 548-549.
52. E. S. Coe (June 14, 1951) Iron Age : 86.
53. S. W. Baier and D. J. Macnaughtan (1950) U.S. patent 2,511,395.
54. A. G. Gray (ed.) (1953) Modern Electroplating, 2<sup>nd</sup> edition. John Wiley and Sons, Inc., New York. Chapman and Hall, Limited, London : 435.
55. A. P. Abbott, J. C. Barron, M. Elhadi, G. Frisch, S. J. Gurman, A. R. Hillman, E. L. Smith, M. A. Mohamoud and K. S. Ryder (2008) ECS Trans., 16(36) : 47-63.
56. P. Walden (1914) Bull. Acad. Imper. Sci., 1 : 1800.
57. F. H. Hurley and T. P. Wier (1951) J. Electrochem. Soc., 98 : 207.
58. H. L. Chum, V. R. Koch, L. L. Miller and R. A. Osteryoung (1975) J. Am. Chem. Soc., 97 : 3264.
59. J. Robinson and R.A. Osteryoung (1979) J. Am. Chem. Soc., 101 : 323.
60. J. S. Wilkes, J. A. Levisky, R. A. Wilson and C. L. Hussey (1982) Inorg. Chem., 21 : 1263.
61. T. B. Scheffeler, C. L. Huseey, K. R. Seddon, C. M. Kear and P. D. Armitage (1983) Inorg. Chem., 22 : 2099.
62. D. Appleby, C. L. Hussey, K. R. Seddon and J. E. Turp (1986) Nature, 323 : 614.
63. H. Ohno (ed.): 'Electrochemical aspects of ionic liquids', 2005, New York, John Wiley & Sons : 1-21, 111-116, 124-125
64. A. R. Hajipour and F. Rafiee (2009) J.Iran.Chem.Soc. , 6(4) : 647-678.

- 
65. H. O. Bourbigou, L. Magna and D. Morvan (2010) *Applied Catalysis A:General*, 373 : 1-56
66. F. Endres, A. P. Abbott and D. R. MacFarlane (eds.) 'Electrodeposition from Ionic Liquids', 2008, WILEY-VCH Verlag GmbH & Co. KGaA, Weinheim: 1-77
67. A. P. Abbott, K. S. Ryder and U. König (2008) *Transactions of the Institute of Metal Finishing*, 86 (4) : 196-204.
68. F. Endres, S. Z. E.Abedin (2006) *Phys. Chem. Chem. Phys.*, 8 : 2101-2116.
69. F. Endres (2002) *Chem. Phys. Chem.*, 3 : 144-154.
70. A. P. Abbott and K. J. McKenzie (2006) *Phys. Chem. Chem. Phys.*, 8 : 4265-4279 .
71. J. S. Wilkes (2002) *Green Chemistry*, 4 : 73-80.
72. K. M. Dieter, C. J. Dymek, N. E. Heimer, J. W. Rovang and J. S. Wilkes (1988) *J. Am. Chem. Soc.*, 110 : 2722-2726.
73. H. Tokuda, K. Hayamizu, K. Ishii, M. Abu Bin Hasan Susan and M. Watanabe (2005) *J. Phys. Chem. B*, 109 : 6103.
74. M. Lipsztajn and R. A. Osteryoung (1985) *J. Electrochem. Soc.*, 132 : 1126.
75. J. M. Crosthwaite, M. J. Muldoon, J. K. Dixon, J. L. Anderson and J. F Brennecke, (2005) *J. Chem. Thermodyn.*, 37 : 559.
76. J. Golding, S. Forsyth, D. R. MacFarlane, M. Forsyth and G. B. Deacon (2002) *Green Chem.*, 4 : 223.
77. J. Sun, D. R. MacFarlane and M. Forsyth (2003) *Electrochim. Acta*, 48 : 1707.
78. S. Forsyth, J. Golding, D. R. MacFarlane and M. Forsyth (2001) *Electrochim. Acta*, 46 : 1753.
79. I.W. Sun and C.L. Hussey (1989) *Inorg. Chem.*, 28 : 2731.
80. I.W. Sun, E.H. Ward, C.L. Hussey, K.R. Seddon and J.E. Turp (1987) *Inorg. Chem.*, 26 : 2140.
81. T. B. Scheffeler and C. L. Huseey (1984) *Inorg. Chem.*, 23 : 1926.
82. C. L. Hussey, L. A. King and R. A. Carpio (1979) *Electrochem. Soc.: Solid-state science and technology*, 126(6) : 1029-1034.
83. C. Nanjundiah and R. A. Osteryoung (1983) *J. Electrochem. Soc.: Electrochemical science and technology*, 130(6) : 1312-1318.
84. K. Murase, K. Nitta, T. Hirato and Y. Awakura (2001) *Journal of applied electrochemistry*, 31 : 1089-1094.
85. S. Z. Abedin, A. Y. Saad, H. K. Farag, N. Borisenko, Q. X. Liu and F. Endres (2007) *Electrochimica Acta*, 52 : 2746-2754.
86. I. B. Assaker and M. Dhahbi (2011) *Journal of Molecular Liquids*, 161 : 13-18.
87. G. Sun and C. Sun (2010) *Microporous and Mesoporous Materials*, 128 : 56-61.
88. F. Endres and A. Schweizer (2000) *Phys. Chem. Chem. Phys.*, 2 : 5455-5462.

89. T. M. Laher and C. L. Hussey (1983) *Inorg. Chem.*, 22 : 3247-3251.
90. J. -F. Huang and I. -W. Sun (2003) *Journal of The Electrochemical Society*, 150(6) : E299-E306.
91. X. -H. Xu and C. L. Hussey (1993) *Journal of The Electrochemical Society*, 140(3) : 618-626.
92. T. -I. Leong, Y. -T. Hsieh and I. -W. Sun (2011) *Electrochimica Acta*, 56 : 3941-3946.
93. N. Tachikawa, N. Serizawa, Y. Katayama and T. Muira (2008) *Electrochimica Acta*, 53 : 6530-6534.
94. Y. -T. Hsieh and I. -W. Sun (2011) *Electrochemistry Communication*, 13 : 1510-1513.
95. Y. -T. Hsieh, T. -I. Leong, C. -C. Huang, C. -S. Yeh and I. -W. Sun (2010) *Chem. Commun.*, 46 : 484-486.
96. K. Murase, R. Kurosaki, T. Katase, H. Sugimura, T. Hirato and Y. Awakura (2007) *Journal of The Electrochemical Society*, 154 (11) : D612-D616.
97. T. Katase, R. Kurosaki, K. Murase, T. Hirato and Y. Awakura (2006) *Electrochemistry and Solid-State Letters*, 9 (4) : C69-C72.
98. K. Murase, A. Ito, T. Ichii and H. Sugimura (2011) *Journal of the Electrochemical Society*, 158 (6) : D335-D341.
99. S.A. Forsyth, J. M. Pringle and D.R. MacFarlane (2004) *Aust. J. Chem.*, 57 : 113-119.
100. L. G. Boxall, H. L. Jones and R. A. Osteryoung (1974) *J. Electrochem. Soc.: Electrochemical Science and Technology*, 121(2) : 212-219.
101. U. Anders and J. A. Plambeck (1969) *Canadian Journal of Chemistry*, 47 : 3055-3060.
102. M. Fleischmann and D. Pletcher (1970) *J. Electroanal. Chem.*, 25 : 449.
103. R. A. Carpio, L. A. King, R. E. Lindstrom, J. C. Nardi and C. L. Hussey (1976) *J. Electrochem. Soc.: Electrochemical science and technology*, 126(10) : 1644-1650.
104. R. J. Gale, B. Gilbert and R. A. Osteryoung (1978) *Inorg. Chem.*, 17 : 2728.
105. E. M. Arnett and J. F. Wolf (1975) *Journal of American Chemical Society*, 3264.
106. J. S. Wilkes, J. A. Levisky, R. A. Wilson and C. L. Hussey (1981) *American Chemical Society*, 21 : 1263-1264.
107. A. A. Fannin Jr., D. A. Floreani, L. A. King, J. S. Landers, B. J. Piersma, D. J. Stech, R. L. Vaughn, J. S. Wilkes and W. John L (1984) *J. Phys. Chem.*, 88 (12) : 2614-2621.
108. T. Welton (1999) *Chem. Rev.*, 99 : 2071-2083.
109. F. Endres (2002) *Chem. Phys. Chem.*, 3 : 144-154.

- 110.A. P. Abbott, G. Capper, K. J. McKenzie and K. S. Ryder (2007) *Journal of Electroanalytical Chemistry*, 599 : 288-294.
- 111.A. P. Abbott, G. Capper, D. L. Davies, R. Rasheed and V. Tambyrajah (2003) *Chem. Commun.* : 70.
- 112.A. P. Abbott, G. Capper, D. L. Davies, H. Munro and R. Rasheed (2004) *Inorg. Chem.*, 43 : 3447.
- 113.S. A. Bolkan and J. T. Yoke (1986) *Inorg. Chem.*, 25 : 3587.
- 114.J. Z. Yang, W. G. Xu, P. Tian and L. -L. He (2003) *Fluid Phase Equilib.*, 204 : 295-302.
- 115.E. R. Schreiter, J. E. Stevens, M. F. Ortwerth and R. G. Freeman (1999) *Inorg. Chem.*, 38 : 3935.
- 116.M. Hasan, I. V. Kozhevnikov, M. R. H. Siddiqui, C. Femoni, A. Steiner and N. Winterton (1999) *Inorg. Chem.*, 38 : 5637.
- 117.A. P. Abbott, D. Boothby, G. Capper, D. L. Davies and R. Rasheed (2004) *J. Am. Chem. Soc.*, 126 : 9142.
- 118.A. P. Abbott, G. Capper, D. L. Davies, H. L. Munro, R. K. Rasheed and V. Tambyrajah (2001) *Chemical Communications*, 2010-2011.
- 119.A. P. Abbott, G. Capper, D. L. Davies, H. L. Munro, R. K. Rasheed and V. Tambyrajah (2003) *Ionic Liquids as Green Solvents: Progress and Prospects*, 856 : 439-452.
- 120.A. P. Abbott, C. A. Eardley, N. R. S. Farley, G. A. Griffith and A. Pratt (2001) *Journal of Applied Electrochemistry*, 31 : 1345-1350.
- 121.A. P. Abbott, G. Capper, D. L. Davies, R. K. Rasheed and P. Shikotra (2005) *Inorganic Chemistry*, 44 : 6497-6499.
- 122.A. P. Abbott, G. Capper, B. G. Swain and D.A. Wheeler (2005) *Transactions of the Institute of Metal Finishing*, 83 : 51-53.
- 123.A. P. Abbott, G. Capper, D. L. Davies, K. J. McKenzie and S. U. Obi (2006) *Journal of Chemical and Engineering Data*, 51 : 1280-1282.
- 124.A. P. Abbott, G. Capper, D. L. Davies, R. K. Rasheed, J. Archer and C. John (2004) *Transactions of the Institute of Metal Finishing*, 82 : 14-17.
- 125.E. N. Golubeva, A. I. Kokorin, D. I. Kochubei, V. I. Pergushov and V. V. Kriventsov (2002) *Kinetics and Catalysis*, 43 : 408-411.
- 126.A. P. Abbott, J. C. Barron, G. Frisch, S. Gurman, K. S. Ryder and A. F. Silva (2011) *Physical Chemistry Chemical Physics*, 13 : 10224-10231.
- 127.A. P. Abbott, G. Capper, D. L. Davies, and R. Rasheed (2004) *Chem. Eur. J.*, 10 : 3769.
- 128.K. Haerens, E. Matthijs, K. Binnemans and B. V. Bruggen (2009) *Green Chem.*, 11 : 1357-1365



129. Different chemical price and availability, available from  
<<http://www.sigmaaldrich.com/united-kingdom.html>> [accessed date  
12/11/2011]
130. S. Roy, N. Pawnim and S. Ghosh (2012) Proceedings, International workshop  
on Electrochemical techniques for nano-scale surface engineering -2012  
(ECTNSE-2012), BARC, India.
131. P. Wasserscheid and W. Keim (2000) *Angew. Chem. Int. Ed.*, 39 : 3772-3789.
132. M. Freemantle (1998) *Chem. Eng. News*, 76 : 32-37.
133. (a) M. Freemantle (1999) *Chem. Eng. News*, 77 : 23.  
(b) D. Bradley (1999) *Chem. Ind.*, 86.  
(c) M. Freemantle (2000) *Chem. Eng. News*, 78 : 37-50.
134. T. L. Merrigan, E. D. Bates, S. C. Dorman and J. H. Davis (2000) *Chem. Commun.* : 2051-2052.
135. J. S. Wilkes (2002) *Green Chem.*, 4 : 73-80.
136. R. D. Rogers and K. R. Seddon (2003) *Science*, 302 : 792-793.
137. K. R. Seddon (2003) *Nat. Mater.*, 2 : 363-365.
138. A. B. McEwen, H. L. Ngo, K. LeCompte and J. L. Goldman (1999)  
*J. Electrochem. Soc.*, 146 : 1687-1695.
139. S. Carda-Broch, A. Berthod and A. W. Armstrong (2003) *Anal. Bioanal. Chem.*,  
375 : 191-199.
140. D. R. MacFarlane, P. Meakin, J. Sun, N. Amini and M. Forsyth (1999) *J. Phys. Chem. B*, 103 : 4164-4170.
141. (a) K.R. Seddon (1997) *J. Chem. Tech. Biotechnol.*, 68 : 351-356.  
(b) K.R. Seddon (1996) *Kinet. Catal. Engl. Transl.*, 37 : 693-697.
142. S.V. Dzyuba and R.A. Bartsch (2001) *Chem. Commun.*, 16 : 1466-1467.
143. K. N. Marsh, J. A. Boxall and R. Lichtenthaler (2004) *Fluid Phase Equilib.*, 219 :  
93.
144. J. Jacquemin, P. Nancarrow, D.W. Rooney, M.F. Costa Gomes, P. Husson, V.  
Majer, A.A.H. Pádua and C. Hardacre (2008) *J. Chem. Eng. Data*, 53 : 2133-  
2143.
145. A. P. Fröba, H. Kremer, A. Leipertz (2008) *J. Phys. Chem. B*, 112 : 12420.
146. C. D'Agostino, R. C. Harris, A. P. Abbott, L. F. Gladden and M. D. Mantle  
(2011) *Phys. Chem. Chem. Phys.*, 13 : 21383-21391.
147. L.C. Branco, J.N. Rosa, J.J. Moura Ramos and C.A.M. Alfonso (2002) *Chem. Eur. J.*, 8 : 3671-3677.
148. H. Waffenschmit (2000) Dissertation, RWTH Aachen, Germany.
149. P. Bonhôte, A. -P. Dias, N. Papageorgiou, K. Kalyanasundaram and M. Grätzel  
(1996) *Inorg. Chem.*, 35 : 1168.

- 150.P. Wasserscheid and T. Welton (eds.) (2003) *Ionic Liquids in Synthesis*, Wiley-VCH, Weinheim : 103-126, 112-116.
- 151.K. R. Seddon, A. Stark and M. J. Torres (2002) *Am. Chem. Soc., Symp. Ser.*, 819 : 34-49.
- 152.D. R. Lide (ed.) (1994) *CRC Handbook of Chemistry and Physics*, 75 edn, CRC Press, Boston, Section 6 : 243.
- 153.A. P. Abbott, R. C. Harris and K. S. Ryder (2007) *J. Phys. Chem. B*, 111 : 4910-4913.
- 154.A. P. Abbott (2004) *ChemPhysChem*, 5 : 1242-1246.
- 155.A. P. Abbott (2005) *ChemPhysChem*, 6 : 2502-2505.
- 156.A. P. Abbott, G. Capper and S. Gray (2006) *ChemPhysChem*, 7 : 803-806.
- 157.O. O. Okoturo and T. J. VanderNoot (2004) *Journal of electroanalytical chemistry*, 568 : 167-181.
- 158.J. R. Sanders, E. H. Ward and C. L. Hussey (1986) *J. Electrochem. Soc.*, 133 (2) : 325.
- 159.P. Hapiot and C. Lagrost (2008) *Chem. Rev.*, 108 : 2238-2264.
- 160.M. Galinski, A. Lewandowski and I. Stepniak (2006) *Electrochim. Acta*, 51 : 5567.
- 161.D. MacFarlane, J. Sun, J.J. Golding, P. Meakin and M. Forsyth (2000) *Electrochim. Acta*, 45 : 1271.
- 162.H.A. Every, A.G. Bishop, D. Macfarlane, G. Orädd and M. Forsyth (2004) *Phys. Chem. Chem. Phys.*, 6 : 1758.
163. J. Sun, D. R. MacFarlane and M. Forsyth (1998) *Phys. Chem. B*, 102 : 8858.
- 164.B.D. Fitchett, T.N. Knepp and J.C. Conboy (2004) *J. Electrochem. Soc.*, 151 : E219.
- 165.H. Tokuda, K. Hayamizu, K. Ishii, M.A.B.H. Susan and M.J. Watanabe (2005) *J. Phys. Chem. B*, 109 : 6103.
- 166.H. Matsumoto, M. Yanagida, K. Tanimoto, M. Nomura, Y. Kitagawa and Y. Miyazaki (2000) *Chem. Lett.*, 922.
- 167.H. Tokuda, S. Tsuzuki, M. A. B. H. Susan, K. Hayamizu and M. Watanabe (2006) *J. Phys. Chem. B.*, 110: 19593-19600.
- 168.R. Mills (1973) *J. Phys. Chem.*, 77 : 685-688.
- 169.W. Ogihara, J. Sun, M. Forsyth, D. R. MacFarlane, M. Yoshizawa and H. Ohno (2004) *Electrochim. Acta*, 49 : 1797-1801. 164.
- 170.(a) K.Hayamizu, Y.Aihara, H.Nakagawa, T.Nukuda and W.S.Price (2004) *J. Phys. Chem. B*, 108 : 19527-19532.
- (b) I.Nicotero, C.Oliviero, W.A.Henderson, G.B.Appetecchi and S.Passerini (2005) *J. Phys. Chem. B*, 109 : 22814 -22819.

- 171.F. Endres, C. Schrodtr (2000) *Phys. Chem. Chem. Phys.*, 2 : 5517.
172. D. MacFarlane, P. Meakin, N. Amini, M. Forsyth (1999) *J. Phys. Chem. B*, 103 : 4164.
- 173.J. Sun, D. R. MacFarlane and M. Forsyth (1997) *Ionics*, 3 : 356.
- 174.A. Alhaji (2011) "Electrodeposition of Alloys from Deep Eutectic Solvents", PhD, University of Leicester, Leicester.
- 175.S. Schaltin, N. R. Brooks, L. Stappers, L. D'Urzo, H. Plank, G. Kothleitner, C. Gspan, K. Binnemans and J. Fransaer (2011) *Journal of The Electrochemical Society*, 158(11) : D647-D650.
- 176.S. Schaltin, N. R. Brooks, K. Binnemans and J. Fransaer (2011) *Journal of The Electrochemical Society*, 158(1) : D21-D27.
- 177.N. R. Brooks, S. Schaltin, K. V. Hecke, L. V. Meervelt, K. Binnemans and J. Fransaer (2011) *Chem. Eur. J.*, 17 : 5054-5059.
- 178.A. P. Abbott, K. E. Ttaib, G. Frisch, K. J. McKenzie and K. S. Ryder (2009) *Phys. Chem. Chem. Phys.*, 11 : 4269-4277.
- 179.A. Popescu, V. Constantin, A. Cojocaru and M. Olteanu (2011) *Rev. Chim. (Bucharest)* 62(2) : 206- 211.
- 180.D. Lloyd, T. Vainikka, L. Murtomäki, K. Kontturi and E. Ahlberg (2011) *Electrochimica Acta*, 56 : 4942-4948.
- 181.B. G. Pollet, J. Hihn and T. J. Mason (2008) *Electrochimica Acta*, 53 : 4248-4256.
- 182.T. Tsuda, L. E. Boyd, S. Kuwabata and C. L. Hussey (2010) *Journal of The Electrochemical Society*, 157(8) : F96-F103.
- 183.A. Popescu, V. Constantin, A. Cojocaru, M. Olteanu, O. Demindenko and K. Yanushkevich (2011) *Rev. Chim. (Bucharest)* 62(6) : 626- 632.
- 184.C. P. D. Leon and F. C. Walsh (2003) *Trans. Inst. Met. Fin.*, 81(5) : B95.
- 185.C. D. Gu, Y. H. You, X. L. Wang and J. P. Tu (2012) *Surface and Coating Technology*, 209 : 117-123.
- 186.M. -J. Deng, J. -K. Chang, T. -I. Leong, S. -W. Fang, P. -Y. Chen and I. -W. Sun (2009) *Electrochemistry*, 77(8) : 588-590.
- 187.M. -J. Deng, T. -I. Leong, I. -W. Sun, P. -Y. Chen, J. -K. Chang and W. -T. Tsai (2008) *Electrochemical and Solid-State Letters*, 11(11) : D85-D88.
- 188.W. Yang, H. Cang, Y. Tang, J. Wang and Y. Shi (2008) *Journal of Applied Electrochemistry*, 38 : 537-542.
- 189.M. Morimitsu, Y. Nakahara, Y. Iwaki and M. Matsunaga (2003) *Journal of Mining and Metallurgy*, 39(1-2)B : 59-67.
- 190.B. C. M. Martindale, S. E. W. Jones and R. G. Compton (2010) *Physical Chemistry Chemical Physics*, 12 : 1827-1833.

191.A. Cojocaru, Ș. Costovici, L. Anicăi and T. Vișan (2009) *Metalurgia International*, 14(11) : 38-46.

## **Chapter 2 : FUNDAMENTAL ASPECTS**

The basic of electrodeposition technique is related to film growth on the cathodic substrate surface. This conveys the information on electrochemical reduction of metallic ions on the electrode surface from the electrolyte. In order to predict the interaction of the metal ion with electrode surface and reaction in the bulk electrolyte, different aspects of the electrochemistry need to be considered. Thus, this chapter consist of information required to understand the different processes occurring at the electrode surface and bulk electrolyte. Description of the structure of the metal-solution interface, electrochemical thermodynamics, kinetics, mass transfer in general aqueous electrolyte and the variation with electrolyte's media like IL is presented. In addition, to these some basic information is presented on the crystalline structure of the deposited metal and their solid state phases achieved as an end product.

### 2.1. Fundamentals of electrochemical deposition

An electrochemical system consists of a two electrodes separated by an electrolyte and connected via an external electronic circuit. The potentials formed at the electrode and electrolyte interface helps in ion movement from one electrode to the other. The electron flow is generated from the ionic neutralization during which donation or acceptation of electrons from or to the ions occurs. These electron flows through the externally connected conductors to complete the circuit. The basic diagram of an electroplating cell is shown in fig. 2-1. The principal components required for an electroplating process are:

1. An electroplating solution consists of a conducting solution of a metallic salt, the source for supplying of metallic ions to be plated, the buffer and additives required for specific purpose for effective quality deposition.
2. A conducting cathode, i.e. working electrode or substrate, on which the metal is to be deposited.
3. A conducting anode, which may be soluble or insoluble in the electrolyte.
4. An electroplating tank which is electrically and chemically insulated. The inert vessel also fulfills the parameters mentioned in the 1-3 of above. The electroplating tank/vessel is insulated by putting insulated steel, rubber-lined steel etc at its inner and outer surface.
5. A direct current electrical power source, usually regulated by transformer and rectifier applied across the anode and cathode to control and guide the ion flow.

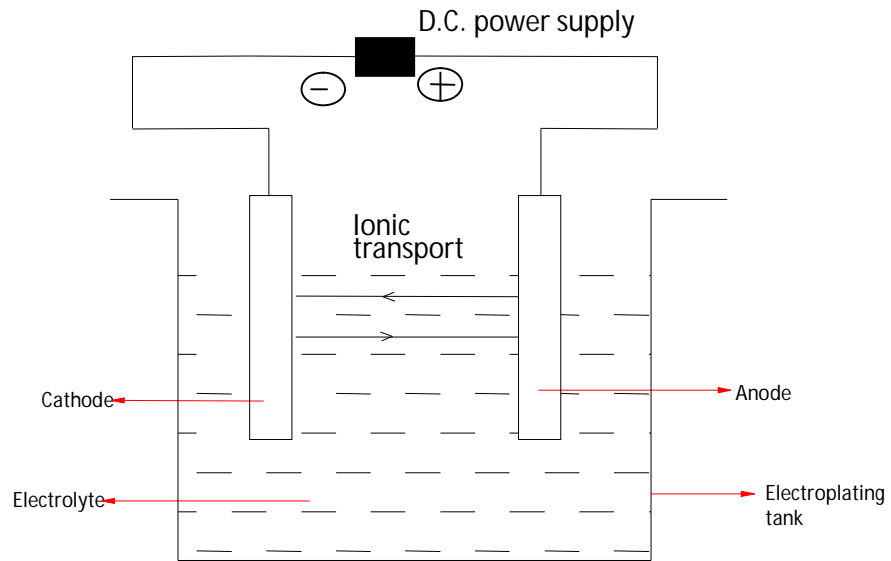


Figure 2-1 : General electrochemical cell adapted from ref. <sup>[1]</sup>

When a metal  $M$  is introduced to the electrolyte it produces metal ions  $M^{n+}$ . With time, the system will reach a equilibrium between the metal  $M$  and its ions in the solution, shown as <sup>[1]</sup> :



Where  $n$  is the number of the electrons involved in the reaction. The reactions occurring from left to the right consumes electrons, known as reduction and the reactions occurring from right to the left liberates electrons, known as oxidation. This electron transfer for a particular reaction is a complex process. It involves different steps from the electrolyte bulk to the electrode surface region. To understand the deposition mechanism more thoroughly, the processes in the interface of the electrolyte and double layer formed need to be studied. The oxidation and reduction process on the electrode surface follows different steps <sup>[2]</sup> like,

1. Mass transport of the reactant towards the electrode surface
2. Adsorption of the reactant
3. Electron transfer to the reactant
4. Surface migration of the reduced products
5. Nucleation and growth of the reduced products on the electrode surface
6. Mass transport of the remaining products to the bulk

The slowest step of the reaction is the rate determining step of the reaction. For electron transfer at the electrode surface the reactants needs to travel through a diffusion layer, then outer Helmholtz plane (OHP) and inner Helmholtz plane (IHP) from bulk solution. At the IHP the adsorbed ions or molecules are situated and the solvated

adsorbed are found beyond the OHP <sup>[1]</sup>. The supply of the reactant or the rate of the electron transfer controls the reaction. The double layer formed at the interface gives an idea about the relationship between potential, surface tension and the composition of the bulk solution <sup>[3]</sup>. It also helps in determining surface concentration of various species in the interface. Model of the electrochemical double layer is shown in the fig. 2-2. The thickness of this Helmholtz layer is found to be in the nanometer range and for the diffusion layer in micrometer range.

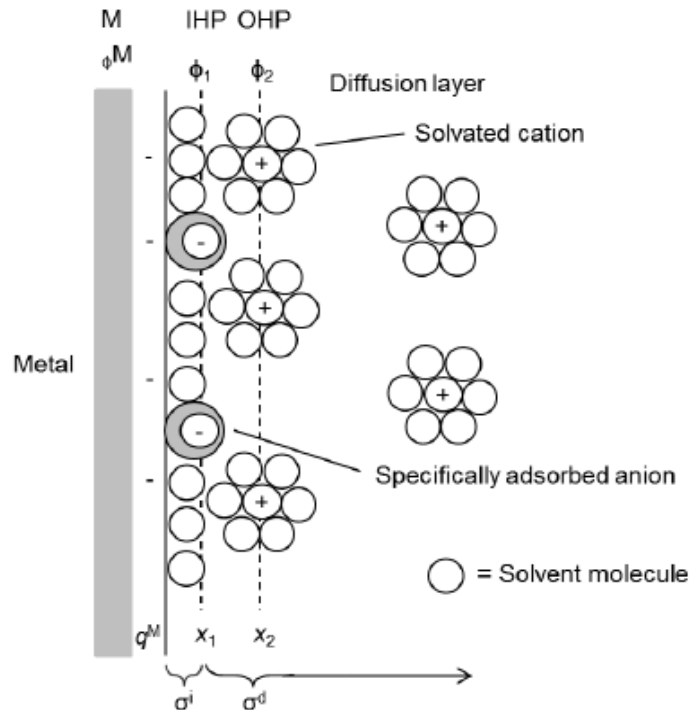


Figure 2-2 : Structure of the electrochemical double layer showing the inner and outer Helmholtz plane and diffusion layer after outer Helmholtz plane <sup>[1]</sup>

In the case of aqueous electrolytes, water molecules are found in the interface and with different orientations of oxygen and hydrogen molecules at close to the solid surface <sup>[4]</sup>. The interfacial region is electrically neutral with a possibility of the presence of non-uniform salt concentration. By charge-potential relationship of a system the value of the electric capacity of the double layer was determined. For an ideally polarizable electrode, the double-layer capacity can measure with an alternating current <sup>[3]</sup>. During electrodeposition the applied current is firstly consumed to charge this double layer. This current is referred as non-Faradic current or capacitive current as no charge is transferred across the double layer. The remaining of the applied current is spend to drive the electrodeposition reactions which is referred as Faradic current.

In case of IL electrolytes the structure of the double layer at the interface was observed to be different than aqueous electrolyte <sup>[5]</sup>. This is due to high concentration

and large size of ions of the electrolyte. Due to the large ionic radii, the electrode is assumed to be coated with minimum (6-7)Å thick layer of ions <sup>[6]</sup>. These highly concentrated ionic species lead to strong interaction between the ions which can be the reason of very different solvation property <sup>[7-8]</sup>. Moreover complex interfacial structure is expected due to lattice saturation and adsorption of the solvent ions <sup>[9]</sup>. Adsorption of the solvent ions and solute species participates on the electric double layer construction <sup>[10]</sup>. In the interface adsorption of solvent ions is possible depending on the types of the anion and cation.

The strength of the interaction in cations and anions affects the cation approach to the electrode. Moreover, strongly coordinated cations are unable to reach closely. At the interface the ions are distributed in a multilayer arrangement at the electrified interface due to lattice saturation. This also occurs due to high concentration and the large size of ions <sup>[9-10]</sup>. The structure also affects the orientation and configuration, which changes as a function of potential. The structure of asymmetric ions and their counter ions near to interface and bulk is shown in the fig. 2-3.

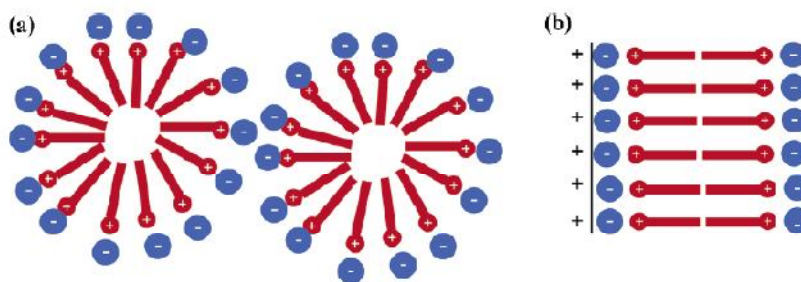


Figure 2-3 : The configuration and orientation of different anions and cation in [a] bulk of the electrolyte, [b] near a strongly charged interface <sup>[9]</sup>

In case of ChCl based ILs, the double layer in negative potential region showed similar structure as observed for the interface in the aqueous electrolyte. Here cations approaches to the electrode surface in a hydrated form which are separated from electrode surface by a layer of hydrogen bond donor molecules like urea, oxalic acid, glycerol, malonic acid, or ethylene glycol. At positive potential region the capacitance increases due to the adsorption of Cl<sup>-</sup> anion which might be not coordinated with the hydrogen bond donor molecules <sup>[11]</sup>.

### 2.1.1. Electrochemical thermodynamics

With the help of electrochemical thermodynamics the condition of the system at equilibrium can be described. Due to exchange of ions and electrons in the ionic media, a potential is built up and at equilibrium condition the potential between the metal and the solution is known as the equilibrium potential. The equilibrium potential



for the solution appears in absence of any external potential and as the system remains in open circuit condition it is defined as the open circuit potential. This equilibrium potential  $E_e$  is measured versus a reference electrode and calculated from the Nernst equation as,

$$E_e = E^0 + \frac{2.3RT}{nF} \log a_{M_i} \quad (2.2)$$

Where,  $E^0$  = standard electrode potential,

$R$  = universal gas constant,

$T$  = absolute temperature,

$F$  = Faraday constant and

$a_{M_i}$  = activity of the ion

The activity of the ion is related to the concentration of the components  $[C_{M_i}]$  of the electrolyte by a relationship,

$$a_{M_i} = \gamma_i' C_{M_i} \quad (2.3)$$

where  $\gamma_i'$  is an activity coefficient

Now the eqn. 2.2 can be rewritten as,

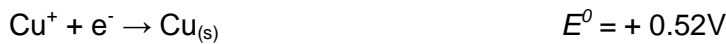
$$E_e = E^0 + \frac{2.3RT}{nF} \log[\gamma' C_{M_i}]$$

$$\text{or, } E_e = E^0 + \frac{2.3RT}{nF} \log \gamma' + \frac{2.3RT}{nF} \log C_{M_i}$$

$$\text{or, } E_e = E^0 + \frac{2.3RT}{nF} \log C_{M_i} \quad (2.4)$$

The term  $E^0$  is the formal potential of the reaction

The standard electrode potential in aqueous electrolyte at 25 °C of Cu <sup>[12]</sup> and Sn <sup>[10]</sup> reaction is :



By rearranging the eqn. 2.2, the equation can be written as <sup>[12]</sup> :

$$nFE_e = nFE^0 + RT \ln a_{M_i} \quad (2.5)$$

The eqn. 2.2 can be compared with equation used for the relationship between Gibbs free energy ( $\Delta G$ ) of the reaction and standard state Gibbs free energy ( $\Delta G^0$ ) of the reaction <sup>[12]</sup>,

$$\Delta G = \Delta G^0 + RT \ln a_{M_i} \quad (2.6)$$

The equilibrium potential of an reaction relates to Gibbs free energy denoted as <sup>[10]</sup>,

$$\Delta G = -nFE_e \quad (2.7)$$

Again from the equation (2.6) the  $\Delta G^0$  value can relate to the reaction constant of the reaction, at equilibrium the driving force of the reaction will become zero, as a result  $\Delta G = 0$ , and  $a_{Mi}$  will transform to equilibrium constant of cell reaction ( $K$ ), then the equation (2.4) will be <sup>[12]</sup>,

$$\Delta G^0 = -RT \ln K \quad (2.8)$$

The equilibrium constant of cell reaction ( $K$ ) can be expressed as ratio of the rate constants of the forward and backward reaction <sup>[12]</sup>, shown as

$$K = \frac{k_f}{k_b} \quad (2.9)$$

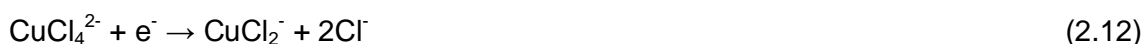
The crystal lattices of substances of IL are similar with salt hydrate. At very low temperatures ILs become thermodynamically unstable with respect to their liquid phases comparative to their cohesive energies. It is considered that at low temperature the Gibbs energy at crystalline phase is greater than liquid phase. It is likely to be due to the different size of anions and cations of the IL and their arrangement in the IL system <sup>[13]</sup>.

The variation in formal potential is expected with change in electrolytes from aqueous electrolyte to IL and with the range of ILs available. This is due to change in different physicochemical properties with the IL systems. The measurement for  $E^0$  values were carried in a series of substituted nitrobenzene and aliphatic nitro compounds RTILs like [BMIm-Tf<sub>2</sub>N] and [Et<sub>3</sub>BuN-Tf<sub>2</sub>N] <sup>[14]</sup>. A trend in variation of the  $E^0$  value was found with variation of molecular structure. As the donor groups were introduced on the aromatic ring, this leads to more and more negative values of  $E^0$  of the systems. The distance between cation and radical anion and the charge density are the influencing parameters for ion-pairing stabilization. This stabilization increases with change in cation from ammonium to imidazolium <sup>[14]</sup>. This is due to the planar geometry and ability to make hydrogen bonds of imidazolium cations <sup>[15]</sup>. The equilibrium potential value in chloroaluminate IL system for Cu <sup>[13]</sup> and Sn <sup>[13]</sup> is shown in table 2.1.

The formal potential value for different Cu and Sn redox couple in ChCl IL is not available. Thus to understand the metallic interactions within the ChCl IL electrolyte, reaction between the anionic and cationic species and metal reduction in the IL system is presented as,



In case of the metal reduction in IL electrolyte [13] :



Based on eqn. (2.10 - 2.13), In the present system the reactions are likely to be,



Table 2.1: Formal potential values Cu & Sn interaction in chloroaluminate IL electrolyte at 40 °C [13]

Redox Couple	$E^0$ (V)	$\text{AlCl}_3$ (mol%)	Cation
$\text{Cu}^{2+} + \text{e}^- \rightarrow \text{Cu}^+$	0.784	66.7	BP
	0.837	60.0	EMI
	0.843	66.7	EMI
	0.777	66.7	MP
$\text{Cu}^+ + \text{e}^- \rightarrow \text{Cu}_{(s)}$	1.825	66.7	BP
	1.851	66.7	MP
$\text{Sn}^{2+} + 2\text{e}^- \rightarrow \text{Sn}_{(s)}$	0.550	66.7	EMI
	-0.850	44.4	EMI

It is evident from the above equation that the formal potential value for the redox couples as described in the table 2.1 can be different due to the formation of different species in the metal side and component involved in the IL used. In general for a large range of ILs the Cu compounds have limited solubility [16-19]. For some electrolytes the cations were introduced by anodic dissolution. For Sn compounds, it has a lower solubility in IL than any other metal [20-21]. This solvent-solute interaction, solvation property can affect the equilibrium potential of the metal.

### 2.1.2. Electrochemical kinetics

The rate of an electrochemical reaction can be described by electrochemical kinetics. The reactions involving electron transfer can easily be explained by using electrochemical kinetics phenomenon. This transfer of electron is also depends on the potential of the electrochemical system. At equilibrium condition no net current is flowing through the system. To achieve metal deposition on the cathode surface, the system has to move away from its equilibrium condition and an external potential must be applied to the electrode system. The difference between the externally applied

potential ( $E$ ) and equilibrium potential ( $E_e$ ) is known as overpotential. It is essential to supply extra energy to the electrode reaction to proceed at a required rate.

If  $E$  is the externally applied potential then,

$$\eta = E - E_e \quad (2.16)$$

where  $\eta$  is the activation or kinetic overpotential of the system.

Thus due to the application of an external potential, a current is set up between the anode and cathode.

The anodic current is represented by,

$$i_a = i_0 \exp \left[ \frac{\alpha_a n F \eta}{RT} \right] \quad (2.17a)$$

The cathodic current is represented by,

$$i_c = i_0 \exp \left[ -\frac{\alpha_c n F \eta}{RT} \right] \quad (2.17b)$$

At  $\eta = 0$ ,  $i_a = i_c = i_0$ ,  $i_0$  is known as exchange current.

The net current flowing through the system is  $i_a - i_c$ .

$$i_T = i_0 \left[ \exp \left[ \frac{\alpha_a n F \eta}{RT} \right] - \exp \left[ -\frac{\alpha_c n F \eta}{RT} \right] \right] \quad (2.18)$$

The above equation is known as the Butler-Volmer equation and  $\alpha_a$ ,  $\alpha_c$  are known as transfer co-efficients.

For large values of overpotential (either positive or negative), then equation (2.18) becomes

$$i = i_0 \exp \frac{\alpha_a n F \eta}{RT} \quad (2.19)$$

Now, taking the logarithm of equation (2.19)

$$\log i = \log i_0 + \frac{\alpha_a n F \eta}{2.3RT}$$

$$\text{or, } \eta = \log \left( \frac{i}{i_0} \right) \times \frac{2.3RT}{\alpha_a n F} \quad (2.20)$$

The above equation is known as the Tafel equation.

Now the value of  $i_0$ ,  $\alpha_a$  and  $\alpha_c$  can be calculated by plotting  $\log i$  vs. the surface overpotential  $\eta$ , the slope of the linear part is  $\frac{\alpha_a n F}{2.3RT}$  and  $i_0$  is calculated from the intercept, shown in the fig. 2-4.

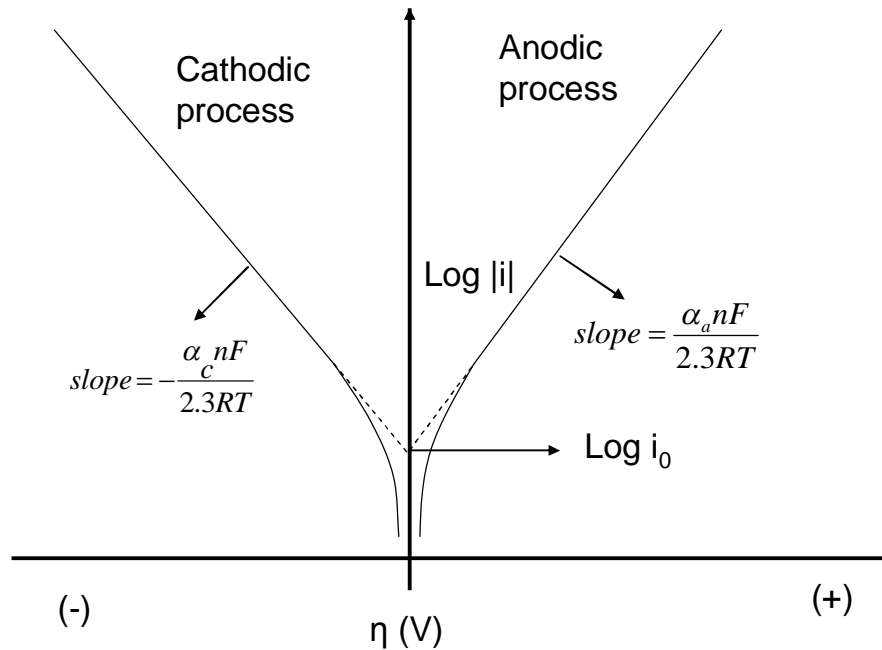


Figure 2-4 : Tafel plots for anodic and cathodic process

In the case of an IL electrolyte, the system follows Butler-Volmer type kinetics [14,22-23] and transfer co-efficient ( $\alpha$ ) and heterogeneous electron transfer rate constant ( $k_b$  or  $k_f$ ) value can be determined using different equation based on this theory [24-25]. These measurements were carried out in several RTIL electrolytes like [C<sub>2</sub>MIm-Tf<sub>2</sub>N] and imidazolium RTILs [24,26-27]. The rate constant value depends on the electrolyte viscosity, as a result low rate constant value was obtained [28]. The obtained value was smaller in IL electrolyte with respect to other molecular solvent [24]. With variation of ILs molecular structure the rate constant value varies in a wide range. It is reported that the presence of H-bonding and  $\pi$ - $\pi$  interaction in IL structure gives different electron transfer kinetics [14]. The parameter value can be improved by increase in temperature. However, for IL systems the relationship between heterogeneous electron transfer rate constant, viscosity and temperature was not reported.

### 2.1.3. Electrochemical mass transport conditions

For some electrodeposition reactions the kinetics is not limited by surface reaction. The reactant in this case is supplied from the bulk electrolyte by diffusion, migration and convection. When the reaction rate is increased further, the supply of reactant from the bulk electrolyte may suffer from mass transfer limitations. If the fast kinetic rate and mass transfer couple together, then mass transfer becomes a rate limiting process.

Considering equation 2.1, where  $M^{n+}$  consumes electrons at the electrode surface and is reduced to  $M$ . When there is a concentration difference between  $M^{n+}$  and  $M$ , a depletion layer is formed on the electrode surface due to the mass transfer limitation for  $M^{n+}$  and  $M$ . This layer is known as the Nernst diffusion layer which doesn't correspond to any real layer, shown in the Fig. 2-5. It is also known as the concentration boundary layer.

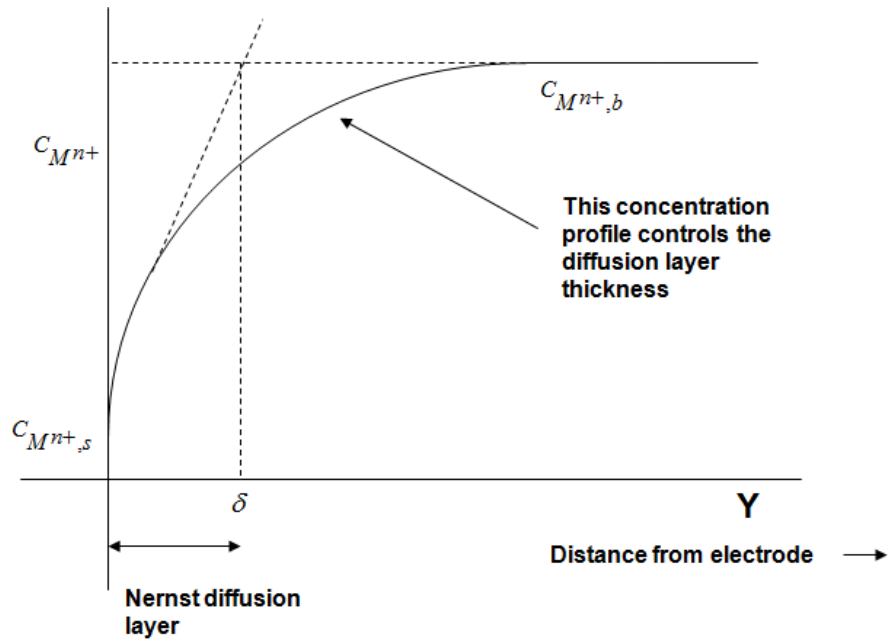


Figure 2-5 : Variation of concentration and formation of diffusion layer

This can be well explained by Fick's second law :

$$N_{M^{n+}} = -D_{M^{n+}} \left. \frac{dC_{M^{n+}}}{dy} \right|_{y=0} \quad (2.21)$$

Again it can be written as,

$$N_{M^{n+}} = -D_{M^{n+}} \frac{C_{M^{n+},s} - C_{M^{n+},b}}{\delta} \quad (2.22)$$

Where,  $N_{M^{n+}}$  = Flux of the species at the electrode surface, mol/m<sup>2</sup>s

$D_{M^{n+}}$  = diffusion coefficient of the depositing species  $M^{n+}$ , cm<sup>2</sup>/s

$C_{M^{n+},s}$  = surface concentration of the depositing species  $M^{n+}$  ions in the solution, mol/cm<sup>3</sup>

$C_{M^{n+},b}$  = bulk concentration of the depositing species  $M^{n+}$  ions in the solution, mol/cm<sup>3</sup>

$\delta$  = diffusion layer thickness, cm.

This Nernst diffusion layer is used to understand the mass transfer conditions at the electrode surface. As for example, when the fluid convection is low, then the

concentration profile becomes less steep and as a result the Nernst diffusion layer is large. Again the diffusion layer may be smaller due to steeper concentration profile of the reactant at high fluid convection. The mass transfer diffusion limiting current can be derived with the help of the Nernst diffusion layer.

In equation 2.22, when  $C_{M^{n+},s}$  comes close to zero, then the equation 2.22 becomes,

$$N_{M^{n+}} = D_{M^{n+}} \frac{C_{M^{n+},b}}{\delta} \quad (2.23)$$

This is possible due to the slow mass transfer and fast reaction at the electrode surface. This implies reaction at the surface cannot be increased anymore and the maximum of the  $M^{n+}$  is transferred to the electrode surface.

Now the flux can be represented in terms of limiting for the system  $i_{M^{n+},L}$ , as

$$\frac{i_{M^{n+},L}}{nF} = D_{M^{n+}} \frac{C_{M^{n+},b}}{\delta} \quad (2.24)$$

$$\therefore i_{M^{n+},L} = nFD_{M^{n+}} \frac{C_{M^{n+},b}}{\delta} \quad (2.25)$$

In case of IL electrolyte, the mass transfer behavior in the IL electrolyte largely depends on viscosity and solvent structure [4,29-31]. The other influential factors to be mentioned are the concentration of the solvent ions and co-solute in the IL electrolyte. In RTILs, ions movement is possible via series of discrete jumps in the hole available [4,32-33]. The availability of suitable hole size is totally dependent on the structure of the IL [32,34]. An idea on the structure of the IL can be achieved by correlation length determined by Stokes-Einstein equation. These hole size is described by correlation length which strongly depends on the hole radius [4]. Again the relationship between correlation length and void volume leads to mass transport phenomenon in RTILs. As a result it is expected that the diffusion co-efficient values depend on the size of the diffusing species [4].

To characterize the mass transport properties in various RTILs, Stokes-Einstein equation was used for a range of redox species [35]. The diffusion in RTILs can also explained by hole-hopping mechanism. It has been observed the diffusion co-efficient decreases with increase in IL viscosity [36]. With change in electrolyte to acetonitrile the diffusion co-efficient increases by two orders of magnitude due to lower viscosity of the electrolyte. It also has been observed for the ILs with same anion but different cations shows variation in diffusion co-efficient [36]. This inversely proportional relationship between diffusion co-efficient and viscosity of the electrolyte was observed for other redox species too [35]. These measurements were carried out by potential step chronoamperogram using Cottrell plot [35].

Due to higher viscosity value of RTILs, the rate of transport of the redox species becomes very slow. As the rate of mass transfer is very low, this affects the electrochemical behavior of the redox species. It is also important to mention that the dissolved gases and water have noticeable effect on mass transfer rate in IL electrolyte [37-38]. The equation and techniques used for aqueous systems can also be applied for the IL systems, to study the behavior of redox species in mass transfer controlled region.

#### 2.1.4. Faraday's law of electrolysis

For deposition purpose, Faraday's law provides the information regarded the mass produced and amount of electricity applied to the system. The Faraday's law of electrolysis does not change with variation of electrolyte media or with single metal, alloy system and it is a basis of all quantitative aspects of metal deposition. According to Faraday's law of electrolysis, the amount of electrochemical reaction occurs at an electrode is proportional to the quantity of electric charge (Q) passed through an electrochemical cell. Thus, if the weight of the deposited metal from the electrolysis is W, then according to Faraday's law :

$$W = Z Q \quad (2.26)$$

Here Z is the electrochemical equivalent, the constant of proportionality.

Faraday's law is also represented in terms of integral of cell current  $i$ , with respect to time,  $t$  as

$$Q = \int i dt \quad (2.27a)$$

For a particular case of constant current operation, charge is the product of current and time

$$Q = it \quad (2.27b)$$

$$W = Z it \quad (2.28)$$

Again from Faraday's law, it is known that the production of one-gram equivalent of a product at the electrode ( $W_{eq}$ ) in a cell requires 96,487 Coulombs. The constant 96,487 is termed as Faraday constant  $F$ , it is associated with a unit amount of electrons which is equal to the product of the Avogadro constant ( $N_A$ ) and the charge on the single electron,  $e$

$$F = N_A e \quad (2.29)$$

Again,

$$Z = \frac{A_{wt}}{nF} \quad (2.30)$$

$$W = \frac{A_{wt}}{nF} Q \quad (2.31)$$



Deposit thickness:

The deposit thickness can be calculated from deposit volume and can be represented as :

$$V = \Delta A_s \quad (2.33)$$

Where  $V$  = deposit volume,  $A_s$  = plated surface area,  $\Delta$  = thickness,

$$\Delta = \frac{V}{A_s} = \frac{w}{A_s \rho} \quad (2.34a)$$

Here  $w$  = mass of the deposit,  $\rho$  = density. By introducing eqn. 2.28 in eqn. (2.34a) and the eqn. (2.34a) becomes,

$$\Delta = \frac{ZQ}{A_s \rho} = \frac{ZIt}{A_s \rho} \quad (2.34b)$$

$$t = \frac{\Delta A_s \rho}{Zi} \quad (2.35)$$

The equation (2.34b) can be rewritten as

$$\Delta = \frac{A_w t}{nFA_s \rho} i \quad (2.36)$$

Current efficiency:

Current efficiency of a system can be measured by the ratio of the amount of deposited metal at cathode and amount of the charge applied during the deposition process. This can be qualified in terms of % of utilized charge to the charge passed to the system. Thus in principle, measure of the efficiency gives the estimation of cathode reactions.

Thus, *Current efficiency = (no. of coulombs used for depositing the metal or alloy) / (total no. of coulombs injected or passed) x 100%*

As an electrochemical system deal with different electrolytes and one or many metals, so some side reduction reactions can take place along with main cathodic reactions. The side reactions reduce the total amount of the deposited metal at the cathode. As an outcome current efficiency can be 100% or lower than 100%.

## 2.2. Alloy classification

Alloy deposition proceeds when two different metals are discharged at the electrode surface. The total alloy plating current is the sum of individual currents for each metal and current due to any side reaction associated during the process<sup>[39]</sup>. Let us assume an alloy formed by the co-deposition of metals  $M_1$  and  $M_2$ . If the alloy and single metal currents are  $i_{alloy}$ ,  $i_{M_1}$ ,  $i_{M_2}$  respectively, then :

$$i_{\text{alloy}} = i_{M_1} + i_{M_2} + i_{\text{other reaction}} \quad (2.37)$$

The above equation shows the relationship between the alloy current from the deposited metal and individual metal current involved in alloy deposition (if the metals are deposited individually under the same conditions). The individual metal currents and the alloy current are shown in the fig. 2-6. Then one can find the effect of other factors or calculate any other metal current when there is more than two metals or to modify the metal current. One can also determine the behavior of individual metals in alloy system. The behavior can be similar or different from the single metal property when it forms an alloy.

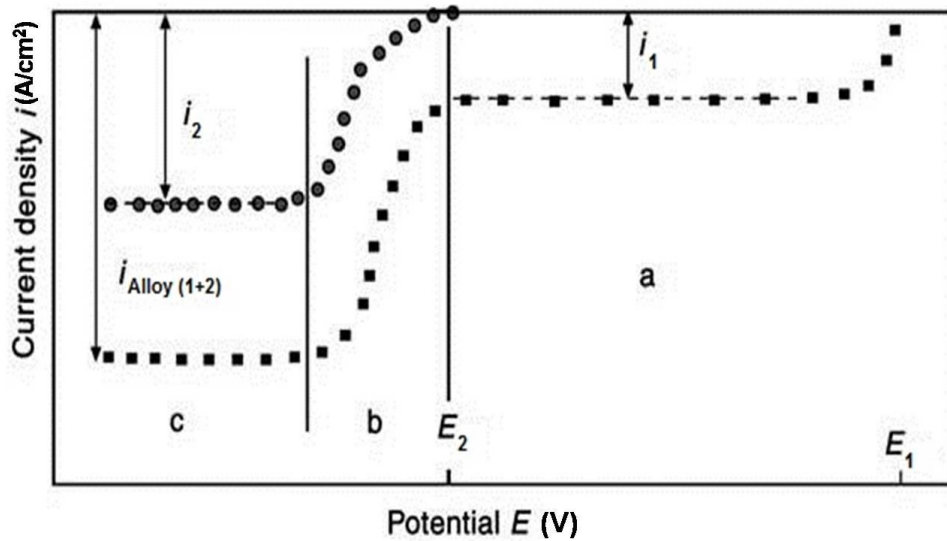


Figure 2-6 : Current-potential relationship during alloy deposition from individual metals 1 and 2, (a) deposition of metal 1 (b) irregular co-deposition, (c) regular co-deposition adapted from ref. <sup>[40]</sup>

In alloy deposition if the deposition of metal  $M_2$  and  $M_3$  is independent of each other, then the alloy current becomes the summation of the parent metal currents, as described in the equ. (2.37) and shown in the fig. 2-6. This type of alloy deposition is known as normal co-deposition. In fig 2-6,  $i_{M_1}$  is an example of normal co-deposition <sup>[40]</sup>. In the case of abnormal deposition the total current or the alloy current may not be the sum of individual metal reduction currents. In this case the total current diagram would be different than the fig 2-6. The alloy current can be partially charge transfer controlled and partially mass transfer controlled or one metal reduction can be influenced by the other metal reduction.

Some time in alloy deposition partial current in the alloy system cannot be determined using eqn. 2.37. This can be due to the mixed control in the system. For overall reaction mass transport control is the slowest step for the transportation of the species from or to the electrode. In a few cases the reaction rate is partly controlled by

electron transport in case of large over-potential region. This reaction condition is known to be under mixed controlled region. The total overpotential can be subdivided into three terms and the contributions are from charge transfer, mass transfer and resistance.

Mixed potential theory can be applied when the chemical composition of alloy is different than that of the electrolyte composition [41]. The corrosion model based on simple mixed potential theory gives a good description of actual behaviour of individual metals in the alloy system. In a mixed potential system, co-deposition can be many types and non interactive co-deposition one of them [41]. For this deposition type, the partial currents are largely independent of each other and the alloy composition can be predicted from the kinetics of the pure metals. In codeposition the partial current of the component depends on the transport of other components. Different alloy deposition based on the co-deposition method is shown in fig. 2-7. It is observed from fig. 2-7, deposition of the individual metal in the alloy system can be controlled by Tafel kinetics only or Tafel kinetic with mass transfer control deposition. In case of IL system, alloy deposition can be under mixed controlled region. Alloy system may suffer from galvanic corrosion due to equilibrium potential of the both metal redox couples present in the electrolyte. As a result displacement of one metal was observed due to the presence of thermodynamic driving force from the difference in equilibrium potentials of both the metal redox couple.

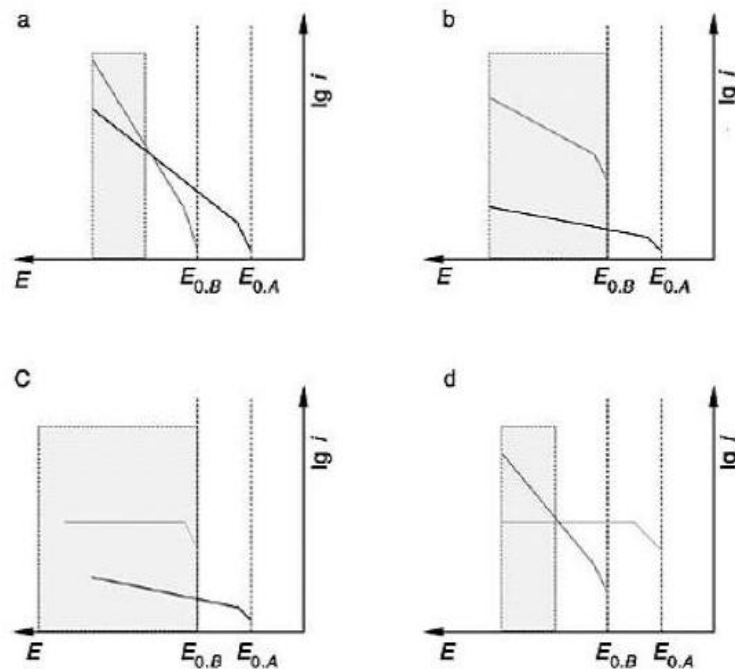


Figure 2-7 : Alloy deposition under different conditions, (a)& (b) both metal follows Tafel kinetics, (c) & (d) one of the component deposits under mass transfer control [41]

For IL system, the potentiostatic deposition of Cu-Al from lewis acidic  $\text{AlCl}_3\text{-EtMelmCl}$  suffers from thermodynamically unstable deposit in the plating solution [42-43]. This happens due to the absence of cathodic protection and Al gets displaced by Cu and Al content decreased in the achieved alloy deposit. This is due to the choice of metals in the alloy system and the difference in the deposition mechanism. If deposition for one metal is mass transfer limited and other is kinetically controlled, then one metal will not be able to keep pace with the reduction of the other metal. Moreover, the bulk electrodeposits of thermodynamically unstable alloys often exhibit high chloride content [42-43]. So keeping this problem in mind all the plating parameters need to control while considering the co-deposition of Cu-Sn alloy.

### 2.3. Material crystalline structure at solid state

The obtained deposit at solid state conditions consists of one or many metals and most of these metals are crystalline in nature. Depending on the crystalline structure, the properties of the alloy can be determined with the help of a phase diagram. To study the crystallography of a material, lattice and unit cell parameters of the crystalline structure are required. The structural pattern of a crystal can be represented by point pattern known as a space lattice. The space lattice is an infinite array of points, with each of these points is surrounded in an identical way by its neighbours in three dimensions to define the basic structure of the crystal [12].

Using Miller indices, the intersection distances for a particular plane can be determined. The notation for an individual plane is denoted by  $\langle hkl \rangle$ . In a unit cell, length of the each side is denoted as  $a, b, c$  and angle between them denoted as  $\alpha, \beta, \gamma$ . Depending on the symmetry and asymmetry of the sides and co-relation of the angles the crystal system can be divided into several types like orthorhombic, tetragonal, hexagonal and cubic. The spacing between the planes in atomic lattice can be defined as  $d_{hkl}$ . The crystalline plane and crystalline structure is shown in fig. 2-8.

For cubic lattice the interplanner distance for  $\langle hkl \rangle$  plane can determined as [12], shown in the equation below :

$$\frac{1}{d_{hkl}^2} = \frac{h^2 + k^2 + l^2}{a^2} \quad (2.38a)$$

In the case of tetragonal lattices, the interplanner distance can be determined as [12],

$$\frac{1}{d_{hkl}^2} = \frac{h^2 + k^2}{a^2} + \frac{l^2}{c^2} \quad (2.38b)$$

For orthorhombic lattice the expression [12] is:

$$\frac{1}{d_{hkl}^2} = \frac{h^2}{a^2} + \frac{k^2}{b^2} + \frac{l^2}{c^2} \quad (2.38c)$$

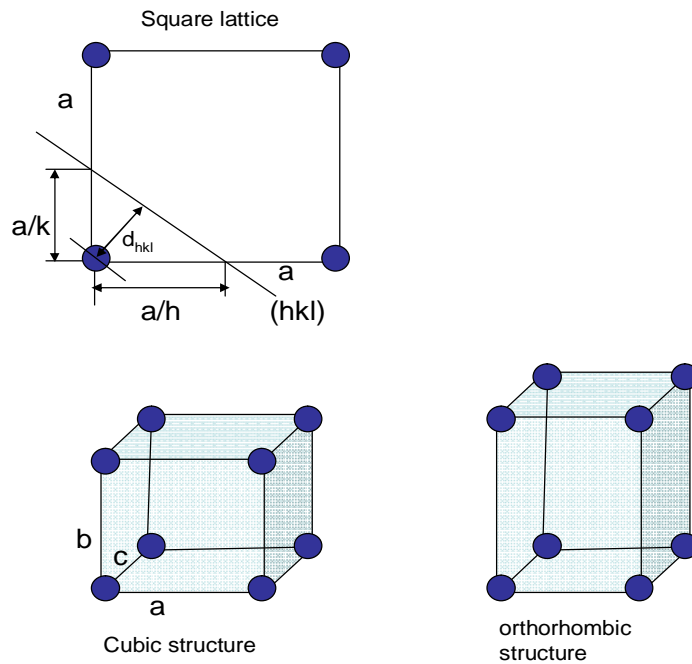


Figure 2-8 : Crystalline plan and crystalline structure

The determination of the position of atoms in a solid can be determined by analysis of diffracted X-ray patterns from a single crystal or powder. The angle of incidence of X-rays and the separation of lattice planes can be determined by using Bragg's law. The diffracted radiation of an atom can be determined by scattering factor. A wave diffracted by the  $\langle hkl \rangle$  planes gives measure of the structure factor by the overall amplitude.

According to Bragg's law,

$$m\lambda = 2d_{hkl} \sin\theta \quad (2.39)$$

The  $d_{hkl}$  can be determined using Bragg's law, the angle  $\theta$  corresponds to the reflection angle. For a deposited metal or alloy the diffracted x-ray pattern gives different information related to the crystalline phases, grain size or crystallite size, strain within the metal.

The obtained diffracted x-ray pattern represents as a line profile with sharp or broadened peak, shown in fig. 2-9. Using these peaks, all the above mentioned parameters can be determined. The grain size or crystallite size of the material can be determined using the Scherrer formula<sup>[44]</sup> shown in equation 2.40 below,

$$D' = \frac{0.9\lambda}{\beta' \cos\theta} \quad (2.40)$$

Where  $D'$  = grain size or crystallite size,  $\beta'$  = full line broadening at the half of the maximum intensity (FWHM),  $\lambda$  = x-ray wave length.

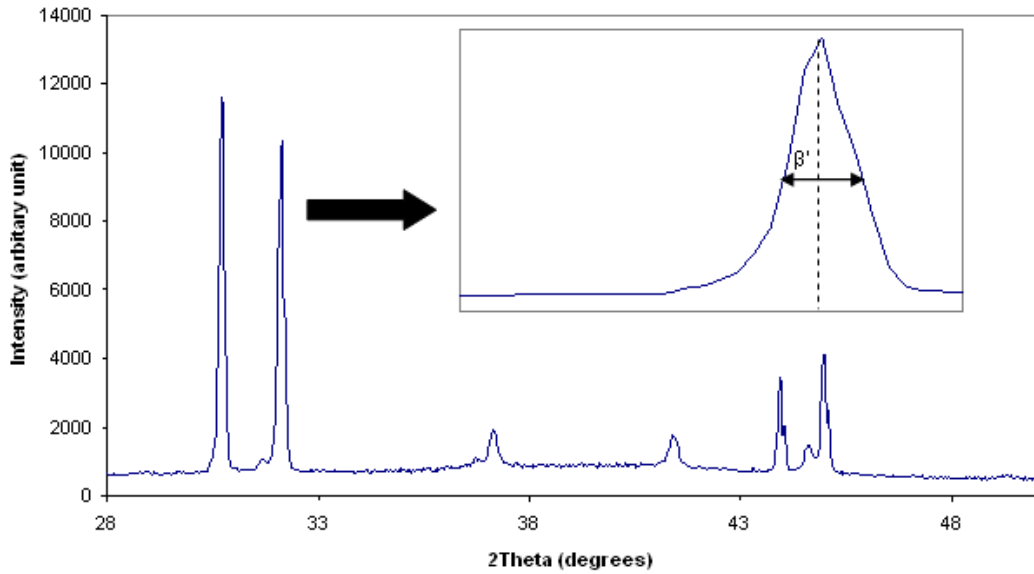


Figure 2-9 : Diffracted x-ray pattern for a metal and determination of  $\beta'$  from FWHM

The equation 2.40 is valid when the material is strain free. A material with no strain shows sharp peaks in a powder diffractogram, broadening of the diffracted peak is usually due to the defects in the crystalline structure or instrumental broadening. Due to the presence of strain within the crystal, the d spacing get change. As a result, the reflected angle  $\theta$  changes. Depending on the nature of the strain, the diffracted peak shifts or broadening of the peak is noticed [45-46]. Peak broadening is observed due to the presence of inhomogeneous strain within the crystallite. When a crystalline structure suffers from defects such as vacancies, dislocations and layer faults, then the presence of inhomogeneous strain is expected. The strain ( $\epsilon$ ) [47] in a crystalline structure is defined as

$$\epsilon = \frac{D'_s - D_s}{D_s} \quad (2.41)$$

Where  $D_s$  = strain free lattice spacing or crystallite size and  $D'_s$  = strained lattice spacing or crystallite size.

The inhomogeneous strain within a crystallite can be calculated from peak broadening using Williamson-Hall method [48]. The relationship between crystalline size, strain and line broadening is represented as,

$$\frac{2\cos\theta \cdot \beta'}{\lambda} = \frac{0.9}{D'_s} + \epsilon \frac{2\sin\theta}{\lambda}$$

$$\therefore \epsilon = \frac{\beta'}{\tan\theta} - \left( \frac{\lambda}{D'_s} \times \frac{1}{2\sin\theta} \times 0.9 \right) \quad (2.42)$$

## Reference :

1. A. J. Bard and L.R. Faulkner (eds.) (2001) *Electrochemical Methods Fundamentals and Applications*, 2nd ed., A John Wiley & Sons, Inc. publication : 1-153.
2. F. C. Walsh (1992) *Trans. Inst. Metal Finish.*, 70 (1) : 50.
3. J. Newman and K. E. Thomas-Alyea (2004) *Electrochemical Systems*, 3rd ed., New Jersey, A John Wiley & Sons, INC Publication : 177-194.
4. A. W. Taylor, P. Licence and A. P. Abbott (2011) *Phys. Chem. Chem. Phys.*, 13 : 10147-10154.
5. A.P.Abbott, G.Frisch and K.S.Ryder (2013) *Annu. Rev. Mater. Res.* 43 : 335-358.
6. F. Endres, A. P. Abbott and D. R. MacFarlane (eds.) 'Electrodeposition from Ionic Liquids', 2008, WILEY-VCH Verlag GmbH & Co. KGaA, Weinheim: 1-77
7. H. Weingärtner (2008) *Angew. Chem.*, 120 : 664-682; (2008) *Angew. Chem. Int. Ed.*, 47 : 654-670.
8. I. Krossing, J. M. Slattery, C. Daguene, P. J. Dyson, A. Oleinikova and H. Weingärtner (2006) *J. Am. Chem. Soc.*, 128 : 13427-13434.
9. A. A. Kornyshev (2007) *J. Phys. Chem. B*, 111 : 5545-5557.
10. Y. Z. Su, Y. C. Fu, Y. M. Wei, J. W. Yan and B. W. Mao (2010) *Chem Phys Chem*, 11 : 2764-2778.
11. A. P. Abbott, J. C. Barron, G. Frisch, S. Gurman, K. S. Ryder and A. F. Silva (2011) *Phys. Chem. Chem. Phys.*, 13 : 10224-10231.
12. P. Atkins and J. D. Paula (2010) *Atkins' Physical Chemistry*, 9th ed. Oxford university press : 928-929, 209-240, 695-712, 796-797.
13. H. Ohno (ed.): 'Electrochemical aspects of ionic liquids', 2005, New York, John Wiley & Sons : 1-21, 111-116, 124-125.
14. P. Hapiot and C. Lagrost (2008) *Chem. Rev.*, 108 : 2238-2264.
15. A. J. Fry (2003) *J. Electroanal. Chem.*, 546 : 35.
16. C. L. Hussey, L. A. King and R. A. Carpio (1979) *Electrochem. Soc.: Solid-state science and technology*, 126(6) : 1029-1034.
17. C. Nanjundiah and R. A. Osteryoung (1983) *J. Electrochem. Soc.: Electrochemical science and technology*, 130(6) : 1312-1318.
18. L. G. Boxall, H. L. Jones and R. A. Osteryoung (1974) *J. Electrochem. Soc.: Electrochemical Science and Technology*, 121(2) : 212-219.
19. U. Anders and J. A. Plambeck (1969) *Canadian Journal of Chemistry*, 47 : 3055-3060.

20. T. -I. Leong, Y. -T. Hsieh and I. -W. Sun (2011) *Electrochimica Acta*, 56 : 3941-3946.
21. N. Tachikawa, N. Serizawa, Y. Katayama and T. Muira (2008) *Electrochimica Acta*, 53 : 6530-6534.
22. C. A. Brooks and A. P. Doherty (2005) *J. Phys. Chem. B*, 109 : 6276-6279.
23. L. E. Barrosse-Antle, A. M. bond, R. G. Compton, A.M.O'Mahony, E.I.Rogers and D.S.Silvester (2010) *Chem. Asian J.*, 5 : 202-230.
24. A. W. Taylor, F. Qiu, J. Hu, P. Licence and D. A. Walsh (2008) *J. Phys. Chem. B*, 112 : 13292-13299.
25. Y.Pan, W.E.Cleland,Jr., and C.L.Hussey (2012) *Journal of the electrochemical Society*, 159(5) : F125-F133.
26. A. S. Barnes, E. I. Rogers, I. Streeter, L. Aldous, C. Hardacre and R. G. Compton (2008) *J. Phys. Chem. B*, 112, 7560.
27. J. Zhang and A.M. Bond (2003) *Anal. Chem.*, 75 : 2694.
28. X. Zhang, J. Leddy and A. J. Bard (1985) *J. Am. Chem. Soc.*, 107 : 3719.
29. K. R. J. Lovelock, A. W. Taylor, F. N. Cowling, P. Licence and D. A. Walsh (2010) *J. Phys. Chem. B*, 114 : 4442.
30. M. Carano and A. M. Bond (2007) *Aust. J. Chem.*, 60 : 29.
31. O. Fontaine, C. Lagrost, J. Ghilane, P. Martin, G. Trippé, C. Fave, J. C. Lacroix, P. Hapiot and H. N. Randriamahazaka (2009) *J. Electroanal. Chem.*, 632 : 88.
32. A. P. Abbott (2005) *ChemPhysChem*, 6 : 2502-2505.
33. A. P. Abbott, G. Capper and S. Gray (2006) *ChemPhysChem*, 7 : 803-806.
34. A. P. Abbott (2004) *ChemPhysChem*, 5 : 1242-1246.
35. K. R. J. Lovelock, A. Ejigu, S. F. Loh, S. Men, P. Licence and D. A. Walsh (2011) *Phys. Chem. Chem. Phys.*, 13 : 10155-10164.
36. A. Ejigu, K. R. J. Lovelock, P. Licence and D. A. Walsh (2011,) *Electrochimca Acta*, 56 : 10313-10320.
37. D. S. Silvester and R. G. Compton (2006) *Z. Phys. Chem.*, 220 : 1247-1274.
38. L. E. Barrosse-Antle, L. Aldous, C. Hardacre, A. M. bond and R. G. Compton (2009) *J. Phys. Chem. C*, 113 : 7750-7754.
39. C. Wagner and W. Traud (1938) *Z. Elektrochem.*, 44 : 391.
40. W. Plieth (2008) *Electrochemistry for Materials Science*, Hungary, Elsevier : 232-233.
41. D. Landolt (1994) *Electrochimica Acta*, 39 (8/9) : 1075-1090.
42. Q. Zhu and C. L. Hussey (2001) *Journal of the Electrochemical Society*, 148 (5) : C395-C402.



43. Q. Zhu and C. L. Hussey (2002) *Journal of the Electrochemical Society*, 149 (5) : C268-C273.
44. P. Scherrer, *Göttinger Nachrichten Gesell.* 2 (1918) p 98. (as referred to in B. D. Cullity and S. R. Stock, *Elements of X-ray Diffraction*, 3<sup>rd</sup> Ed. Prentice Hall Inc. , 2001, pp. 167-171.
45. Particle Size and Strain Analysis Application Note, available from <[http://www.h-and-m-analytical.com/pdfs/size\\_strain.pdf](http://www.h-and-m-analytical.com/pdfs/size_strain.pdf) > [accessed date 25/5/2012].
46. Crystallite Size and Strain, available from <<http://pd.chem.ucl.ac.uk/pdnn/peaks/size.htm> > [accessed date 25/5/2012].
47. R. P. Vinci, E. M. Zielinski and J. C. Bravman, *Thin Solid Films* 262 (1995) 142-153.
48. G. K. Williamson and W. H. Hall, *Acta Metallurgica* 1 (1953) 22-31.

## **Chapter 3: EXPERIMENTAL**

The electrodeposition of individual metals and alloys from ethaline melt is not a single step procedure but a multistep one. Thus the conducted experiments were divided into four main steps, the first step was related to electrolyte characterization. In this section different physical properties of the ethaline melt were determined to understand the behaviour of the electrolyte with and without any metal ions. In the next step, experiments were carried out to determine the electrochemical behaviour of different metals in the ethaline melt. There after electrodeposition of different metals from ethaline melt were carried out. The stability of these electrolytes was also examined as a part of electrolyte characterization for long term deposition. The final step was related to the analysis of material property of the achieved deposits. These experiments helped in characterizing the obtained deposit in order to determine the different metal content, their crystalline structure and different phases before and after heat treatment. For the plating experiments the deposition was carried out for 6 times for reproducibility check. Other experiments were carried out for at least 3 times for the reproducibility check.

### 3.1. Electrolyte preparation

Ethaline melt was prepared by mixing of choline chloride [ $C_5H_{14}NOCl$ ] and ethylene glycol [ $C_2H_6O_2$ ] in 1:2 ratio <sup>[1-3]</sup>. This mixture was kept in a thermostatic heater at 40 °C and stirred for 24 h until it forms a colourless liquid. After preparation, the electrolyte was stored in an airtight glass bottle to minimize the interactions of the electrolyte with the atmospheric conditions.

Later  $CuCl_2 \cdot 2H_2O$  was added to the prepared ethaline melt in increasing concentration ranging from 0.01 to 0.2 M. The solubility for Cu ion in ethaline melt was found to be 0.25 M. For Sn experiments,  $SnCl_2 \cdot 2H_2O$  was added in increasing concentration in the order of 0.01 to 0.1 M. The solubility of  $SnCl_2 \cdot 2H_2O$  in ethaline melt was 0.1 M. With increase in metal salt concentration beyond 0.1 M a white powdery layer was observed at the top surface of the electrolyte.

For Cu-Sn alloy system, the concentration of  $SnCl_2 \cdot 2H_2O$  was kept constant as 0.1 M while the concentration of  $CuCl_2 \cdot 2H_2O$  was varied in the range of 0.02 to 0.1 M. The preparation of this electrolyte consists of two steps,  $SnCl_2 \cdot 2H_2O$  was first added to ethaline melt for complete dissolution. At the end of this step,  $CuCl_2 \cdot 2H_2O$  was added in the previously prepared mixture.

For all electrolytes preparation, the mixing process was carried out at 40 °C, to facilitate the dissolution process. The prepared electrolytes were then stored in airtight glass bottles to minimize contact with air as mentioned in the previous section. During experimentation, the temperature of the electrolyte was kept above 25 °C, because re-crystallization of IL started to take place at temperatures below 20 °C. This process was visible to naked eye, an example of recrystallisation due to temperature reaching 15 °C is shown in fig. 3-1.



Figure 3-1 : Re-crystallization of the prepared ethaline melt at 15 °C, these crystals disappeared when the ethaline melt was heated to a temperature >20 °C

A summary of all bath formulations is presented in Table 3.1. For the experiments reagent grade chemicals were used obtained from Sigma-Aldrich.

Table 3.1: Electrolytes used for different studies on metal and alloy system

Electrolytes	Components	Concentration	Preparation temperature	Storing temperature
Ionic liquid (IL)	Ethylene Glycol (EG)	2 mol	40 °C	25 °C
	Choline Chloride (ChCl)	1 mol		
IL + Cu salt	(1ChCl:2EG)+	2:1		
	CuCl <sub>2</sub> .2H <sub>2</sub> O	0.01 to 0.2 M		
IL + Sn salt	(1ChCl:2EG)+	2:1		
	SnCl <sub>2</sub> .2H <sub>2</sub> O	0.01 to 0.1 M		
IL + Cu salt + Sn salt	(1ChCl:2EG)+	2:1		
	CuCl <sub>2</sub> .2H <sub>2</sub> O+	0.02 to 0.1 M		
	SnCl <sub>2</sub> .2H <sub>2</sub> O	0.1 M		

### 3.2. Electrolyte characterization

Various physical properties of the ethaline melt with and without metal ions were carried out. These measurements are relevant for the characterization of the electrolytes for metal deposition with respect to aqueous electrolytes or other IL electrolytes used for Cu, Sn and their alloy deposition purpose. Here density, viscosity and conductivity measurements were carried out as function of temperature.

#### 3.2.1. Density measurements

Density measurements were carried out by measuring the volume and weight of the examined electrolyte. For this measurement volumetric bottle and weighing machine was used. The volumetric bottle involved in density measurement is known as density bottle or specific gravity bottle (Fisher Scientific). In the experiment the weight of the empty bottle and the bottle filled with electrolyte upto a specified volume (marked on the bottle) was determined. The density ( $\rho$ ),  $\text{g/cm}^3$  of a material is related to the volume ( $V$ ),  $\text{cm}^3$  and weight ( $W$ ),  $\text{g}$ , the mathematical representation <sup>[4]</sup> is shown in equation 3.1,

$$\rho = \frac{W}{V} \quad (3.1)$$

Then using the equation 3.1, the density of the electrolyte was determined.

The concentration of the individual metal salts in the ethaline melt for these measurements is shown in the table 3.2. For these measurements 50 ml solution was used in each experiment in a temperature range of 20 to 60 °C, recorded by an externally supplied thermometer. This temperature variation was possible through glass beaker, magnetic stirrer and heater. At the end of each experiment the experimental set up was washed with deionised water and acetone and then dried completely.

Table 3.2: Concentration of individual metal salts used for density measurement

Metal salts	Concentration (M)
$\text{CuCl}_2 \cdot 2\text{H}_2\text{O}$	0.05, 0.1, 0.2
$\text{SnCl}_2 \cdot 2\text{H}_2\text{O}$	0.025, 0.5, 0.1
$\text{CuCl}_2 \cdot 2\text{H}_2\text{O}$ - $\text{SnCl}_2 \cdot 2\text{H}_2\text{O}$	0.02 - 0.1, 0.04 - 0.1, 0.1 - 0.1

### 3.2.2. Conductivity measurements

The conductivity measurement was carried out using an InLab730 conductivity probe from Mettler Toledo, attached to the SevenMulti Mettler Toledo bench meter. The set up is shown in fig. 3-2.

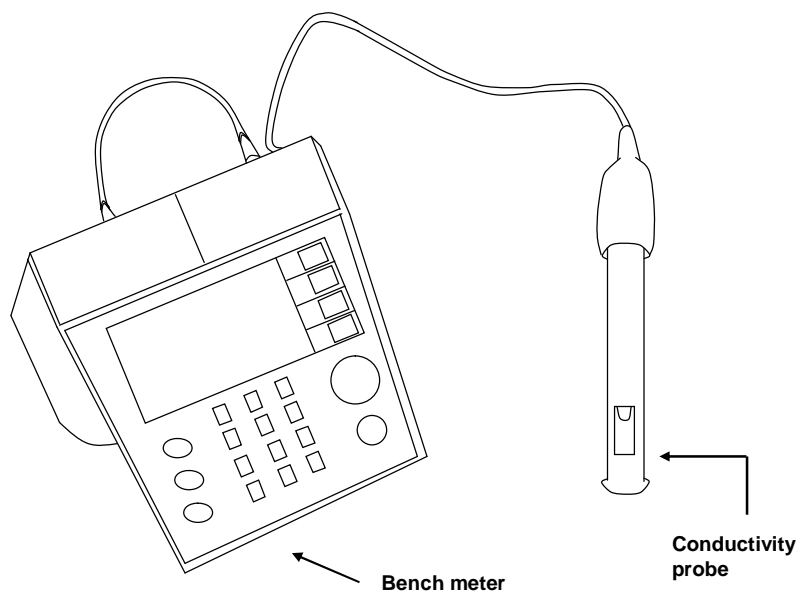


Figure 3-2 : Conductivity measurement equipment : Conductivity probe along with bench meter

The conductivity probe can be used for wide measurement range such as 0.01 to 1000 mS/cm. A temperature sensor of 0 to 100 °C range is attached to the conductivity probe or electrode which allows in determining the temperature during each measurements. For accurate and reproducible measurements the calibration of the electrode is required in an interval of certain period of time. Calibration was performed by five predefined conductivity standard solutions (Mettler Toledo).

The measurements were carried out using 50 ml electrolyte and examined as a function of temperature. For this measurement the experiments was carried out in temperature range 20 to 60 °C. The concentration of the individual metal salts in the ethaline melt used for the conductivity measurements are shown in the table 3.3.

Table 3.3: Concentration of individual metal salts used for conductivity measurement

Metal salts	Concentration (M)
$\text{CuCl}_2 \cdot 2\text{H}_2\text{O}$	0.01, 0.2
$\text{SnCl}_2 \cdot 2\text{H}_2\text{O}$	0.01, 0.1
$\text{CuCl}_2 \cdot 2\text{H}_2\text{O} - \text{SnCl}_2 \cdot 2\text{H}_2\text{O}$	0.02 - 0.1, 0.04 - 0.1, 0.1 - 0.1

For each measurement conductivity probe was inserted in the solution and then the conductivity value was noted from the bench meter. At the end of the each experiment, the conductivity probe was washed with deionised water and then wiped with a tissue paper. To increase the temperature of the experimental electrolyte, the electrolyte was placed in the heater using a glass beaker. To facilitate the temperature increase a magnetic stirrer was used. The temperature measurement for each set of experiments was carried out by an externally supplied thermometer.

### 3.2.3. Viscosity measurements

Viscosity measurements were carried out in a Visco 88 viscometer from Bohlin instruments. This viscometer is equipped with a constant speed motor along with a torque detection system. The instrument involved here consists of a solid cylinder with a conical base which rotates inside a double walled cylinder. The experimental sample was placed between these two cylinders. The instrument applies a controlled shear rate to the liquid and the resultant shear stress for the applied shear rate was recorded by the instrument. The applied torques and movements were converted into rheological format by using a set of measuring system constants <sup>[5]</sup>. The related measurements and calculations were carried out in a computer with the help of Bohlin software. The detail of the experimental set up is shown in the fig. 3-3.

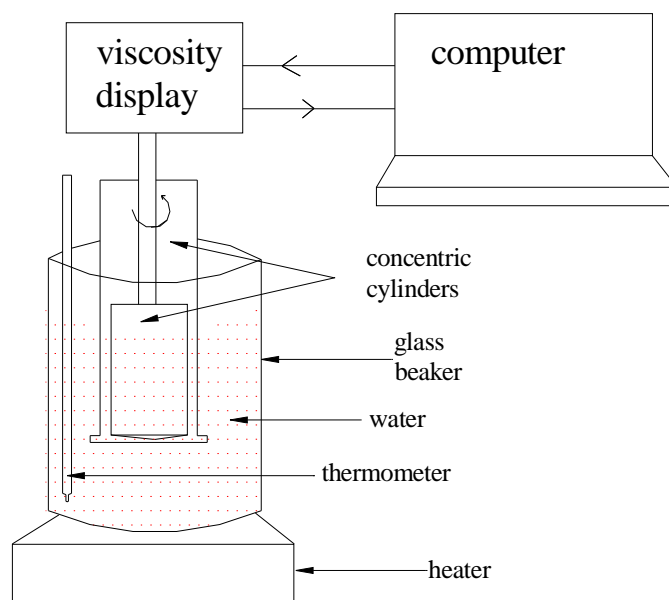


Figure 3-3 : The viscosity measurement setup showing the viscometer along with computer display from data collection

The viscosity of the electrolyte was obtained by the measured shear stress and shear rate by the instrument. The relationship between viscosity ( $\mu$ ), cP, shear stress ( $\tau$ ), Pa and shear rate ( $\gamma_s$ ),  $s^{-1}$  is given in the equation [4] below.

$$\mu = \frac{\tau}{\gamma_s} \quad (3.2)$$

For each measurement the solution was heated through a glass beaker and the glass beaker in warm water bath. For these measurements in each case 50 ml of solution was used where experimental temperature range was 20 to 60 °C. At the end of each experiment, the apparatus was washed with deionised water and acetone and dried completely before next use. The concentration of the individual metal salts in the ethaline melt used for this measurement is shown in the table 3.4.

Table 3.4: Concentration of individual metal salts used for viscosity measurement

Metal salts	Concentration (M)
CuCl <sub>2</sub> .2H <sub>2</sub> O	0.01, 0.2
SnCl <sub>2</sub> .2H <sub>2</sub> O	0.01, 0.1

### 3.3. Electrochemical characterization of the electrolytes

These experiments were carried out to determine the oxidation and reduction potential for ethaline melt itself and different metals in this electrolyte. Other parameter related to metal deposition like limiting current density can be obtained from these experiments. Moreover parameter like current efficiency can be determined too.

#### (a) Three electrode cell

For electrochemical characterization experiments a three electrode glass cell was used. The main cylindrical part is of diameter of 7 cm and height of 8 cm. In this cell the experiments were carried out using 250 ml electrolyte. It is also equipped with a luggin capillary of 1.5 cm diameter with a bent nozzle to connect the jacketed part of the cylindrical cell. This luggin capillary was used as an opening for reference electrode in the cell. Using this luggin capillary very close placement of working electrode and reference electrode was possible which helps in minimizing the ohmic or i-R drop between these electrodes. Here this distance between the working and reference electrode was kept approx. 2 mm for all the experiments to minimize ohmic or i-R drop. The lid of the cell consisted of five openings to insert electrodes, gas purger and gas

removal tube. This lid is of 7 cm diameter, and each of the diameters of the opening is of 1.5 cm. This three electrode cell described above is shown in the fig 3-4.

The main cylindrical part of this cell is jacketed with another cylindrical glass layer to control the temperature of the cell. Fluid at a particular temperature was then allowed to pass through this outer glass jacket which maintained the temperature of the electrolyte. For the present experiment a water bath was used for temperature control. This water bath (Haake) contains B<sub>3</sub> bath vessel and DC<sub>1</sub> temperature control module. For experimentations the temperature of water could be varied from ambient temperature to 95 °C. The accuracy of the instrument is  $\pm 0.02$  °C. The flow rate during circulation is 12.5 L/min and the heater wattage is 1050 W [6]. For the present experiments temperature of the electrolyte was varied in the range of 20 to 60 °C.

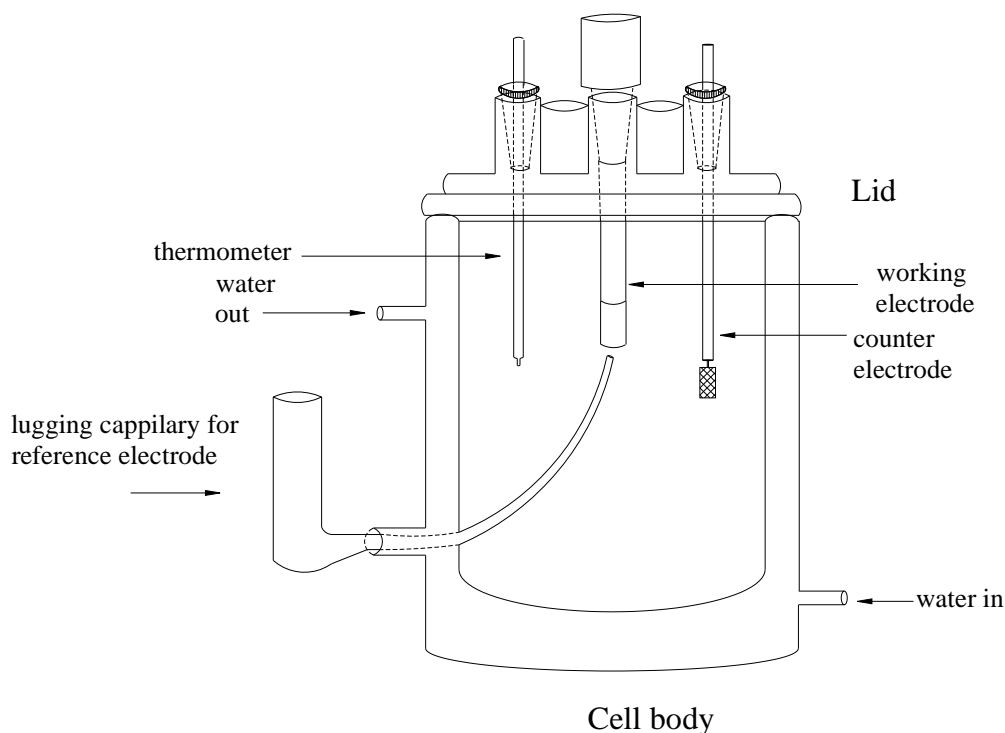


Figure 3-4 : Side view of the three electrode jacketed cell used for electrochemical characterization showing the position of working electrode, counter electrode and reference electrode

#### (b) Potentiostat

The current-potential behaviour of the electrolyte was recorded using a potentiostat recording system. Here experiments were carried out using a  $\mu$ Autolab Type II potentiostat/galvanostat instrument (EcoCheme). It is equipped with software named as General Purpose Electrochemical System (GPES) software. This software allowed the collection of data from potentiostat on to a personal computer. This



particular potentiostat is equipped with a maximum output current as 80 mA and potential as 12 V. For measurements the instrument controls the potential between the counter electrode and working electrode. With this arrangement the applied potential difference remains constant between the working electrode and reference electrode. It is basically a control and measuring device, which acts on the change of resistance in the system. The electrical circuit within the potentiostat vary with the current supply to control the potential according to the solution resistance [7].

(c) *Electrodes*

Rotating disc electrode (RDE) is one of the most widely used electrodes for electroanalysis which works on forced convection mass transfer under steady state condition. The fluid flow in RDE is laminar for wide range of velocity, up to Reynolds number ( $Re$ ) $>30,000$ . This property of RDE helps in testing mathematical models of electrochemical systems [7]. For these experiments EDI 101 rotating disc electrode (Radiometer Analytical) was used. The electrode set up is shown in the fig. 3-5.

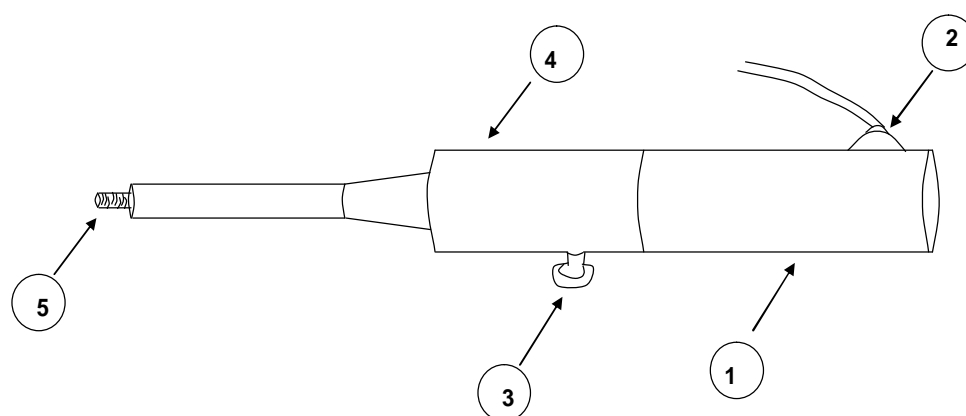


Figure 3-5 : Rotating disc electrode, 1: The electrode motor, 2: 5-pin female DIN socket for the connection of speed control unit, 3: Banana socket for the contact between the disc and potentiostat, 4: The electrode body, 5: The screw for electrode disc holder

The rotating disc electrode is equipped with an electrode motor and an electrode body. The electrode body consists of connections for potentiostat, speed control unit as shown in the fig. 3-5. At the very front of the body a screw is available to attach the electrode tip. The tip is cylindrical in shape and the disc in the tip is imbedded in a rod of insulating material. This insulating material is made from PTFE. The disc can be of platinum, gold, or copper or other metal according to need of the experiments. The tip along with the disc is shown in the fig. 3-6 below.

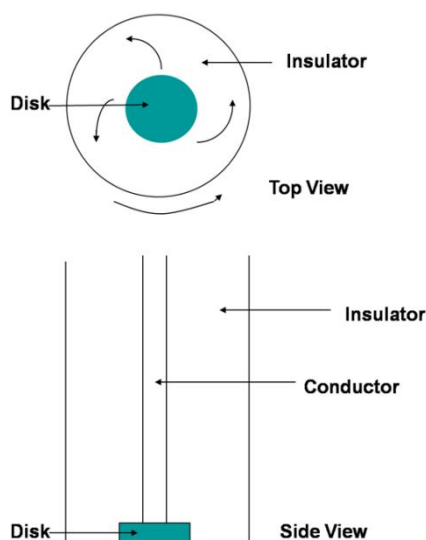


Figure 3-6 : Tip of the rotating disc electrode

The rod of the insulating metal is attached to a motor directly by a flexible rotating shaft and the linear frequency of rotation is denoted by  $f$ . The rotation rate is usually defined by angular velocity,  $\omega$ , where  $\omega = 2\pi f$ . Due to this circular motion a radial velocity is developed in the fluid system and the adjacent layer start moving it away from the disc centre. Thus, due to the forced convective flow by the disc surface, fresh electrolyte is brought to the surface of the disc continuously. The rotating structure of RDE helps in pulling the fresh solution upward and throwing it outward. Due to the centrifugal force the disc drags the solution at its surface from the center to the radial direction. The equations for the velocity profile near to the RDE [7] can be written as,

$$V_y = -0.51 \omega^{3/2} \nu^{-1/2} y^2 \quad (3.3)$$

$$V_r = -0.51 \omega^{3/2} \nu^{-1/2} r y \quad (3.4)$$

Near the surface of the rotating disk,  $y=0$

The equations for the velocity profile away to the RDE, can be written as

$$U_o = \lim_{y \rightarrow \infty} v_y = -0.88447 (\omega \nu)^{1/2} \quad (3.5)$$

Again the Nernst diffusion layer thickness is related to diffusion co-efficient ( $D$ ), rotation speed ( $\omega$ ) of the electrode and other parameters. The relationship in RDE system [7-8] can be represented as,

$$\delta = 1.61 D^{1/3} \omega^{-1/2} \nu^{1/6} \quad (3.6)$$

The limiting current was determined from eqn. 3.6, represented as

$$i_L = \frac{nFDC}{1.61 D^{1/3} \omega^{-1/2} \nu^{1/6}} \quad (3.7)$$

$$i_L = 0.623nFCD^{2/3}\omega^{1/2}\nu^{-1/6} \quad (3.8)$$

$$\text{or, } \frac{i_L}{nFC} = 0.623D^{2/3}\omega^{1/2}\nu^{-1/6} \quad (3.9)$$

Putting,  $k_m = \frac{i_L}{nFC}$  and  $\omega = U/d$  in eqn. (3.9)

$$\text{or, } k_m = 0.623D^{2/3} \left[ \frac{U}{d} \right]^{1/2} \nu^{-1/6} \quad (3.10)$$

Now multiplying both side of eqn. (3.10) with  $d/D$ ,

$$\text{or, } \frac{k_m d}{D} = 0.623D^{-1/3} [Ud]^{1/2} \nu^{-1/6} \quad (3.11)$$

Using dimensionless numbers, the dimensionless form of equation 3.8 can be obtained from (3.11) as,

$$Sh = 0.623 Sc^{1/3} Re^{1/2} \quad (3.12)$$

The rotation speed of the RDE was controlled using a CTV 101 speed control unit (Radiometer Analytical). The applied rotation speed can be maintained in the range of 0 to 5000 rpm (revolution per minute) and the accuracy of the instrument is  $\pm 2$  rpm<sup>[9]</sup>. During operation the rotating disc electrode unit was attached to the speed control unit pin of the cable. Here experiments were carried out in the RDE speed range of 0 to 3000 rpm.

RDE tip was polished by 4000 grit paper and then washed with deionised water and acetone before placing into the solution. After each set of experiments the three electrode cell, the working electrode, the counter electrode and the reference electrodes were washed thoroughly with distilled water, acetone and then dried thoroughly. Experiments were carried out using platinum rotation disk (Radiometer Analytical) as working electrode, platinum mesh (Good Fellow) as counter electrode and silver wire (Good Fellow) reference electrode.

The silver wire was used as quasi-reference electrode for study in ChCl based ILs was used before<sup>[1,3]</sup>. It was found that this pseudo reference electrode has stable reference potential<sup>[10]</sup>. The potential difference was measured between the Ag wire and the standard calomel electrode before the experiments and the obtained value was 79 mV.

### 3.3.1. Formal potential determination experiments

The formal potential of the reactions were determined by measuring open circuit potential across the electrode using 175 true RMS Multimeter (Fluke) at  $22 \pm 2$  °C. The multimeter was connected across the working electrode and reference

electrode for measurements. The potential measurements were carried out between a 1 h and 24 h span of time. Measurements were noted for every hour and the measurements after 12 h were found to be stable.

### 3.3.2. Voltammetry experiments

The voltammetry experiments were carried out to locate redox potentials of electroactive species. In these experiments, measurement of current is conducted across the electrode as a function of potential applied between the electrodes. The potential applied to the electrode varies linearly with time from a potential where oxidation or reduction of the solute takes place. The applied potential form in the working electrode is shown in fig. 3-7. Due to the inverted triangular wave of the applied potential, the electrode potential becomes more negative and varies linearly with time. When the potential reaches to the predetermined switching potential, the potential of the working electrode was scanned to more positive potential changing linearly with time <sup>[7,11]</sup>.

In the forward sweep, increase in negative current was observed followed by one or multiple reduction steps. The region (0-1) in fig 3-7 is showing forward sweep. In the forward sweep, scan is carried out by applying negative potential and reduction potential of the reaction along with limiting current for metal deposition can be determined. After the occurrence of one or more reactions in the negative region, the direction of the sweep was reversed. The region (1-2) in fig 3-7 is showing reverse sweep. In the reverse sweep, scan carried out in positive potential help in stripping off the deposited metal and stripping currents can be determined. The time required for the experimentation can be controlled by the speed of the scan or sweep rate. The current returns to zero at the end of each scan.

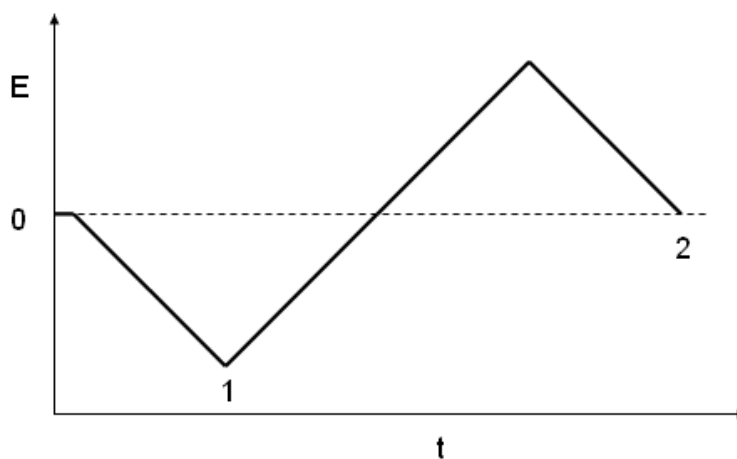


Figure 3-7 : The potential to the system as a function time

The voltammetry experiments were performed for the ethaline melt with and without metal salts. The voltammetry experiments with ethaline melt were carried out to determine the reduction potential of the electrolyte, to define the scan range for the voltammetry experiments for ethaline melt with metal salts. These experiments were carried out by varying RDE speed and temperature to determine changes during the scans. From voltammetry scans determination of the reduction potential of the metal along with limiting current for metal deposition was determined. From this limiting current value, using eqn. 3.8 diffusion co-efficient for the particular metal was determined. These experiments were carried out with different concentration of  $\text{CuCl}_2 \cdot 2\text{H}_2\text{O}$ ,  $\text{SnCl}_2 \cdot 2\text{H}_2\text{O}$  and  $\text{CuCl}_2 \cdot 2\text{H}_2\text{O} - \text{SnCl}_2 \cdot 2\text{H}_2\text{O}$  with various operation parameters were listed in table 3.5.

Table 3.5: Voltammetry experiments in ethaline melt with and without metal salts

Electrolyte	Concentration of the metallic salt mention (M)	Scan Potential range (V)	Rotation Speed (rpm)	Temperature ( $^{\circ}\text{C}$ )	Scan rate (V/s)
IL	-	+1 to -1	0 to 2500	25 to 55	0.03
IL+ $\text{CuCl}_2 \cdot 2\text{H}_2\text{O}$	0.1	+0.6 to -0.7	0	25	0.01 to 0.05
	0.01 to 0.2	+0.6 to -0.7	100 to 3000	25 to 55	0.03
		+0.6 to 0	500 to 2000	25	
IL+ $\text{SnCl}_2 \cdot 2\text{H}_2\text{O}$	0.05	+0.1 to -0.7	0	25	0.01 to 0.2
	0.01 to 0.1		300 to 2000	25 to 55	0.01
IL+ $\text{CuCl}_2 \cdot 2\text{H}_2\text{O} - \text{SnCl}_2 \cdot 2\text{H}_2\text{O}$	0.02 - 0.1, 0.04 - 0.1	+1 to -1	220	25	0.01

With the help of voltammetry scans, charge calculation of the anodic and cathodic part was carried out. Then from this charge calculation current efficiency of individual metal and alloy system was calculated. Current efficiency was calculated from the ratio of the charge at the cathodic side and the anodic side of the obtained scan for each system. Later the ratio was multiplied by 100, to represent the current efficiency in percentage.

### 3.3.3. Anodic Stripping Voltammetry experiments

The anodic stripping voltammetry (ASV) experiments were used for separation and analysis of different trace metals in the electrolyte [11]. These experiments were carried out to analysis the stripping currents noted in the anodic region of the voltammetry scan. ASV can be simplified as linear sweep voltammetry, here scan is performed at positive potential range. By this procedure metal was stripped off from the substrate surface and stripping currents was noted. This helps in determining different reactions during deposition procedure at substrate surface. ASV for the alloy system helps in determining ratio of the individual metal in the deposited alloy. This was possible by calculating charge for each individual stripping current obtained during the scan.

In these experiments, at first the metal deposition was carried out at the chosen potentials for duration of 3 to 10 min. Then the deposit surface was scanned in the positive potential range. This range was chosen according to the obtained voltammetry scans. These experiments were carried out for Cu-Sn alloy system to establish the anomalies or different stripping current observed in the voltammetry experiments. The summery of the above mentioned anodic stripping voltammetry experiments are shown in table 3.6.

Table 3.6: Anodic Stripping Voltammetry experiments in ethaline melt with metal ions

Electrolyte	Concentration of the metallic salt mention (M)	Deposition potential range (V)	Rotation Speed (rpm)	Temperature (°C)	Scan rate (V/s)	Anodic scan range (V)
IL+ CuCl <sub>2</sub> .2H <sub>2</sub> O - SnCl <sub>2</sub> .2H <sub>2</sub> O	0.04 - 0.1	-0.3 to - 0.6	220	25	0.01	-0.5 to +1

### 3.4. Electrodeposition experiments

#### 3.4.1. Individual metal deposition

The plating experiments were performed by potentiostatic and galvanostatic method. For deposition by potentiostatic method, the potentiostat was used for maintaining the specific potential during deposition experiments. For galvanostatic deposition PL320 constant power supply (Thurlby-Thandar) and the multimeter was used. The arrangement and connection of the instruments involved in potentiostatic/galvanostatic deposition is shown in the fig. 3-8.

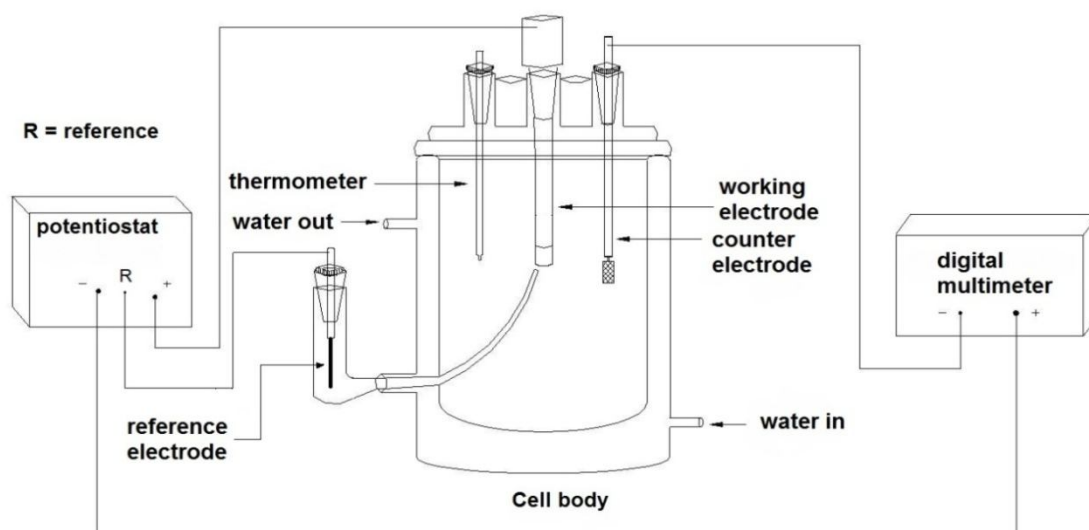


Figure 3-8: Arrangement for potentiostatic/galvanostatic deposition experiments showing the connection between different instrument and three electrode cell. The potentiostat was replaced by a power supply during galvanostatic experiments.

For plating purpose commercially available stainless steel substrate was used. Thus deposition experiments was carried out in stainless steel RDE, along with the platinum mesh as counter and silver wire as reference electrode. The plating experiments were carried out in the three electrode cell along with water bath to control the temperature of the electrolyte. Potentiostatic and galvanostatic deposition experiments were carried out by varying various parameters like metal ion concentration, rotation speed, temperature and duration of deposition. The details of experiments are summarised and presented in the table 3.7 and 3.8.

At the end of the deposition process current efficiency was calculated by direct weighing of the obtained deposit. The stainless steel disc was weighed before the deposition experiment and it was weighed again after the deposition experiments. Then using eqn. 2.36, efficiency was calculated by dividing the weight of the deposit obtained with the value obtained from theory. Later the ratio was multiplied by 100, to represent the current efficiency in percentage.

Table 3.7: Potentiostatic deposition of Cu, Sn and Cu-Sn alloy

Potentiostatic experiments	Applied potential (V)	Electrolyte	Concentration of the metallic salt mention (M)	Rotation Speed (rpm)	Temperature (°C)	Duration (min)
Cu deposition	-0.6	IL+ CuCl <sub>2</sub> .2H <sub>2</sub> O	0.05,0.2	700, 1300	25, 45	10 to 105
Sn deposition	-0.5 to 0.6	IL+ SnCl <sub>2</sub> .2H <sub>2</sub> O	0.05	700	25, 45	10 to 30

Table 3.8: Galvanostatic deposition of Cu, Sn and Cu-Sn alloy

Galvanostatic experiments	Applied current density $\times 10^{-3}$ (A/cm <sup>2</sup> )	Electrolyte	Concentration of the metallic salt mention (M)	Rotation Speed (rpm)	Temperature (°C)	Duration (min)
Cu deposition	2.4 to 6.3	IL+ CuCl <sub>2</sub> .2H <sub>2</sub> O	0.05,0.2	0, 700, 1300	25, 45	10-105
Sn deposition	1.57 to 3.14	IL+ SnCl <sub>2</sub> .2H <sub>2</sub> O	0.05	0, 700, 1300	25, 45	10-120

To determine the stability of an electrolytic bath, several deposition experiments were carried out from a single bath over a period of a month. During each deposition experiment cell potential, deposit thickness and current efficiency was measured each time. The metal deposition experiments were carried out by galvanostatic method involving two types of anodes, soluble and inert anode to ascertain changes during the deposition process. The Cu deposition experiments were carried out involving Pt mesh and Cu sheet as the counter electrode. The Sn deposition experiments were carried out involving only Pt mesh as the counter electrode. During these experiments the temperature was maintained at 25 °C.

Solution was analysed visually to note any changes in colour, odour or formation of precipitation or powdery layer. These analyses were carried out during several deposition experiments and at the end of these one month period of experiments.



## 3.4.2. Alloy deposition

*(a) Preliminary studies*

For alloy deposition purpose a Rota-Hull cell was used for preliminary studies. In Hull cell the distance between the anode and the cathode was varied by inclining the cathode and the shape of the cathode controls the variation in the current density. The range of current density covered can be determined by the dimensions of the cell, the cathode plate and angle with cell wall. The traditional Hull cell was modified to Rotating Cylinder Hull cell as this cell was well designed for critical mass transfer controlled processes. A Rota Hull cell consists of a rotating cylindrical electrode (RCE) system as a working electrode, a concentric counter electrode and a stationary concentric insulator cylinder. Presently Autolab HT Rota-Hull cell (Eco Chemie B.V) was used. The detail on the different features of the Rota Hull cell is shown in the fig. 3-9.

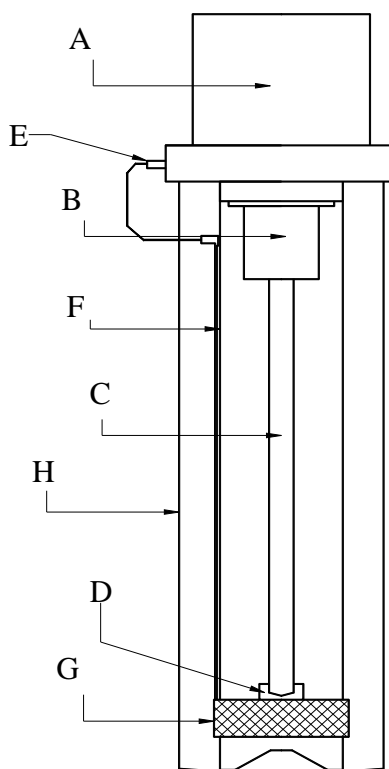


Figure 3-9 : Schematic diagram of a Rota Hull cell, where, A: Driving unit, B: Electrode holder, C: Rotating cylinder electrode, D: Electrode end piece, E: Plug connector for counter electrode connection, F: Insulator (of polycarbonate), G: Counter electrode /anode, H: Glass electrolyte container

The driving unit of the Rota-Hull cell contains a motor, a tachometer and a sliding contact of current lead to connect the rotating electrode and counter electrode. A holder for the cylinder electrode at its lower end is present along with a connector

cable at the upper end. The cylindrical rotating electrode was 12 cm in length and 0.6 cm in diameter and made from brass. The active surface area used for deposition was 15.07 cm<sup>2</sup>. Pt mesh was used as the counter electrode. With the help of a mini banana plug on the upper end of the counter electrode, connection with the driving unit was established. The counter electrode was placed outside of a cylindrical concentric polycarbonate insulator. Additionally two pieces of PTFE cylindrical insulators were placed on top and bottom of the cylinder to limit the active length on the working electrode. A bayonet lock was used to hold the insulator with the driving unit [12]. For current flow between the working and counter electrode, the bottom of the insulator was kept open. The whole set up was placed into a cylindrical glass electrolyte container. The Rota Hull cell also contains a power driving system, which controls the current supply to the cell, rotation speed of the cylindrical electrode and the duration of deposition.

Due to the position of counter and working electrode, the current density varies along the working electrode. The current density was found to be highest at the bottom and lowest at the top along the working electrode surface. Due to the variations in obtained current density along the working electrode non-uniform plating thickness distribution was observed. The highest current density was found at  $x = 0$  shown in fig. 3-10, because it is nearest to the counter electrode. The lowest current density was found at  $x = 8$ , as it is the furthest distance from the counter electrode. The composition of the deposit and its thickness could be represented as the function of position along the cathode length after a deposition experiment. This is very useful property for alloy deposition to save an enormous amount of time to understand deposition process from a single experiment. For the present system, to simplify the distribution of the deposit composition, the obtained deposited counter electrode was divided in to 4 parts as shown in the fig. 3-10.

The mass transfer in RCE can be controlled by varying rotation speed and applied current densities. The mass transport to a rotating cylinder electrode is described by empirical dimensionless correlations of the form [13-16]:

$$Sh = 0.079 Re^{0.65} Sc^{0.35} \quad (3.13)$$

Where  $Sh$  is Sherwood number,  $Re$  is Reynolds number and  $Sc$  is Schmidt number. The equation can be written in terms of limiting current as,

$$i_L = 0.079 n C F U^{0.654} d^{-0.346} \nu^{-0.298} D^{0.644} \quad (3.14)$$

For these experiments, ethaline melt containing SnCl<sub>2</sub>.2H<sub>2</sub>O of concentration 0.05 to 0.1 M and CuCl<sub>2</sub>.2H<sub>2</sub>O of concentration 0.02 to 0.1 M was used. The rotation speed of the working electrode was kept constant as 600 rpm and temperature was

maintained as  $22 \pm 2$  °C. These experiments were carried out by applying current density in the range of 1 to  $1.7 \times 10^{-3}$  A/cm<sup>2</sup> for duration of 180 min. The applied current density range was determined from the applied current density of the individual metals. The maximum and minimum current density at the bottom and top of the cylinder were determined to be  $2.9 \times 10^{-3}$  A/cm<sup>2</sup> and  $0.15 \times 10^{-3}$  A/cm<sup>2</sup>. The experiments were carried out using brass cylinders as working electrode and platinum mesh as the counter electrode. Before deposition, the cylinders were polished using 500, 1200 and 4000 grid papers accordingly. Then the polished cylinders were consequently washed with distilled water, acetone and dried before placing in the electrolyte. It should be mentioned that after each set of experiments the Rota-Hull cell, the working and the counter electrode were washed with distilled water, acetone and dried before the deposit analysis or to commence next set of experiments.

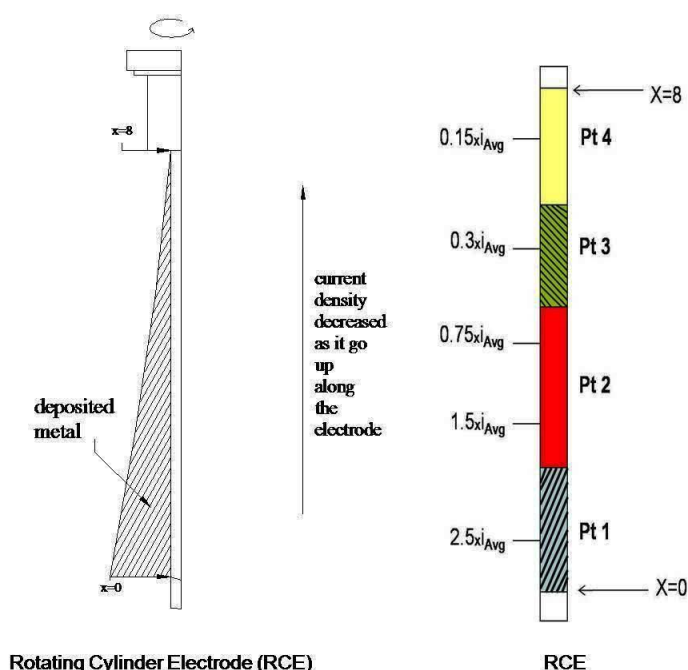


Figure 3-10 : Metal deposition along the cathode length in a Rota hull cell,  $x=0$  to  $x=8$  is the active cathode length used for metal deposition,  $x=0$  the point on cathode nearest to anode and  $x=8$  the point on cathode farrest to anode,  $i_{Avg}$  = current density applied

### (b) Deposition experiments

With the help of Rota Hull experiments, several suitable parametric values were determined for potentiostatic and galvanostatic deposition experiments for alloy system. These deposition experiments were carried out in 220 rpm RDE speed at 25 °C for duration of 60 to 240 min. The suitable  $\text{CuCl}_2 \cdot 2\text{H}_2\text{O}$  -  $\text{SnCl}_2 \cdot 2\text{H}_2\text{O}$  concentration for the deposition was determined as 0.04 - 0.1 M and 0.02 - 0.1 M. For potentiostatic deposition, the potential range for deposition was determined as -0.34 to -0.38 V vs Ag wire. For galvanostatic deposition, the applied current density for deposition was 0.63 to

$0.94 \times 10^{-3} \text{ A/cm}^2$ . These deposition experiments were carried out involving same instruments and electrodes as described for individual metal deposition experiments. Later current efficiency for the deposited alloy was carried out as mentioned for individual metal deposition experiments.

To determine the stability and aging property of Cu-Sn alloy electrolyte, some voltammetry experiments and visual examination were carried out. These experiments were carried out in the fresh solution in a regular time interval in a time span of one month without any deposition experiment. Some other sets of experiments were carried out with the solution used in alloy deposition for a time span of one month. In this period when the deposition quality deteriorated, then metal salts were added up externally in the used solution. Then different experiments were carried out in these solutions with freshly added metal salts. This adding up of extra metal salt process was carried out maximum for 3 times in a particular type of electrolyte.

### 3.5. Annealing experiments

Annealing experiments were carried out to examine the variation in the deposit from visual, material composition and crystallographic point. Annealing experiments were carried out in a SSL (Service Science Limited) furnace. For temperature control the furnace is equipped with a thermo-couple. For the heat treatment experiments the samples were placed inside a glass tube as shown in fig. 3-11.

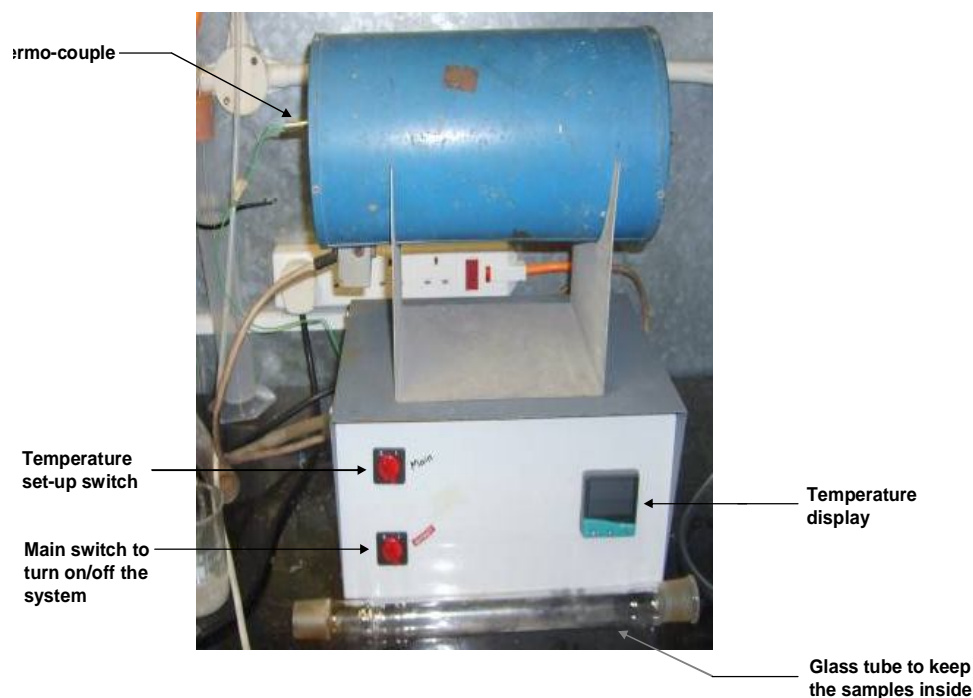


Figure 3-11 : Furnace for heat treatments showing the thermocouple to note the temperature increase and the glass tube for sample insertion in the furnace and the rubber tube for  $\text{N}_2$  flow was connected to the both ends of this glass tube

This process was carried out in an inert atmosphere maintained by N<sub>2</sub> gas supplied by rubber tubes attached to the glass tube at both ends. The nitrogen purging was carried out for 20 min before switching on the furnace to remove all the oxygen from the glass tube. After the heat treatment, the previous ambience was maintained until the furnace temperature cool down to room temperature. Heat treatment experiments were carried out in a temperature range of 250 to 730 °C for two different durations such as 10 min and 30 min. The heat treatment was carried out on the alloy deposits obtained from ethaline melt containing 0.04 M CuCl<sub>2</sub>.2H<sub>2</sub>O – 0.1 M SnCl<sub>2</sub>.2H<sub>2</sub>O.

### 3.6. Deposit characterization

The obtained deposits were examined using different instrument for visual examination, determination of elemental composition, crystalline structure, grain size and phase transformation with temperature.

#### 3.6.1. *Optical microscope*

To determine the external morphology and the thickness of the deposit optical microscope was used. Optical microscope is the oldest and simplest instrument of the entire microscopic system to visualise the fine surface region. For imaging metal microstructure, reflected optical microscopy is one of the common imaging methods. For the current study BX41 (Olympus) optical microscope was used. This was used for sample surface examination which is accompanied with Altra 20 close circuit camera. The attached close circuit camera helped in capturing the movement and allowed digitization with the help of Olympus stream software. Currently analyses of the specimen were carried out in 20 x magnification lens. Analysis was carried out with individual metal and alloy deposit and also with the annealed samples.

For deposit thickness calculation, the substrate surface was marked with lacquer mark before deposition. Then the substrate was placed into the electrolyte when the lacquer mark was dried completely. After deposition the lacquer mark was removed using acetone. Due to lacquer mark, deposition did not take place at the point of lacquer mark at substrate surface. Thus the thickness of the deposit was obtained by adjusting Z-stage height difference operation of the microscope. Now the substrate surface with and without deposition forms a height difference which helped in thickness measurement. To minimize the error in the thickness due to the lacquer mark, at least four measurements was carried out by revolving the single sample.

The thickness value obtained from the above measurements was used for current efficiency calculation. The thickness of the deposit was calculated from the theory using eqn. 2.36. Current efficiency calculation was carried out by dividing the thickness value obtained from light microscopy measurement with the value obtained from theory. Later the ratio was multiplied by 100, to represent the current efficiency in percentage.

### 3.6.2. Scanning Electron Microscope

The scanning electron microscopy was used here to determine elemental composition and internal morphology of the obtained deposit. With compare to light microscope the present microscope includes higher magnifying capability. It creates various images of sample surface through high energy electron beam and the signals received from the interaction between the incident electron and sample's surface. These different signals consist of secondary electrons, backscattered electrons, diffracted backscattered electron, photons or continuum x-ray, visible light and heat. The secondary electrons and backscattered electrons used to produce SEM images. The morphology and topography analysis is carried out using secondary electrons and the contrasts in composition in multiphase sample are determined using backscattered electrons. Each element in a sample produce different x-rays when excited by the electron beam, so elemental analysis is possible using photons or continuum x-ray. The diffracted backscattered electron helped in determining crystalline structure and orientation of the elements in a sample <sup>[17-19]</sup>.

A scanning electron microscope consists of an electron source gun, electron lenses, sample stage, detectors for all signals of interest, display or data output device, vacuum system and cooling system <sup>[20]</sup>. The details of the microscope with the schematic arrangement of different component are shown in fig. 3-12.

In the present analysis a Hitachi S2400 Scanning Electron Microscope fitted with an Oxford Instruments Isis 200 Ultra Thin Window X-ray Detector was used. The morphology of Cu, Sn and Cu-Sn alloy deposit was examined. For the elemental analysis of each deposit energy dispersive x-ray (EDX) spectroscopy was performed. The cross sectional image of Cu, Sn and Cu-Sn alloy deposit were visualized through the microscope. To visualize the cross-sectional image of the deposited stainless disc was placed in the sample holder at particular angle. Additionally cross-sectional imaging for alloy deposit was possible by detached from the stainless disc. Then the deposit was twisted in middle line then placed in the microscope for the cross sectional view.

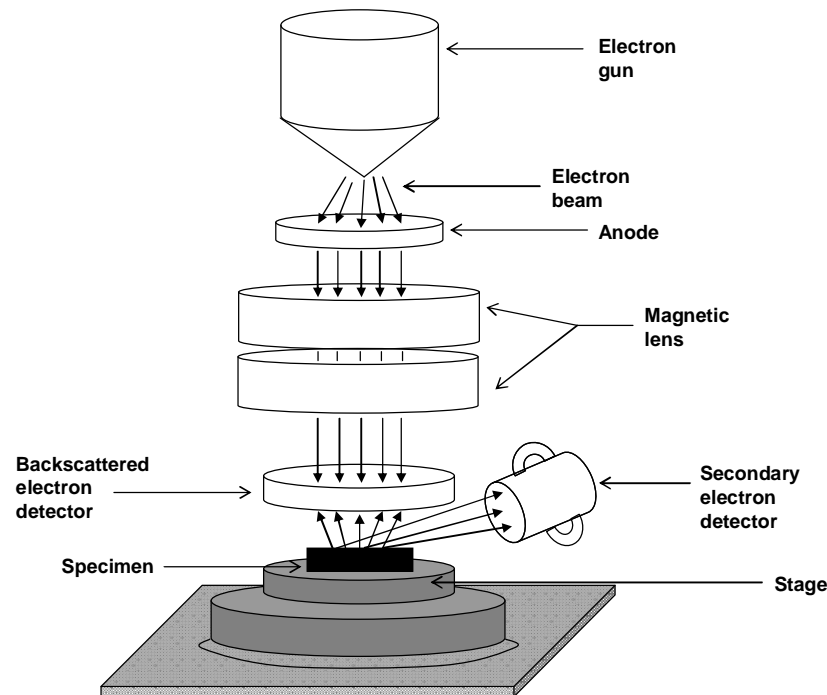


Figure 3-12 : Schematic diagram of scanning electron microscope (SEM) showing various of the microscope

### 3.6.3. X-ray diffractometer

The crystal structure analysis and determination of grain size of the deposited metal was performed by X-ray diffractometry (XRD). Using this technique average spacing between layers and rows of the atoms is possible. Moreover, the orientation of the single crystal, size, shape and internal stress of small crystalline regions can be determined by using this technique. In this technique, the involved instruments are an x-ray tube as a source of x-ray beam for analysis and a goniometer. The goniometer consists of sample holder, detector arm and associated gearing required for the technique <sup>[21-23]</sup>. The details of the x-ray tube are shown in the fig. 3-13. When high speed electrons collide with a metal [such as Cu, Al, Mo, Mg] target [anode] in a vacuum system x-rays are produced. The high speed electrons are produced by hot tungsten filament [cathode] which is coupled to a high voltage cable. A cold water supply is arranged under the anode to prevent the metal from melting due to high temperature generation during x-ray formation <sup>[23]</sup>.

The arrangement for XRD measurements and sample position for the analysis in an x-ray diffractometry is shown in the fig. 3-13. During measurements the x-ray tube remains stationary, the specimen or the examined surface moves in an angle of  $\theta$  and the detector moves in an angle of  $2\theta$ .

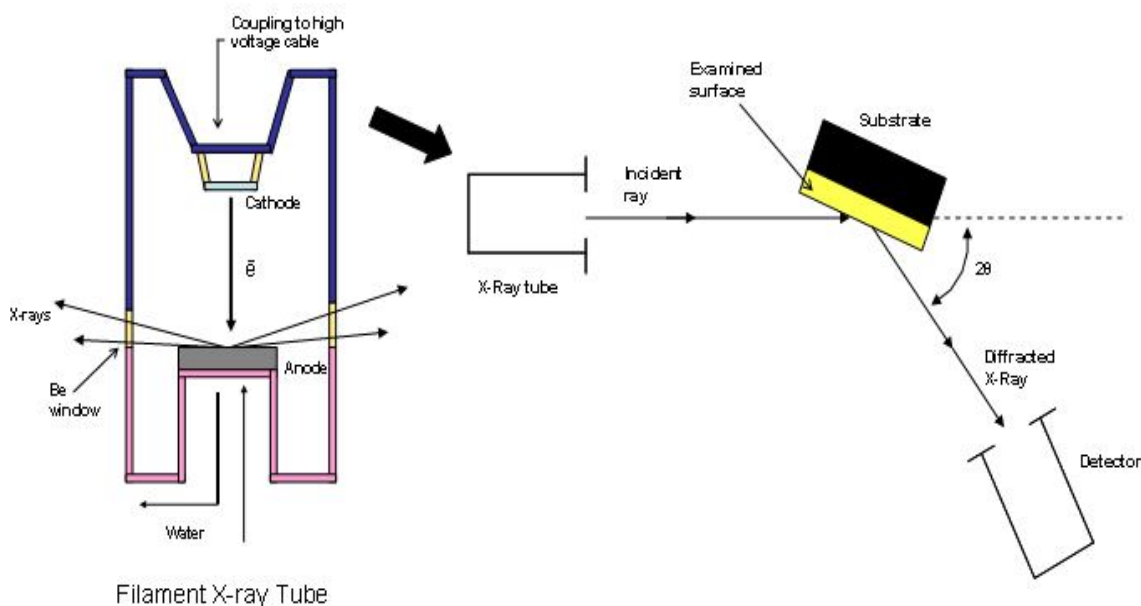


Figure 3-13 : Details of the XRD tube along with position of the substrate surface for XRD analysis

For the present measurements PANalytical X'Pert Pro MPD, powered by a Philips PW3040/60 X-ray generator and fitted with an X'Celerator were used. The instrument was operated in a scan range of  $5^\circ$  to  $99^\circ$  (in  $2\theta$  scan mode) with a step size of  $0.0334^\circ$  and nominal time per step of 100 seconds. The scan was carried out using  $\text{CuK}\alpha$  radiation of 1.54keV. The scans were performed in 'continuous' mode using the X'Celerator RTMS detector. The analysis was carried out over the Cu deposit, Sn deposit and Cu-Sn deposit. In case of Cu-Sn alloy deposit analysis was also carried out on both annealed and non-annealed samples. The phase identification of the obtained scans were carried out by the X'Pert accompanying software program PANalytical High Score Plus in combination with the ICDD Powder Diffraction File 2 database (1999), the American Mineralogist Crystal Structure Database (March 2010) and the Crystallography Open Database (September 2011; [www.crystallography.net](http://www.crystallography.net)) system.



## Reference :

1. A. P. Abbott, J. C. Barron, M. Elhadi, G. Frisch, S. J. Gurman, A. R. Hillman, E. L. Smith, M. A. Mohamoud and K. S. Ryder (2008) ECS Trans., 16(36) : 47-63.
2. A. P. Abbott, K. S. Ryder and U. König (2008) Transactions of the Institute of Metal Finishing, 86 (4) : 196-204.
3. A. P. Abbott, K. E. Ttaib, G. Frisch, K. J. McKenzie and K. S. Ryder (2009) Phys. Chem. Chem. Phys., 11 : 4269-4277.
4. W. L. McCabe, J.C.Smith and P.Harriott (2001) Unit operations of chemical engineering, 6<sup>th</sup> edition, McGraw-Hill Companies, Inc., New York.
5. Visco 88 User Manual, man0378 issue 1.0, Malvern Instruments Ltd., October 2006.
6. Instruction Manual C1,DC1,DC3, DL3 and DL5 Circulators including all bath, Haake, Part no. 002-4088A, 1-1-0355-2/11.1996.
7. A. J. Bard and L.R. Faulkner (eds.), Electrochemical Methods Fundamentals and Applications, 2001, 2nd ed., A John Wiley & Sons, Inc. publication : 156-159, 226-228, 335-339.
8. J. Nikolic, E. Expósito, J. Iniesta, J. González-García and V. Montiel (2000) Journal of Chemical Education, 77(9) : 1191-1194.
9. CTV101 Speed Control Unit, EDI101 Rotating Disc Electrode, User's Guide, D21V009, Printed by Radiometer Analytical SAS, 2002-10C.
10. F. Endres, A. P. Abbott and D. R. MacFarlane (eds.) 'Electrodeposition from Ionic Liquids', 2008, WILEY-VCH Verlag GmbH & Co. KGaA, Weinheim.
11. Cyclic Voltametry and Anodic Stripping Voltametry, available from <http://www.chem.missouri.edu/Greenlief/courses/4200F04/Electrochemistry.pdf> [accessed date 25/5/2012].
12. Autolab HT Rota-Hull manual, march 2001.
13. J. Low, C. Ponce de Leon and F.C. Walsh (2005) Aust. J. Chem., 58 : 246.
14. D. R. Gabe, G.D. Wilcox, J. Gonzalez-Garcia and F.C. Walsh (1998) J. Appl. Electrochem., 28 : 759.
15. D. R. Gabe (1974) J.Appl.Electrochem., 4 : 91-108.
16. F. F Rivera and J. L. Nava (2007) Electrochimica Acta, 52 : 5868-5872.
17. D. K. Bowen and C. R. Hall, Microscopy of Materials. Halsted, 1975, John Wiley and Sons Press.
18. D. J. O'Connor, B. A. Sexton and R. St. C. Smart (eds.), Surface Analysis Methods in Material Science, 2003, 2<sup>nd</sup> ed. Springer.

19. The principles of SEM and Microanalysis, available from  
<<http://portal.tugraz.at/portal/page/portal/felmi/research/Scanning%20Electron%20Microscopy/Principles%20of%20SEM> > [accessed date 25/5/2012].
20. Scanning electron microscope, Encyclopaedia Britannica, Inc., 2008.
21. Scintag, Inc., Providing solution to your diffraction needs, available from  
<<http://epswww.unm.edu/xrd/xrdbasics.pdf> > [accessed date 25/5/2012].
22. X-ray Diffraction (XRD), available from  
<<http://web.pdx.edu/~pmoeck/phy381/Topic5a-XRD.pdf> > [accessed date 25/5/2012].
23. V. K. Pecharsky and P. Y. Zavalij (eds.) Fundamentals of Powder Diffraction and Structural Characterization of Materials, 2008, 2<sup>nd</sup> ed. Springer.

## **Chapter 4: PHYSICAL PROPERTY MEASUREMENTS**

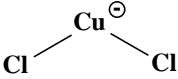
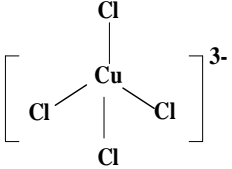
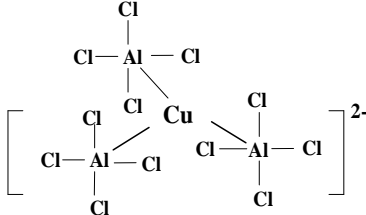
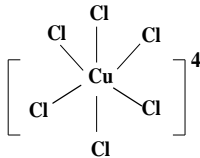
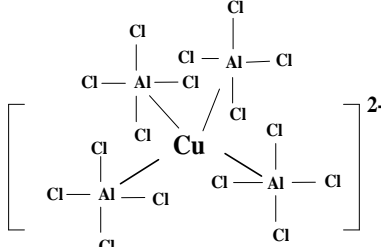
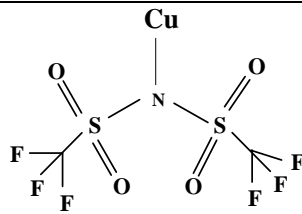
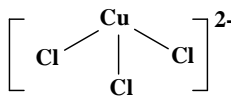
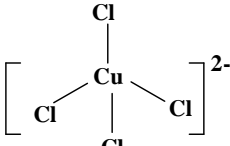
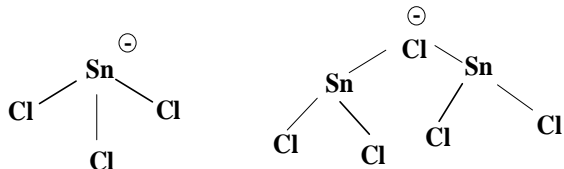
### 4.1. Introduction

Knowledge of physical properties is essential to characterise the electrochemical properties of the electrolyte. To quantify the deposit quality these electrochemical properties have a significant role. Thus for electrodeposition of individual metals or alloys the physical properties of the electrolyte play an important role on the deposit qualities and characteristics. The electrolytes are sensitive to temperature and metal ion content, thus to electrodeposit consistently and predictably, effect of these parameters on physical properties should be evaluated. Moreover, these parameters are also influenced by the change in speciation in the liquid due to metal concentration <sup>[1]</sup>, water content <sup>[2-3]</sup> as well as the break-down of the IL itself <sup>[4]</sup>. To adopt this electrolyte for practical plating purposes proper information on influence of chemical composition and temperature is essential. In the current literature very limited information is available on these aspects.

A range of Cu and Sn complexes was reported for Cu and Sn study in various ILs. It has been observed that with change in electrolyte nature and source of Cu and Sn in the electrolyte, different Cu and Sn complexes were formed. With inclusion of water in the electrolyte change in Cu complexes was observed. The change was prominent when the water content in the electrolyte was more than 40 wt% <sup>[3]</sup>. Formed Cu and Sn complexes in the various ILs are presented in the table 4.1.

Different physical properties of the ethaline melt with and without metal salts are discussed in sections of this chapter. Due to the use of hydrated metal salts the water content in the ethaline melt is only 10-11%, thus it should produce the same species as those observed in hydrate-free salts. Here measurements and studies on physical properties like density, viscosity and conductivity were carried out. In some cases predictive equations have been developed, which were used to determine these properties. The studies on the variation of these properties are reported in this chapter. The examined factors are various metal ions and the variation in concentration with applied temperature on the electrolytes.

Table 4.1 : Formation of different Cu and Sn complexes in various ILs

ILs	Introduction Cu and Sn in the electrolyte	Formed complex	
[NaCl-AlCl <sub>3</sub> ] <sup>[9]</sup>	Anodic dissolution of Cu wire		
[BuPyCl-AlCl <sub>3</sub> ] <sup>[6]</sup>	Anodic dissolution of Cu foil		Basic electrolyte
			Acidic electrolyte
	Dissolution of CuCl <sub>2</sub>		Basic electrolyte
			Acidic electrolyte
[BMP-Tf <sub>2</sub> N] <sup>[7]</sup>	Anodic dissolution of Cu electrode		
ChCl based ILs <sup>[8-10]</sup>	Dissolution of CuCl <sub>2</sub>	 <p>Complex formed for Cu(I)</p>	 <p>Complex formed for Cu(II)</p>
ChCl based ILs <sup>[11-13]</sup>	Dissolution of SnCl <sub>2</sub>		

## 4.2. Ethaline melt

### 4.2.1. Density measurement

The density of the ethaline melt for temperature range between 20 °C to 60 °C is shown in the fig 4-1. The density decreased linearly by 4% with increase in temperature span of 40 °C. Using standard regression technique the correlation coefficient, |R| was determined and the fit was drawn as shown in fig. 4-1. The variation in the three different measurements was within  $\pm 0.01$  g/cm<sup>3</sup>, within 1% of the measured value. The regression line of these plots was drawn from the average value of three measurements. The decrease in density is <5% decreases with increasing temperature which implies that for practical plating purposes near room temperature the density of pure ethaline can be assumed to be constant.

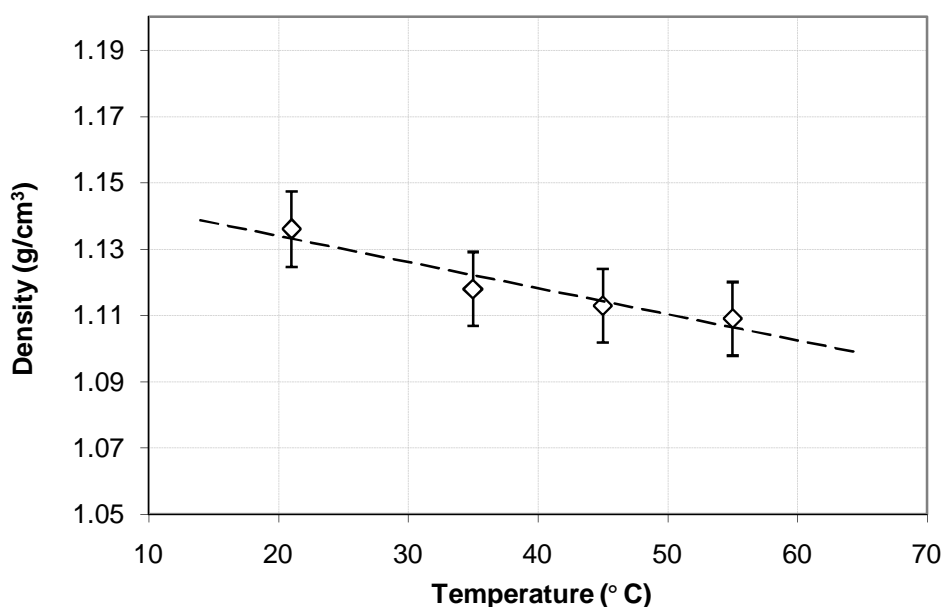


Figure 4-1 : A typical variation of density measurements for ethaline melt as a function of temperature, R = 0.96

Compared to other ChCl based IL electrolyte, i.e. glyceline, reline, maline, [1.18 g/cm<sup>3</sup> to 1.25 g/cm<sup>3</sup>] the density value is lowest [1.13 $\pm$ 0.005 g/cm<sup>3</sup> at 25 °C] for the electrolyte used here [14-18]. It has been reported that the density of ChCl based IL depends on the density of the hydrogen bond donor (HBD) [17]. Among all these ChCl based ILs the HBD of ethaline i.e. ethylene glycol has lowest density.

### 4.2.2. Viscosity and Conductivity measurement

The variation of conductivity and viscosity of the ethaline melt for the same range of temperatures are shown in the fig 4-2. The viscosity decreased and

conductivity increased with an increase in temperature. The decrease in viscosity is 58% and conductivity is 63% for temperature span of 35 °C. Three different data points were collected for each temperature and the variation in these measurements were within  $\pm 8\%$ . The regression line shown was drawn from the average value of three measurements.

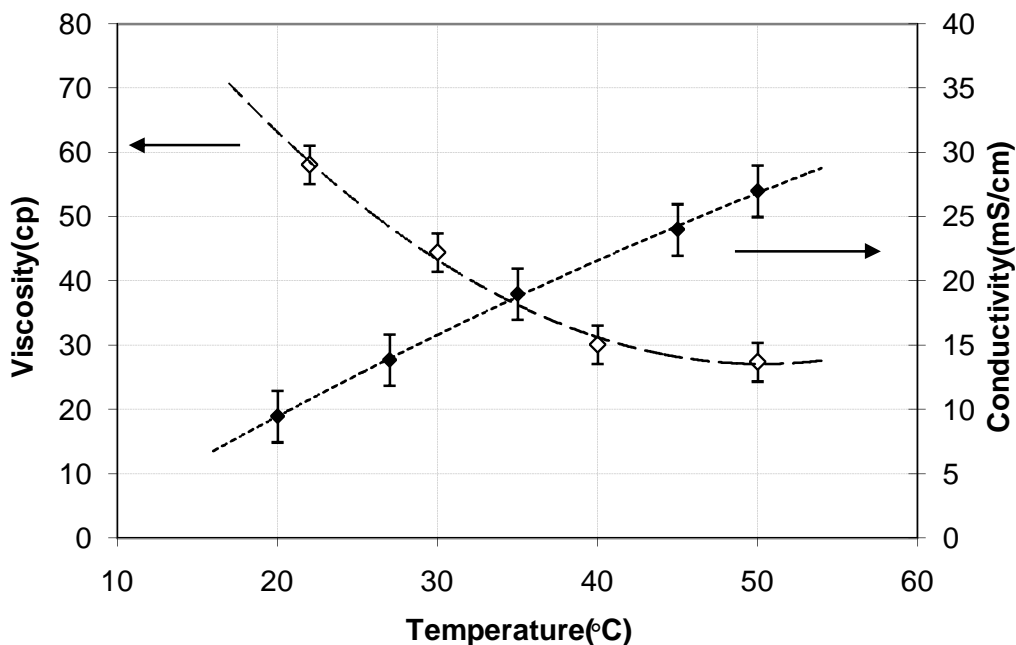


Figure 4-2 : Conductivity and viscosity measurements as a function of temperature for ethaline melt, [ $\blacklozenge$ ] conductivity, [ $\diamond$ ] viscosity

At 25 °C, in the case of viscosity the value for the present electrolyte was  $60 \pm 3$  cP vs. 259 cP to 1124 cP <sup>[19,17]</sup> in compare to the other ChCl based IL electrolyte, i.e. glyceline, reline, maline. Again the conductivity value for present electrolyte was  $9.47 \pm 1$  mS/cm against 0.75 ms/cm to 1 ms/cm <sup>[19,16]</sup> as found for reline electrolyte.

These variations in the transport property depend on the electrolyte. The higher viscosity value could be due to large radii ( $\approx 3-4$  Å) of the solvent species compared to the average radius of the holes ( $\approx 2$  Å) <sup>[20]</sup>. The mobility of the ions also depends on the size of the migrating species, the radii of the cations and complexed anions. The previous researchers explained this variation in viscosity based on hole theory <sup>[20-23]</sup>. According to hole theory ILs contain empty spaces or holes. These holes are randomly distributed and the radius of the average size holes is responsible for viscosity value of the ILs. Compared to other ILs (1.48 Å to 1.32 Å), the radius of the average size holes is higher (1.54 Å) for present electrolyte <sup>[17]</sup>. With increase in hole radius surface tension decreases, so the electrolyte contain large cavities which enhance ions mobility <sup>[21]</sup>. Moreover, the availability of free volume and probability of finding holes of suitable

dimensions for the solvent molecules are the factors for the higher or lower viscosity values. This free volume in the present electrolyte is reported to be 13.5% vs 9% to 11% for other type 3 eutectic IL electrolytes [17].

The behaviour of the viscosity–conductivity curve vs. the temperature as shown in fig. 4-2 can be compared with many compatible models present. It is assumed that this variation may follow Arrhenius model. In addition to this Vogel-Tamman-Fulcher (VTF) model is more suitable for glass forming ILs. The Arrhenius and VTF equation [19,20] is shown in eqn. 1.7 and 1.8.

According to Arrhenius equation,  $\ln\mu = \ln\mu_{\infty} + \frac{E_{\mu}}{RT}$

According to VTF equation,  $\ln\mu = \ln(A_{\mu}^{VTF}\sqrt{T}) - \frac{k_{\mu}}{T-T_g}$

Within the examined temperature range, the temperature dependence of  $T^{1/2}$  within the pre-exponent is expected to change <8-9%, in which case an Arrhenius type plot is sufficient to test the behaviour of the data. To determine this model's validity for this system and other unknown parameters of the Arrhenius equation,  $\ln(\text{viscosity})$  vs  $[\text{temperature (T)}]^{-1}$  was carried out. These plots for viscosity and conductivity measurements are shown in fig. 4-3.

For viscosity measurements, the R value appeared as 0.98 according to Arrhenius model. As the R value obtained as >0.95, so this model fits well for ethaline melt.

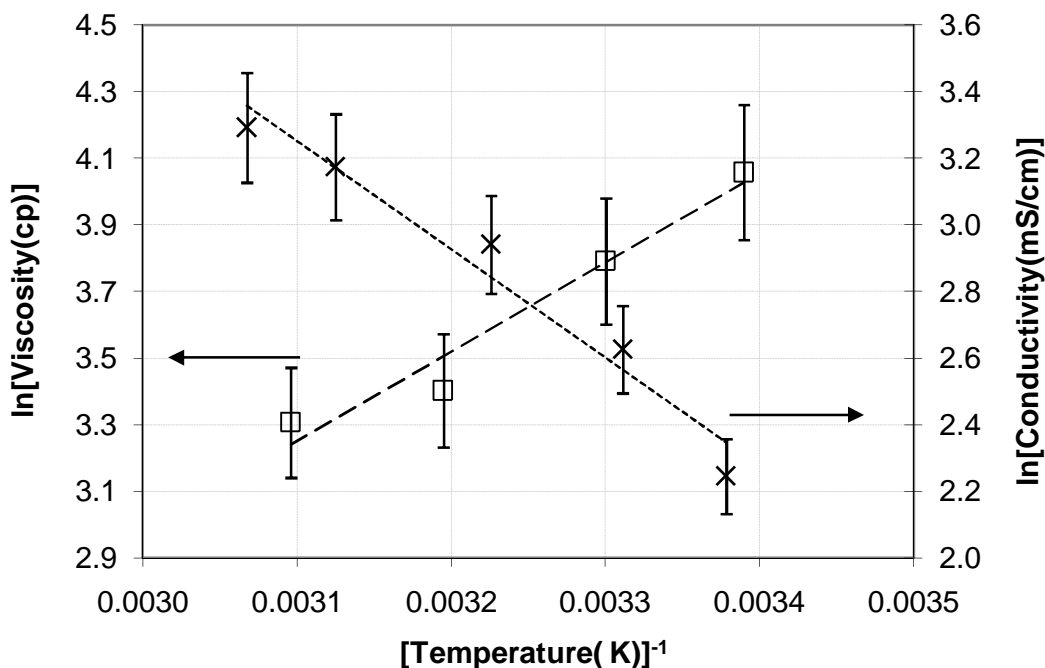


Figure 4-3 : Conductivity and viscosity measurements as a function of temperature according to Arrhenius model for ethaline melt, [x] conductivity, [□] viscosity

From Arrhenius model the activation energy for viscous flow for ethaline melt was determined. The plot of  $\ln \mu$  vs  $(1/T)$  should yield the value of  $(E_a/R)$  as the slope. Using this procedure the value for activation energy of viscosity was determined from the data presented in fig. 4-3. The value for activation energy of ethaline melt was determined as 22 kJ/mol. For other range of ILs the activation energy for viscous flow was found in the range of 17 kJ/mol to 30 kJ/mol [20]. It is reported that decrease in activation energy for a typical viscous flow implies to more mobile ions within the melt. Thus for ethaline melt average mobility of the ions are expected from the activation energy value.

#### 4.3. Ethaline melt with individual metal ions

##### 4.3.1. Density measurement

The effect of the individual metal salt on the physical properties was determined by adding  $\text{CuCl}_2 \cdot 2\text{H}_2\text{O}$  and  $\text{SnCl}_2 \cdot 2\text{H}_2\text{O}$  in ethaline melt. With the addition of metal salt to the ethaline melt some notable variation in the density was observed. The density value for a range of electrolyte at different temperature is shown in table 4.2. The variation in density measurement with the variation in metal salt concentration with a range of temperature is shown in fig. 4-4. The density decreases by 2% for temperature span of 35 °C. With compared to ethaline melt only, the density increases by 3% for addition of various metal salts. However, with variation in metal salts or their individual concentrations in ethaline melt any notable change in density was not observed.

Table 4.2 : The variation in the value of different physical parameters with change in metal ion concentrations and temperature

		Density (g/cm <sup>3</sup> )		Conductivity (mS/cm)		Viscosity (cP)	
		Error : ±0.01		Error : ±2.0		Error : ±5.0	
		20 °C	55 °C	20 °C	55 °C	20 °C	55 °C
IL		1.14	1.10	9	27	58	27
IL + $\text{CuCl}_2 \cdot 2\text{H}_2\text{O}$	0.01 M	1.13	1.11	4	24	53	26
	0.2 M	1.15	1.13	4.7	25	57	24
IL + $\text{SnCl}_2 \cdot 2\text{H}_2\text{O}$	0.01 M	1.14	1.12	7.5	24	55	27
	0.1 M	1.15	1.13	7	23	50	23



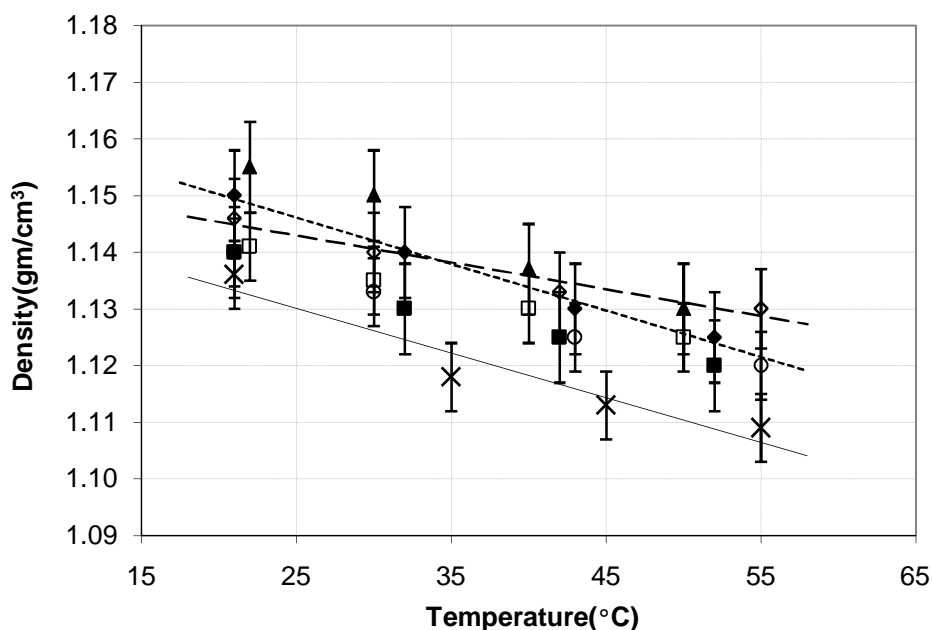


Figure 4-4 : Density measurements for ethaline melt with and without metal salts as a function of temperature, [▲] IL+0.2 M  $\text{CuCl}_2 \cdot 2\text{H}_2\text{O}$ , [◆] IL+0.1 M  $\text{CuCl}_2 \cdot 2\text{H}_2\text{O}$ , [■] IL+0.04 M  $\text{CuCl}_2 \cdot 2\text{H}_2\text{O}$ , [◇] IL+0.1 M  $\text{SnCl}_2 \cdot 2\text{H}_2\text{O}$ , [□] IL+0.05 M  $\text{SnCl}_2 \cdot 2\text{H}_2\text{O}$ , [○] IL+0.025 M  $\text{SnCl}_2 \cdot 2\text{H}_2\text{O}$ , [x] IL only

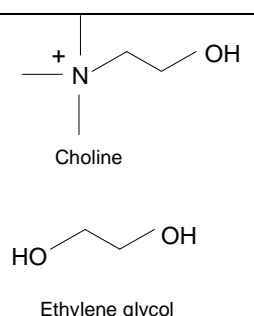
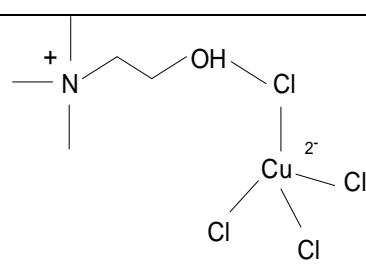
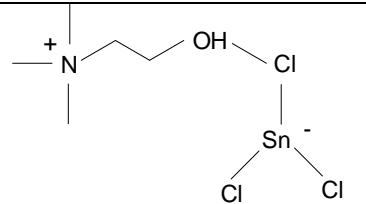
The density of hydrated metal salts is consistently 1-2% higher than pure ethaline. Previous studies in  $\text{ChCl}$ -based ILs have shown that a  $\text{CuCl}_4^{2-}$  complex<sup>[18]</sup> is expected to form as shown in Table 4.3 when  $\text{CuCl}_2 \cdot 2\text{H}_2\text{O}$  is added to it. Complexation studies of  $\text{SnCl}_2 \cdot 2\text{H}_2\text{O}$  in imidazolium based ILs have shown that  $\text{SnCl}_3^-$  complexes, as shown in Table 4.3, is expected to form<sup>[16, 24]</sup>. As shown in Table 4.3, when copper and tin salts were introduced in ethaline, new ionic species were created. The waters of hydration within the salt would also result in the formation of new ionic species, although metal ion complexes as shown in Table 4.3 remain unchanged unless water content exceeds 40%. The increase in density upon introduction of metal salts in the melt suggests that a denser structure was formed.

#### 4.3.2. Viscosity and Conductivity measurement

Table 4.2 is showing the variation in conductivity and viscosity value of the ethaline melt when various metal salts was added. The viscosity decreased by 54% and conductivity increased by 75% when the temperature was increased from 20 to 55 °C. The viscosity and conductivity variation with temperature is shown in fig. 4-5 and 4-6 respectively. Error measurements were carried out with three different data points where the variation was obtained within  $\pm 6\%$ . The regression line shown was drawn from the average value of three measurements. With the addition of metal salts or

increase in metal salt concentration, significant change in viscosity and conductivity value of the electrolytes was not observed.

Table 4.3 : Reactions and Speciation in Ethaline melt with and without metal salts

	Reaction scheme	Complexes formed
Ethaline	$[\text{HOC}_2\text{H}_4\text{N}(\text{CH}_3)_3^+][\text{Cl}^-] + [\text{OHCH}_2\text{CH}_2\text{OH}]$ $\Downarrow$ $[\text{HOC}_2\text{H}_4\text{N}(\text{CH}_3)_3^+] + [\text{OHCH}_2\text{CH}_2\text{OH}] \text{Cl}^-$	 <p>Choline</p> <p>Ethylene glycol</p>
Ethaline + $\text{CuCl}_2 \cdot 2\text{H}_2\text{O}$	<ol style="list-style-type: none"> <li><math>\text{Cl}^- + [\text{CuCl}_3]^- \leftrightarrow [\text{CuCl}_4]^{2-}</math></li> <li><math>\text{Cl}^- + \text{CuCl}_2 \leftrightarrow [\text{CuCl}_3]^-</math></li> </ol>	
Ethaline + $\text{SnCl}_2 \cdot 2\text{H}_2\text{O}$	<ol style="list-style-type: none"> <li><math>\text{Cl}^- + [\text{SnCl}_3]^- \leftrightarrow [\text{SnCl}_4]^{2-}</math></li> <li><math>\text{Cl}^- + \text{SnCl}_2 \leftrightarrow [\text{SnCl}_3]^-</math></li> </ol>	

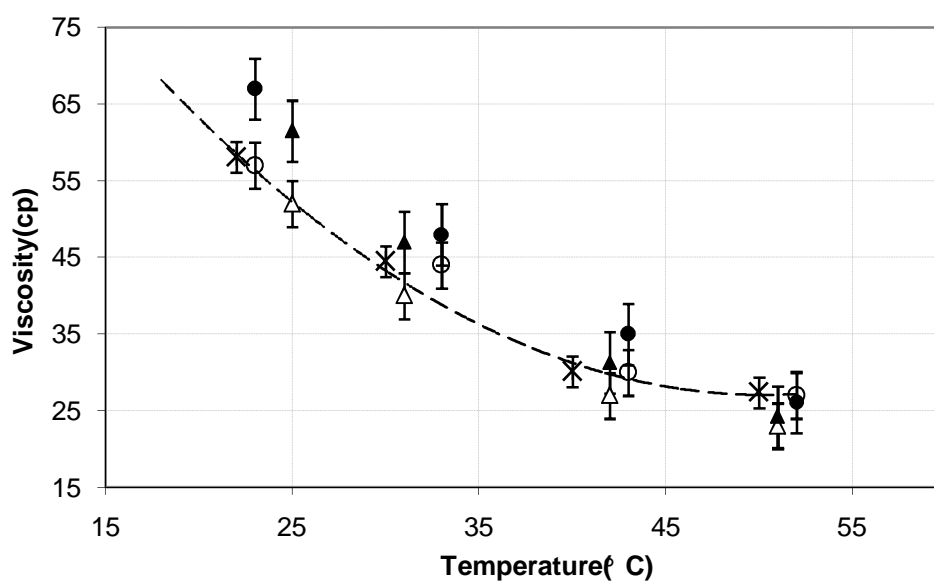


Figure 4-5 : Viscosity measurements for ethaline melt with and without metal salts as a function of temperature, [▲] IL+0.2 M  $\text{CuCl}_2 \cdot 2\text{H}_2\text{O}$ , [●] IL+0.01 M  $\text{CuCl}_2 \cdot 2\text{H}_2\text{O}$ , [△] IL+0.1 M  $\text{SnCl}_2 \cdot 2\text{H}_2\text{O}$ , [○] IL+0.01 M  $\text{SnCl}_2 \cdot 2\text{H}_2\text{O}$ , [x] IL only

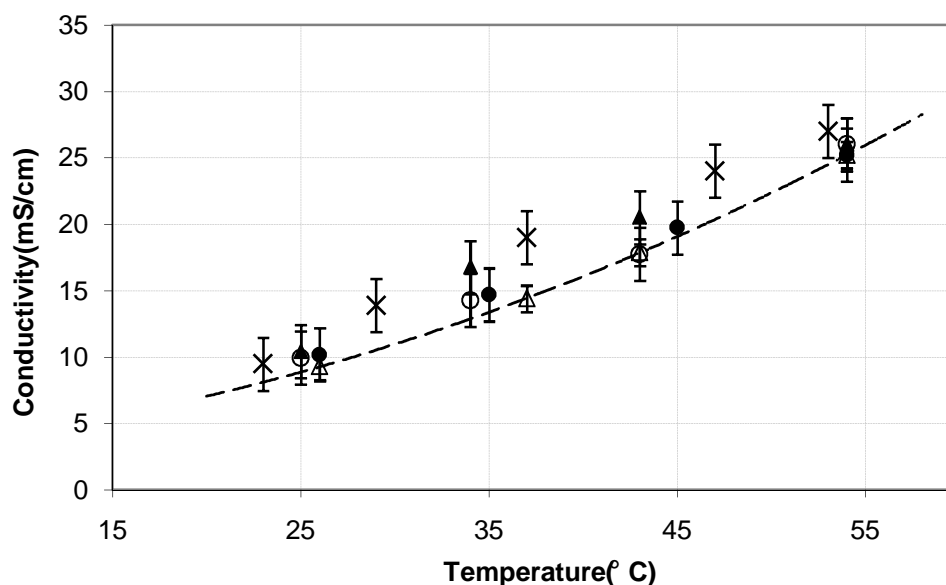


Figure 4-6 : Conductivity measurements for ethaline melt with and without metal salts as a function of temperature, [▲] IL+0.2 M  $\text{CuCl}_2 \cdot 2\text{H}_2\text{O}$ , [●] IL+0.01 M  $\text{CuCl}_2 \cdot 2\text{H}_2\text{O}$ , [Δ] IL+0.1 M  $\text{SnCl}_2 \cdot 2\text{H}_2\text{O}$ , [○] IL+0.01 M  $\text{SnCl}_2 \cdot 2\text{H}_2\text{O}$ , [x] IL only

If one examines the difference in viscosity between the two different metal salts, there is virtually no difference (within experimental error). There is also very little change in density with increasing concentration of metal ions within the melt. The density decreases with increasing temperature, similar to that observed for pure ethaline.

To determine the appropriate model for ethaline melt with different concentration of the individual metal, only Arrhenius fit was carried out. For Arrhenius model fit, the dependence of viscosity and conductivity on temperature according to Arrhenius equation was carried out. To perform this fit a plot of  $\ln(\text{viscosity})$  vs  $[\text{temperature}]^{-1}$  as shown in fig 4-7 was carried out. Similar analysis for conductivity measurement as shown in fig. 4-8 was also carried out.

In the case of viscosity measurements, the R values for Cu and Sn systems was determined as  $>0.99$ . For conductivity measurements the obtained R value for both the metal systems as  $>0.99$ . Thus for both the measurements, the Arrhenius model fitted very well.

From Arrhenius model the activation energy for viscous flow for these electrolytes with metal ions was determined. For Cu systems the activation energy varies in the range of 26 to 29 kJ/mol and for Sn systems the activation energy varies in the range of 22 to 25 kJ/mol. The value of activation energy for the ethaline melt without the metal ions was determined as 22 kJ/mol. With increase in activation energy for viscous flow implies to less mobile ions within the melt. The increase in activation

energy with addition of hydrated metal ions suggesting less mobile complexes forming new networks (shown in table 4.3). Formation of these new species initiates the changes and forms new networks of ions. Increase in activation energy upon introduction of metal salts in the melt suggests that a denser structure is formed. The variation in density value with addition of hydrated metal salt suggested similar phenomenon.

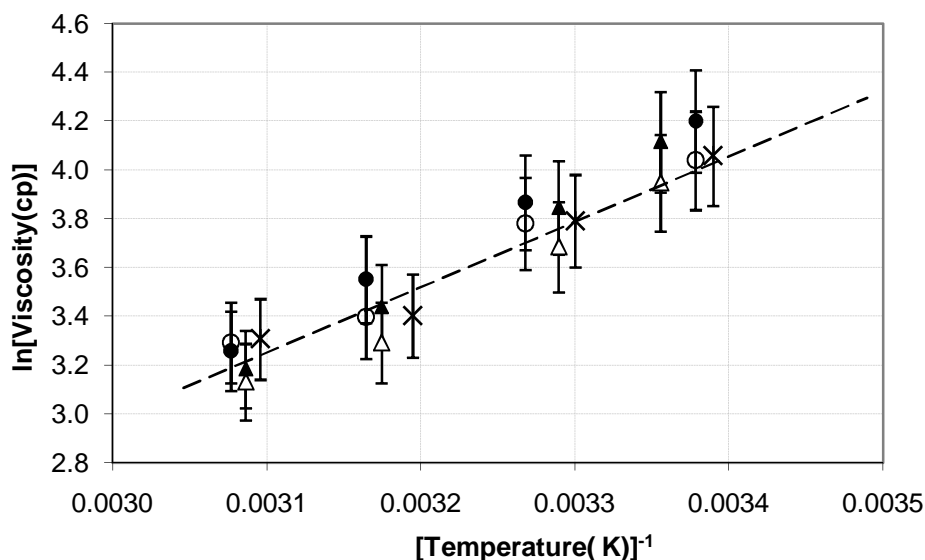


Figure 4-7 : Viscosity measurements for ethaline melt with and without metal salts as a function of temperature for Arrhenius model comparison, [▲] IL+0.2 M  $\text{CuCl}_2 \cdot 2\text{H}_2\text{O}$ , [●] IL+0.01 M  $\text{CuCl}_2 \cdot 2\text{H}_2\text{O}$ , [Δ] IL+0.1 M  $\text{SnCl}_2 \cdot 2\text{H}_2\text{O}$ , [○] IL+0.01 M  $\text{SnCl}_2 \cdot 2\text{H}_2\text{O}$ , [x] IL only

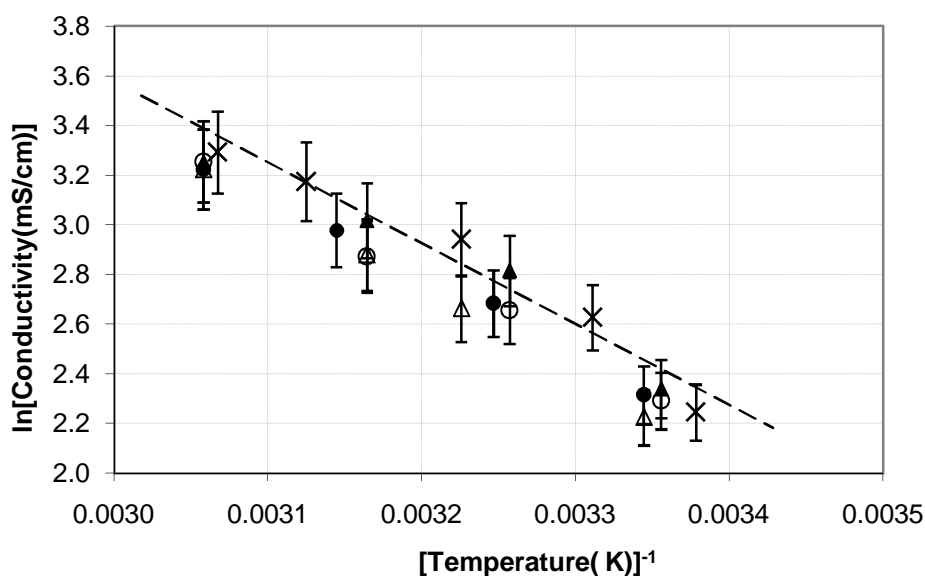


Figure 4-8 : Conductivity measurements for ethaline melt with and without metal salts as a function of temperature for Arrhenius model comparison, [▲] IL+0.2 M  $\text{CuCl}_2 \cdot 2\text{H}_2\text{O}$ , [●] IL+0.01 M  $\text{CuCl}_2 \cdot 2\text{H}_2\text{O}$ , [Δ] IL+0.1 M  $\text{SnCl}_2 \cdot 2\text{H}_2\text{O}$ , [○] IL+0.01 M  $\text{SnCl}_2 \cdot 2\text{H}_2\text{O}$ , [x] IL only

## 4.4. Ethaline melt with both metal ions

## 4.4.1. Density measurement

After individual metal studies, measurements on physical properties were carried out with both metal salts in one electrolyte. By this measurement the overall effect of the both metals in the electrolyte system was determined. For these measurements  $\text{SnCl}_2 \cdot 2\text{H}_2\text{O}$  concentration was kept constant as 0.1 M and  $\text{CuCl}_2 \cdot 2\text{H}_2\text{O}$  concentration was varied in the range of 0.02 to 0.1 M in a temperature range of 20 to 55 °C. For the above mentioned electrolytes the density value was found in the range of 1.11 to 1.14  $\text{g}/\text{cm}^3$  at 20 °C. Three different data points were collected for each temperature and the variation in these measurements were within  $\pm 1\%$ . The regression line shown was drawn from the average value of three measurements. The R value is obtained to be in the range of 0.97 to 0.99. With change in concentration of the hydrated  $\text{CuCl}_2$  in the system, the density changes by 3%. This variation might be due to formation of new complexes by the change in concentrations of hydrated Cu and Sn salts. It is assumed that with change in the formula weight of the anionic and cationic part denser metal ion species might have formed.

The variation in the changing density value over a range of applied temperature is shown in the fig. 4-9. The variation of density is a linear function with temperature change as observed for ethaline melt with individual metal ion.

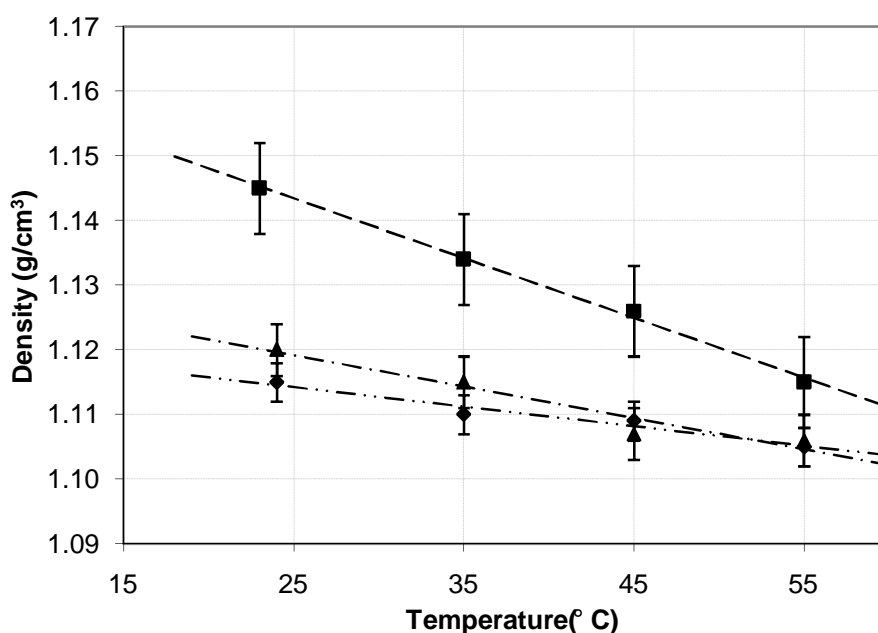


Figure 4-9 : Density measurements for ethaline melt with two metal salts as a function of temperature, [◆] IL+0.01 M  $\text{SnCl}_2 \cdot 2\text{H}_2\text{O}$ + 0.02 M  $\text{CuCl}_2 \cdot 2\text{H}_2\text{O}$ , [▲] IL+0.1 M  $\text{SnCl}_2 \cdot 2\text{H}_2\text{O}$ + 0.04 M  $\text{CuCl}_2 \cdot 2\text{H}_2\text{O}$ , [■] IL+0.1 M  $\text{SnCl}_2 \cdot 2\text{H}_2\text{O}$ +0.1 M  $\text{CuCl}_2 \cdot 2\text{H}_2\text{O}$

## 4.4.2. Conductivity measurement

The study on conductivity of the electrolytes was carried out in same way with the concentration combination of both metal ions and same temperature range as was in density measurements. Their behaviour is shown in the fig 4-10. Three different data points were collected for each temperature and the variation in these measurements were within  $\pm 12\%$ . The regression line shown was drawn from the average value of three measurements. Similar to the individual metals, the conductivity increased with increase in temperature.

The linear fashion of the conductivity curve is assumed to be an effect from formation of another new network by both hydrated metal ions with anionic and cationic part of ethaline. The change in network influences the hydrogen bonding and Van der Waals interactions within the anionic and cationic structure within the electrolyte.

However, any significant change in conductivity value was observed for change in individual metal ion concentration. The individual metal study in the previous section showed that change in concentration had almost no effect in the conductivity value.

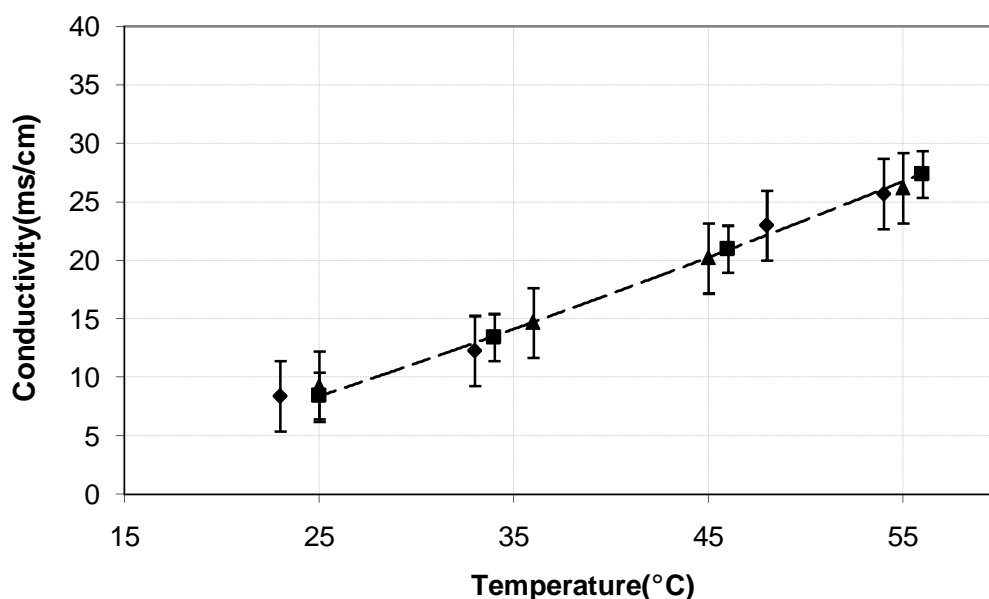


Figure 4-10 : Conductivity measurements for ethaline melt with two metal salts as a function of temperature, [◆] IL+0.01 M  $\text{SnCl}_2 \cdot 2\text{H}_2\text{O}$ + 0.02 M  $\text{CuCl}_2 \cdot 2\text{H}_2\text{O}$ , [▲] IL+0.1 M  $\text{SnCl}_2 \cdot 2\text{H}_2\text{O}$ + 0.04 M  $\text{CuCl}_2 \cdot 2\text{H}_2\text{O}$ , [■] IL+0.1 M  $\text{SnCl}_2 \cdot 2\text{H}_2\text{O}$ +0.1 M  $\text{CuCl}_2 \cdot 2\text{H}_2\text{O}$

## 4.5. Discussion

Glass transition temperature is important for glass forming ILs. It is reported previously that reline is a glass-forming liquid like many other RTILs <sup>[15]</sup>. Ethaline is

another ChCl-based IL, thus ethaline system was also tested according to VTF model. For this  $\ln(\text{viscosity})$  vs  $[\text{temperature } (T-T_g)]^{-1}$  plot was carried out. The glass transition temperature for reline melt is reported as 209 K [15]. For VTF model verification for ethaline melt, the value obtained for reline melt was used. These plots for viscosity and conductivity measurements are shown in fig. 4-11.

For viscosity measurements, the R value appeared as 0.98 and 0.99 for conductivity measurements according to VTF model. As for this measurement the model showed R value  $>0.95$ , so this model fits ethaline system as well. The viscosity and conductivity of Cu and Sn system might follow VTF model too. Thus for large range of examined temperature, the system should tested using VTF model. However the glass transition temperature for ethaline system with different metal salt was not known. Variation in glass transition temperature is expected due to change in speciation with addition of different metal salts as described in table 4.3.

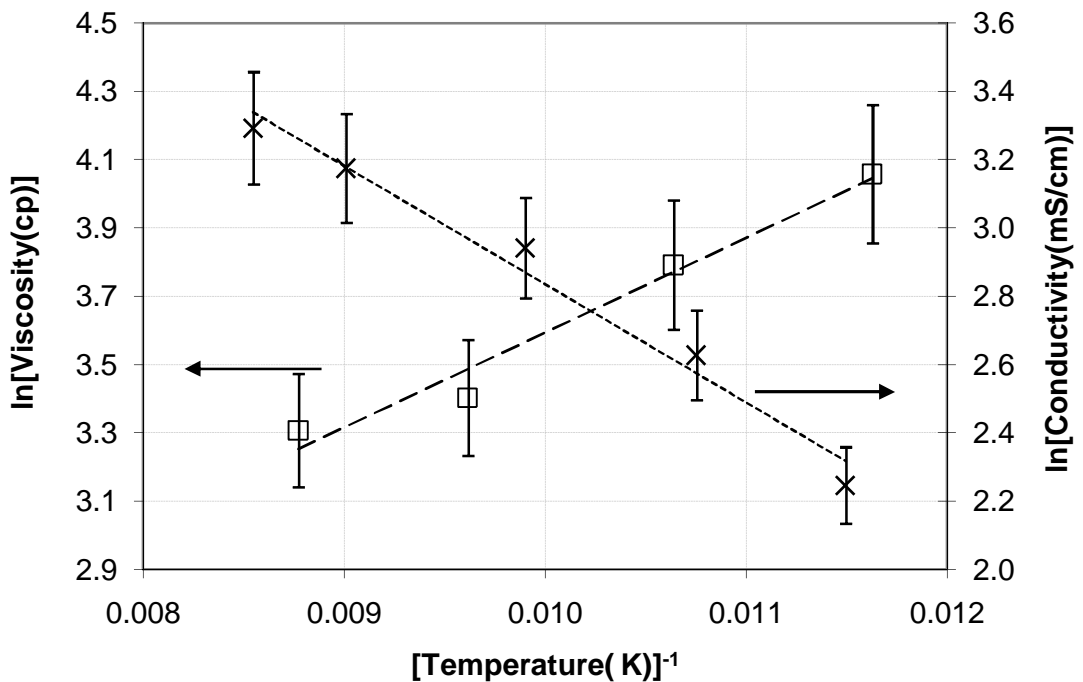


Figure 4-11 : Conductivity and viscosity measurements as a function of temperature according to VTF model for ethaline melt, [x] conductivity, [□] viscosity

The density value of an aqueous electrolyte is much lower than the electrolytes used here. The viscosity and conductivity value for aqueous electrolytes used for Cu deposition was reported as 0.653 cP and 40 to 110 mS/cm respectively, [25-26] at room temperature. With compared to aqueous electrolytes, the viscosity value is almost 100 times higher and conductivity value is 4 to 11 times lower for the ethaline melt used for Cu deposition. This variation in physical properties influenced the transportation of ions

in the electrolyte. The ethaline melt used for metal deposition with high viscosity will showed slower movement of the metal ions. As an outcome these physical property values indicate slower mass transport rate and lower limiting current value for metal deposition. A comparison of the factors like mass transfer rate and limiting current of the present system with aqueous electrolytes will be discussed in the subsequent chapters.

#### 4.6. Conclusion

From the above results and discussion on physical properties about ethaline melt with two different metal salt as  $\text{CuCl}_2 \cdot 2\text{H}_2\text{O}$  and  $\text{SnCl}_2 \cdot 2\text{H}_2\text{O}$ , it can be concluded as :

- The density and viscosity decreases and conductivity increases with the increase in electrolyte temperature.
- With addition of different concentration of hydrated  $\text{CuCl}_2$  and  $\text{SnCl}_2$  in ethaline melt, no significant changes in the response of density, conductivity and viscosity as a function of temperature was observed.
- The Arrhenius model fitted very well for ethaline systems with and without metal ions with response to temperature.
- With addition of metal ions density and activation energy for viscous flow increased by 2% and 12% respectively. This was assumed to be due to the formation of denser structure within the IL by forming new networks of species.
- For ethaline system with inclusion of both metal ions the conductivity increased with temperature following a linear relationship. This was assumed to be due to formation of another new network of species with hydrated metal ions along anionic and cationic part of ethaline.



## Reference :

1. M. Currie, J. Estager, P. Licence, S. Men, P. Nockemann, K. R. Seddon, M. Swadźba-Kwaśny and C. Terrade (2013) *Inorganic Chemistry*, 52 : 1710-1721.
2. G. Li, D. M. Camaioni, J. E. Amonette, Z. C. Zhang, T. J. Johnson and J. L. Fulton (2010) *Journal of Physical Chemistry B*, 114 : 12614-12622.
3. P. D. Vreese, N. R. Brooks, K. V. Hecke, L. V. Meervelt, E. Matthijs, K. Binnemans and R. V. Deun (2012) *Inorganic Chemistry*, 51 : 4972-4981.
4. K. Haerens, E. Matthijs, K. Binnemans and B. V. D. Bruggen (2009) *Green Chemistry*, 11 : 1357-1365.
5. L. G. Boxall, H. L. Jones and R. A. Osteryoung (1974) *J. Electrochem. Soc.*, 121(2) : 212-219.
6. C. Nanjundiah and R. A. Osteryoung (1983) *J. Electrochem. Soc.*, 130(6) : 1312-1318.
7. S. Z. Abedin, A. Y. Saad, H. K. Farag, N. Borisenko, Q. X. Liu and F. Endres (2007) *Electrochimica Acta*, 52 : 2746-2754.
8. A. P. Abbott, K. E. Ttaib, G. Frisch, K. J. McKenzie and K. S. Ryder (2009) *Phys. Chem. Chem. Phys.*, 11 : 4269-4277.
9. D. Lloyd, T. Vainikka, S. Schmachtel, L. Murtomäki and K. Kontturi (2012) *Electrochimica Acta*, 69 : 139-145.
10. D. Lloyd, T. Vainikka, L. Murtomäki, K. Kontturi and E. Ahlberg (2011) *Electrochimica Acta*, 56 : 4942-4948.
11. A. Cojocaru, Ş. Costovici, L. Anicăi and T. Vişan (2009) *Metalurgia International*, 14(11) : 38-46.
12. A. P. Abbott, G. Capper, K. J. McKenzie and K. S. Ryder (2007) *Journal of Electroanalytical Chemistry*, 599 : 288-294.
13. A. P. Abbott, G. Capper, D. L. Davies, and R. Rasheed (2004) *Chem. Eur. J.*, 10 : 3769.
14. A. P. Abbott and K. J. McKenzie (2006) *Phys. Chem. Chem. Phys.*, 8 : 4265-4279 .
15. T. Tsuda, L. E. Boyd, S. Kuwabata and C. L. Hussey (2010) *Journal of The Electrochemical Society*, 157(8) : F96-F103.
16. R. Böck and S.-E. Wulf (2009) *Transactions of the Institute of Metal Finishing*, 87 : 28-32.
17. C. D'Agostino, R.C. Harris, A.P. Abbott, L.F. Gladden and M.D. Mantle (2011) *Phys. Chem. Chem. Phys.*, 13 : 21383-21391.
18. K. Shahbaz, F. S. Mjalli, M. A. Hashim, I. M. AlNashef (2011) *Thermochimica Acta*, 515 : 67-72.

19. F. Endres, A. P. Abbott and D. R. MacFarlane (eds.) (2008) 'Electrodeposition from Ionic Liquids', WILEY-VCH Verlag GmbH & Co. KGaA, Weinheim: 1-77
20. O. O. Okoturo and T. J. VanderNoot (2004) Journal of electroanalytical chemistry, 568 : 167-181.
21. A. P. Abbott (2004) ChemPhysChem, 5 : 1242-1246.
22. A. P. Abbott (2005) ChemPhysChem, 6 : 2502-2505.
23. A. P. Abbott, G. Capper and S. Gray (2006) ChemPhysChem, 7 : 803-806.
24. P. Illner, A. Zahl, R. Puchta, N. van E. Hommes, P. Wasserscheid and R. van Eldik (2005) Journal of Organometallic Chemistry, 690 : 3567-3576.
25. B. G. Pollet, J. Hihn and T. J. Mason (2008) Electrochimica Acta, 53 : 4248-4256.
26. R. Walker and S.D. Cook (1980) Surface Technology, 11 : 189-203.

## **Chapter 5: ELECTROCHEMICAL CHARACTERISATION OF INDIVIDUAL METALS**

### 5.1. Introduction

It was mentioned in the previous chapters that electrodeposition is a function of electrochemical properties of the electrolytes. Thus, electrochemical parameter measurement is necessary for metal deposition, as using the values of these parameters various metal depositions is possible. To complete the measurements on the electrochemical parameters different physical parametric values were used, those were determined in the previous chapter. The electrochemical study involves evaluation of formal potential, metal reduction potential, nature of the reduction system and diffusion coefficient of the individual metals. It was reported previously that variation in equilibrium constant was possible due to the stabilization of different oxidation state of the species at the operating temperature <sup>[1]</sup>. For a particular metal the variation in formal potential was possible with variation in donor ability of the anion and solvation energy of the metal <sup>[2-3]</sup>. The kinetic study of Cu in ChCl based IL showed that the Cu<sup>+</sup> species diffuses faster than the Cu<sup>2+</sup> species and the charge transfer reaction rate of Cu<sup>+</sup> to Cu<sup>0</sup> is about three times faster than Cu<sup>2+</sup> to Cu<sup>+</sup> <sup>[4]</sup>. The experimental results indicated that electroreduction of Cu is diffusion controlled in ChCl based ILs and the system followed a Levich like equation <sup>[5]</sup>.

The experimentally obtained cathode current efficiency was in the range of 97-101 % for Cu <sup>[6-7]</sup> and that of 27-100 % for Sn <sup>[2,8-9]</sup>. The variation in Sn system was assumed to be due to study in various ILs and various substrates. In case of Cu study from [TMHA-Tf<sub>2</sub>N] electrolyte <sup>[6]</sup>, the cathodic efficiency value was reported as 185% and 226%. The high stability of Cu(I) species in the electrolyte and dissolution of Cu(II) species resulted this high efficiency value. The comproportionation reaction of the Cu species and the effect of the co-existence of both species lead to twice current efficiency from the expected value. When the bulk electrodeposition became saturated with Cu(I) ions, the current efficiency dropped down to the expected level <sup>[6]</sup>.

In the following section electrochemical measurements related to reversibility and mass transfer study is presented. For these measurements, formal potential, reduction potential, limiting current and cathode current efficiency was determined for individual metal like Cu and Sn in ethaline melt.

## 5.2. Voltammetry of ethaline melt

The voltammetry studies with ethaline melt was carried out to determine the potential window or the range of potential where ethaline melt was suitable for electrochemical characterization. The voltammetry scans on ethaline melt was carried out using Pt RDE, scan rate 30 mV/s at a range of rotation speeds as 0 to 2500 rpm, in a temperature range of 25 to 55 °C. Few of them are shown in fig. 5-1.

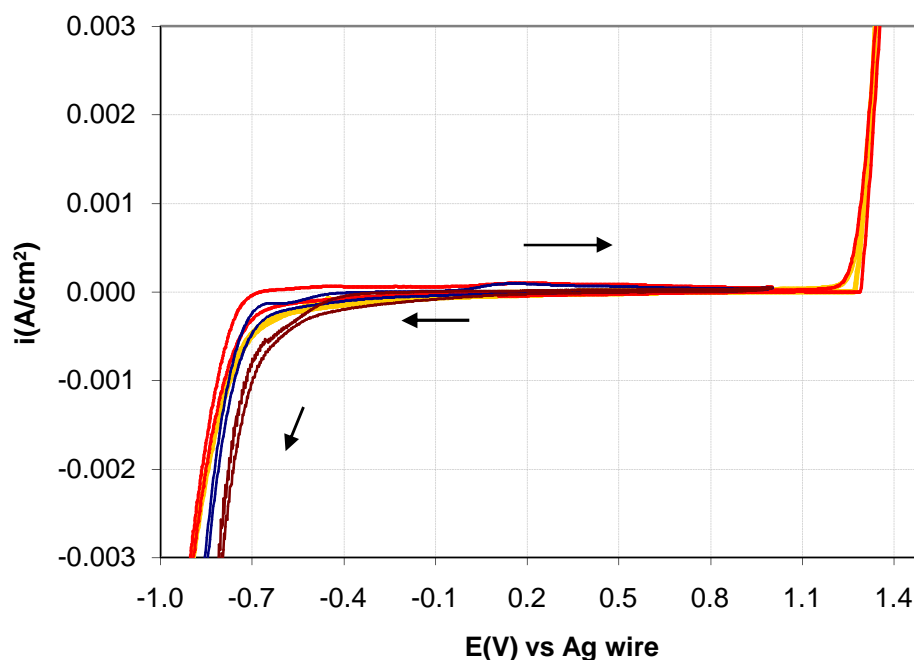


Figure 5-1 : Voltammetry on ethaline melt using various RDE speeds and a range of temperatures using Pt substrate, scan rate 30 mV/s, 25 °C (—) 100 rpm, 25 °C (—) 2500 rpm, 45 °C (—) 1000 rpm, 55 °C (—) 2500 rpm

The reduction of ethaline melt started at a potential of -0.7 V for all rotation speeds of RDE and temperatures, as observed from fig. 5-1. This means that metal deposition as well as voltammetry scans should be limited to the potentials less cathodic to -0.7 V. In the positive direction the oxidation starts at the potential of +1.3 V. Then the operation range for ethaline melt stands in -0.7 V to +1.3 V for all temperature range. For reline melt this range was found to be -1.2 V to +1.25 V [10]. The variation in potential window is assumed to be due to the nature of hydrogen bond donor (HBD) used for reline and ethaline.

## 5.3. Electrochemical characterisation of copper in ethaline melt

### 5.3.1. Formal potential measurements

To determine the formal potential for  $\text{Cu}^{2+}/\text{Cu}^+$  couple, the open circuit potential (OCP) was measured by dissolving  $\text{CuCl}_2 \cdot 2\text{H}_2\text{O}$  in a concentration range of 0.01 to 0.2

M at 25 °C in ethaline melt. The OCP value was monitored in the time span of 2 to 24 h. The value obtained after 2 h did not change in the time span of 24 h. Thus, the final OCP value for each concentration was noted after a duration of 2 h, in this time span the system was observed to attain its equilibrium state. The values after a measuring time of 2 h are reported in fig 5-2.

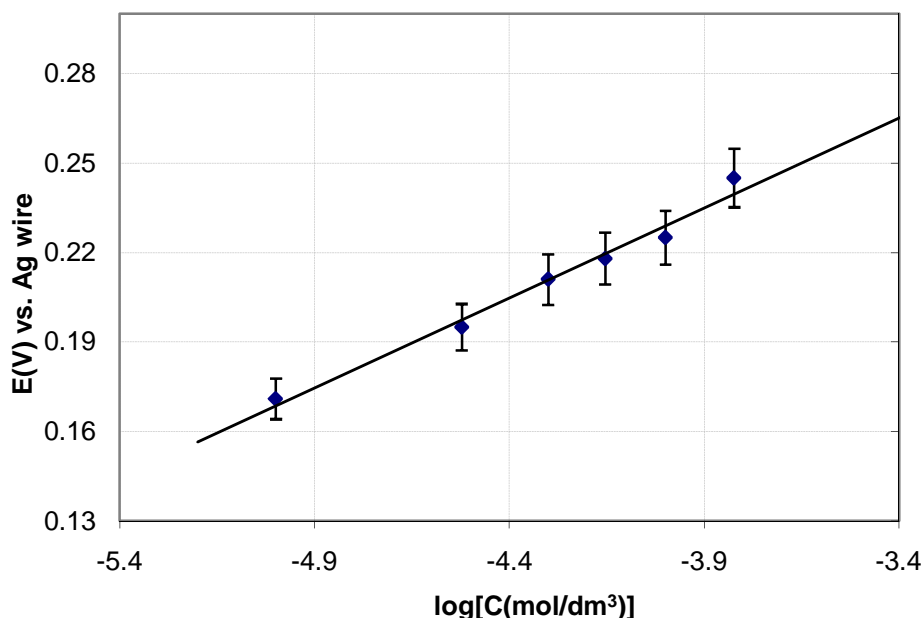


Figure 5-2 : The formal potential plot with concentration change of  $\text{CuCl}_2 \cdot 2\text{H}_2\text{O}$  for  $\text{Cu}^{2+}/\text{Cu}^+$  couple at Pt substrate in ethaline melt, regression equation is  $y=0.06x+0.47$  with  $R= 0.99$

The measured OCP value followed a linear relationship with logarithmic concentration of the metal salt added as shown in fig. 5-2. The formal potential of this system was determined from Nernst equation. According to Nernst equation,

$$E_e = \frac{2.3RT}{nF} \log C + E^{0'} \quad (5.1)$$

Using standard regression technique, the constant and the slope of the data lines were determined from fig. 5-2 as a log function of concentration of metal salt added. The regression showed that the dependence of the potential on  $\text{Cu}^{2+}$  is 60 mV/decade. The theoretical value for the dependence of the potential at 25 °C for one electron transfer is 59 mV/decade calculated from the eqn. 5.1. Since the formal potential measures the potential for a reaction and the reaction involved in this study is shown in eqn. 5.2.



where a single electron was exchanged. The value determined in the present study for Cu in the ethaline melt showed an excellent agreement with the theoretical data. Thus this measurement support that the active species in solution is  $[\text{CuCl}_4]^{2-}$  as reported in [11] where measurements were carried out with anhydrous Cu salt.

The intercept was 0.47 V as determined from fig. 5-2, so the formal potential of  $\text{Cu}^{2+}/\text{Cu}^+$  in ethaline melt should be 0.47 V. The formal potential of  $\text{Cu}^{2+}/\text{Cu}^+$  was determined previously in different  $\text{AlCl}_3$  based IL, the reported value was in the range of 0.046 V to 1.825 V at 40 °C [12-13].

### 5.3.2. Voltammetry for ethaline melt containing $\text{CuCl}_2 \cdot 2\text{H}_2\text{O}$

A voltammetry study was carried out in an ethaline melt containing 0.1 M of  $\text{CuCl}_2 \cdot 2\text{H}_2\text{O}$ . The scan range was maintained as -0.7 V to +0.6 V at 25 °C and the scan rates were in the range of 10 to 50 mV/s. The fig. 5-3 shows the voltammetry with a static RDE.

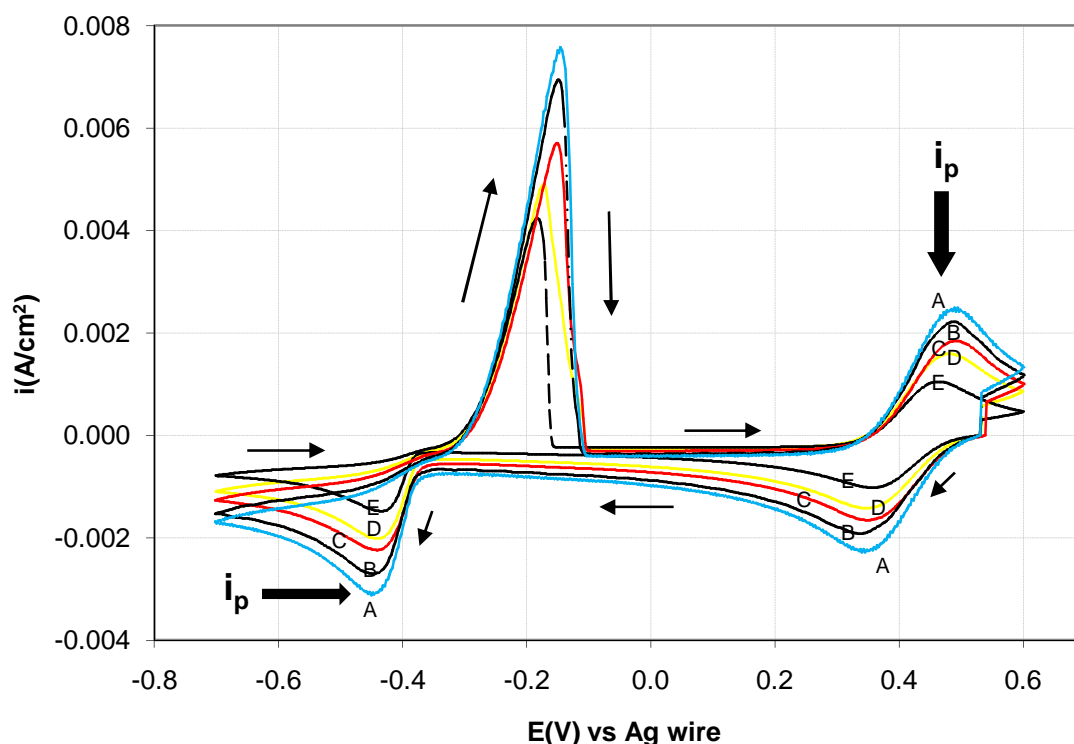


Figure 5-3 : Voltammetry at various scan rates using a static Pt RDE at 25 °C for ethaline melt containing 0.1 M  $\text{CuCl}_2 \cdot 2\text{H}_2\text{O}$ , (A) 50 mV/s, (B) 40 mV/s, (C) 30 mV/s, (D) 20 mV/s, (E) 10 mV/s

In the forward sweep the first reduction step started at a potential of +0.5 V and the second step of reduction started at a potential of -0.4 V. In the reverse sweep two

stripping peaks were observed as expected. The first step starts at the potential of - 0.45 V and the next step started at a potential of +0.35 V.

It has been proposed that the reduction process from  $\text{Cu}^{2+}$  to  $\text{Cu}^0$  took place in two steps, first formation of  $\text{Cu}^{2+}$  to  $\text{Cu}^+$  and then  $\text{Cu}^+$  reduces to  $\text{Cu}^0$  and in the reverse sweep it follows the same steps. The reduction of  $\text{Cu}^{2+}$  to  $\text{Cu}^0$  via  $\text{Cu}^+$  was also reported for Cu reduction in aqueous electrolyte [14] and in various ILs [15-21]. The two oxidation and reduction steps in fig. 5-3 correspond to such a reaction scheme, as shown in eqn. (5.2) and (5.3).



It is clear from the voltammetry scans [shown in fig. 5-3] that the position of current maximums or peak current appeared at potential 0.45 V at the forward and reverse sweep did not vary with variation of scan rates. Thus, it is a reversible electron transfer reaction. Moreover, the ratio of peak current for oxidation and reduction ( $i_{pa}/i_{pc}$ ) of the peak appeared at (0.45 V/0.35 V) is 1. This value remains constant with variation of scan rates which was expected for a reversible couple. This reversible behaviour of redox process  $\text{Cu}^{2+}$  to  $\text{Cu}^+$  is similar with the results obtained previously for  $\text{CuCl}_2$  in aqueous electrolyte [14] and reline melt [7]. The formal potential value was also determined from potential values of peak currents appeared at (0.45 V/0.35 V). The determined value was 0.4 V [for reversible system,  $E^{0'} = (E_{pa} + E_{pc})/2$ ]. This value is very similar with the value obtained from OCP measurements at various concentrations of  $\text{CuCl}_2 \cdot 2\text{H}_2\text{O}$  as obtained in previous section 5.3.1. However, peak current for oxidation and reduction ( $i_{pa}/i_{pc}$ ) of the peak appeared at (-0.15 V/-0.45 V) did not showed the properties of reversible couple.

The scan showed in fig. 5-3 can help in determining diffusion co-efficient. The diffusion coefficient value was determined using the Randles-Sevcik equation [22] for reversible couple :

$$i_p = 2.69 \times 10^5 n^{\frac{3}{2}} A D^{\frac{1}{2}} s^{\frac{1}{2}} C \quad (5.4)$$

Where  $i_p$  = peak current,  $A$ ,  $n$  = number of electrons,  $A$  = area of the electrode,  $\text{cm}^2$ ,  $C$  = concentration of metal salt in the electrolyte,  $\text{mol}/\text{cm}^3$ ,  $D$  = diffusion coefficient,  $\text{cm}^2/\text{s}$ ,  $s$  = scan rate,  $\text{V}/\text{s}$ .

The  $i_p$  values were collected from the peak appeared at 0.35 V and later plotted with the corresponding scan rate values. A typical  $i_p$  vs.  $s$  plot is shown in fig. 5-4. For a reversible couple, peak current increases linearly with square root of the sweep rate. The characteristics of the trend line and value of the slope, obtained from fig 5-4 is

satisfying eqn. 5.4. The calculated diffusion co-efficient using eqn. 5.4 is  $1.22 \times 10^{-7}$   $\text{cm}^2/\text{s}$ . The diffusion co-efficient value for  $\text{Cu}^{2+}/\text{Cu}^+$  in aqueous electrolyte was reported as  $4.3 \times 10^{-6}$   $\text{cm}^2/\text{s}$  [14] and for reline and glycine melt was in the range of 0.14 to  $0.82 \times 10^{-7}$   $\text{cm}^2/\text{s}$  [5,7,21]. The diffusion co-efficient of Cu in ethaline melt was high compared to other ChCl based ILs. This is due to faster diffusion ability of the ethylene glycol compared to choline cation [23]. Slower molecular mobility was observed for reline and glycine with compared to ethaline as the self diffusion ability of the hydrogen bond donor (HBD). This was due to the presence of widespread hydrogen bonding network between choline chloride and HBD and the within the HBD itself [23]. This leads to variation in mobility of other compounds with respect to ethaline.

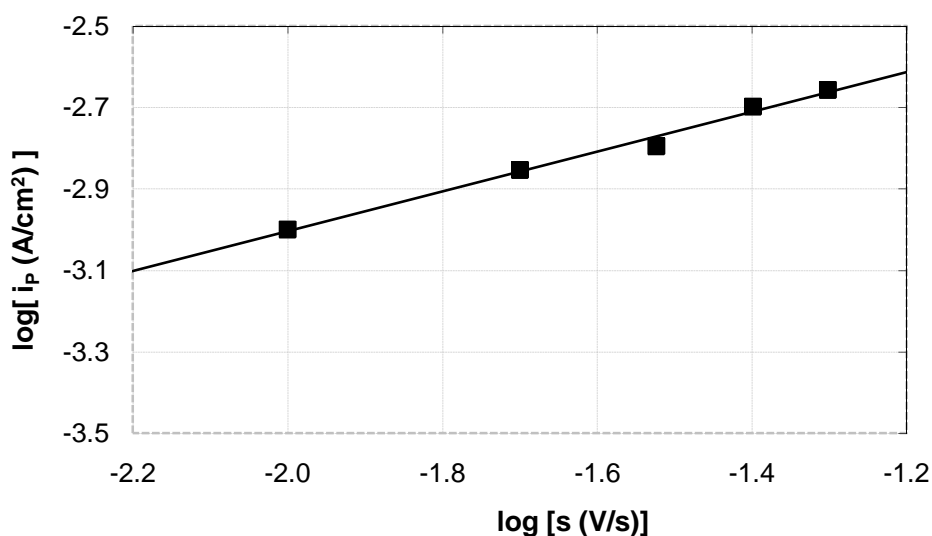


Figure 5-4 : The relationship between the peak current and scan rate (calculated from fig. 5-3) to determine diffusion co-efficient of Cu in ethaline melt, regression equation is  $y=0.49x-2.03$  with  $R= 0.99$

In the fig. 5-3 shows that peak current for oxidation and reduction ( $i_{pa}/i_{pc}$ ) of the peak appeared at (-0.15 V/-0.45 V) and this did not showed the properties of reversible couple. The ratio of current maximums or peak current at the forward and reverse sweep is not 1. The above study indicated that it is not a reversible electron transfer reaction. Thus Randles-Sevcik equation could not be used to determine the diffusion co-efficient for this reduction step. The relationship between the peak current and scan rate for an irreversible system is given by [22] the equation 5.5,

$$i_p = 2.99 \times 10^5 nAD^{\frac{1}{2}}s^{\frac{1}{2}}C(\alpha n)^{\frac{1}{2}} \quad (5.5)$$

Here,  $\alpha$  = transfer coefficient. In this case  $i_p$  values were collected from the peak near -0.45 V and later plotted against the corresponding scan rate as shown in fig. 5-5.



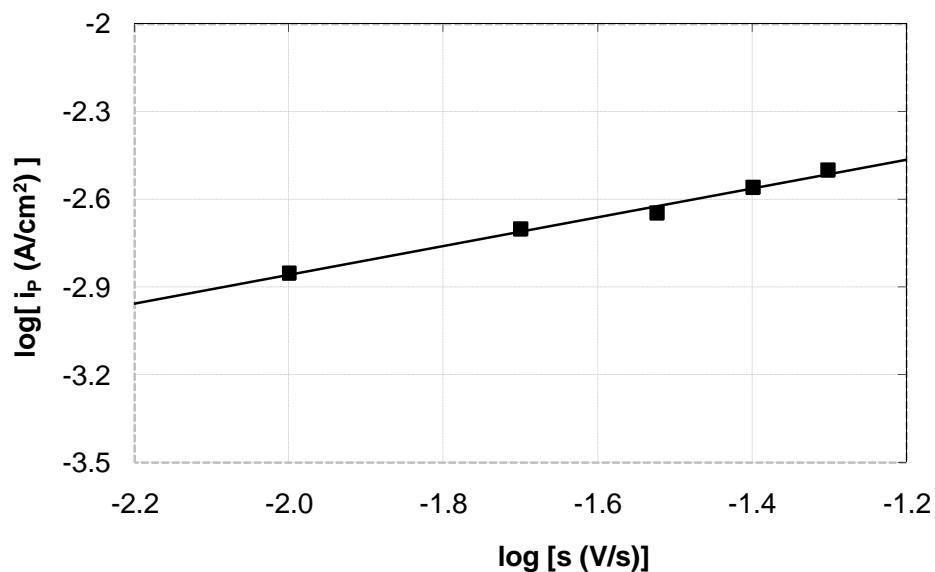


Figure 5-5 : The relationship between the peak current and scan rate (calculated from fig. 5-3) to determine diffusion co-efficient of Cu in ethaline melt, regression equation is  $y=0.49x-1.87$  with  $R= 0.99$

The calculated diffusion coefficient for the reduction  $\text{Cu}^+/\text{Cu}^0$  couple using eqn. 5.5 and fig. 5-5 is  $2 \times 10^{-7} \text{ cm}^2/\text{s}$ . Thus the diffusion coefficient of this couple is higher (almost twice) than the diffusion coefficient value for  $\text{Cu}^{2+}/\text{Cu}^+$ . This behaviour was expected due to the formation of copper complexes. This justified the ion pairing between the cation of the IL used and double charged  $\text{Cu}^{2+}$  complexes [4]. However, the diffusion coefficient value in ethaline melt showed 10 times smaller value than the diffusion coefficient value in aqueous electrolyte. This might be due to the high viscosity of the ethaline melt which was 100 times larger compared to aqueous electrolyte.

Another set of voltammetry studies were carried out with RDE in agitated condition to determine the limiting current of the system. For these experiments the previous scan range was used with varying temperature range of 25 to 55 °C, concentration range of 0.01 to 0.2 M and RDE speed range as 100 to 3000 rpm.

The fig. 5-6 shows the voltammetry scans in ethaline melt with 0.1 M  $\text{CuCl}_2 \cdot 2\text{H}_2\text{O}$  at 25 °C for different rotation speed of RDE. The voltammetry scan showed similar reduction and stripping steps as static RDE voltammetry scans. The limiting current for reduced species  $\text{Cu}^0$  was determined from the potential region of -0.6 V in the forward scan. The experiments with various temperatures, i.e. 35 °C, 45 °C, 55 °C and concentrations such as 0.01 M, 0.05 M, 0.2 M were found to show similar current-potential behaviour as shown in the fig. 5-6 and are included in the appendix A.1.

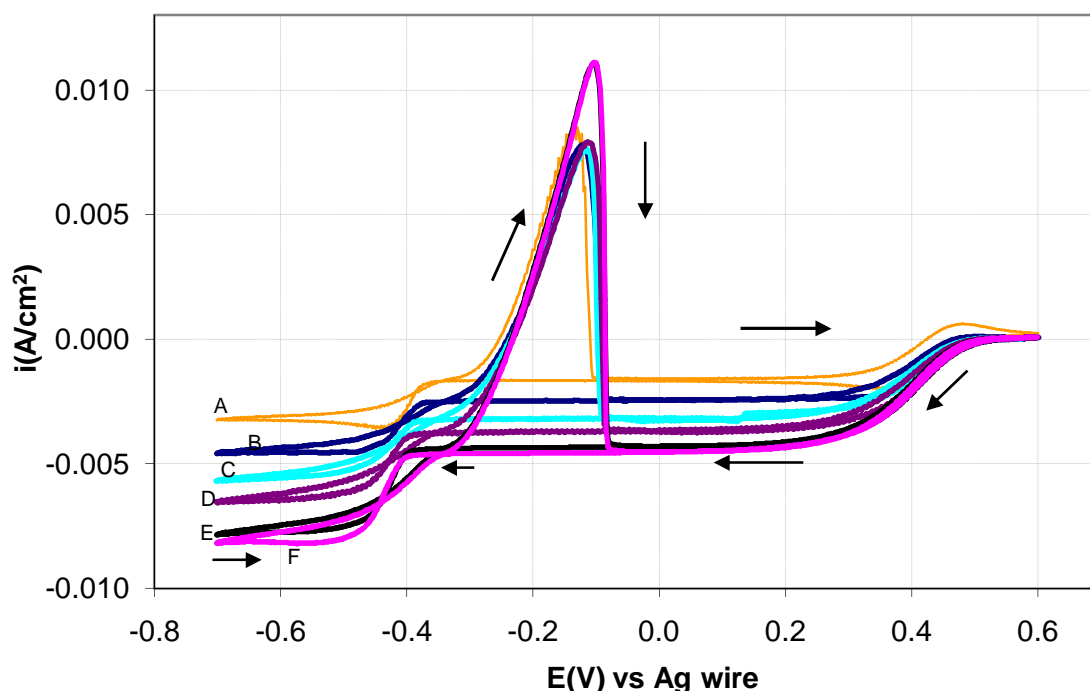


Figure 5-6: Voltammetry for ethaline melt containing 0.1 M  $\text{CuCl}_2 \cdot 2\text{H}_2\text{O}$  at 25 °C and scan rate 30 mV/s using various RDE speeds, (A) 300 rpm, (B) 700 rpm, (C) 1000 rpm, (D) 1700 rpm, (E) 2500 rpm, (F) 3600 rpm

Since there are two reduction steps in this process, the ratio of the two current plateaus is expected to be 1:2 when there is no loss of  $\text{Cu}^+$  before the second electron exchange step. This assumption was made on the basis of electron transfer process during reduction of Cu. The limiting current was estimated for both the reduction steps at a potential near to 0 V and -0.6 V. The correlations between different parameters of Levich equation was evaluated for both of these limiting current densities.

To establish the relationship between the two reduction steps, the limiting current data for both the reduction steps were collected for the entire range of experiments. The limiting current relationship calculated from the experimental results is shown in the fig. 5-7. The slope between the limiting currents from the first and second reduction steps was calculated from the trend line of these data points and the calculated value is 1.76 (after excluding the scattered data points from the plot). This shows that some  $\text{Cu}^+$  ions formed in the reduction step 1 are dispersed into the solution before the second electron get transfer as a result the obtained slope value is  $<2$ . It was observed during the static experiments, the ratio of the diffusion coefficient of  $\text{Cu}^+:\text{Cu}^{2+}$  is 1.64, which also agreed with the ratio of the limiting current. This might be due to the nature of diffusion of these Cu complexes in the electrolyte.

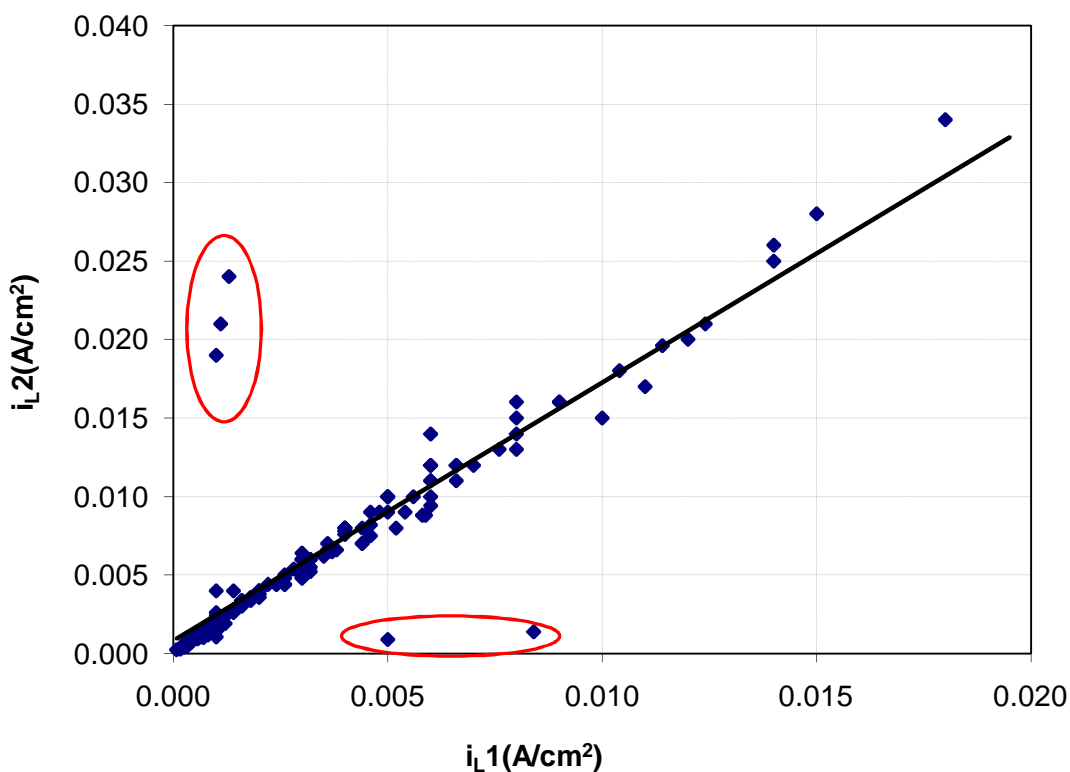


Figure 5-7 : The relationship between the two reduction steps, regression equation of the trend line is  $y = 1.76x$  with  $R = 0.99$ , the trend line was drawn after excluding the scattered data points

For a metal system when reduction of the metal was controlled by its mass transfer, then the system might follow Levich equation. The Levich equation is shown in equation 5.6.

$$i_L = 0.623nFCD^{2/3}\omega^{1/2}\nu^{-1/6} \quad (5.6)$$

Where  $i_L$  = limiting current density,  $\text{A/cm}^2$ ,  $C$  = concentration of the metal ion,  $\text{mol/cm}^3$ ,  $n$  = number of electron transferred,  $\omega$  = RDE rotation speed,  $\text{rad/s}$ ,  $F$  = Faradays constant,  $\text{C/mol}$ ,  $\nu$  = viscosity,  $\text{cm}^2/\text{s}$ . Thus to test the reduction mechanism, the influence of these parameters need to be tested.

To test the validity of Levich equation in the Cu system, relationship between the parameters like concentration and RDE rotation speed with limiting current of the system were tested irrespective of reduction steps. The limiting currents for each of the concentrations were collected and a log-log plot of limiting current vs. concentration was carried out for both the reduction steps. The typical log-log plot of limiting current vs. concentration at various temperatures is shown in fig. 5-8. The expected value for these slopes was 1 according to Levich equation. The best fit line was drawn for each

data set and the slope of these plots was determined as  $0.85 \pm 5\%$  for Cu system. This variation in slope value might be from the error in limiting current value.

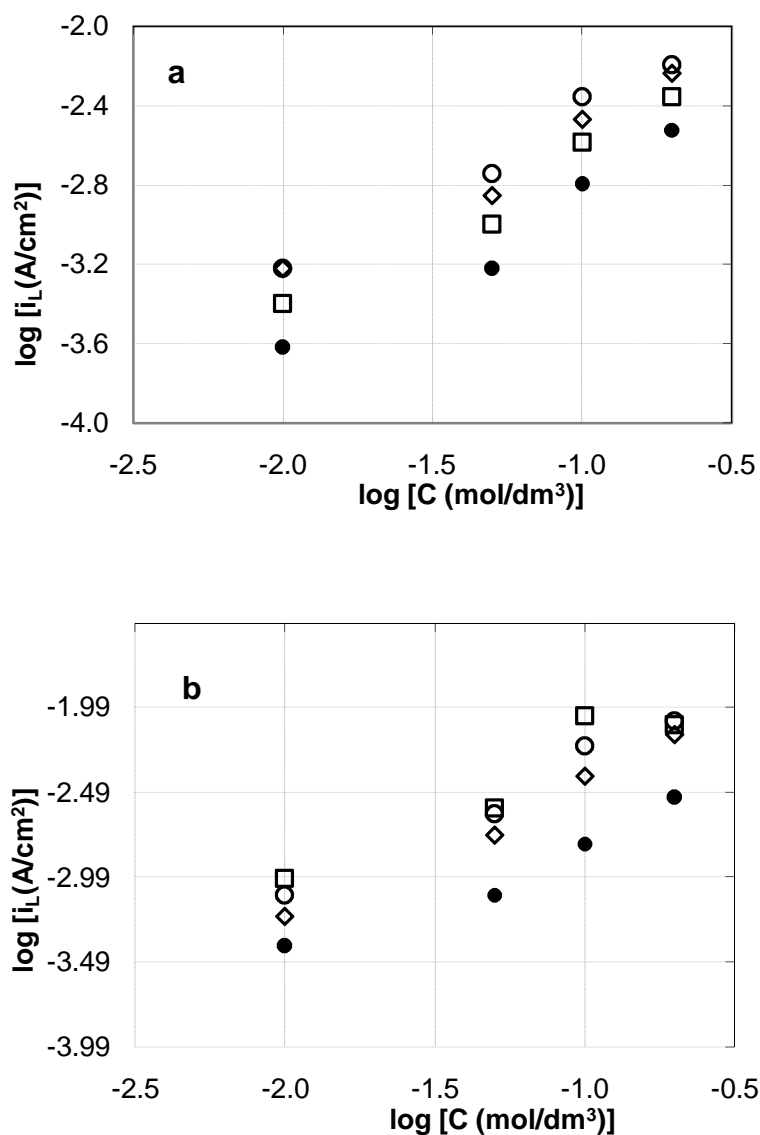


Figure 5-8 (A): Verification of Levich equation by Limiting current vs. concentration of the Cu ion using various RDE speeds, [●] 500 rpm, [□] 1000 rpm, [◇] 2000 rpm, [○] 3000 rpm for various temperatures, [a] 25 °C for  $i_{L1}$ , [b] 35 °C for  $i_{L1}$

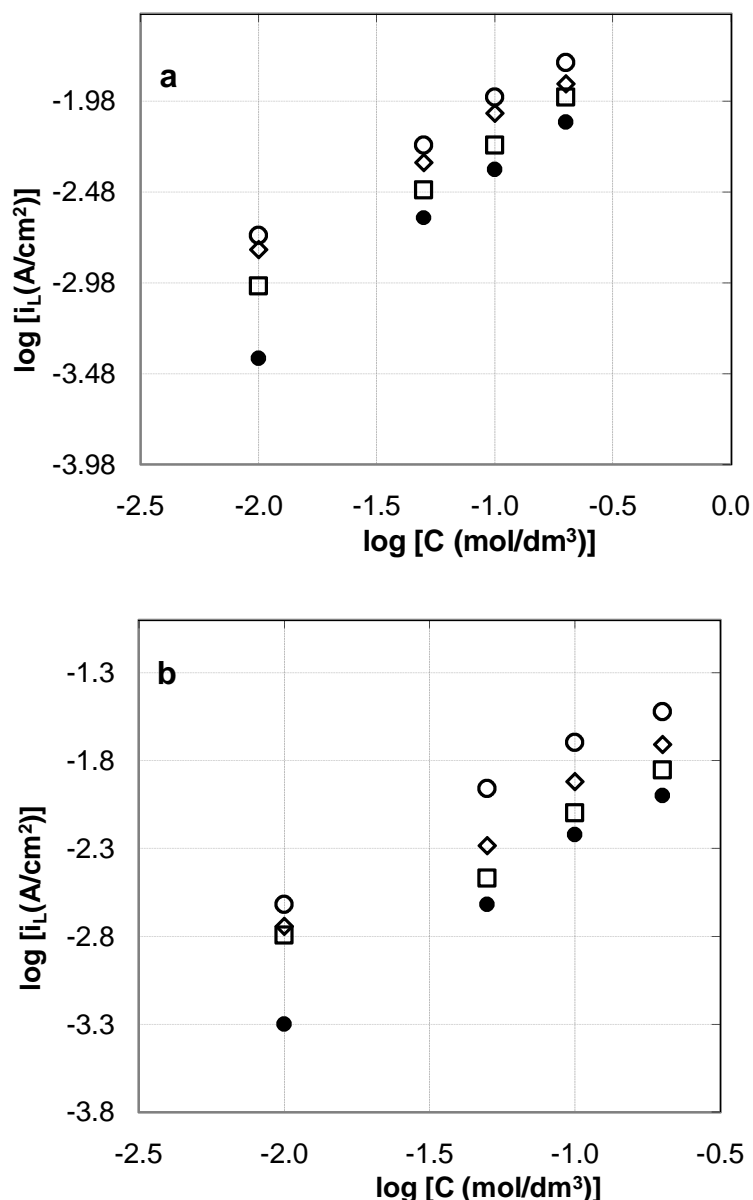


Figure 5-8 B: Verification of Levich equation by Limiting current vs. concentration of the Cu ion using various RDE speeds, [●] 500 rpm, [□] 1000 rpm, [◇] 2000 rpm, [○] 3000 rpm for range of applied temperatures, [a] 45 °C for  $i_{L2}$ , [b] 55 °C for  $i_{L2}$

To examine the relationship between the limiting current and RDE rotation speed for each temperature, the normalized data points (divided by particular concentration and reduction step value) were plotted against the RDE rotation speed. The typical log-log plot of (limiting current/concentration) vs. rotation speed of the RDE for each temperature is shown in fig. 5-9. The slope value was determined for each of the trend line for the data spread in fig. 5-9 a, b, c and d using standard regression technique and the determined value was estimated as  $0.48 \pm 10\%$ . According to Levich equation the expected slope value is 0.5. The R values were in the range of 0.85 to 0.81 for each data set (calculated after removing scattered data points in the fig. 5-9).

This low R value was due to the error within the data points as collected by varying various parameters of Levich equation. This error calculation is shown in the appendix A.2. Thus from above correlations, it appeared that Cu system in ethaline melt presumably following Levich equation. It is to be noted that previously the researchers calculated the diffusion coefficient of Indium species in reline melt using Levich equation <sup>[24]</sup>. The diffusion co-efficient in various temperature was calculated from the intercept values of the trend lines using Levich equation. The determined diffusion coefficient values were  $1.4 \times 10^{-7} \text{ cm}^2/\text{s}$ ,  $1.8 \times 10^{-7} \text{ cm}^2/\text{s}$  at  $25 \text{ }^\circ\text{C}$  for  $\text{Cu}^{2+}$  and  $\text{Cu}^+$  respectively.

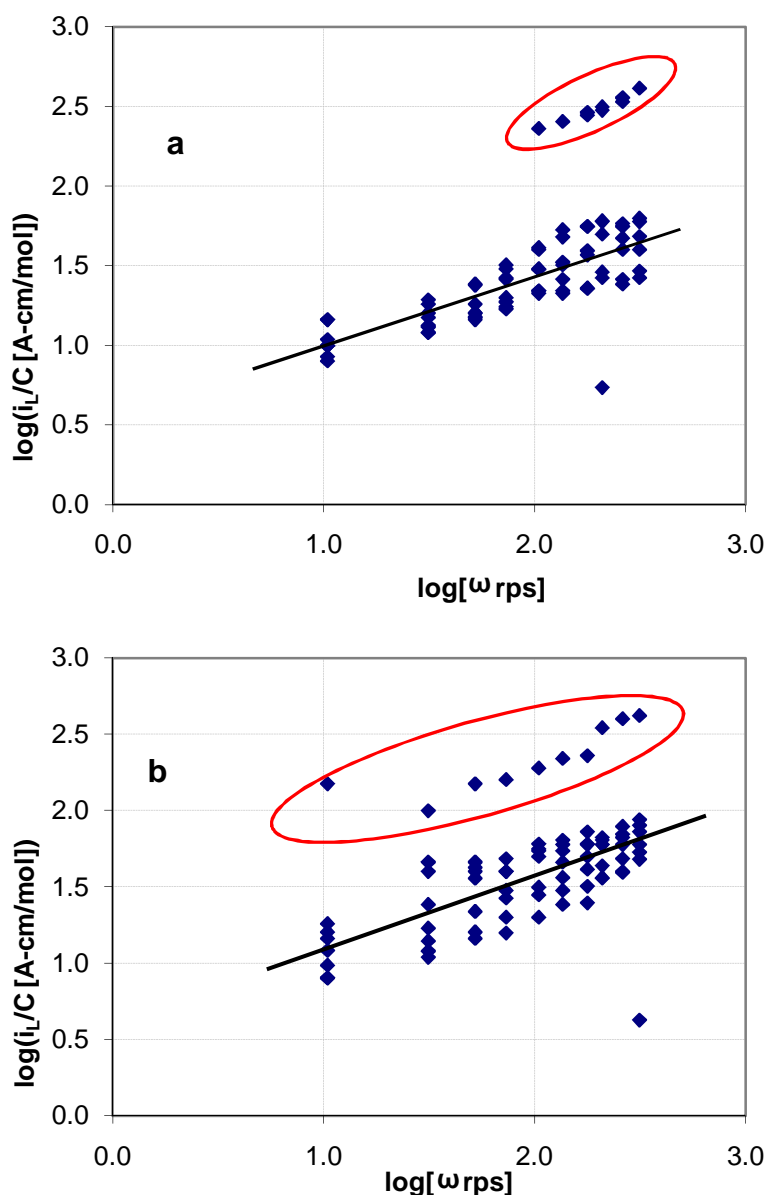


Figure 5-9 (A): Verification of Levich equation by [Limiting current / concentration of  $\text{CuCl}_2$  in the electrolyte] verses rotation speed of RDE log- log plot for various temperatures, [a]  $25 \text{ }^\circ\text{C}$ , [b]  $35 \text{ }^\circ\text{C}$

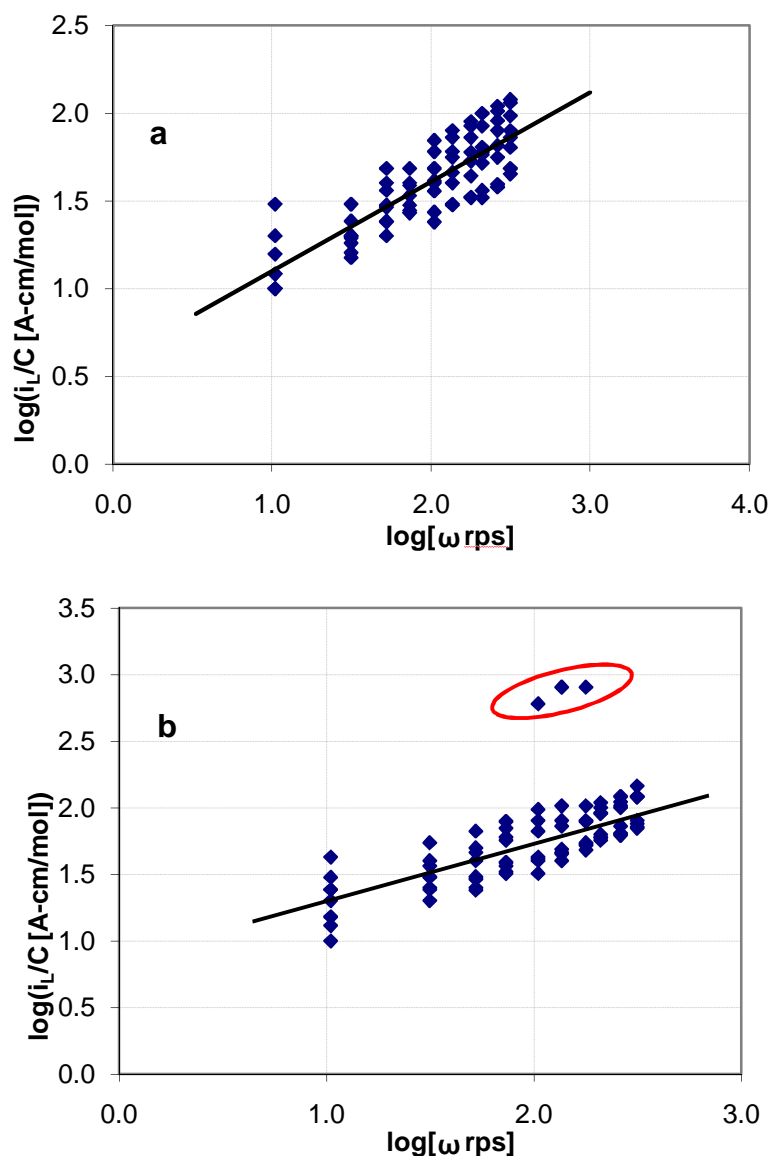


Figure 5-9 (B): Verification of Levich equation by [Limiting current / concentration of  $\text{CuCl}_2$  in the electrolyte] versus rotation speed of RDE log- log plot for various temperatures, [a] 45 °C, [b] 55 °C

#### 5.4. Electrochemical characterization of tin in ethaline melt

##### 5.4.1. Formal potential measurements

Similar to Cu study, formal potential of Sn reduction couple was measured by open circuit potential (OCP). The formal potential for  $\text{Sn}^{2+}/\text{Sn}^0$  couple was measured by dissolving hydrated  $\text{SnCl}_2$  in a concentration range of 0.01 to 0.1 M at 25 °C. The OCP value was monitored in the time span of 1 to 24 h and the final value was recorded when the system attained its equilibrium state as carried out during Cu study experiments. The values after a measuring time of 2 h were presented in fig 5-10. The measured OCP value followed a linear relationship with logarithmic concentration of

metal salt added. Formal potential was determined using Nernst equation [shown in eqn. 5.1].

Using standard regression technique, the constant and the slope of the data lines were determined from fig. 5-10 as a log function of concentration of metal salt added. The regression shows that the dependence of the potential on  $\text{Sn}^{2+}$  is 28 mV/decade. The theoretical value of the slope for two-electron transfer reaction at 25 °C is 29.5 mV/decade calculated from eqn. 5.1.

Since the formal potential measures the potential for a reaction, the reaction in this system is shown below,



where two electrons were exchanged. The value determined in the present study for Sn in the ethaline melt showed an excellent agreement with the theoretical one. This indicated that  $\text{SnCl}_3^-$  is the likely electroactive species in the solution. This formal potential data for metal salts extend over a reasonably large concentration range, which suggested that the electroactive species did not change over this range.

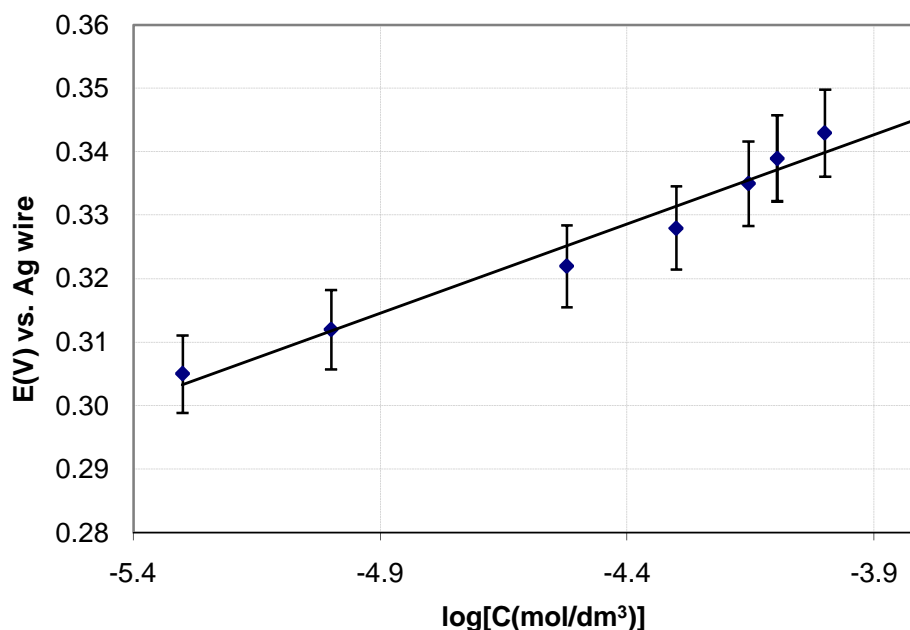


Figure 5-10 : The formal potential plot with concentration change of  $\text{SnCl}_2 \cdot 2\text{H}_2\text{O}$  for  $\text{Sn}^{2+}/\text{Sn}^0$  couple at Pt substrate in ethaline melt, regression equation is  $y=0.028x+0.45$  with  $R=0.98$

The intercept was 0.45 V as determined from fig. 5-10, so the formal potential of  $\text{Sn}^{2+}/\text{Sn}^0$  should be 0.45 V in ethaline melt. In other IL electrolyte this value was reported as in the range of 0.55 V to (-0.85 V) [2-3,25].



5.4.2. Voltammetry for ethaline melt containing  $\text{SnCl}_2 \cdot 2\text{H}_2\text{O}$ 

The voltammetry scans are presented in fig. 5-11 for ethaline melt containing 0.5 M  $\text{SnCl}_2 \cdot 2\text{H}_2\text{O}$  on Pt RDE at static condition. The experiments were carried out within a scan range of -0.7 V to 0 V at 25 °C. Applied scan rates were in the range of 10 to 50 mV/s.

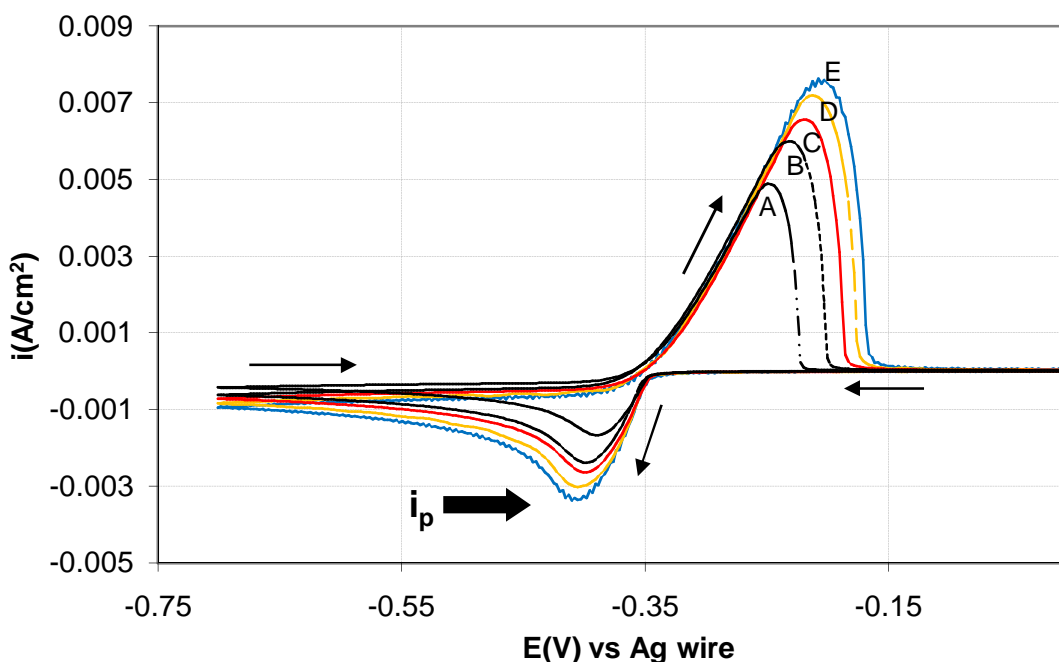


Figure 5-11 : Voltammetry at various scan rates using a static Pt RDE at 25 °C for ethaline melt containing 0.05 M  $\text{SnCl}_2 \cdot 2\text{H}_2\text{O}$ , (A) 10 mV/s, (B) 20 mV/s, (C) 30 mV/s, (D) 40 mV/s, (E) 50 mV/s

The reduction process started at a potential of -0.36 V, after reaching a maximum a decrease in current was observed. In the reverse sweep the oxidation process started at the potential of -0.36 V and then went through a maximum. For this process a single reduction and oxidation peak was observed which was due to reduction of  $\text{Sn}^{2+}$  to  $\text{Sn}^0$  [shown in eqn. (5.7)]. This current potential behaviour was similar with the results obtained previously for Sn used as  $\text{SnCl}_2$  in other IL electrolytes [8, 25-26].

This was not likely to be the reaction scheme for the formation of  $\text{Sn}^{4+}$  to  $\text{Sn}^{2+}$  as stated above. This reaction is likely to occur in basic electrolyte, as  $\text{Sn}^{4+}$  with six chloride complex which was not stable in acidic electrolyte [2]. Moreover, if this reaction took place during the reduction step observed in the forward sweep, then it is expected to appear in the reverse sweep in positive potential. In the reverse sweep only one stripping peak was observed, even when the scan was extended upto +1 V.

The fig. 5-11 shows that the position of current maximums or peak current at the forward and reverse sweep varied with variation of scan rates. The above study indicated that it is not a reversible electron transfer reaction. It was reported that  $\text{Sn}^{2+}$  to  $\text{Sn}^0$  is a quasi reversible or irreversible process in other IL electrolyte [2,27]. Thus diffusion co-efficient for Sn was determined using equation 5.5. Figure 5-12 is showing a typical log log plot of peak current vs. scan rate.

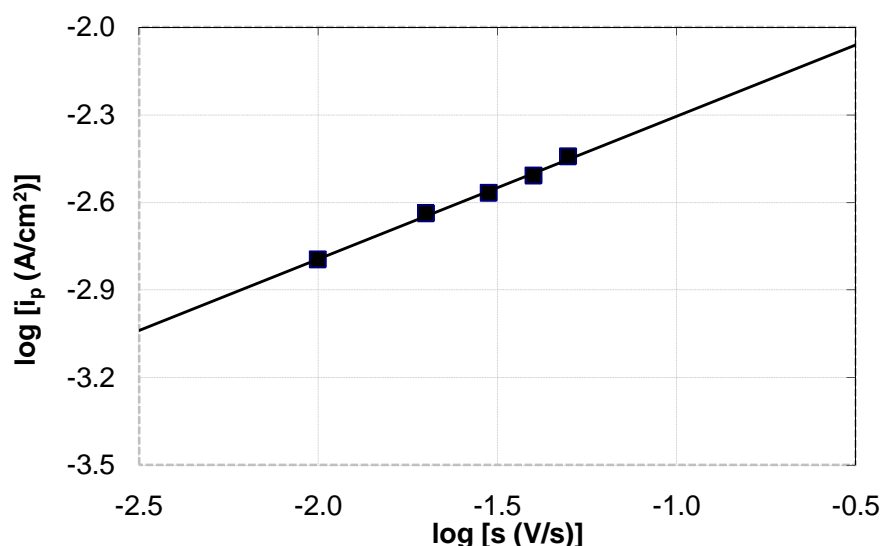


Figure 5-12 : The relationship between the peak current and scan rate (calculated from fig. 5-11) to determine diffusion co-efficient of Sn in IL (1 ChCl:2 EG) electrolyte, regression equation is  $y=0.49x-1.82$  with  $R= 0.99$

The calculated diffusion co-efficient using eqn. 5.5 and fig. 5-12 for the reduction step is  $1.96 \times 10^{-7} \text{ cm}^2/\text{s}$  in ethaline melt. Since the value of diffusivity of  $\text{Sn}^{2+}$  species in ChCl-based ILs is still unknown, one can compare this value against those observed for [BMP-NTf<sub>2</sub>] and [BMP-DCA]. These have been found to be in the range of  $0.35$  to  $3.0 \times 10^{-7} \text{ cm}^2/\text{s}$  [9], which is similar to the value calculated in this study.

In other set of experiments by agitation, the bath temperature was maintained in the range of 25 to 55 °C. The monitored RDE speeds were in the range of 0 to 2000 rpm at 0.01 to 0.1 M  $\text{SnCl}_2 \cdot 2\text{H}_2\text{O}$ . A similar scan range like the static experiments was used maintaining a scan rate of 10 mV/s.

The obtained scans in the agitated condition showed similar reduction and oxidation steps as observed for the static scans. The voltammetry scan in 0.01 M concentration at 35 °C for various RDE speed is shown in fig. 5-13. The limiting current for formation of  $\text{Sn}^0$  was determined from the flat plateau region of the forward scan. The experiments at other temperatures, i.e. 25 °C, 45 °C, 55 °C and the concentrations such as 0.025 M and 0.04 M were found to show similar current-potential behaviour as shown in the fig. 5-13 and are included in the appendix A.3. At

higher concentration above 0.07 M, the system is not mass transfer controlled for all temperatures. Thus limiting current value could not be determined from those voltammetry scans for RDE speed above 300 rpm.

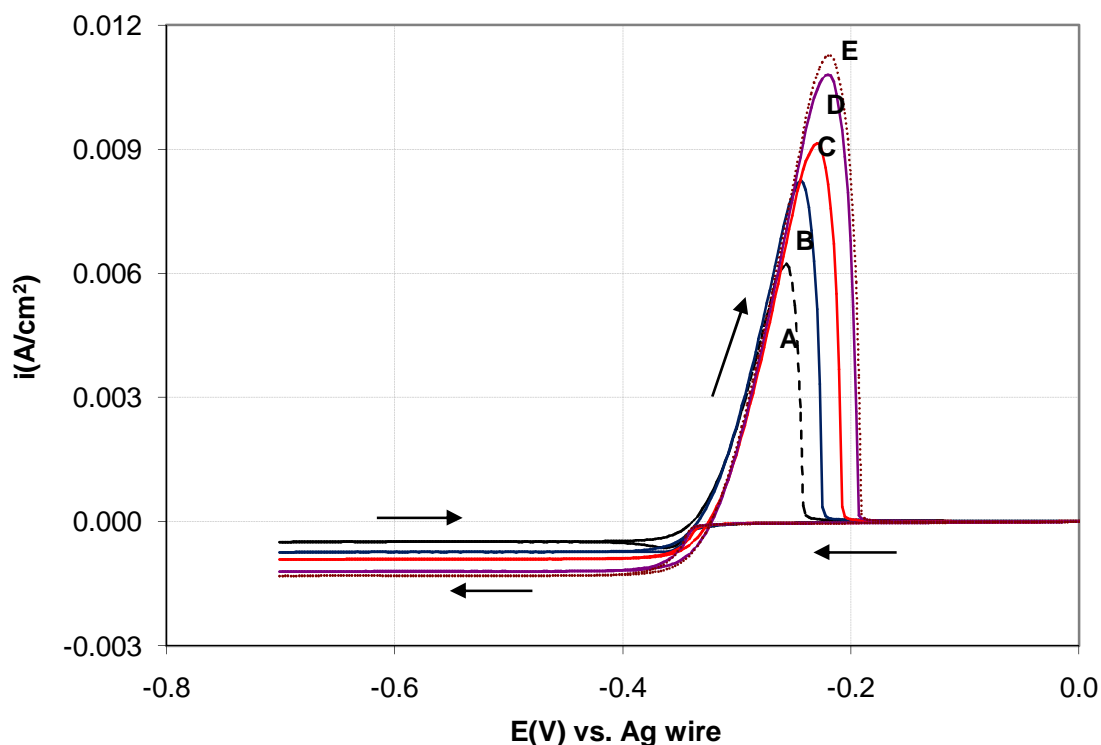


Figure 5-13 : Voltammetry for ethaline melt containing 0.01 M  $\text{SnCl}_2 \cdot 2\text{H}_2\text{O}$  at 35 °C and scan rate 10 mV/s using various RDE speeds, (A) 300 rpm, (B) 700 rpm, (C) 1000 rpm, (D) 1700 rpm, (E) 2000 rpm

From the results of the above studies the concentration for the limiting current analysis was kept in the range of 0.01 M to 0.05M. To establish the relationship between concentration, temperature and limiting current similar studies like Cu were carried out and are included in the appendix A.4. Similar to Cu system it appeared that Sn system in ethaline might following Levich equation. The diffusion co-efficient of Sn was found  $1.4 \times 10^{-7} \text{ cm}^2/\text{s}$  in the ethaline melt determined by Levich equation.

#### 5.5. Mass transfer co-relation of individual metals

To eliminate the errors originated in various parametric measurements, the correlation is represented in terms of dimensionless numbers. The mass transfer correlations for individual metals in the present electrolyte are represented with the help of different dimensionless numbers like Schmidt number (Sc), Sherwood number (Sh), Reynolds number (Re). Sc is ratio of the molecular diffusivity of momentum and

mass transfer.  $Sh$  is the ratio of the convective mass transfer coefficient and diffusive mass transfer co-efficient.  $Re$  is the ratio of the inertia forces and viscous forces.

The correlation in dimensionless form in case of aqueous electrolyte was derived previously in chapter 3, is shown in equation 3.12, is presented here as,

$$Sh = 0.623 Sc^{\frac{1}{3}} Re^{0.5} \quad (5.8)$$

The above relationship is valid for  $Sc < 100$  [28-29]. Currently the range of  $Sc$  for Cu and Sn system in ethaline melt was determined in the range of  $3 \times 10^5$  to  $32 \times 10^5$  respectively. For large  $Sc > 1000$ , correction of the  $Sc$  is required, as it influences the diffusion in liquids. The  $Sc > 250$  can be corrected using Gregory and Riddiford [30] and the corrected representation is shown below,

$$0.62Sc^{\frac{2}{3}} \rightarrow \frac{0.55Sc^{\frac{2}{3}}}{0.89 + 0.316Sc^{-0.36}} \quad (5.9)$$

Thus the new presentation of eqn. (5.8) is modified by replacing the term from eqn. (5.9) as,

$$Sh \times \frac{0.55Sc^{\frac{2}{3}}}{0.89 + 0.316Sc^{-0.36}} = K Re^{0.5} \quad (5.10)$$

$$\text{Or, } Sh \times Sc_{new} = K Re^{0.5} \quad (5.11)$$

Here  $K$  is a constant. To determine the dimensionless numbers, diffusion coefficient was calculated by Randle-Sevcik equation. To determine the mass transfer relationship for these metals, a log-log plot of  $Sh \times Sc_{new}$  vs.  $Re$  was carried out. In this case the data were taken only at 25 °C. Fig. 5-14 is showing the relationship between  $Sh$ , corrected  $Sc$  and  $Re$  for Cu and Sn system. The slope and intercept of the plots of each metal were determined.

For Cu system the regression equation was obtained as  $y = 0.44x - 2.29$  from fig. 5-14. Thus using these values, the new mass transfer correlation for Cu in IL electrolyte is presented as,

$$Sh \times Sc_{new} = 0.005 \times (Re)^{0.44} \quad (5.12)$$

For Sn system the regression equation was obtained as  $y = 0.53x - 2.12$  presented in fig. 5-14. Thus using these values, the new mass transfer correlation for Sn in IL electrolyte is presented as,

$$Sh \times Sc_{new} = 0.008 \times (Re)^{0.53} \quad (5.13)$$

The mass transfer correlation obtained for individual metal does not show similarity with the equation showed in aqueous electrolyte. Even the correlation obtained for Cu system is different than the equation for Sn system. Again the studies showed that R values are <0.99 for both the metals. This might be due to the errors in the data points. Using the above calculations, only error from Sc was eliminated, but the Re and Sh still suffers from 13% and 26% of errors respectively. The Sc for Cu<sup>2+</sup>, Cu<sup>+</sup>, Sn<sup>2+</sup> system in IL electrolyte was obtained as 4.4x10<sup>6</sup>, 2.7x10<sup>6</sup>, 2.8x10<sup>6</sup> respectively at 25 °C. In aqueous system for Cu<sup>2+</sup> the Sc is 1.4x10<sup>3</sup> at 25 °C. Similar to Sc large variation in Sh is expected, due to the variation in limiting current and diffusion coefficient value. Due to this large variation in Sc and Sh variation in the mass transfer correlation in the ethaline melt with respect to aqueous electrolyte is possible.

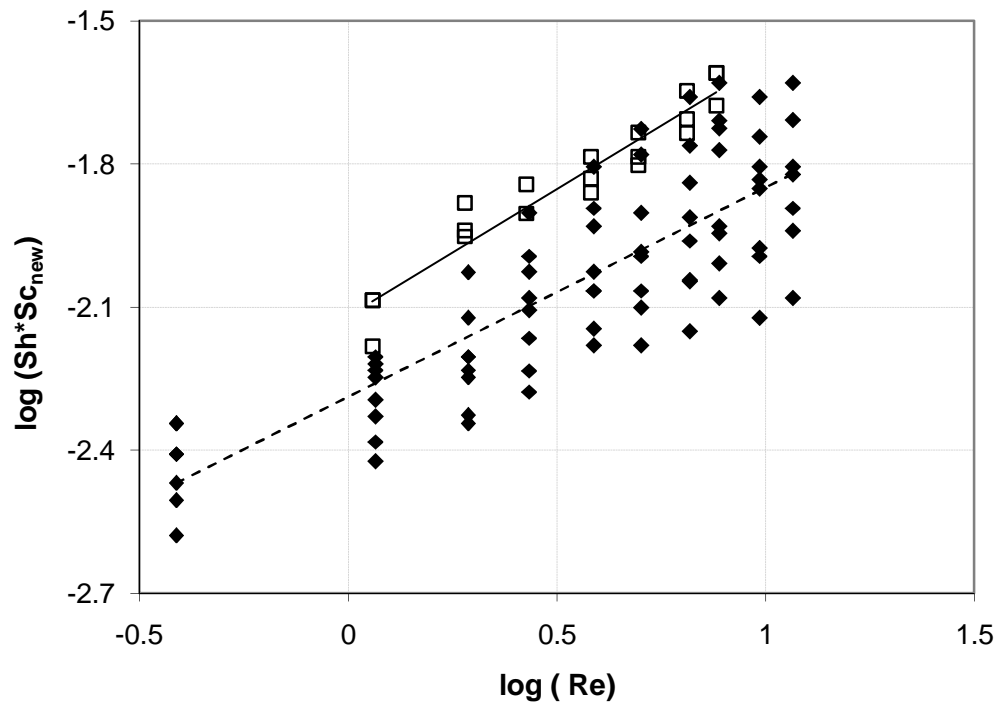


Figure 5-14 : Mass transfer correlation for individual metal system using dimensionless numbers like Sh, Sc, Re for individual metals, [♦] Cu, regression equation :  $y = 0.44x - 2.29$ ,  $R = 0.84$ , [□] Sn study, regression equation :  $y = 0.53x - 2.12$ ,  $R = 0.96$

#### 5.6. Current efficiency calculation of individual metals

To calculate the current efficiency ( $\eta_Q$ ) of the individual metals a charge balance analysis was carried out using the voltammograms at agitated condition for both metals. To calculate the charge (Q) from the voltammetry data, the obtained current

density (i) data obtained during the voltammetry need to be converted. During voltammetry measurements the current value was recorded in short interval of time (t) depending on the applied scan rate. The Cu voltammetry was carried out at 30 mV/s and Sn voltammetry was carried out at 10 mV/s. The time interval for Cu voltammetry was 0.04 s and Sn voltammetry was 0.12 s. Thus current value obtained at each point was measured for 0.04 s or 0.12 s and charge value can be obtained from the product of current value at each point multiplying by the time interval ( $Q = i \times t$ ). The chosen potential range for charge calculation is shown in fig. 5-15.

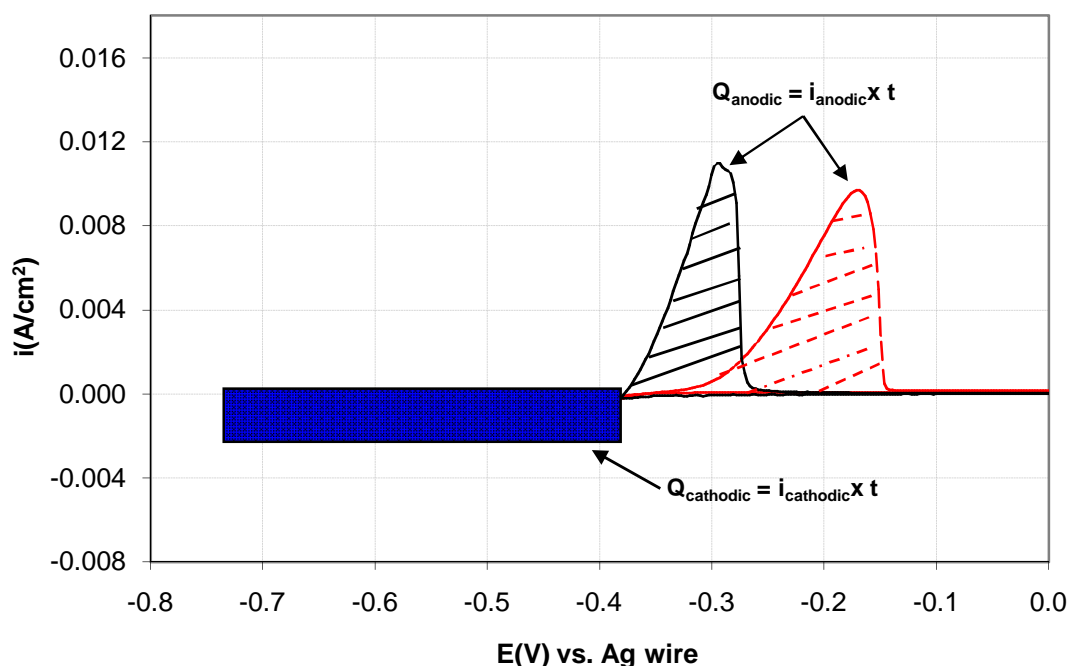


Figure 5-15 : The cathodic and anodic potential range from voltammetry scans at agitated condition used for current efficiency calculation, (---)Cu scan, (—)Sn scan

The charge calculation was carried out for both anodic part and cathodic part of each voltammetry scan and the ratio was determined to find out the efficiency of the process as shown in eqn. 5.14. The charge accumulation at cathodic and anodic region was calculated from the voltammetry measurement at various concentrations and temperature used for both metal at various RDE speed. Thus,

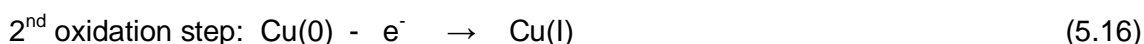
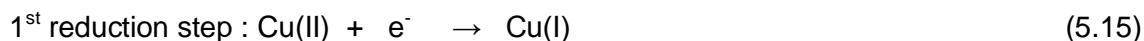
$$\eta_Q = \frac{Q_{anodic}}{Q_{cathodic}} \times 100 \% \quad (5.14)$$

In case of Cu, the current efficiency for concentration range of 0.2 to 0.01 M in the temperature span of 25 to 55 °C was in the range of 98% to 110%. The large error range could be due to very small currents in the lower concentrations and slower rotation speeds. The reported current efficiency was 100% for Cu in other IL electrolyte [6-7] and the aqueous electrolytes [31] also.

In case of Sn, the obtained cathode current efficiency for deposition from a concentration range of 0.01 to 0.025 M in the temperature span of 25 to 55 °C was found to be in the range of 86% to 93%. The current efficiency value increased up to 97% with increase in metal ion concentration in the electrolyte. For a concentration range of 0.04 to 0.1 M in the temperature span of 25 °C to 55 °C the value was determined as 93% to 97%. The current efficiency value in other IL electrolyte varied in a range of 82% to 100% [3,8,21]. In aqueous electrolyte the current efficiency value is reported as 75% to 95% [31].

### 5.7. Discussion

For the ethaline melt containing  $\text{CuCl}_2 \cdot 2\text{H}_2\text{O}$ , the voltammetry scans at agitated condition showed a noticeable variation. During these scans the 2<sup>nd</sup> stripping peak starts disappearing and at a rotation speed of 700 rpm this peak completely disappeared. Moreover the stripping current for the oxidation of  $\text{Cu}^0$  to  $\text{Cu}^+$  proceeds when the current is still cathodic. This process was observed in the potential range of -0.35 V to 0.6 V, where Cu comproportionation reaction might takes place [6]. In this potential region the reduction of  $\text{Cu}^{2+}$  ions to  $\text{Cu}^+$  ions and oxidation of  $\text{Cu}^0$  ions to  $\text{Cu}^+$  ions took place at the same time. Thus the two simultaneous reactions at the electrode surface are,



In case of present process, the obtained total current in this potential region are the summation of the partial currents for copper oxidation and reduction, so such current potential behaviour is expected [32]. However, in the reverse scan any higher current was not observed. Thus it can be assumed that due to high diffusivity of  $\text{Cu}^+$  ions [4] any accumulation of  $\text{Cu}^+$  ions near the electrode surface did not occurred.

The mass transfer correlation for individual metal showed two different relationships for each metal. This might be due to Sc correction correlation. Thus a log-log plot of  $\text{Sh} / \text{Sc}^{1/3}$  vs.  $\text{Re}$  was carried out following the eqn. 5.8 which is appropriate for the Levich system. Thus, diffusion coefficient was determined from Levich equation. Figure 5-16 is showing a typical plot for Cu and Sn system using dimensionless numbers.

For Cu system the regression equation was obtained as  $y = 0.48x - 0.2$  from fig. 5-16. Thus using these values, the new mass transfer correlation for Cu in the IL electrolyte is presented as,

$$\frac{Sh}{Sc^{1/3}} = 0.63 \times (Re)^{0.48} \quad (5.17)$$

For Sn system the regression equation was obtained as  $y = 0.48x + 0.17$  from fig. 5-16. Thus using these values, the new mass transfer correlation for Sn in the IL electrolyte is presented as,

$$\frac{Sh}{Sc^{1/3}} = 1.49 \times (Re)^{0.48} \quad (5.18)$$

The above two equations appeared to be very close to each other and these equations are close to the equation of the aqueous electrolyte (eqn. 5.8). However, the R values of these systems are lower than 0.99 which might be due to the error of the dimensionless numbers.

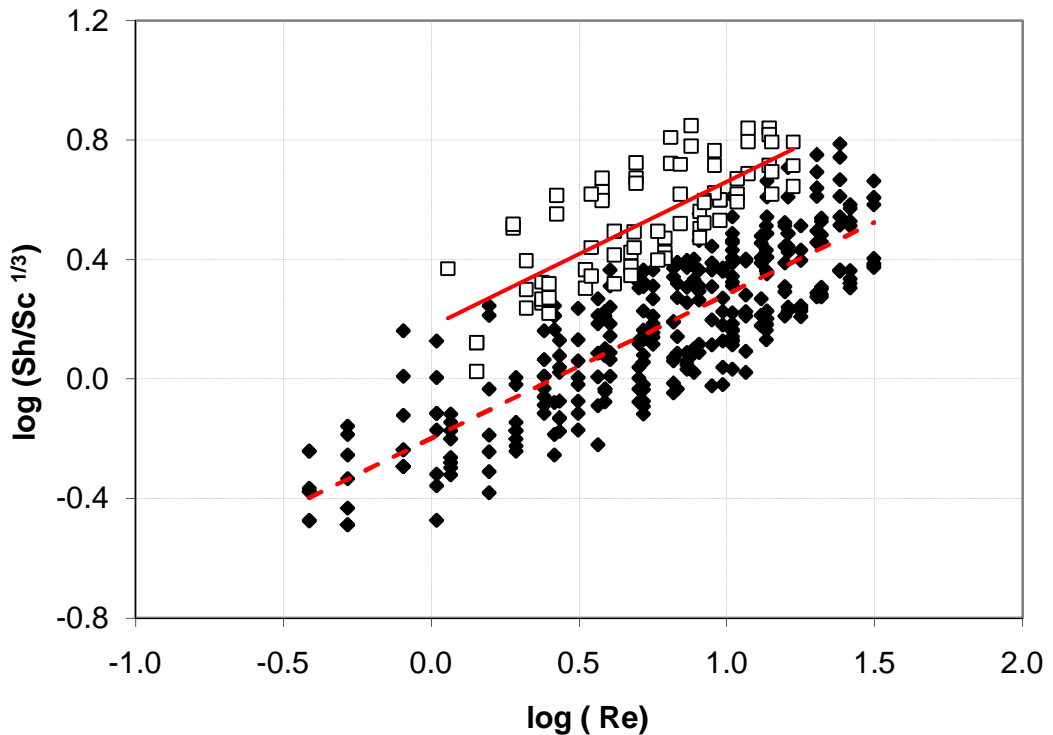


Figure 5-16 : Mass transfer correlation for individual metal system using dimensionless numbers like Sh, Sc, Re for individual metals, [ $\blacklozenge$ ] Cu, regression equation :  $y = 0.48x - 0.2$ ,  $R = 0.84$ , [ $\square$ ] Sn study, regression equation :  $y = 0.48x + 0.17$ ,  $R = 0.77$

#### 5.8. Conclusion:

From the above results and discussion, the following conclusions were drawn,

- The voltammetry studies on the ethaline melt showed that the operation range for this melt stands in the range of -0.7 V to +1.3 V for all temperatures.



- The Formal potential measurements on the individual metal indicated that Cu was reduced through a two step mechanism from a  $\text{CuCl}_4^{2-}$  complex and Sn was reduced via a two electron transfer route from  $\text{SnCl}_6^{2-}$  ligand. Both Cu and Sn species did not change over the examined concentration range.
- The voltammetry studies on individual metals at static condition showed reduction of  $\text{Cu}^{2+}$  to  $\text{Cu}^+$  is a reversible system. However reduction of  $\text{Cu}^+$  to  $\text{Cu}^0$  and  $\text{Sn}^{2+}$  to  $\text{Sn}^0$  did not showed any reversibility. The diffusion co-efficient values of  $\text{Cu}^{2+}$ ,  $\text{Cu}^+$  and  $\text{Sn}^{2+}$  was determined using Randles-Sevcik type analysis and the values were obtained as  $1.22 \times 10^{-7} \text{ cm}^2/\text{s}$ ,  $2 \times 10^{-7} \text{ cm}^2/\text{s}$  and  $1.96 \times 10^{-7} \text{ cm}^2/\text{s}$ , respectively.
- The reduction to  $\text{Cu}^0$  or  $\text{Sn}^0$  was found to be mass transfer controlled when examined with agitation. So the limiting current value was determined which will be useful for deposition of individual metals. This reduction mechanism appeared to be matching with Levich like equation for both the metals when examined with various agitation rate and concentration of metal ions at a temperature range of 25 to 55 °C.
- For Cu system the current efficiency of the process was determined as  $98 \pm 5\%$  and this value did not vary with various range of temperature, concentration of metal ion and RDE speeds. For Sn system the current efficiency value varies in the range of  $93 \pm 4\%$ .

## Reference:

1. C. L. Hussey, L. A. King and R. A. Carpio (1979) *Electrochem. Soc.: Solid-state science and technology*, 126(6) : 1029-1034.
2. X. -H. Xu and C. L. Hussey (1993) *Journal of The Electrochemical Society*, 140(3) : 618-626.
3. J. -F. Huang and I. -W. Sun (2003) *Journal of The Electrochemical Society*, 150(6) : E299-E306.
4. D. Lloyd, T. Vainikka, L. Murtomäki, K. Kontturi and E. Ahlberg (2011) *Electrochimica Acta*, 56 : 4942-4948.
5. B. G. Pollet, J. Hihn and T. J. Mason (2008) *Electrochimica Acta*, 53 : 4248-4256.
6. K. Murase, K. Nitta, T. Hirato and Y. Awakura (2001) *Journal of applied electrochemistry*, 31 : 1089-1094.
7. A. P. Abbott, K. E. Ttaib, G. Frisch, K. J. McKenzie and K. S. Ryder (2009) *Phys. Chem. Chem. Phys.*, 11 : 4269-4277.
8. T. -I. Leong, Y. -T. Hsieh and I. -W. Sun (2011) *Electrochimica Acta*, 56 : 3941-3946.
9. B. C. M. Martindale, S. E. W. Jones and R. G. Compton (2010) *Physical Chemistry Chemical Physics*, 12 : 1827-1833.
10. A. Alhaji (2011) "Electrodeposition of Alloys from Deep Eutectic Solvents", PhD, University of Leicester, Leicester.
11. A. P. Abbott, G. Frisch, H. Garrett and J. Hartley (2011) *Chemical Communications*, 47 : 11876-11878.
12. C. Nanjundiah and R. A. Osteryoung (1983) *J. Electrochem. Soc.: Electrochemical science and technology*, 130(6) : 1312-1318.
13. T. M. Laher and C. L. Hussey (1983) *Inorg. Chem.*, 22 : 3247-3251.
14. C. P. D. Leon and F. C. Walsh (2003) *Trans. Inst. Met. Fin.*, 81(5) : B95-B100.
15. L. G. Boxall, H. L. Jones and R. A. Osteryoung (1974) *J. Electrochem. Soc.: Electrochemical Science and Technology*, 121(2) : 212-219.
16. U. Anders and J. A. Plambeck (1969) *Canadian Journal of Chemistry*, 47 : 3055-3060.
17. S. Z. Abedin, A. Y. Saad, H. K. Farag, N. Borisenko, Q. X. Liu and F. Endres (2007) *Electrochimica Acta*, 52 : 2746-2754.
18. I. B. Assaker and M. Dhahbi (2011) *Journal of Molecular Liquids*, 161 : 13-18.
19. G. Sun and C. Sun (2010) *Microporous and Mesoporous Materials*, 128 : 56-61.
20. F. Endres and A. Schweizer (2000) *Phys. Chem. Chem. Phys.*, 2 : 5455-5462.

21. B. C. M. Martindale, S. E. W. Jones and R. G. Compton (2010) *Physical Chemistry Chemical Physics*, 12 : 1827-1833.
22. A. J. Bard and L.R. Faulkner (eds.) : 'Electrochemical Methods Fundamentals and Applications', 2001, 2nd ed., A John Wiley & Sons, Inc. Publication, pp. 235-236.
23. C. D'Agostino, R.C. Harris, A.P. Abbott, L.F. Gladden and M.D. Mantle (2011) *Phys. Chem. Chem. Phys.*, 13 : 21383-21391.
24. J. C. Malaquias, M. Steichen, M. Thomassey and P.J. Dale (2013) *Electrochimica Acta*, 103, 15-22.
25. N. Tachikawa, N. Serizawa, Y. Katayama and T. Muira (2008) *Electrochimica Acta*, 53 : 6530-6534.
26. T. -I. Leong, Y. -T. Hsieh and I. -W. Sun (2011) *Electrochimica Acta*, 56 : 3941-3946.
27. W. Yang, H. Cang, Y. Tang, J. Wang and Y. Shi (2008) *Journal of Applied Electrochemistry*, 38 : 537-542.
28. V. Levich (1942) *Acta Physicochim.*, URSS, 17 : 257.
29. J. Newman (1966) *the Journal of Physical Chemistry*, 70 (4) : 1327-1328.
30. D. P. Gregory and A. C. Riddiford (1956) *J. Chem. Soc.*: 3756.
31. M. Schlesinger and M. Paunovic (eds.) (2000) *Modern Electroplating*, 4<sup>th</sup> ed. John Wiley and Sons, Inc. : 62-129, 258-260.
32. R. G. Evans, O. V. Klymenko, P. D. Price, S. G. Davies, C. Hardacre and R. G. Compton, *ChemphysChem*, 6, 526-533 (2005).

## **Chapter 6: ELECTRODEPOSITION OF INDIVIDUAL METALS**

### 6.1. Introduction

For metal deposition using electroplating technique, determination of electrochemical properties of the electrolyte is necessary which indirectly influence of physical properties on deposition parameters. The deposition in the present system i.e. ethaline melt is possible by using different electrochemical properties as determined in the previous chapter. These parameters are limiting current and reduction potential value of individual metals. It was reported that the deposit quality can be improved by increasing the operating temperature, as it improved the nucleation process on the substrate surface <sup>[1-2]</sup>. The deposit is also influenced by factors like substrate material and the deposition parameters like applied current or potential and bath temperature <sup>[3-4]</sup>.

Another important factor for electrodeposition is the stability of the electrolyte itself. Unstable electrolytes lead to co-deposition of other elements along with the targeted elements during the deposition process. The cathodic and anodic stability of various ILs were reported in literature <sup>[5-8]</sup> which showed various factors like anion, temperature <sup>[6-7]</sup> influences on the stability of the IL. Due to the side reactions the water in the electrolyte reduces and forms H<sub>2</sub> and oxidised to form O<sub>2</sub>. Ethaline melt after decomposition showed various organic compounds like acetaldehyde, ethanol, trimethylamine, methylene chloride, dichloromethane, chloroform, 2-methyl-1,3-dioxolane and ethylene glycol <sup>[5]</sup>. This decomposition can be avoided by using sacrificial anode or by introducing some sacrificing agent like acetic acid, oxalic acid, formic acid and water <sup>[5]</sup>. However decomposition of ethaline melt cannot be totally resolved by these processes. Moreover there is also chances of low cathodic efficiency and dissolution of the deposit due to the deterioration of the electrolyte <sup>[5]</sup>.

In the present chapter deposition of the individual metal is presented with varying various factors like deposition process, temperature, concentration of the metal ions and agitation rate. The obtained deposits were analysed using standard material analysis techniques. Finally the stability of these plating baths was also evaluated. The present plating baths contain a small amount of water due to the addition of hydrated metal salts as mentioned in the earlier chapter 4. As a result there are possibilities of decomposition of the electrolyte during metal plating.

## 6.2. Electrodeposition of Cu

It was clear in the previous chapter on electrochemical behaviour of Cu deposition that the reduction of Cu took place in two steps,  $\text{Cu}^{2+}$  to  $\text{Cu}^+$  and  $\text{Cu}^+$  to  $\text{Cu}^0$ . Both the reduction current in each step is mass transfer controlled in ethaline melt. Thus the maximum plating current is fixed by agitation rate and metal ion concentration. As the reduction takes place in two steps, so during deposition the deposition potential need to be fixed between the 1<sup>st</sup> and 2<sup>nd</sup> limiting current, otherwise Cu deposit cannot be achieved. If the applied potential range exceeds the mass transfer limiting current of the 2<sup>nd</sup> reduction step then there are the possibilities of decomposition of the electrolyte itself.

### 6.2.1. Potentiostatic deposition

The potentiostatic deposition was carried out by setting potential values to -0.6 V vs. Ag wire which was within the mass transfer controlled region to achieve the deposit at fastest rate. The deposition duration was kept in between 600 to 3600 s to achieve reasonable thick deposit. The deposited surface in two different concentrations is shown in fig. 6-1. For low metal concentration poor and thin brown deposit was obtained. With increase in metal concentration deposit surface became homogeneous. The bright pink colour of the deposit indicates metallic Cu. This indicates low metal loading is not suitable for deposition. Thus the suitable concentration for all the deposition experiments was chosen as 0.2 M  $\text{CuCl}_2 \cdot \text{H}_2\text{O}$ .

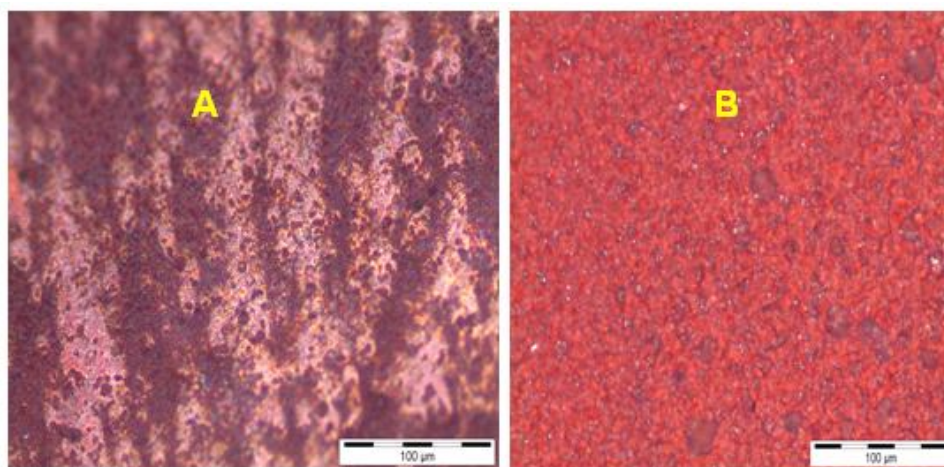


Figure 6-1 : Deposit obtained on stainless steel RDE from ethaline melt containing various concentration hydrated  $\text{CuCl}_2$  by applying -0.6 V and the RDE speed was 700 rpm, the deposition duration was 1800 s at 25 °C, (A) 0.05 M  $\text{CuCl}_2 \cdot 2\text{H}_2\text{O}$ , (B) 0.2 M  $\text{CuCl}_2 \cdot 2\text{H}_2\text{O}$

Typical Cu deposit in two different RDE speeds is shown in fig. 6-2 and better deposit was obtained at lower rotation speed of 700 rpm. With increase in RDE speed deposit surface became rough. Thus by potentiostatic condition homogeneous deposit was obtained when the applied current density was low and was in the range  $-0.6 \times 10^{-3}$  A/cm<sup>2</sup>. At higher plating currents the deposit roughens quickly so higher agitation speed for potentiastatic deposition was discarded. Thus the suitable RDE speed was chosen as 700 rpm for all the deposition experiments.

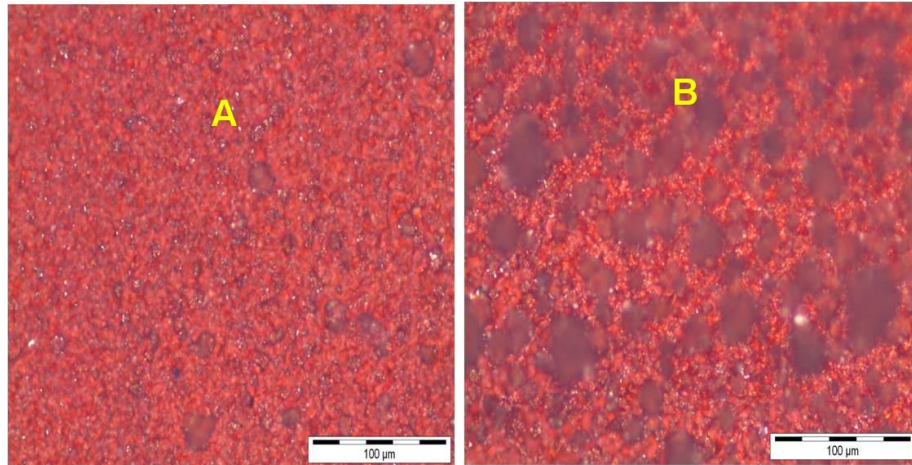


Figure 6-2 : Deposit obtained on stainless steel RDE from ethaline melt containing 0.2 M CuCl<sub>2</sub>.2H<sub>2</sub>O by applying -0.6 V using various RDE speed, the deposition duration was 1800 s at 25 °C, (A) 700 rpm, (B) 1300 rpm

The Cu deposit at higher temperature is shown in fig. 6-3. It was observed that with increase in temperature, surface became very rough. As observed previously that at higher plating currents the deposit roughens quickly. With rise in temperature of the electrolyte the plating current increases rapidly. Thus the chosen temperature was 25 °C for all the deposition experiments.

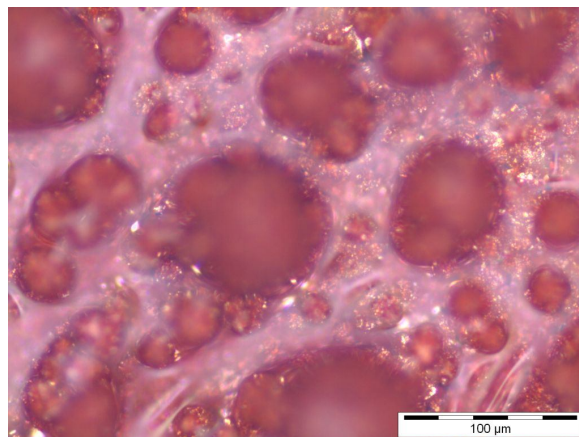


Figure 6-3 : Deposit obtained on stainless steel RDE from ethaline melt containing 0.2 M CuCl<sub>2</sub>.2H<sub>2</sub>O by applying -0.6 V and the RDE speed was 700 rpm, the deposition duration was 3600 s at 45 °C

At 25 °C the growth rate was  $0.1 \pm 7\%$   $\mu\text{m}/\text{min}$  and with increase in the deposit thickness the quality deteriorated. These thick deposits are included in the appendix A.5. With increase in duration the deposit surface started to turn into powdery.

### 6.2.2. Galvanostatic deposition

The potentiostatic deposition in mass transfer limited zone showed good deposit, thus the galvanostatic deposition was carried out in mass transfer limit zone. The galvanostatic deposition was carried out by setting current densities of range  $3.15$  to  $6.3 \times 10^{-3}$   $\text{A}/\text{cm}^2$ . The deposition process was carried out on stainless steel RDE from ethaline melt containing  $0.2$  M  $\text{CuCl}_2 \cdot 2\text{H}_2\text{O}$  and the RDE speed was  $700$  rpm, the deposition duration was  $3600$  s at  $25$  °C.

The homogeneous, smooth and shiny deposit was obtained at an applied current density of  $4.7 \times 10^{-3}$   $\text{A}/\text{cm}^2$  shown in fig. 6-4 which was at 78% of mass transfer limiting current. The obtained deposit was dense and homogeneous. The growth rate was  $0.15 \pm 10\%$   $\mu\text{m}/\text{min}$  in galvanostatic method and the deposit thickness increases without compromising deposit quality and obtained deposits are included in the appendix A.6.

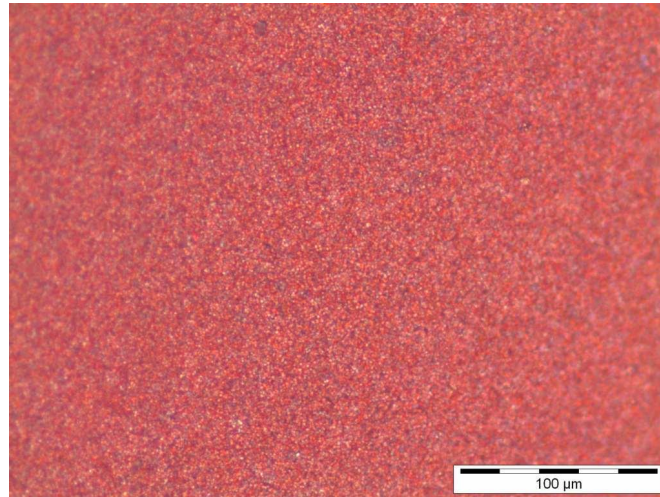


Figure 6-4 : Deposit obtained on stainless steel RDE from ethaline melt containing  $0.2$  M  $\text{CuCl}_2 \cdot 2\text{H}_2\text{O}$  by applying  $4.7 \times 10^{-3}$   $\text{A}/\text{cm}^2$  and the RDE speed was  $700$  rpm, the deposition duration was  $1800$  s at  $25$  °C

The obtained growth rate for Cu in ethaline melt was in the range of  $0.1$  to  $0.15$   $\mu\text{m}/\text{min}$ . The reported growth rate for Cu in aqueous baths was in the range of  $0.32$  to  $55$   $\mu\text{m}/\text{min}$  <sup>[9-10]</sup>. The obtained deposit morphology from ethaline melt was visually similar with the uniform smooth deposit obtained from aqueous baths <sup>[10-11]</sup>. The deposit obtained from other ILs were nodular, dense and compact with good adhesion property as reported in <sup>[1-2, 12-15]</sup>.

The current efficiency for deposition experiments was determined by the gravimetric measurement. For this measurement, the substrates were weighed before and after the deposition experimentation. The expected weight gain was obtained using Faraday's law and later compared with the weight gain of the deposit. The efficiency of the process was determined from the ratio of the weight for theoretical and experimental. The obtained efficiency by gravimetric method was  $97\pm 5\%$ . This value was cross checked by comparing the deposit thickness of the obtained deposit and as was expected by Faraday's law. The deposit thickness calculation was carried out using optical microscope. The current efficiency in this experiment was  $97\pm 2\%$ . The current efficiency in these experiments was similar with values obtained from voltammetry experiments. The values obtained in aqueous<sup>[16-17]</sup> and other ChCl based IL electrolytes<sup>[18]</sup> were also about 100% which matches with the above result.

### *6.2.3. Long term deposition experiments*

In order to investigate the bath stability after series of experiments, several deposition from a single electrolyte bath was carried out. Deposition was carried out by galvanostatic method using same electrochemical parameters as determined previously and reported in the section 6.2.2. In a time span of one month a total of 24 experiments amounting to 27 hrs of deposition from the bath were carried out. During these experiments approximately 0.018 moles of  $\text{Cu}^{2+}$ , corresponding to a thickness 200  $\mu\text{m}$  of metal was deposited out from a single electrolyte.

These long term depositions were carried out using two type of anode these helped in monitoring the effect of the sacrificial anode in deposition process. The variation in cell voltage during these deposition experiments are presented in the table 6.1. It was observed that the current efficiency or deposit morphology remains relatively unchanged for several deposition processes which implied about the stability of the bath. However, for few cases fluctuation in cell potential was observed and the obtained deposits were at low current efficiency. This irregularity was observed only when Pt anode was used. Smooth and uniform deposits with higher current efficiency were obtained again when additional hydrated  $\text{CuCl}_2$  was added in the old solution to increase the metal content of the electrolyte. Thus the irregularity in the deposition process was due to the decrease in metal ion content which was resolved by direct addition of metal salt to the electrolyte and the stability of the electrolyte was re-established.

The instabilities in the electrolytes using inert anode might be due to the breakdown of the ethaline melt itself. It was reported that the ethaline melt get decompose over time and  $\text{H}_2$  evolution occurred at the cathode, due to the discharge



of protons [5]. In addition, water breakdown also lead to release of hydrogen gas, and OH<sup>-</sup> [5]. During static experiments gas evolution at the cathode was observed, which might be due to hydrogen evolution. This outcome specify breakdown of choline due to formation of OH<sup>-</sup>. There might be some anodic reaction in the electrolyte too which lead to oxygen evolution and the breakdown of ethylene glycol. Since the addition of hydrated copper chloride stabilised the system, the cathode breakdown products seem to be more crucial.

Table 6.1 : Long term experiments for Cu deposition

Type of anode	Metal deposited out Moles/( $\mu\text{m}$ )	Duration of operation (hours)	Cell potential vs. Ag wire (V)
Pt mesh	0.018/200	28	0.65 to 0.55
			0.58 to 0.53
Cu sheet	0.017/192	26	0.60 to 0.55
			0.55 to 0.5

The experiments with sacrificing anode did not showed any poorer deposit quality or fluctuation in cell voltage or current efficiency during these one month long experiments. Thus additional metal salt was not added. Towards the end of these experiments a red powdery layer appeared at the top of electrolyte surface. This layer could be copper, copper chloride or copper oxide, because it has been shown that these products can be directly dissolved into various choline chloride based ILs [13, 19-20]. The excess copper observed in the plating operation would be due to the difference in current consumption by copper reduction vs. cupric ions introduced into the solution due to dissolution of the copper anode which would lead to an increasing amount of Cu<sup>2+</sup> in solution. Although the process is a slower one since the current efficiencies were very similar, i.e. 95-97% and 100%, but over a long period of time Cu would exceed it solvable limit.

Visually a change in colour of the electrolyte was noted with respect to the solution freshly prepared for deposition. The change in colour of the electrolytes is shown in fig. 6-5, when inert or soluble anode was used for deposition. During deposition experiments using inert anode the colour of the solution start fading as shown in fig. 6-5, [2] (B). The deposit quality and efficiency was checked carefully and metal ions were added in the electrolyte for refilling. With this treatment the electrolyte colour regains its previous colour as shown in fig. 6-5, [1]. The electrolyte used for

several depositions using soluble anode the deeper coloration was observed after few depositions. This change in colour with experiments was due to the change in metal ion concentration in the electrolyte. This variation in electrolyte colour was previously observed during preparation of electrolyte with various metal ion concentration. This indicates the speciation of copper in solution remains as a chloride complex during the long term plating process. Although there is a chance for water and glycol lose for anodic and cathodic reactions. Due to the presence of water content there were the possibilities for formation of aquo or aquo-chloro complexes <sup>[21]</sup> during long term plating. However formation of these complexes was not identified as any such colour change of the electrolyte was not observed.

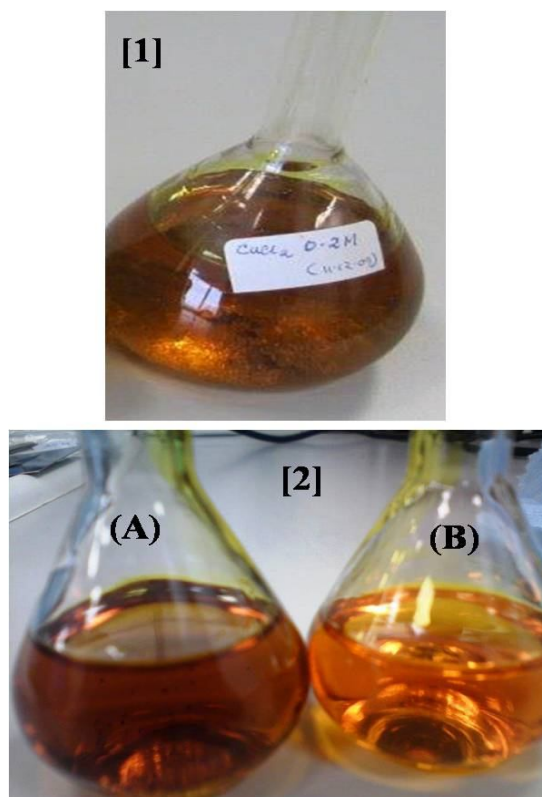


Figure 6-5 : Monitoring the variation in colour of the ethaline melt with 0.2 M  $\text{CuCl}_2 \cdot 2\text{H}_2\text{O}$  used for several electrodeposition experiment to test the stability of the bath, [1] electrolyte after preparation, [2] electrolyte after deposition experiments, (A) electrolyte after several deposition using soluble anode , (B) electrolyte after several deposition using inert anode

#### 6.2.4. SEM, EDAX and XRD measurements on deposited Cu

To examine the growth and morphology of the obtained deposit, a cross sectional view other than top view of the deposit is presented as shown in fig. 6-6. In this figure a dense deposit which contains very small grains was observed. The grains

are approximately 100 to 200 nm and the size did not increased with increase in deposit thickness.

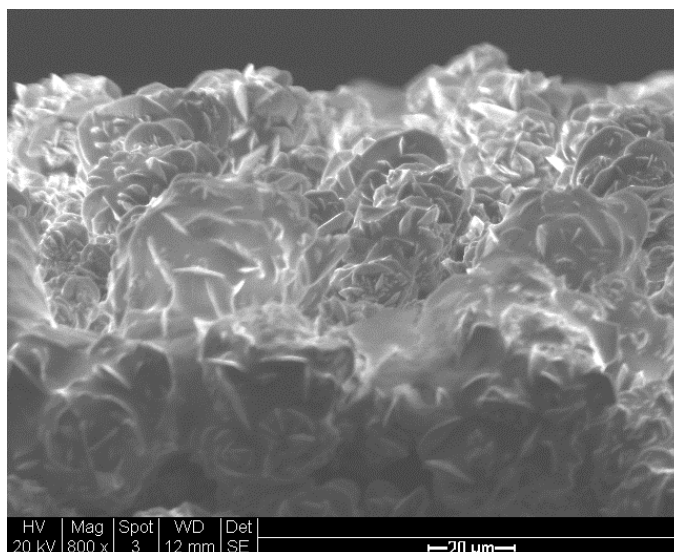


Figure 6-6 : Cross sectional view of the Cu deposit on stainless steel substrate by applying  $4.7 \times 10^{-3} \text{ A/cm}^2$  from ethaline melt containing 0.2 M  $\text{CuCl}_2 \cdot 2\text{H}_2\text{O}$ . The deposition duration was 1800 s and RDE speed of 700 rpm at 25 °C

The obtained deposits were analysed using EDAX to determine the elemental composition and purity of the deposited metal. The EDAX analysis confirmed the presence of mostly metallic Cu in the obtained deposit with small amounts of chlorine and carbon. The obtained EDAX spectrum is shown in fig. 6-7. The inclusion of chlorine and carbon (2%) within the deposit could have proceeded from the co-reduction of the ethaline melt.

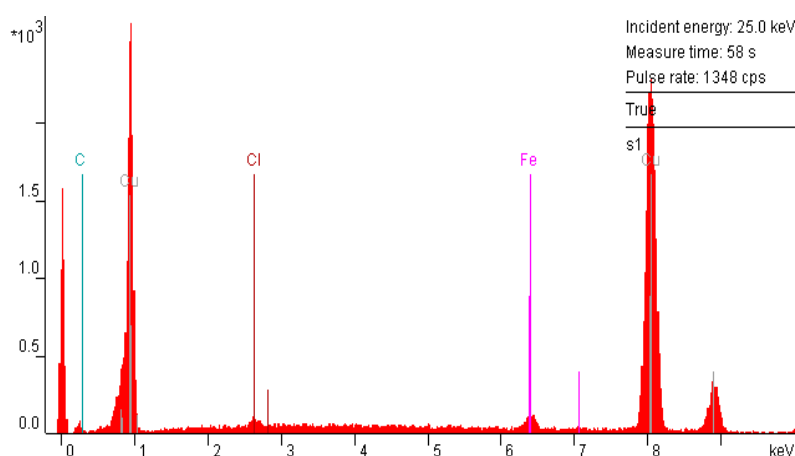


Figure 6-7 : EDAX spectra of the Cu deposit on stainless steel substrate by applying  $4.7 \times 10^{-3} \text{ A/cm}^2$  from ethaline melt containing 0.2 M  $\text{CuCl}_2 \cdot 2\text{H}_2\text{O}$ . The total deposition time was 3600 s and RDE speed of 700 rpm at 25 °C

The crystalline structure of the electrodeposited Cu films from the ethaline melt was characterized by X-Ray diffraction (XRD) experiments. The XRD pattern along

with corresponding (hkl) value for each of the peak obtained for the deposit is shown in the figure 6-8. The pattern corresponds to the face centered cubic Cu phase <sup>[22]</sup>. Except the Cu peaks, few other peaks were determined for Fe-Cr <sup>[23]</sup> and PTFE, those were due to the influence from substrate surface.

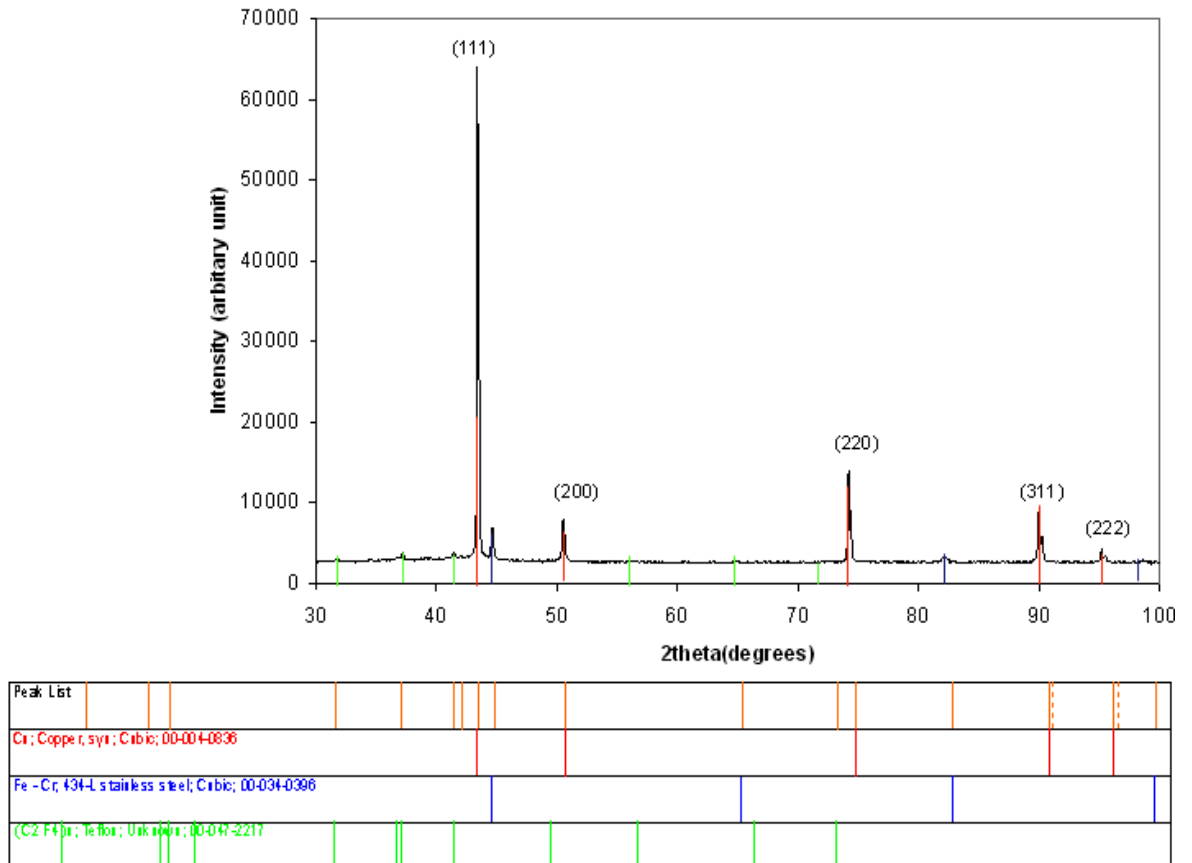


Figure 6-8 : XRD pattern of the Cu deposit on stainless steel substrate by applying  $4.7 \times 10^{-3} \text{ A/cm}^2$  from ethaline melt containing 0.2 M  $\text{CuCl}_2 \cdot 2\text{H}_2\text{O}$ . The deposition duration was 3600 s and RDE speed of 700 rpm at 25 °C, [—]Cu, [—]Fe-Cr, [—]PTFE

For powder Cu sample the ratio of intensity (in %) for (111) : (200) : (220) : (311) : (222) peaks are obtained as 100: 46 : 20 : 17 : 5 <sup>[22]</sup>. In case of deposited Cu from ethaline melt, the ratio of the above mentioned peaks were obtained as 100 : 12 : 21 : 13 : 6. Thus the obtained XRD pattern corresponds to polycrystalline structure with mostly (111) orientation. Similar crystalline structure was obtained for Cu deposit obtained from aqueous electrolytes <sup>[10,24]</sup> and deposits from ethaline melt <sup>[12]</sup> with and without additives. However XRD pattern obtained from reline melt, the peak at (200) showed equal intensity as the peak in (111) <sup>[13]</sup>.

Figure 6-9 is showing the individual (111), (220), and (311) peaks which have formed doublets, these are high intense peaks as shown in fig. 6-8. This was due to presence of  $K\alpha_1$  and  $K\alpha_2$  components in incident and diffracted beams from Cu source

[25]. According to Bragg's law the relationship [25] between the positions of the diffraction peaks of the doublets is shown in the equation below,

$$\frac{\sin \theta_1}{\lambda_{K\alpha_1}} = \frac{\sin \theta_2}{\lambda_{K\alpha_2}} \quad (6.1)$$

The intensities of the two peaks related as,

$$I_{K\alpha_1} : I_{K\alpha_2} = 2 : 1 \quad (6.2)$$

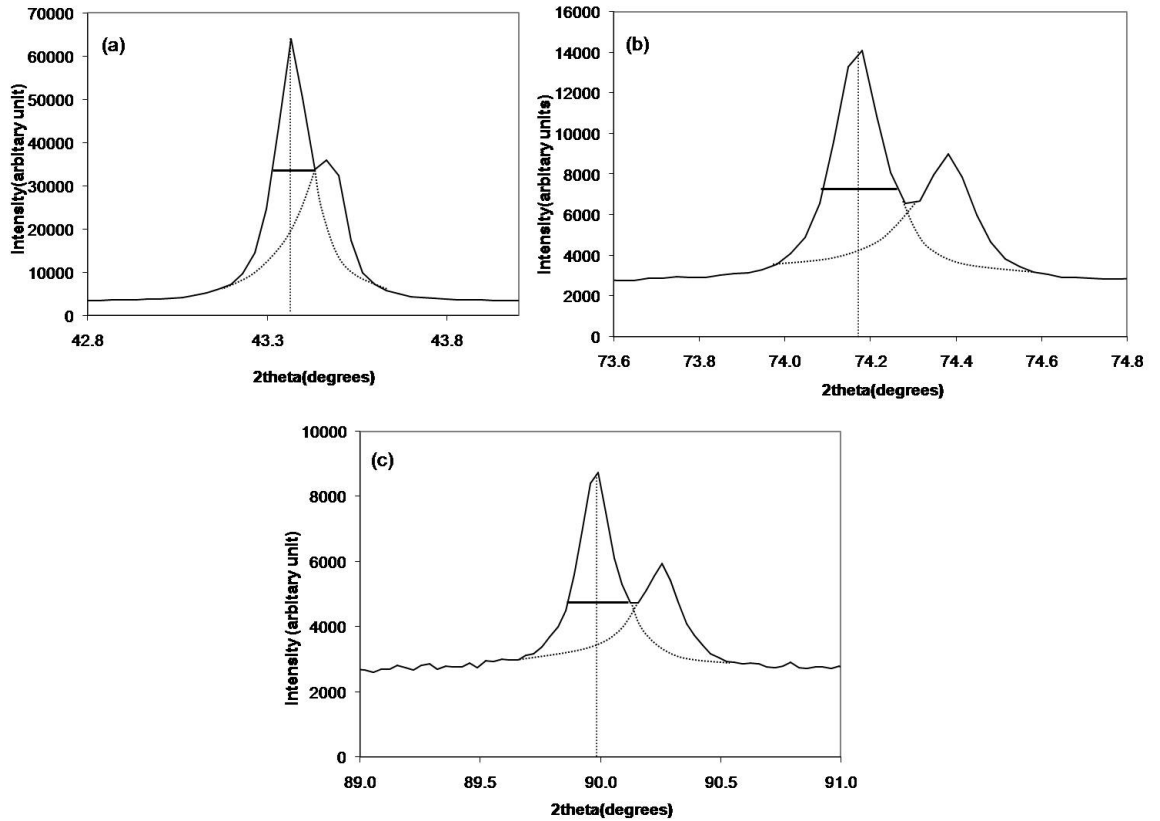


Figure 6-9 : Zoomed peaks from XRD pattern as shown in fig. 6-8 which were used for grain size calculation [a] (111), [b] (220), [c] (311)

According to fig. 6-9, for (111), (220), and (311) peaks the values of  $\theta_1$  are  $21.68^\circ$ ,  $37.09^\circ$  and  $44.95^\circ$  for wavelength of ( $\lambda_{K\alpha_1}$ )  $1.540 \text{ \AA}$  and  $\theta_2$  are  $21.73^\circ$ ,  $37.19^\circ$ ,  $45.13^\circ$  for wavelength of ( $\lambda_{K\alpha_2}$ )  $1.544 \text{ \AA}$ . These peaks are shown in fig. 6-9, the obtained value for  $\sin\theta_1/\lambda_{K\alpha_1}$  is  $0.52\pm0.07$  and the obtained value for  $\sin\theta_2/\lambda_{K\alpha_2}$  value is  $0.45\pm0.1$ . The intensity ratio equation is obtained as 1.7:1.

The grain size or crystallite size of the material was determined using the Scherrer formula [26] presented previously in eqn. 2.40 and shown below,

$$D' = \frac{0.9\lambda}{\beta' \cos \theta} \quad (6.3)$$

Where  $D'$  = grain size or crystallite size,  $\beta'$  = full line broadening at the half of the maximum intensity (FWHM),  $\lambda$  = x-ray wave length. For grain size calculation most intense peaks such as (111), (220), and (311) were used. The crystalline size of the deposit was determined from the line broadening of the high intense peaks in figure 6-8 and the zoomed version is presented in figure 6-9. The value of the crystalline size was determined as  $66 \pm 10$  nm. The crystalline size of electrodeposited Cu from aqueous electrolyte was reported in the range of  $115 \pm 15$  nm<sup>[27]</sup> and ultra-fine grained Cu was in the range of  $120 \pm 20$  nm<sup>[28]</sup>.

There is a possibility of strain formation within the deposit due to number of defects in the deposit. The strain contribution to the line broadening was determined by Williamson-Hall method<sup>[29]</sup>. The line broadening from XRD measurement, as shown in figure 6-9, was used to calculate the strain in the deposit. The relationship between crystalline size, strain and line broadening is represented previously in equation and shown below,

$$\varepsilon = \frac{\beta'}{\tan\theta} - \left( \frac{\lambda}{D'} \times \frac{1}{2\sin\theta} \times 0.9 \right) \quad (6.4)$$

The strain value was determined using same peaks used for grain size calculation and the obtained value from eqn. 6.4 was  $0.0022 \pm 0.0007$ .

The strain value for Cu films deposited by electroless method was obtained as  $0.0028 \pm 0.0002$ <sup>[30]</sup>. In case of continuous  $0.8 \mu\text{m}$  thick Cu film with random grain orientation obtained by d.c. magnetron sputtering on Si wafers showed the strain values as  $0.0018 \pm 0.0002$ <sup>[31]</sup>. For ultrafine-grained Cu samples, the reported strain value was  $0.0013 \pm 0.0007$ <sup>[28]</sup>. These reported strain values were obtained using similar peaks as mentioned for grain size calculation of figure 6-8.

### 6.3. Electrodeposition of Sn

It was clear in the previous chapter on electrochemical behaviour of Sn deposition that the reduction of Sn took place from  $\text{Sn}^{2+}$  to  $\text{Sn}^0$ . As the reduction process changes with increase in metal ion concentration, thus to deposit Sn within mass transfer controlled region the hydrated  $\text{SnCl}_2$  should be  $<0.7$  M in ethaline melt.

#### 6.3.1. Potentiostatic deposition

For potentiostatic deposition, Sn was deposited using  $0.05$  M  $\text{SnCl}_2 \cdot 2\text{H}_2\text{O}$ . The experimental potential was in the range of  $-0.5$  V to  $-0.6$  V for a time span of  $600$  s to

3600 s. The RDE speed was maintained at 700 rpm and the bath temperature was chosen as 25 °C. Among all the potentials applied for deposition, a potential of -0.6 V was observed to produce a homogeneous deposit. Typical Sn deposit on stainless steel substrate for various durations is shown in fig. 6-10. The silvery white colour of the deposit indicates metallic Sn. However, with increase in duration for deposition the deposit quality deteriorates. At duration of 60min, a very rough deposit was obtained as shown in fig. 6-10(B).

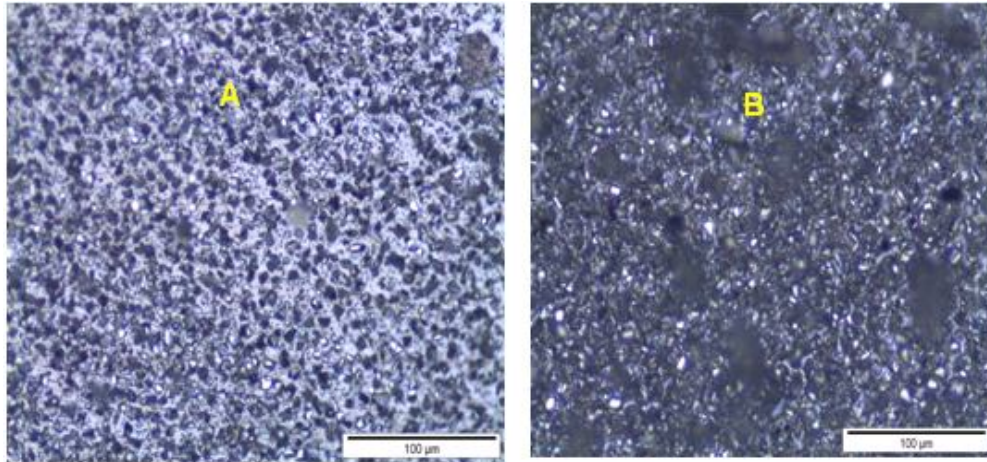


Figure 6-10 : Deposit obtained on stainless steel RDE from ethaline melt containing 0.05 M  $\text{SnCl}_2 \cdot 2\text{H}_2\text{O}$  by applying -0.6 V and the RDE speed was 700 rpm, at 25 °C, (A) 10 min, (B) 60 min

### 6.3.2. Galvanostatic deposition

The potentiostatic deposition in mass transfer limited zone showed homogenous deposits in a shorter duration. Thus for galvanostatic deposition mass transfer limit zone was chosen. For the galvanostatic deposition, experiments were carried out at varied current density of range  $1.57$  to  $4.7 \times 10^{-3} \text{ A/cm}^2$  for duration of 600 to 7200 s. The RDE speed was maintained as 700 rpm and deposition temperature was 25 °C. The best smooth and shiny deposit was obtained at an applied current density of  $1.57 \times 10^{-3} \text{ A/cm}^2$  which is 76% of the mass transfer limiting current ( $i_L$ ). A typical Sn deposit obtained at varying current density is shown in fig. 6-11. During deposition the potential was determined at -0.6 V.

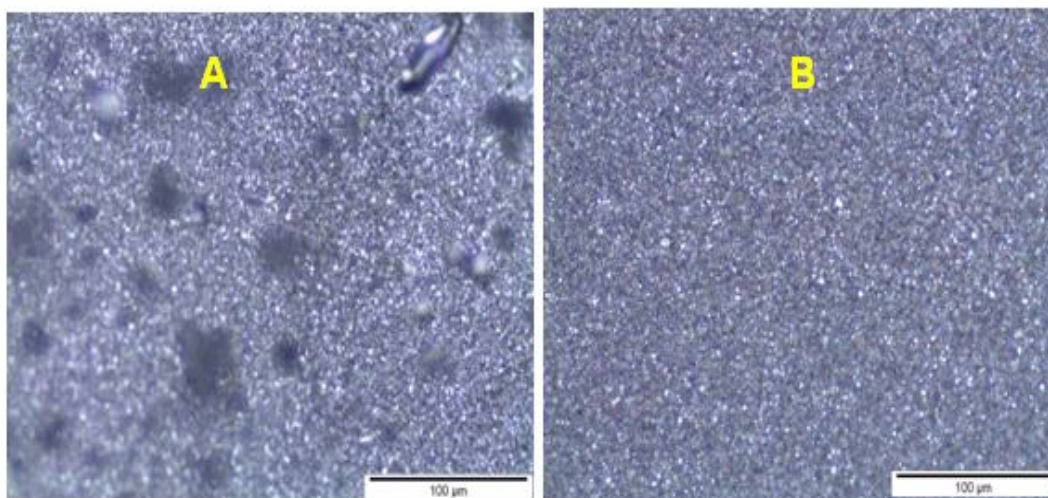


Figure 6-11 : Deposit obtained on stainless steel RDE from ethaline melt containing 0.05 M  $\text{SnCl}_2 \cdot 2\text{H}_2\text{O}$  by applying constant current and the RDE speed was 700 rpm, at 25 °C, 1800 s, (A)  $4.7 \times 10^{-3} \text{ A/cm}^2$ , (B)  $1.57 \times 10^{-3} \text{ A/cm}^2$

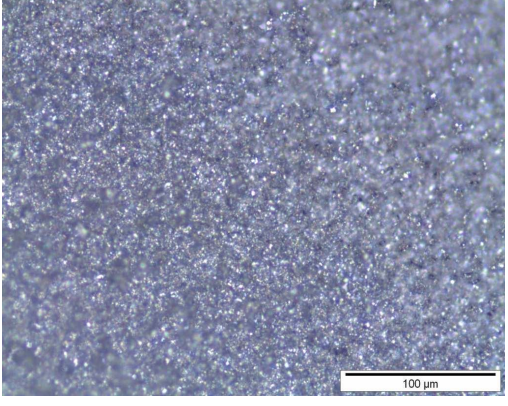
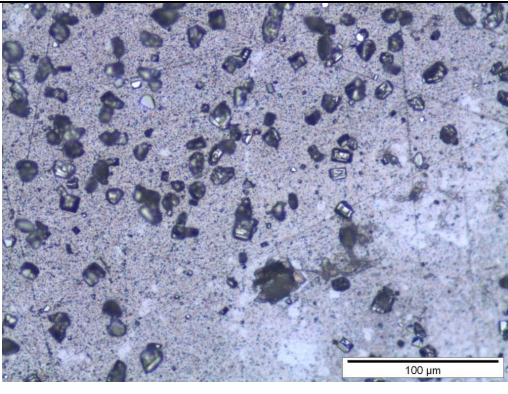
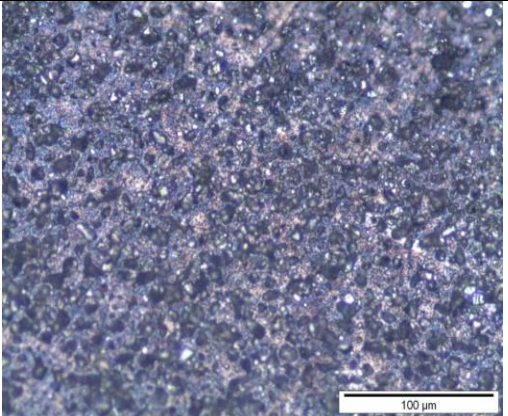
The other parameters like RDE speed was maintained in the range of 700 to 1300 rpm and bath temperature were maintained in the range of 25 to 45 °C. The deposit obtained by variation of these parameters is shown in table 6.2. For deposition in mass transfer region, with increase in RDE speed or temperature leads to increase in limiting current for deposition. It was observed that smooth and shiny deposits were obtained at higher temperature or RDE speed with the increase in the applied current density as was expected.

The deposit growth rate was  $(0.1 \pm 10\%) \mu\text{m}/\text{min}$  in the galvanostatic method and the deposit thickness increased without compromising deposit quality. The deposits obtained at various durations are included in the appendix A.7. The growth rate in the aqueous electrolytes was reported as 0.35 to 0.43  $\mu\text{m}/\text{min}$  <sup>[32-33]</sup>. This growth rate is 3 to 4 times higher than the growth rate obtained in ethaline melt. The deposit from ethaline melt showed similar compact structure which compares well against aqueous electrolytes <sup>[32-36]</sup>. The deposit obtained from other IL was needle-type dendritic as reported in literature previously <sup>[12,37]</sup>.



ELECTRODEPOSITION OF INDIVIDUAL METALS

Table 6.2 : Deposition as obtained by varying different parameters like current density and rotation speed of RDE for galvanostatic Sn deposition, scale in the deposit showing 100  $\mu\text{m}$

Other parameters	Varying parameter		Obtained deposit	Comments
0.05 M using 700 rpm for 600 s by $1.57 \times 10^{-3}$ A/cm <sup>2</sup>	Temperature (°C)	25		Very smooth and shiny deposit as obtained
		45		smooth but very thin deposit as obtained, like the substrate surface
0.05 M for 600 s at 25 °C using $1.57 \times 10^{-3}$ A/cm <sup>2</sup>	Rotation speed (rpm)	1300		smooth but very thin deposit as obtained, as the substrate surface

For Sn current efficiency was calculated by gravimetric method and the obtained value was  $84 \pm 3\%$ . The current efficiency was also obtained from the deposit thickness and the obtained value was  $95 \pm 2\%$ . The current efficiency values varied with

measuring methods which was not seen for Cu. This variation might be due to the porous nature of the deposits. The porous structure might be due to inclusion of other elements formed from the cation of the electrolyte. It is likely to form choline base which later react with chlorine formed at the anode surface and formation of other chlorinated product at the anode <sup>[5]</sup>. The efficiency value for the deposition process in aqueous electrolyte was obtained as 75-95% <sup>[16, 38-39]</sup> and in the other IL electrolyte ranges in between 82% to 100% <sup>[12, 40-41]</sup>.

### 6.3.3. Long term deposition experiments

Several deposition experiments were carried out from a single electrolyte bath to investigate the aging characteristics of the bath. For these experiments, electrodeposition was carried out by galvanostatic method using same electrochemical parameters as determined previously and reported in the section 6.3.2. In a time span of one month total 40 numbers of experiments were carried out, with a total of 37 hrs of deposition. During these experiments approximately 0.010 moles of Sn<sup>2+</sup>, corresponding to a thickness 249 μm of metal was deposited out from a single electrolyte. The observed values of the cell voltage at start and end of these experiments are presented in the table 6.3.

Table 6.3 : Long term experiments for Sn deposition

Type of anode	Metal deposited out Moles/(μm)	Duration of operation (hours)	Cell potential vs. Ag wire (V)
Pt mesh	0.010/249	37	1.60
			1.95

Similar to Cu deposition experiment, during this long term plating test variation in current efficiency or deposit morphology was not observed in the deposition processes. Thus for Sn deposition this bath is reasonably stable. However, similar to Cu experiments for few cases fluctuation in cell potential was observed and the obtained deposits showed low current efficiency when concentration of the Sn<sup>2+</sup> was depleted. To regain the previous deposit morphology and high current efficiency additional hydrated SnCl<sub>2</sub> was added in the old solution to increase the metal content of the electrolyte. The colour change of the used electrolyte could not be examined with respect to the solution freshly prepared as it was a colourless liquid. In addition a white slimy deposit was obtained on the anode surface which was not observed during Cu

plating. An EDAX analysis showed mainly Cl content along with some other element like C and O. This product can be assumed as an outcome of the anodic reaction after decomposition of the electrolyte itself.

#### 6.3.4. SEM, EDAX and XRD measurements on deposited Sn

The morphology of the obtained Sn deposit was analysed through its cross sectional view as presented in fig. 6-12. The cross-sectional view showed that the growth of the metallic grains in the entire length was not uniform. The grains formed near to the substrate surface were small in size and as the deposit thickness increases the grain size was found to be bigger too. In a deposit thickness of 10  $\mu\text{m}$  dendrites were obtained as shown in fig. 6-12. The dendrite in the surface increases with increase in deposit thickness. It might be an effect of the high chloride concentration of the electrolyte [42]. The dendrite formation might be favoured by chloride of the electrolyte which introduces anisotropy among the various crystallographic directions. This high chloride concentration of the electrolyte also influences the grain size and density of growth nuclei [42]. This type of dendritic growth was also reported when Sn was deposited from HCl-SnCl<sub>2</sub> electrolyte [43]. The grain size near the surface was obtained as 300 nm.

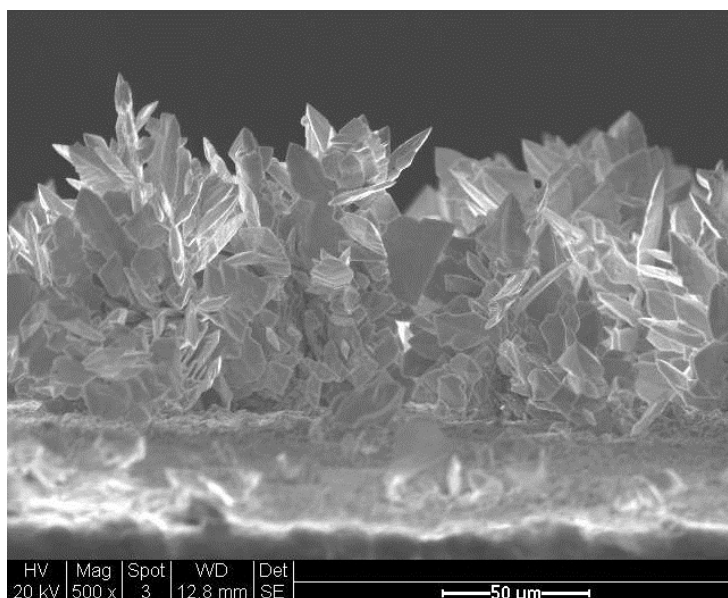


Figure 6-12 : Cross sectional view of the Sn deposit on stainless steel substrate by applying  $1.57 \times 10^{-3} \text{ A/cm}^2$  from ethaline melt containing 0.05 M SnCl<sub>2</sub>.2H<sub>2</sub>O . The total time of deposition was 3600 s and RDE speed of 700 rpm at 25 °C

Similar to the Cu study for elemental composition analysis was carried out using EDAX measurement. The EDAX analysis confirmed about the presence of mostly Sn with very small amount of Cl (<2 wt%) in the deposit. The obtained EDAX

spectrum for the deposit is shown in fig. 6-13. The Cl in the EDAX spectrum might have originated from reduction of the ethaline melt itself. One of the important aspect that the EDAX analysis did not showed any C in the deposit, as was found in Cu deposits. This might be an influence of low applied current density range with respect to Cu deposition currents.

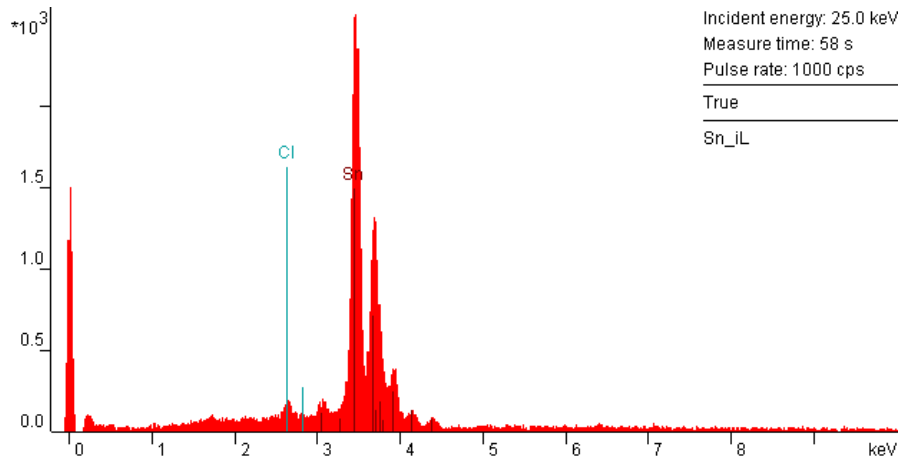


Figure 6-13 : EDAX spectra of the Sn deposit on stainless steel substrate by applying  $1.57 \times 10^{-3} \text{ A/cm}^2$  from ethaline melt containing 0.05 M  $\text{SnCl}_2 \cdot 2\text{H}_2\text{O}$  . The deposition duration was 3600 s and RDE speed of 700 rpm at 25 °C

The XRD pattern along with corresponding (hkl) value for each of the peaks for the Sn deposit obtained by galvanostatic method is shown in the fig. 6-14. The pattern corresponds to the tetragonal structure and is very similar to the patterns shown for powder Sn <sup>[44]</sup>. Except the Sn peaks, few other peaks for Fe-Cr <sup>[23]</sup> and PTFE were obtained from substrate surface.

For powder Sn the ratio of intensity (in %) for most intense peaks such as (200) : (101) : (220) : (211) : (112) : (321) : (312) peaks are mentioned as 100: 90 : 34 : 74 : 23 : 20 : 20 <sup>[44]</sup>. In case of Sn deposited from ethaline melt the ratio of the above mentioned peaks are obtained as 100 : 89 : 32 : 35 : 17 : 14 : 13. Thus the obtained XRD pattern corresponds to polycrystalline structure with mostly (200) texture. The XRD pattern of the deposit obtained from aqueous electrolytes showed (101) <sup>[32,45]</sup>, (220), (200) <sup>[34]</sup> or (112) <sup>[33]</sup> orientation, which are different from this case.

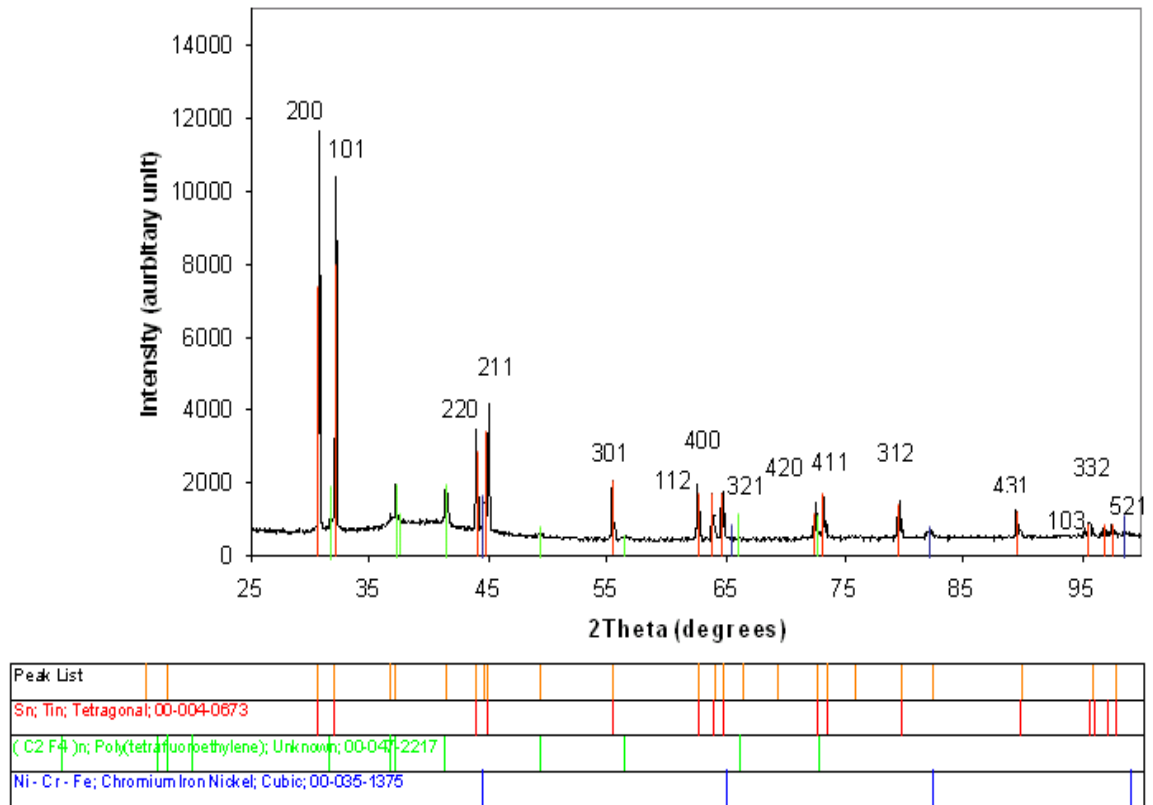


Figure 6-14 : XRD pattern of the Sn deposit on stainless steel substrate by applying  $1.57 \times 10^{-3} \text{ A/cm}^2$  from ethaline melt containing 0.05 M  $\text{SnCl}_2 \cdot 2\text{H}_2\text{O}$ . The total deposition time was 3600 s and RDE speed of 700 rpm at 25 °C, [—]Sn, [—]Fe-Cr, [—]PTFE

Similar to Cu XRD pattern, fig. 6-15 is showing the individual (101), (220), and (211) peaks have formed doublets, the highest peaks taken from fig. 6-14. Similarly this can be due to presence of  $K\alpha_1$  and  $K\alpha_2$  components in incident and the corresponding diffracted beams from Cu. According to Braggs' law the relationship <sup>[25]</sup> between the positions and intensities of the diffraction peaks of the doublets is shown in the equation 6.1 and 6.2.

Thus for (101), (220), and (211) peaks the values of  $\theta_1$  are 16.08°, 21.97° and 22.49° and  $\theta_2$  are 16.11°, 22.02°, 22.54° respectively, and  $\lambda_{K\alpha_1}$  is 1.540 and  $\lambda_{K\alpha_2}$  is 1.544. These peaks as shown in fig. 6-15, the obtained value for  $\sin\theta_1/\lambda_{K\alpha_1}$  and  $\sin\theta_2/\lambda_{K\alpha_2}$  fulfils value expected from eqn. 6.1 and the ratio of these values obtained as 1.07 :1. The intensity ratio ( $I_{K\alpha_1} : I_{K\alpha_2}$ ) determined from eqn. 6.2 is obtained as 1.8 :1 which also fulfils the expected value of eqn. 6.2.

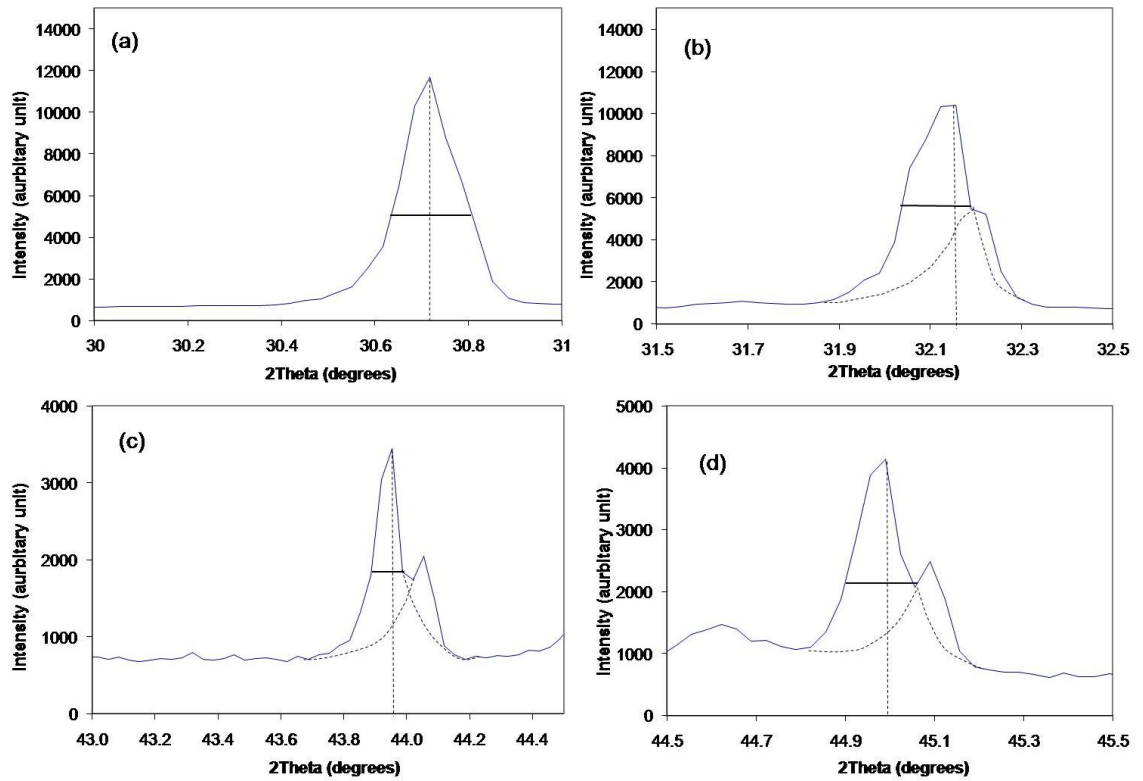


Figure 6-15 : Zoomed peaks from XRD pattern as shown in fig. 6-14, which were used for grain size calculation for the Sn deposit [a] (200), [b] (101), [c] (220), [d] (211)

The grain size or crystallite size of the material was also determined using the Scherrer formula <sup>[26]</sup> shown in eqn. 6.3. Here grain size was calculated using intense peaks such as (200), (101), (220), (211). The crystalline size of the deposit was determined from the line broadening of these peaks of fig. 6-14 and presented in zoomed version as 6-15. The value of the crystalline size was determined as  $62 \pm 10$  nm. The crystalline size of electrodeposited Sn from aqueous electrolyte was reported to be in the range of 50 to 400 nm <sup>[33-35]</sup>.

Similar to Cu crystalline structure strain is expected in Sn crystalline structure also. The strain value was determined from the line broadening from XRD measurement, as shown in figure 6-15. The strain value was determined using eqn. 6.4. The strain value was determined using same peaks used for grain size calculation and the obtained value is  $0.0031 \pm 0.0007$ . This strain value could not be compared with the strain value of deposited Sn by other methods or deposit obtained from aqueous electrolytes, this was not reported in the literature by the other researchers.

#### 6.4. Discussion

For Cu and Sn, the reduction for both metals are mass transfer controlled, thus the maximum plating current for the individual metal was fixed by agitation rate and metal ion concentration in ethaline melt. Moreover, during deposition metal ion concentration and agitation rate should be maintained carefully, as these parameters have significant effect on the obtained deposit.

It is important to compare the plating current achievable in this melt vis-à-vis an aqueous plating system containing similar amount of individual metals. For a 0.2 M  $\text{CuCl}_2$ , operating at a rotation speed of 700 rpm, a mass transfer limiting current of 0.15  $\text{A/cm}^2$  is calculated based on a diffusion coefficient of  $6.0 \times 10^{-6} \text{ cm}^2/\text{s}$  [46], and a viscosity of 0.01  $\text{cm}^2/\text{s}$ . In case of Sn, the solution containing 0.05M  $\text{SnCl}_2$  having diffusion coefficient of  $6.5 \times 10^{-6} \text{ cm}^2/\text{s}$  [47] the mass transfer limiting current was calculated as 0.04  $\text{A/cm}^2$ . The mass transfer limiting current value for both the metal is  $10^{-1}$  to  $10^{-2}$  higher in magnitude than that achieved in this ethaline melt. This was due to the high viscosity and low diffusivity of the both the metals in ethaline melt. Thus the plating rates of both the individual metals at room temperature from an ethaline to be  $10^{-1}$  to  $10^{-2}$  times lower than those achieved for aqueous electrolytes. The obtained plating rate showed, the value in the ethaline melt is only 3 times lower than the value in aqueous electrolyte.

The EDAX analysis indicated that the deposited Cu showed 2% C and Cl content and in Sn there is 1.5% Cl. This may be due to the breakdown of the ethaline melt itself which occurs below -0.7 V. However, low currents were observed at lower cathodic potentials, *i.e.* at  $\sim -0.3$  V. Since the Cu and Sn deposition proceeds at a potential below -0.4 V, the C and Cl detected in the deposits are likely to be the ethaline melt breakdown products.

For Cu the grain size, as observed in the micrograph was small, approximately 100 to 200 nm. The grain size did not get larger as the deposit grows which indicates the continuous generation of new nuclei during the electrodeposition process. This may be due to the co-reduction of carbon along with copper which may block the further grain growth. This may be a reason for smaller crystallite size in comparison to those obtained from aqueous electrolyte. However for Sn the crystalline size increases with deposit thickness and this size was very similar with the crystalline size obtained from aqueous electrolyte. Moreover C was not detected from EDAX measurements. These all supports the different nucleation of Sn with respect to Cu in ethaline melt.

In order to achieve a long term stable plating process, an electrolyte which is stable for long periods of time is required. The long term plating experiments showed that the individual metals such as Cu and Sn could be deposited at room temperature

from ethaline electrolyte containing various metal salts, although there may be some degree of co-reduction of the electrolyte itself. In addition to this if the metal ion concentration is maintained at its highest limit, the plating parameters and deposit characteristics remain constant, as observed for both metals Cu and Sn. To maintain the metal ion concentration during this long term plating for both cases metal salt was added externally or soluble anode was used in case of Cu. As a result water, glycol and metal content of these electrolytes might vary which leads to changes in electrolyte and this can have influences on the decomposition of the choline itself or the anodic reactions.

### 6.5. Conclusion

From the above results and discussion it is clear that,

- Smooth and homogeneous Cu deposits were obtained at  $4.71 \times 10^{-3}$  mA/cm<sup>2</sup> (78%*i<sub>L</sub>*) from ethaline melt containing 0.2 M CuCl<sub>2</sub>·2H<sub>2</sub>O. Smooth and homogeneous Sn deposits were obtained at 1.57 mA/cm<sup>2</sup> (76%*i<sub>L</sub>*) from ethaline melt containing 0.05 M SnCl<sub>2</sub>·2H<sub>2</sub>O. These deposits were obtained at 25 °C using RDE speed of 700 rpm by galvanostatic method for both metals.
- The growth rate for Cu deposition was  $0.15 \pm 10\%$  μm/min and for Sn deposition was  $0.1 \pm 10\%$  μm/min. The efficiency for Cu process was evaluated as  $95 \pm 5\%$ . For Sn deposition, the efficiency value was obtained as  $84 \pm 3\%$ . The XRD analysis confirmed the pattern of the deposit corresponds to the face centred cubic copper phase and the crystalline size of the deposit was obtained as  $66 \pm 10$  nm. For Sn the crystalline pattern matched to tetragonal structure with crystallite size of  $62 \pm 10$  nm. Each of these deposit contain strain values as  $0.0022 \pm 0.0007$  for Cu and  $0.0031 \pm 0.0007$  for Sn.
- Several deposition processes were carried out for one month long from a single electrolyte bath to evaluate the maximum deposition limit of this bath. For these measurements, the deposition of individual metal Cu and Sn was carried out at 25 °C. The equivalent metal deposited out from one electrolyte bath was in the range of 200 to 250 μm with high cathodic efficiency and quality from each deposition experiments. So these baths are stable for several metal deposition processes.



## Reference :

1. S. Z. Abedin, A. Y. Saad, H. K. Farag, N. Borisenko, Q. X. Liu and F. Endres (2007) *Electrochimica Acta*, 52 : 2746-2754.
2. I. B. Assaker and M. Dhahbi (2011) *Journal of Molecular Liquids*, 161 : 13-18.
3. T. -I. Leong, Y. -T. Hsieh and I. -W. Sun (2011) *Electrochimica Acta*, 56 : 3941-3946.
4. M. -J. Deng, J. -K. Chang, T. -I. Leong, S. -W. Fang, P. -Y. Chen and I. -W. Sun (2009) *Electrochemistry*, 77(8) : 588-590.
5. K. Haerens, E. Matthijs, K. Binnemans and B. V. Bruggen (2009) *Green Chem.*, 11 : 1357-1365.
6. J. Mun, Y.S. Jun, T. Yim, H.Y. Lee, H.-J. Kim, Y.G. Kim, S.M. Oh (2009) *Journal of Power Sources*, 194 : 1068-1074.
7. D. Weingarh, I. Czekaj, Z. Fei, A.F.-Schmitz, P.J. Dyson, A. Wokaun and R. Kötz (2012) *Journal of The Electrochemical Society*, 159(7) : H611-H615.
8. M. C. Kroon, W. Buijs, C.J. Peters and G.-J. Witkamp (2006) *Green Chem.*, 8, 241-245.
9. T. Chowdhury, D.P. Casey and J.F. Rohan (2009) *Electrochem. Commun.*, 11 : 1203.
10. M. Hasan and J.F. Rohan (2010) *Journal of The Electrochemical Society*, 157(5) : D278-D282.
11. R. Walker and S.D. Cook (1980) *Surface Technology*, 11 : 189-203.
12. W. Yang, H. Cang, Y. Tang, J. Wang and Y. Shi (2008) *Journal of Applied Electrochemistry*, 38 : 537-542.
13. T. Tsuda, L. E. Boyd, S. Kuwabata and C. L. Hussey (2010) *Journal of The Electrochemical Society*, 157(8) : F96-F103.
14. S. Schaltin, N. R. Brooks, K. Binnemans and J. Fransaer (2011) *Journal of The Electrochemical Society*, 158(1) : D21-D27.
15. A. Popescu, V. Constantin, A. Cojocaru, M. Olteanu, O. Demindenko and K. Yanushkevich (2011) *Rev. Chim. (Bucharest)* 62(6) : 626- 632.
16. M. Schlesinger and M. Paunovic (eds.) (2000) *Modern Electroplating*, 4<sup>th</sup> ed. John Wiley and Sons, Inc . : 62-129, 258-260.
17. E. Olander, Electrochemical Products Inc., New Berlin, WI, <<http://www.epi.com/user/files/AlkalineCyanide-FreeCopperPlating.pdf>> [accessed date 31/5/2013].
18. A. P. Abbott, K. E. Ttaib, G. Frisch, K. J. McKenzie and K. S. Ryder (2009) *Phys. Chem. Chem. Phys.*, 11 : 4269-4277.

19. A. P. Abbott, G. Capper, D. L. Davies, R. K. Rasheed and P. Shikotra (2005) *Inorganic Chemistry*, 44 : 6497-6499.
20. A. P. Abbott, G. Capper, D. L. Davies, K. J. McKenzie and S. U. Obi (2006) *J. Chem. Eng. Data*, 51 : 1280-1282.
21. P. D. Vreese, N. R. Brooks, K. V. Hecke, L. V. Meervelt, E. Matthijs, K. Binnemans and R. V. Deun (2012) *Inorganic Chemistry*, 51: 4972-4981.
22. JCPDS reference code : 00-004-0836, T. Swanson (1953) *Natl. Bur. Stand. (U.S.)*, Cric. 539, I, 15.
23. JCPDS reference code : 00-034-0396, P. Foertsch (1983) Penn state Univ., University Park, PA, USA., *ICDD Grant-in-Aid*.
24. O. Chyan, T.N. Arunagiri and T. Ponnuswamy (2003) *Journal of The Electrochemical Society*, 150(5) : C347-C350.
25. V. K. Pecharsky and P. Y. Zavalij (eds.) (2008) *Fundamentals of Powder Diffraction and Structural Characterization of Materials*, 2<sup>nd</sup> ed. Springer : 266, 352-354.
26. P. Scherrer, *Göttinger Nachrichten Gesell.* 2 (1918) p 98. (as referred to in B. D. Cullity and S. R. Stock, *Elements of X-ray Diffraction* (2001) 3<sup>rd</sup> Ed. Prentice Hall Inc. : 167-171).
27. S.J. Skrzypek, W. Ratuszek, A. Bunsch, M. Witkowska, J. Kowalska, M. Goly, K. Chruściel (2010) *Journal of Achievements in Materials and Manufacturing Engineering*, 43 (1) : 264-268.
28. K. Zhang, I.V. Alexandrov, A.R. Kilmametov, R.Z. Valiev and K. Lu (1997) *J. Phys. D: Appl. Phys.*, 30 : 3008-3015.
29. G. K. Williamson and W. H. Hall (1953) *Acta Metallurgica* 1 : 22-31.
30. R. Brüning, B. Muir, E. McCalla, É. Lempereur, F. Brüning and J. Etzkorn (2011) *Thin Solid Films*, 519 : 4377-4383.
31. R. P. Vinci, E. M. Zielinski and J. C. Bravman (1995) *Thin Solid Films*, 262 : 142-153.
32. A. He, Q. Liu, D. G. Ivey (2008) *J Mater Sci: Mater Electron*, 19 : 553-562.
33. W. Zhang, J. Guebey and M. Toben (2011) *Metalfinishing*, 13.
34. T. Teshigawara, T. Nakata, K. Inoue and T. Watanabe (2001) *Scripta mater.*, 44 : 2285-2289.
35. N.M. Martyak and R. Seefeldt (2004) *Electrochimica Acta*, 49 : 4303-4311.
36. C.T.J. Low and F.C. Walsh (2008) *Surface and coating technology*, 202 : 1339-1349.
37. M. -J. Deng, T. -I. Leong, I. -W. Sun, P. -Y. Chen, J. -K. Chang and W. -T. Tsai (2008) *Electrochemical and Solid-State Letters*, 11(11) : D85-D88.

38. G. I. Medvedev, N. A. Makrushin and A.N. Dubenkov (2002) Russian Journal of Applied Chemistry, 75 (2) : 219-222.
39. B. N. Stirrup and N. A. Hampson (1977) Surface Technology, 5 : 429-462.
40. M. Morimitsu, Y. Nakahara, Y. Iwaki and M. Matsunaga (2003) Journal of Mining and Metallurgy, 39(1-2)B : 59-67.
41. X. -H. Xu and C. L. Hussey (1993) Journal of The Electrochemical Society, 140(3) : 618-626.
42. W. Shao and G. Zangari (2009) J. Phys. Chem. C, 113 : 10097-10102.
43. Z. Dobó, T. Kulcsár and T. Kékesi (2012) Materials Science and Engineering, 37/2 : 19-26.
44. JCPDS reference code : 00-004-0673, T. Swanson (1953) Natl. Bur. Stand. (U.S.), Cric. 539, I, 24.
45. Z. Kovac and K.N. Tu (1984) IBM J. Res. Develop., 28(6) : 726-733.
46. C. P. D. Leon and F. C. Walsh (2003) Trans. Inst. Met. Finishing., 81(5) : B95-B100.
47. C.T.J. Low and F.C. Walsh (2008) Surface and coating technology, 53 : 5280-5286.

## **Chapter 7: ELECTRODEPOSITION OF Cu-Sn ALLOY**

### 7.1. Introduction

With the help of electrochemical and electrodeposition parameters obtained from individual metals study, different electrochemical and electrodeposition parameters for alloy study can be estimated. Previous studies on alloy deposition in an IL system showed different factors will control the crystalline structure of the deposit. They are applied potential, metal composition in the electrolyte and deposition time <sup>[1-3]</sup>. It is worth mentioning that the substrate characteristics influenced the deposit morphology and adhesion property <sup>[3]</sup>. Depending on the substrate type, a matte or lustrous deposit was obtained. Though the uniformity and thickness of the deposit was determined by the initial amount of Cu atom which later controls the total amount of Sn atoms for deposition and this governs the intermetallic phases of the deposit <sup>[3]</sup>.

For Cu-Sn co-deposition from ChCl based ILs, the Cu concentration in the electrolyte controls the quality and composition of the Cu:Sn in alloy system as reported in ref. <sup>[4]</sup>. Interestingly at high current density copper rich or equimolar solution produced only pure Cu due to kinetically slower deposition of Sn phases <sup>[4]</sup>. The use of organic additive can change the morphology of the metallic grains and a dense and homogeneous alloy deposit was obtained <sup>[4]</sup>. Moreover the use of IL might resolve the difficulty of co-deposition of metals due to potential difference.

In this chapter results on electrochemical study and electrodeposition of Cu-Sn alloy deposition in ethaline melt is presented. The study on different physical, electrochemical and plating parameters obtained from individual metal study is used for alloy study. Preliminary experiments were carried out in Rota Hull cell to estimate the combination of metal ion concentration in the ethaline melt corresponding to the deposits. Later electrochemical characterisation and electrodeposition was carried out with the chosen electrolytes. Finally obtained deposits were analysed using standard materials analysis techniques.

### 7.2. Preliminary experiments

These experiments were based on the plating experiments carried out in the Rota-Hull cell. These experiments were carried out in ethaline melt containing 0.1 M  $\text{SnCl}_2 \cdot 2\text{H}_2\text{O}$  and 0.1 to 0.02 M  $\text{CuCl}_2 \cdot 2\text{H}_2\text{O}$ . The Cu-Sn alloy deposition from individual

metal in aqueous electrolyte is a normal co-deposition process [5]. Thus in ethaline melt Cu-Sn alloy system is expected to be a normal co-deposition process. Additionally the suitable deposition current obtained for individual metal deposition in the previous chapter was used for Rota Hull experiments for alloy deposition. However, the RDE speeds and RCE speeds were not the same numbers, so these two systems need to be connected. Using the mass transfer correlation for each system, the RDE speed can be co-related to the RCE speed. The correlation for RCE systems is shown in eqn. (3.13) and for RDE systems is shown in eqn. (3.12).

When,  $i_{L_{RDE}} = i_{L_{RCE}}$  and  $\omega_{RCE} = 600 \text{ rpm} = 10 \text{ rps}$

By comparing both the equations, it can be written as

$$0.079 \text{Re}_{RCE}^{0.65} = 0.623 \text{Re}_{RDE}^{0.5}$$

$$\text{Re}_{RCE} = 21.33$$

$$\therefore U_{RDE}^{0.5} = 1.52$$

$$\text{Or, } \omega_{RDE} = 221.3 \text{ rpm}$$

The applied current range for normal co-deposition, Cu-Sn alloy system was determined using eqn. 2.37.

$$i_{\text{Alloy}} = i_{\text{Cu}} + i_{\text{Sn}}$$

In the above mentioned concentration range,  $i_{\text{Cu}}$  was determined to be in the range of  $0.5$  to  $2.3 \times 10^{-3} \text{ A/cm}^2$  [determined by dividing the suitable current value obtained for  $0.2 \text{ M}$ , with the mentioned concentration range]. The  $i_{\text{Sn}}$  was determined to be  $3 \times 10^{-3} \text{ A/cm}^2$  [determined by multiplying the suitable current value obtained for  $0.05 \text{ M}$ , with the mentioned concentration range]. Thus the obtained  $i_{\text{Alloy}}$  range was determined as  $3.5$  to  $5.3 \times 10^{-3} \text{ A/cm}^2$  for RDE speed of  $700 \text{ rpm}$ . After converting the RDE speed to RCE speed, current density range for Rota Hull experiments was obtained as  $1$  to  $1.7 \times 10^{-3} \text{ A/cm}^2$ . Smooth uniform deposits from these electrolytes were obtained at  $0.66 \times 10^{-3} \text{ A/cm}^2$  using  $600 \text{ rpm}$ . These depositions were carried out for  $10800 \text{ s}$  to achieve reasonable thick deposits at  $25 \text{ }^\circ\text{C}$ . For deposition brass substrate was used as nucleation is easier on Cu or Cu alloys.

The obtained deposit along the cathode length for various combinations of individual metals is shown in the fig. 7-1. With increase in Sn content of the ethaline melt, powdery deposit was obtained. To analysis the Sn content of the deposit, the cathode length was divided into four different parts for an EDAX analysis. Then to determine the deposit thickness and deposit morphology of these sections, analysis on surface with optical microscope was also carried out. It was observed that with variation in Cu-Sn ratio in ethaline melt and applied current density, powdery deposits

were obtained. For EDAX analysis of these powdery deposits, the deposits were scratched out from the cathode length.

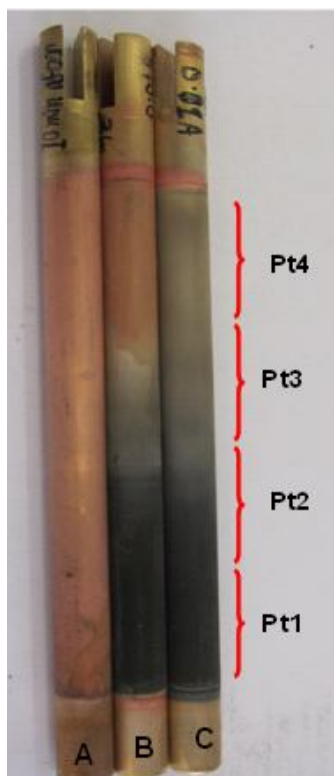


Figure 7-1 : The Cu-Sn alloy deposit along the brass cathode from ethaline melt containing various concentration of hydrated Cu and Sn salts, (A) 0.1 M  $\text{CuCl}_2 \cdot 2\text{H}_2\text{O}$  - 0.1 M  $\text{SnCl}_2 \cdot 2\text{H}_2\text{O}$ , (B) 0.04 M  $\text{CuCl}_2 \cdot 2\text{H}_2\text{O}$  - 0.1 M  $\text{SnCl}_2 \cdot 2\text{H}_2\text{O}$ , (C) 0.02 M  $\text{CuCl}_2 \cdot 2\text{H}_2\text{O}$  - 0.1 M  $\text{SnCl}_2 \cdot 2\text{H}_2\text{O}$ . The point 1-4 is showing the chopped sections for analysis with various current density, Pt1:  $2.5i_{\text{Avg}}$ , Pt2:  $1x_{\text{Avg}}$ , Pt3:  $0.3x_{\text{Avg}}$ , Pt4:  $0.15x_{\text{Avg}}$ , where  $i_{\text{Avg}}$  is current applied for deposition.

To examine the deposit morphology and thickness along the cathode length (as shown in fig. 7-1) at each chopped section is analysed by optical microscope. The obtained deposit thickness was converted to current values using Faradays law. The sample A showed entirely smooth and shiny deposits along the cathode length. EDAX analysis showed that the deposit only contains Cu throughout the entire cathode length. The thickness variation along the cathode length was not carried out for this electrolyte, as the produced deposits contain only Cu. Thus this electrolyte was discarded for further alloy deposition studies.

The EDAX analysis of sample B and sample C showed various combination of metal contained along the cathode length. For sample B, the Pt3 and Pt4 showed smooth film of thickness  $3 \mu\text{m}$  with Sn percentage in the range of 5 to 26 wt%. However, the deposit around point 1 and point 2 was powdery deposits containing 5 wt% of oxygen and 3 wt% of carbon content along with Cu and Sn. For sample C, Pt3 and Pt4 showed smooth film of thickness  $3 \mu\text{m}$  with Sn percentage of the deposit was

in the range of 11 to 23 wt%. The deposit at point 1 and point 2 showed powdery deposits containing oxygen of 8 wt% and carbon of 5 wt% along with Cu-Sn. At higher Sn content of the electrolyte (0.01 M  $\text{CuCl}_2 \cdot 2\text{H}_2\text{O}$  - 0.1 M  $\text{SnCl}_2 \cdot 2\text{H}_2\text{O}$ ) showed 80 wt% Sn content of the deposit. As the obtained deposit from this electrolyte was powdery, so this electrolyte was also discarded from further studies. Thus the electrolyte B and C was chosen for further electrochemical characterization and alloy deposition studies.

The EDAX analysis of sample B and sample C for the Pt3 and Pt4 showed presence of Zn (<3 wt%) along with Cu-Sn. The EDAX analysis of the brass substrate showed that it contains Cu:Zn as 59:41 wt%, thus an effect of Cu-Zn in the deposited alloy might be possible. With respect to deposited Cu:Sn, which is in the range of 75:23 wt%  $\pm$  4 wt%, Zn content is very small. Moreover the obtained Zn content appears to be within the error limit of this analysis. Therefore the Zn content was not considered for alloy analysis.

In case of deposition from aqueous electrolytes the proportion of Cu:Sn in the deposit was varied by varying the Cu:Sn in the electrolyte. For deposition from ethaline melt the Cu concentration was in the range of 0.02 M to 0.1 M. When the ethaline melt contains very little amount of Cu, <0.02 M  $\text{CuCl}_2 \cdot 2\text{H}_2\text{O}$  the Sn content in the alloy increases up to 86 wt%. However, the obtained deposits were mostly powdery. It was further observed that in a reasonable smooth and shiny deposit the Sn content in the alloy was obtained to be in range of 8 to 30 wt%, so achieving good quality alloy with higher Sn content was difficult.

The presence of Sn in smaller amount in the deposited alloy with respect to amount of Sn in the electrolyte might be due to the thermodynamic instability of the alloy system which could be resolved by a cathodic protection<sup>[6]</sup>. Due to the instability and displacement of the metal, the metal content in the alloy always remains in the lower range<sup>[6]</sup>. This displacement or corrosion of one metal in the alloy system was reported for Cu-Al alloy deposition from IL system<sup>[6-7]</sup>. For Cu-Al alloy system, it was very hard to achieve high Al content due to deposition of transition metal in mass-transport limited rate. The deposition of alloy especially along with a transition metal might suffer from the co-deposition mechanism of the alloy system<sup>[7]</sup>. At higher concentration of Sn like 0.1 M, the deposition process was kinetically controlled as observed in individual metal study of Sn. However the Cu deposition is mass transfer controlled for all concentrations so the reduction of one metal might not be in same speed with other metal.

Now the current values at these different points along cathode length was determined using Faradays law from the obtained deposit thickness value. The applied

current value for these individual metal composition combinations along the cathode length from individual electrolyte was estimated. This will help in deposition of alloy on RDE. The electrolyte B and C was chosen for further electrodeposition experiments with RDE, as this electrolyte gave a range of Cu:Sn. Before electrodeposition experiments, electrochemical characterisation was carried out to investigate Cu and Sn behaviour together in ethaline melt.

### 7.3. Electrochemical characterisation

#### 7.3.1. Voltammetry experiments

Voltammetry experiments were carried out in agitated conditions, as this condition was used for electrodeposition purpose. The fig. 7-2 is showing the voltammetry scans on ethaline melt containing 0.04 M  $\text{CuCl}_2 \cdot 2\text{H}_2\text{O}$  - 0.1 M  $\text{SnCl}_2 \cdot 2\text{H}_2\text{O}$  and 0.02 M  $\text{CuCl}_2 \cdot 2\text{H}_2\text{O}$  - 0.1 M  $\text{SnCl}_2 \cdot 2\text{H}_2\text{O}$ . Scans were carried out using Pt RDE as working electrode, Pt mesh as counter electrode and silver wire as the reference electrode. These experiments were with 220 rpm RDE speed at 25 °C and using a scan rate of 10 mV/s. These voltammetry scan was carried out in a scan range of +1 V to -1 V.

In fig. 7-2 the reduction steps can be noted in the forward sweep. The reduction process started at a potential of -0.34 V, where the current increased sharply until it reached a potential value of -0.5 V. After these reduction steps the current reaches its mass transfer limitation. The mass transfer limiting current of the process can be determined at a potential of -0.7 V. In the reverse sweep three clear stripping currents were observed. These stripping processes started at a potential of -0.5 V, -0.3 V and +0.3 V as marked by A, B and C in fig. 7-2.

To explain the behaviour of both metals together, voltammetry studies on ethaline melt containing similar concentration of individual metal study was carried out at similar conditions. The Sn behaviour at 220 rpm RDE speed, 25 °C for 0.1 M is presented in fig. 7-3. The voltammetry scans with different concentrations of Cu as mentioned above was carried out at 10 mV/s and the scans showed similar results with the scans mentioned in individual metal chapter and are included in the appendix A.8.



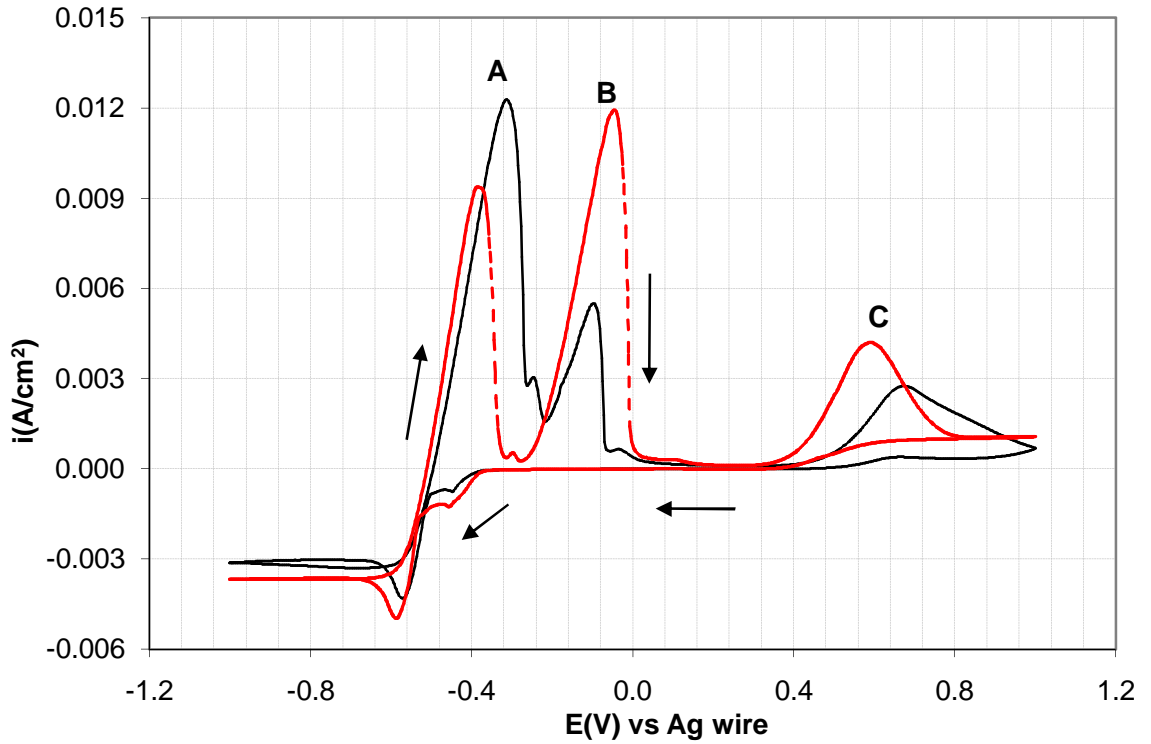


Figure 7-2 : Voltammetry on ethaline melt containing various concentration of Cu salt with constant concentration of Sn salt at Pt RDE with RDE speed of 220 rpm and the scan rate was 10 mV/s at 25 °C, (—) 0.02 M  $\text{CuCl}_2 \cdot 2\text{H}_2\text{O}$  - 0.1 M  $\text{SnCl}_2 \cdot 2\text{H}_2\text{O}$ , (---) 0.04 M  $\text{CuCl}_2 \cdot 2\text{H}_2\text{O}$  - 0.1 M  $\text{SnCl}_2 \cdot 2\text{H}_2\text{O}$

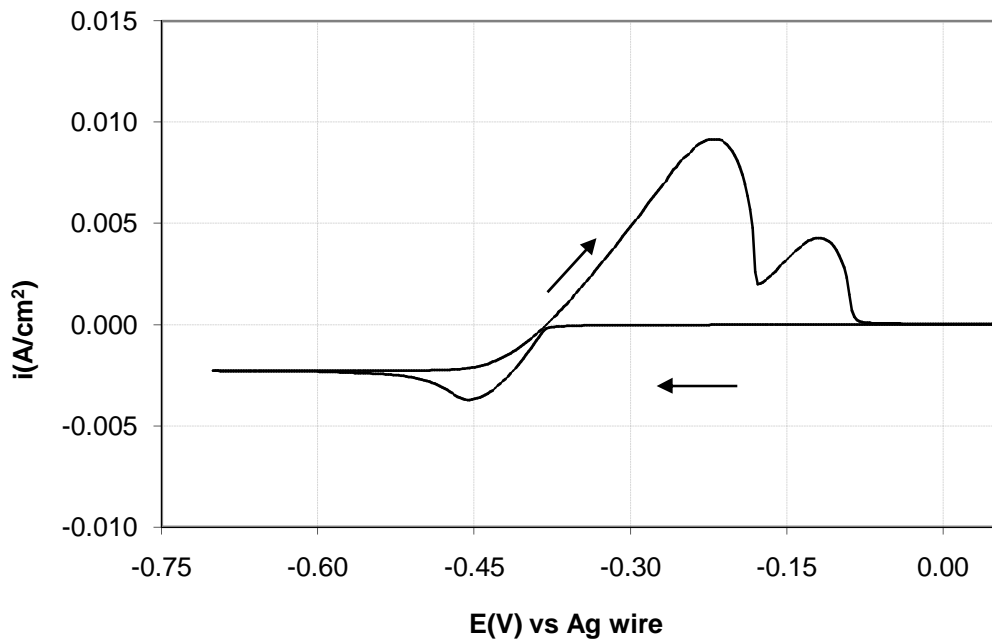


Figure 7-3 : Voltammetry on ethaline melt containing 0.1 M  $\text{SnCl}_2 \cdot 2\text{H}_2\text{O}$  at Pt RDE and rotation speed of the RDE was 220 rpm at 25 °C, scan rate 10 mV/s

When compared to individual metal voltammetry scans, formation of  $\text{Cu}_0$  and  $\text{Sn}_0$  commences beyond the potential of  $-0.35$  V. Thus the reduction steps obtained in the forward sweep could be due to the co-deposition of the both metals. During the Sn study, in reverse sweep two stripping steps were observed. One at a potential of  $-0.35$  V and another at a potential of  $-0.17$  V. For Cu, two stripping steps started to take place at potentials of  $-0.34$  V and  $+0.35$  V. Consequently the third stripping peak in fig. 7-2 might correspond to the second stripping peak of Cu. For the second stripping step of fig. 7-2, this could be due to the stripping process of both metals together. It was predicted according to the potential values in individual metal scans. However, the influence of Cu or Sn on the first stripping peak in fig. 7-2 was not clear. Thus anodic stripping voltammetry was carried out to investigate these different stripping peaks.

### 7.3.2. Anodic stripping voltammetry

To identify the metal combination of the voltammetry peaks anodic stripping voltammetry was carried out in two steps. For these experiments the deposition was carried out on the Pt surface and then the deposited surface was scanned in the anodic region in the potential range of  $-0.55$  V to  $1$  V using  $220$  rpm RDE speed at  $25$  °C, scan rate was  $10$  mV/s. The obtained voltammetry scans in this potential range for ethaline melt containing  $0.04$  M  $\text{CuCl}_2 \cdot 2\text{H}_2\text{O}$  -  $0.1$  M  $\text{SnCl}_2 \cdot 2\text{H}_2\text{O}$  is shown in fig. 7-4.

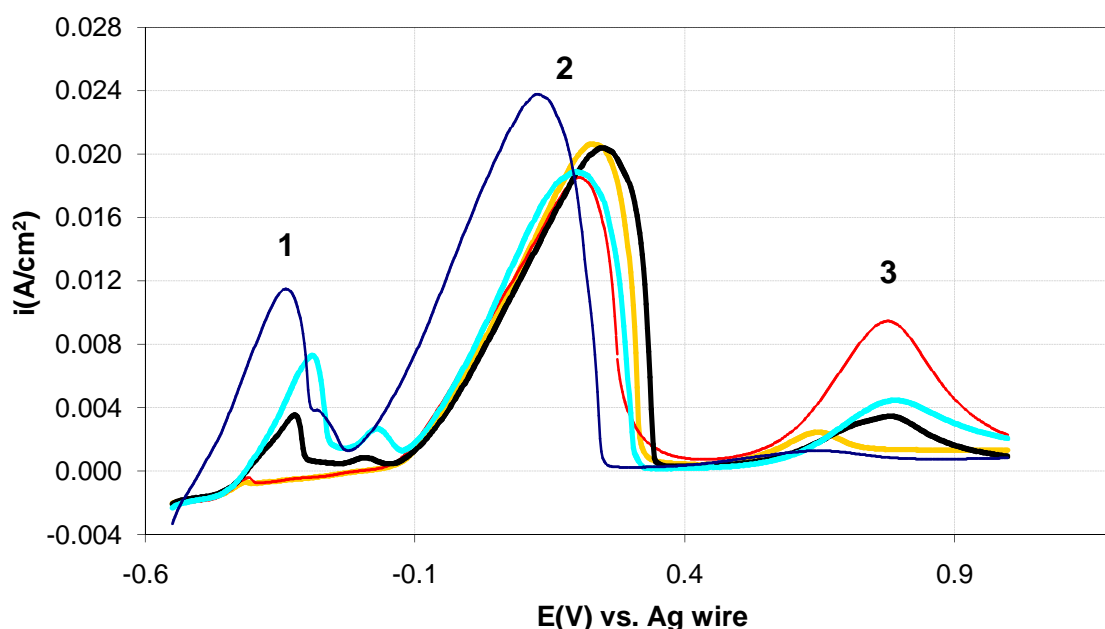


Figure 7-4 : Anodic stripping voltammetry with ethaline melt containing  $0.04$  M  $\text{CuCl}_2 \cdot 2\text{H}_2\text{O}$  -  $0.1$  M  $\text{SnCl}_2 \cdot 2\text{H}_2\text{O}$  at Pt RDE and RDE speed of  $220$  rpm at  $25$  °C, scan rate  $10$  mV/s, (—)  $0.33$  V, (—)  $0.36$  V, (—)  $0.4$  V, (—)  $0.45$  V, (—)  $0.5$  V

To identify the elements involved in different stripping steps, deposition was carried out for 3 to 10 min duration in the potential range of 0.33 V to 0.5 V and EDAX analysis was carried out on the deposits. The EDAX analysis showed that with an increase in applied potential, the carbon and oxygen content in deposit increased. The carbon content in deposit rose from a value of 5 to 20 wt%, from a potential of 0.45 V. From a potential of 0.4 V, oxygen was found along with carbon where the oxygen content varies in the range of 5 to 30 wt%. At a very high potential like 0.5 V, the chlorine content in the deposit increased upto 10 wt%. The quality of the deposit obtained from potential of 0.4 V starts to be rough and with increase in potential it turns to powdery. The Sn content of these deposits in the potential region of 0.35 V to 0.5 V was varied in the range of 16 to 26 wt%. The Cu content at high potentials like 0.5 V, showed a value of 25 wt%.

A comparison study was established with the voltammetry study of fig. 7-4 and element content obtained from EDAX analysis to understand the three different stripping steps of fig. 7-2. The charge values were calculated from each stripping step of fig 7-4. This calculated charge ratios of different stripping peaks from the voltammetry scans were compared with the EDAX ratios obtained for the Cu and Sn in the deposit. This comparison in the different potentials is presented in table 7.1.

Table 7.1 : Comparison of the charge ratios obtained from voltammetry scans and EDAX analysis

Potential (V)	Calculated charges for stripping peaks (C)			Ratio of peak charges (peak 2) / (peak1+peak3)	Ratio of Cu:Sn from EDAX
	Peak 1	Peak 2	Peak 3		
0.33	-	0.50	0.04	-	-
0.36	-	0.45	0.23	1:20	1:2.7
0.40	0.03	0.40	0.10	1:30	1:2.7
0.45	0.09	0.40	0.14	1:1.8	1:2.0
0.50	0.16	0.50	0.05	1:2.4	1:2.3

At a potential of 0.33 V the deposit contained only Cu, any trace from other elements was not found out. The voltammetry showed one very prominent stripping step which started at a potential of -0.2 V and another small stripping step which started at a potential of +0.4 V. The obtained deposit showed only Cu, so stripping steps could be assumed due to Cu in two steps. The charge values determined from

the stripping peaks 2 and 3 in this anodic voltammetry is likely to be due to the Cu content of the deposition. Thus other peaks 1 and 3 are likely to be due to fully or partially due to Sn content of the deposit.

For other potentials the obtained charge from different stripping peaks showed a match with the ratio obtained during EDAX. The differences in the ratio from charge calculation and EDAX analysis for 0.36 V potential could be due to Cu content of peak 3. As the charge content of peak 3 at potential 0.33 V was not zero. When this charge assumed to be due to Cu were subtracted, then the charge ratio matched with the ratio obtained in EDAX. Moreover, the differences in the values from the charge ratio and EDAX analysis could be due to the presence of other elements like C, O and Cl. Thus the stripping peak 1 and 3 of fig. 7-2 is likely to be for the Sn content in the deposit with influences of other elements and peak 2 is likely to be for Cu content in the deposit.

#### 7.4. Deposition experiments

##### 7.4.1. Potentiostatic deposition

Using potentials from anodic stripping voltammetry and Rota-Hull depositions, the potential range to achieve the smooth Cu-Sn film was estimated. For Cu-Sn alloy deposition by potentiostatic method, the applied potential range was estimated to be -0.34 V to -0.38 V for duration spans of 1800 s to 14400 s at 25 °C. The RDE speed was maintained to be 220 rpm as obtained during Rota-Hull experiments. For potentiostatic deposition on stainless steel RDE, the electrolytes were chosen as ethaline melt containing 0.04 M  $\text{CuCl}_2 \cdot 2\text{H}_2\text{O}$  - 0.1 M  $\text{SnCl}_2 \cdot 2\text{H}_2\text{O}$  and 0.02 M  $\text{CuCl}_2 \cdot 2\text{H}_2\text{O}$  - 0.1 M  $\text{SnCl}_2 \cdot 2\text{H}_2\text{O}$ . At potentials < -0.35 V, light pink deposits were obtained. At potentials > -0.36 V bluish powdery deposits were obtained. The smooth and uniform deposits were obtained at 0.36 V for 14400 s is shown in the fig. 7-5 (A). The growth rate was determined as 0.04  $\mu\text{m}/\text{min}$  and the deposit thickness increased without compromising deposit quality.

##### 7.2.1. Galvanostatic deposition

For galvanostatic deposition, the current values were obtained from the potential range used for Cu-Sn co-deposition. The current density was varied in the range of  $0.64 \times 10^{-3}$  to  $0.95 \times 10^{-3}$   $\text{A}/\text{cm}^2$  in a time span of 1800 to 14400 s. The experiments were carried out using the ethaline melt containing 0.04 M  $\text{CuCl}_2$  - 0.1 M  $\text{SnCl}_2$  with 220 rpm RDE speed at 25 °C. Smooth and homogeneous deposits were obtained at  $0.87 \times 10^{-3}$   $\text{A}/\text{cm}^2$  is shown in fig. 7-5 (B). At applied current >  $0.95 \times 10^{-3}$

A/cm<sup>2</sup> rough deposits were obtained. The growth rate was  $0.03 \pm 10\%$   $\mu\text{m}/\text{min}$  and the deposit quality was not compromised with increases in thickness.

Appearances of the deposits obtained by applying constant potential or current appeared to be different in colour which might be due different alloy composition in the applied condition. These deposits were visually homogeneous and uniform in nature. The deposit obtained from various aqueous electrolyte using same methods were obtained was homogeneous deposition [8-10].

Similar to individual metal analysis the current efficiency was calculated from the voltammetry scan and gravimetric method. The obtained efficiency from the voltammetry scan was 90%. The efficiency value determined from gravimetric method was  $92 \pm 3\%$ . These values were cross checked from thickness calculation using optical microscope. The obtained efficiency was  $93 \pm 3\%$ . In case of alloy deposition from aqueous electrolyte, the current efficiency value was obtained as 60-90% [11].

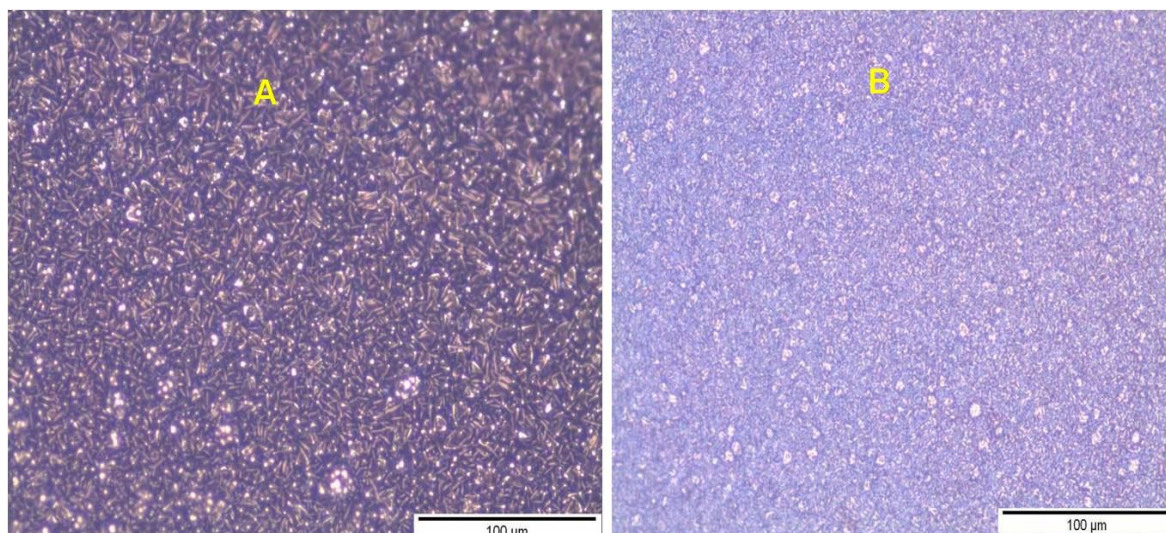


Figure 7-5 : Cu-Sn alloy deposits on stainless steel substrate from ethaline melt containing 0.04 M  $\text{CuCl}_2 \cdot 2\text{H}_2\text{O}$  - 0.1 M  $\text{SnCl}_2 \cdot 2\text{H}_2\text{O}$  electrolyte by applying constant potential or current. The RDE speed was maintained as 220 rpm at 25 °C for 14400 s. (A) 0.36 V, (B)  $0.87 \times 10^{-3} \text{ A}/\text{cm}^2$

## 7.5. Material property analysis of the deposited Cu-Sn alloy

### 7.5.1. SEM analysis of the as-deposited and annealed alloy

To characterise the growth and morphology of the alloy a cross sectional view other than top view of the deposit is presented in fig. 7-6. The cross-sectional view shows that the growth of the grains in the entire length i.e. along the deposit thickness is not uniform. The grains formed near to the substrate surface are very small and the grains increased in size as the deposit thickness increased. Long and large grains

formed from the small grains with increase in deposit thickness. The grain size of the smaller grains near the substrate surface was estimated as 140 nm and the average grain size of the big grains at the top most surface are estimated as 1  $\mu\text{m}$ . After annealing these smaller and larger grains size changed to 300 nm and 1.5  $\mu\text{m}$  respectively. The cross sectional view also shows some voids in the deposit which may be due to the rapid grain growth with increase in deposit thickness. With heat treatment these void size decrease as observed in fig. 7-6(B). These morphological studies were carried out with deposit obtained from ethaline melt containing 0.04 M  $\text{CuCl}_2 \cdot 2\text{H}_2\text{O}$  - 0.1 M  $\text{SnCl}_2 \cdot 2\text{H}_2\text{O}$ . The Cu-Sn layer obtained from other ILs at elevated temperatures like 120 to 140  $^\circ\text{C}$  showed crystallite size of 2-5  $\mu\text{m}$  as obtained from SEM images [2].

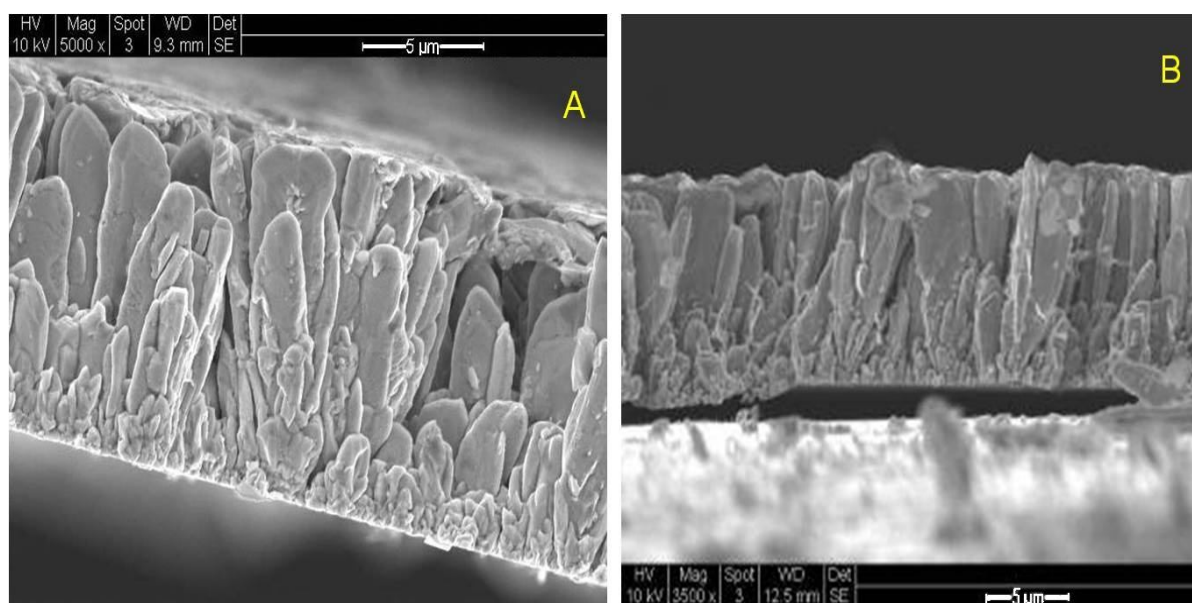


Figure 7-6 : Cross sectional view of the Cu-Sn alloy deposit on stainless steel substrate by applying  $0.87 \times 10^{-3} \text{ A/cm}^2$  from ethaline melt containing 0.04 M  $\text{CuCl}_2 \cdot 2\text{H}_2\text{O}$  - 0.1 M  $\text{SnCl}_2 \cdot 2\text{H}_2\text{O}$ . The deposition time was 14400 s and RDE speed of 220 rpm at 25  $^\circ\text{C}$ . The heat treatment was carried out at 400  $^\circ\text{C}$  for 30 min, to observe the changes in the morphology, (A) as-deposited sample, (B) annealed sample

#### 7.5.2. EDAX analysis of the as-deposited and annealed alloy

To analyse the metal content of the deposit from these solutions and the changes with heat treatment, EDAX were carried out on both the as deposited and annealed samples. The obtained EDAX spectrum for the as-deposited and annealed sample is shown in fig. 7-7.

The EDAX analysis confirmed the presence of Sn in the alloy deposit. For deposits obtained by applying 0.36 V vs. Ag wire, the Sn content was found to be  $25 \pm 1$  wt%. The deposits obtained by applying  $0.87 \times 10^{-3} \text{ A/cm}^2$ , the Sn content was  $22 \pm 5$

wt%. The presence of any other elements like C, O or Cl was not found along with Cu and Sn as indicated in the EDAX spectrum.

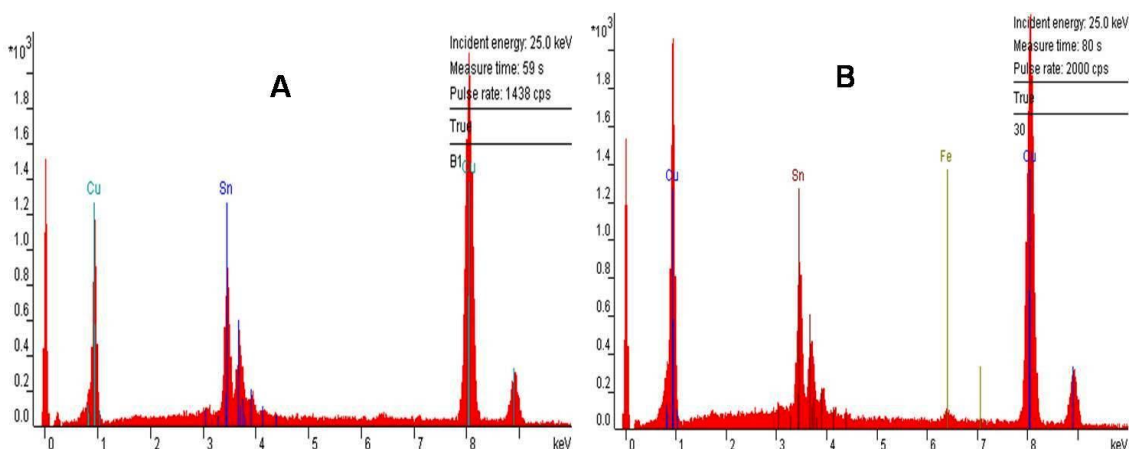


Figure 7-7 : EDAX spectrum of Cu-Sn alloy on stainless steel RDE from ethaline melt containing 0.04 M  $\text{CuCl}_2 \cdot 2\text{H}_2\text{O}$  - 0.1 M  $\text{SnCl}_2 \cdot 2\text{H}_2\text{O}$  by applying  $0.87 \times 10^{-3} \text{ A/cm}^2$ . The RDE speed was 220 rpm at 25 °C for deposition duration of 14400 s. (A) as deposited sample, (B) annealed sample

For potentiostatic deposition, the deposit obtained at potentials  $< -0.35 \text{ V}$ , EDAX showed 5 to 10 wt% of Sn and potentials  $< -0.34 \text{ V}$  showed only Cu in the deposits. At potentials  $> -0.36 \text{ V}$ , the deposit contains 10 to 15 wt% of oxygen. In case of galvanostatic deposition, the deposit at current density greater than  $0.95 \times 10^{-3} \text{ A/cm}^2$  showed oxygen content in the deposit.

For the annealed samples at 400 °C, the deposit analysis showed Sn-Cu content with very small amount of Fe ( $< 2\%$ ). After heat treatment the Sn content was found to decrease and obtained as  $23 \pm 1 \text{ wt}\%$ . It is appeared that some Fe atoms from substrate material was diffused in to the deposit by replacing the Sn content of the deposit. For annealing at higher temperatures like 600 to 730 °C the deposits suffered from 20 to 25 wt% of oxygen. At a lower temperature like 250 °C and for smaller duration like 10 min, any new changes in metal content of the deposit were not observed.

### 7.5.3. XRD analysis of the as-deposited and annealed alloy

#### 7.5.3.1. Analysis of the as-deposited alloy

The crystalline structure of the electrodeposited Cu-Sn alloy films from the ethaline melt was characterized by X-Ray diffraction (XRD). A typical XRD pattern of the deposit obtained from ethaline melt containing 0.04 M  $\text{CuCl}_2 \cdot 2\text{H}_2\text{O}$  - 0.1 M  $\text{SnCl}_2 \cdot 2\text{H}_2\text{O}$  is shown in fig. 7-8. The obtained pattern corresponded to the

orthorhombic  $\text{Cu}_3\text{Sn}$  crystalline structure<sup>[12]</sup>. Along with  $\text{Cu}_3\text{Sn}$  crystalline structure, few peaks were obtained for the hexagonal  $\text{Cu}_6\text{Sn}_5$  crystalline structure<sup>[13]</sup>. Other peaks were obtained for Fe-Cr and PTFE which may appear from the substrate surface.

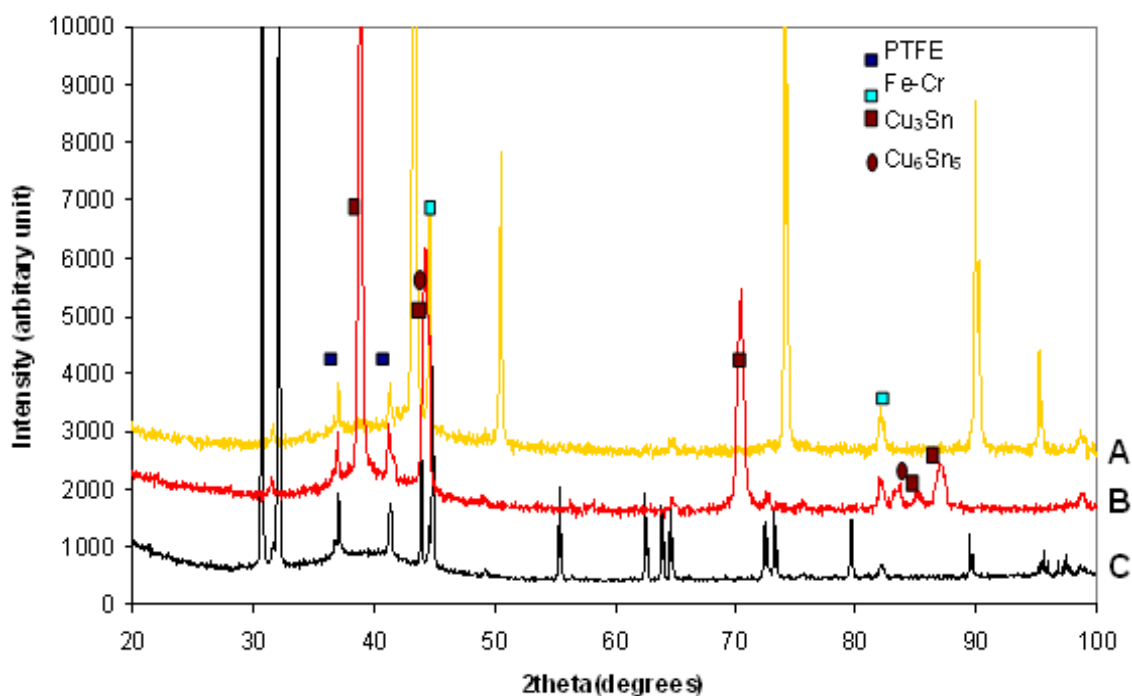


Figure 7-8 : XRD pattern of the as-deposited Cu-Sn alloy deposit on stainless steel substrate obtained from ethaline melt containing 0.04 M  $\text{CuCl}_2 \cdot 2\text{H}_2\text{O}$  - 0.1 M  $\text{SnCl}_2 \cdot 2\text{H}_2\text{O}$ , 220 rpm RDE speed at 25 °C for 14400 s, [A] Cu, [B] Cu-Sn, [C] Sn. The Cu and Sn XRD pattern was used to determine the presence of individual metals in the obtained alloy

The alloy deposits from aqueous electrolytes mainly consist of  $\text{Cu}_6\text{Sn}_5$  crystalline structure<sup>[14-16]</sup>. At elevated temperature > 100 °C, the  $\text{Cu}_6\text{Sn}_5$  crystalline structure is converted to  $\text{Cu}_3\text{Sn}$  crystalline structure by inter diffusion of the method and solid state reaction of the individual items. Thus crystalline structure was prominent in deposits from aqueous electrolyte after annealing process<sup>[14,16]</sup>. The XRD pattern of Cu-Sn layer obtained from other ILs at elevated temperatures like 120 to 140 °C showed various phases like  $\text{Cu}_6\text{Sn}_5$ ,  $\text{Cu}_3\text{Sn}$  and  $\text{Cu}_{10}\text{Sn}_3$  in one sample<sup>[2-3]</sup>.

In powder  $\text{Cu}_3\text{Sn}$  sample the ratio of intensity (in %) for (021) : (002): (121) : (231) : (331) peaks are shown as 70 : 100 : 100 : 70 : 70<sup>[12]</sup>. In case of deposited Cu-Sn alloy from ethaline the ratio of the above mentioned peaks are estimated from fig. 7-8 obtained as 100 : 12 : 35 : 15 : 10, which indicated that obtained XRD pattern corresponds to a structure with mostly (021) orientation.



The grain size or crystallite size of the material was determined using the Scherrer formula as shown in eqn 6.3. For grain size calculation most intense peaks such as (021), (121), and (231) were used. The crystalline size of the deposit was determined from the line broadening of the high intense peaks of figure 7-8 and in zoomed version as shown in figure 7-9. The value of the crystalline size was determined as  $21 \pm 10$  nm. The crystalline size of the electrodeposited Cu-Sn alloy was found in the range of 30-100 nm<sup>[17]</sup> when deposited from citrate bath.

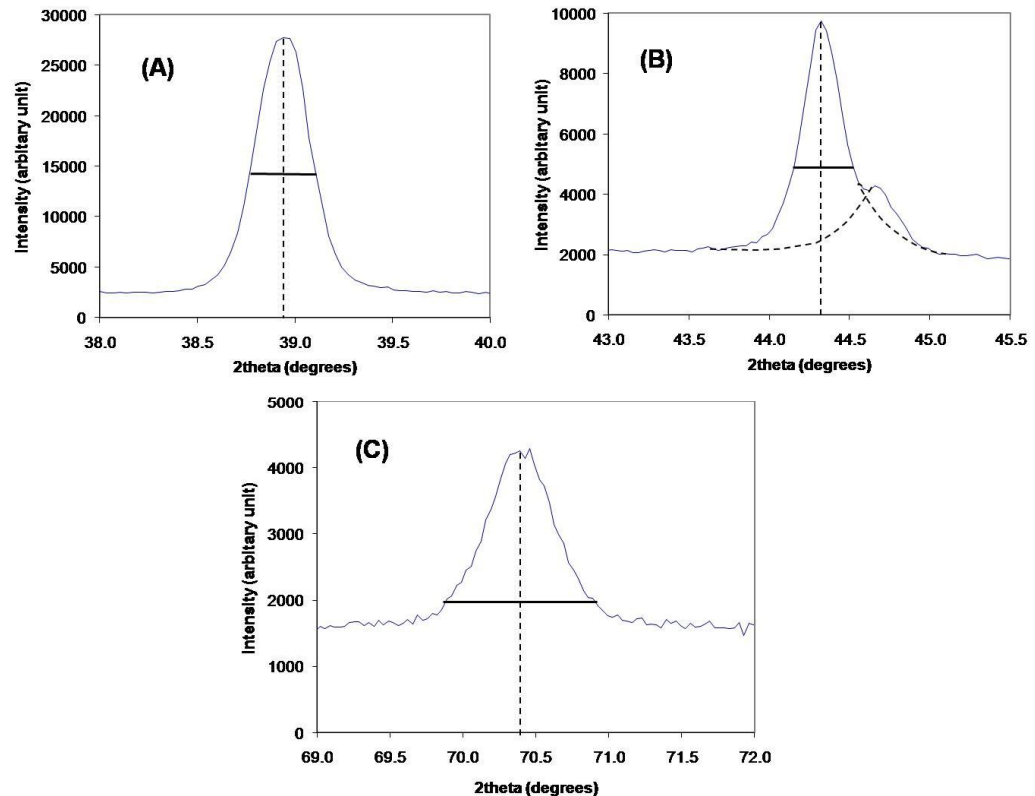


Figure 7-9 : Zoomed peaks from XRD pattern as shown fig. 7-8, which were used for grain size calculation for the Cu-Sn alloy deposit, [A] (021), [B] (121), [C] (231)

Figure 7-9 is showing the individual (121) peak have formed doublets. This might be due to presence of  $K\alpha_1$  and  $K\alpha_2$  components in incident as discussed during individual metal study<sup>[18]</sup>.

Smaller grain size of the crystalline structure indicated some defects in crystalline structure similar to individual metal study. This strain developed within the deposit was determined by calculating the line broadening and using Williamson-Hall equation<sup>[19]</sup>. The line broadening from XRD measurement, as shown in figure 7-9, was calculated to determine the strain in the deposit. The obtained strain value was  $0.0122 \pm 0.005$ , determined from the same peaks used for grain size calculation.

## 7.5.3.2. Analysis of the annealed alloy

Annealing was carried out at two different temperatures in two different durations, to determine the effect of heat treatment in the crystalline structure of the as-deposited alloy. For the annealed sample at 400 °C for 30 min, the XRD pattern of Cu-Sn alloy along with Cu and Sn XRD pattern is shown in the fig. 7-10.

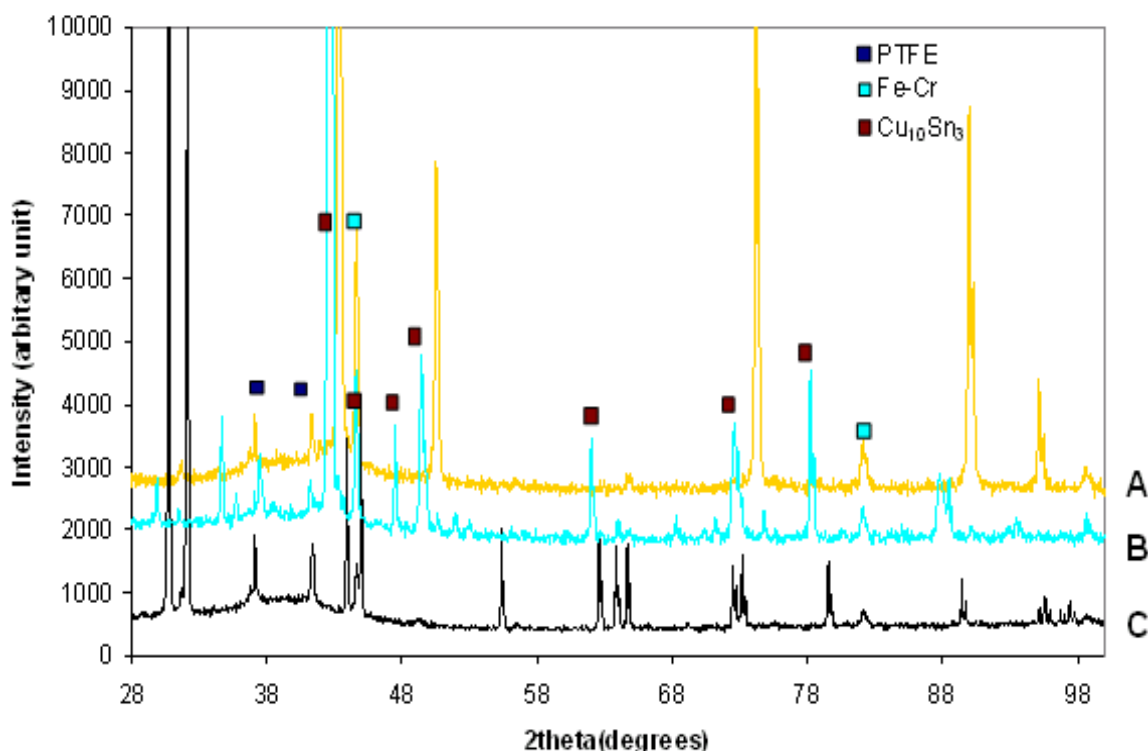


Figure 7-10 : XRD pattern of the annealed Cu-Sn alloy deposit on stainless steel substrate obtained from ethaline melt containing 0.04 M  $\text{CuCl}_2 \cdot 2\text{H}_2\text{O}$  - 0.1 M  $\text{SnCl}_2 \cdot 2\text{H}_2\text{O}$ . The RDE speed was 220 rpm at 25 °C for 14400 s. The annealing was carried out at 400 °C for 30 min, [A] Cu, [B] Cu-Sn, [C] Sn. The Cu and Sn XRD pattern was used to determine the presence of individual metals in the obtained alloy

Studies above indicated that crystalline structure of the annealed sample corresponds to the hexagonal  $\text{Cu}_{10}\text{Sn}_3$  crystalline structure<sup>[20]</sup>. A few other peaks from substrate material corresponding to Fe-Cr and PTFE were obtained. The pattern obtained for annealed deposit at 250 °C was similar pattern to the as deposited sample, included in the appendix A.9. It was observed that annealing at low range of temperature did not show any phase transformation. In this range of temperature the inter diffusion of Cu and Sn and the solid state reactions did not occurred.

For powder  $\text{Cu}_{10}\text{Sn}_3$  sample the ratio of intensity (in %) for (113) : (212): (104) : (220) : (402) : (412) : (330) peaks are shown as 100 : 45 : 40 : 10 : 10 : 40 : 80<sup>[20]</sup>. In case of annealed Cu-Sn alloy used for analysis, the ratio of the above mentioned

peaks in fig. 7-10 are obtained as 100 : 16 : 13 : 16 : 12 : 13 : 16. The obtained XRD pattern corresponds to  $\text{Cu}_{10}\text{Sn}_3$  polycrystalline structure with mostly (113) orientation.

The grain size or crystallite size of the material was determined using the Scherrer formula shown in eqn. 6.3. For grain size calculation most intense peaks such as (113), (212), (220) and (330) were used. The crystalline size of the deposit was determined from the line broadening of the high intense peaks shown in figure 7-10 and in zoomed version as figure 7-11. The value of the crystalline size was determined as  $77 \pm 50$  nm.

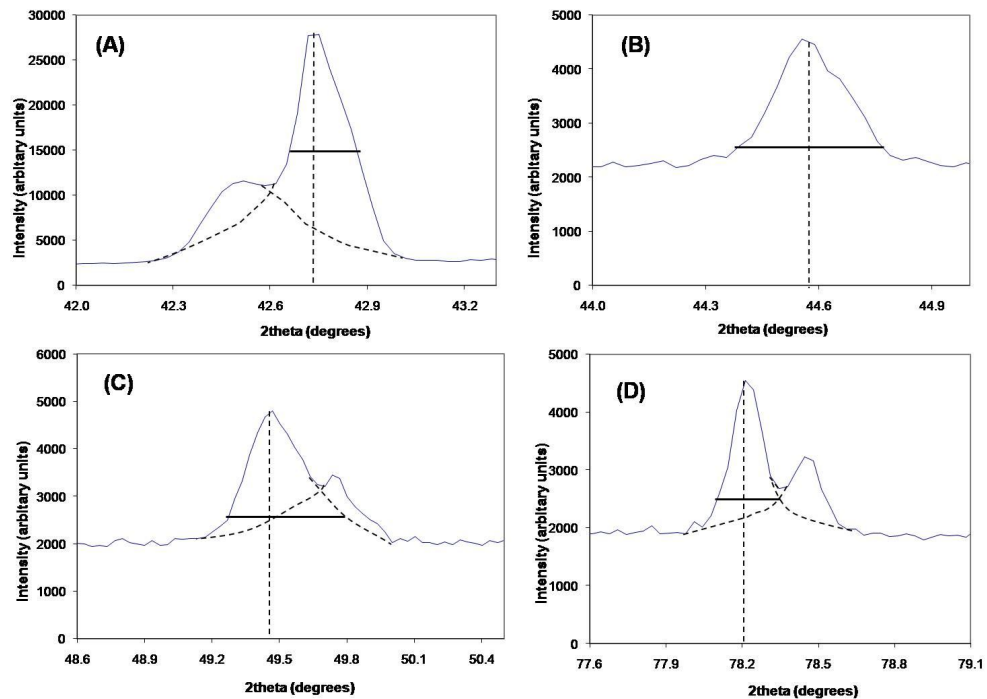


Figure 7-11 : Zoomed peaks from XRD pattern of the annealed sample as shown in fig. 7-10 which were used for grain size calculation for the Cu-Sn alloy deposit [A] (113), [B] (212), [C] (220), [D] (330)

Figure 7-11 is showing the individual (113), (220), and (330) peaks which have formed the doublets. Similar to individual metal study, this doublet formation is also explained by assuming the presence of  $K\alpha_1$  and  $K\alpha_2$  components in incident and diffracted beams from Cu source. For (113), (220), and (330) peaks the values of  $\theta_1$  are  $21.36^\circ$ ,  $24.74^\circ$  and  $39.11^\circ$  and  $\theta_2$  are  $21.24^\circ$ ,  $24.87^\circ$ ,  $39.23^\circ$  respectively, and  $\lambda_{K\alpha_1}$  is 1.540 and  $\lambda_{K\alpha_2}$  is 1.544. These peaks as shown in fig. 7-11, the obtained ratio of  $\sin\theta_1/\lambda_{K\alpha_1}$  vs  $\sin\theta_2/\lambda_{K\alpha_2}$  value is determined as  $0.96 \pm 0.05$ . The intensity ratio ( $I_{K\alpha_1} : I_{K\alpha_2}$ ) is obtained as 1.75 : 1. These values were matched with the values as expected from Bragg's law relationship between the positions of the diffraction peaks of the doublets and intensities [18].

Similar to all previous analysis Williamson-Hall method was used to estimate the change in strain with annealing process. Using the relationship between crystalline size, strain and line broadening the strain within the deposit was calculated using eqn. 6.4 mentioned earlier. The strain value was determined using same peaks used for grain size calculation and the obtained value is  $0.0059 \pm 0.002$ .

## 7.6. Bath stability for long term deposition

### 7.6.1. Bath stability without any deposition process

For long term metal deposition it is important to note the bath ageing property with time. This changes can easily be noted by visual observation of these bath containing different proportions of Cu:Sn in the electrolyte. The change in the electrolyte in the time span of 2 month is shown in fig. 7-12 when these electrolytes were not used for deposition experiments.

The colour change indicates that the property of the ethaline melt containing various concentrations of metal salts may have changed when it is kept for storage only. It can be due to formation different Cu – Sn network involving Cl, anion and cation of the ethaline melt. With variation in concentration, the water content in these electrolytes varies in the range of 8% to 13%. In case of Cu study it was reported that inclusion of water did not change the complexation unless water content exceeds 40% [21]. Thus the water content might have minimum effect on these electrolytes.

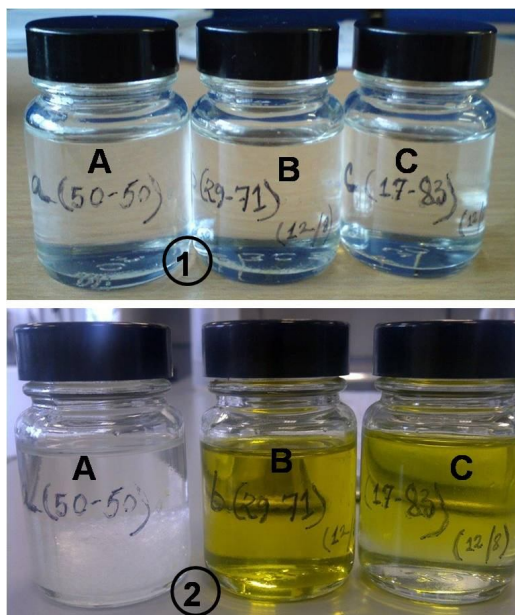


Figure 7-12 : The colour change in a time span of 2month, for ethaline melt containing various concentration of hydrated  $\text{CuCl}_2$  along with constant concentration of hydrated  $\text{SnCl}_2$ , (1) freshly prepared electrolyte, (2) after 2 month, when any deposition experiments was not carried out, [A] 0.1 M  $\text{CuCl}_2 \cdot 2\text{H}_2\text{O}$  – 0.1 M  $\text{SnCl}_2 \cdot 2\text{H}_2\text{O}$ , [B] 0.04 M  $\text{CuCl}_2 \cdot 2\text{H}_2\text{O}$  – 0.1 M  $\text{SnCl}_2 \cdot 2\text{H}_2\text{O}$ , [C] 0.02 M  $\text{CuCl}_2 \cdot 2\text{H}_2\text{O}$  – 0.1 M  $\text{SnCl}_2 \cdot 2\text{H}_2\text{O}$

To monitor these variations in terms of electrochemical parameters, a set of voltammetry scans were performed in a time span of two month on the single electrolyte bath. These scans showed the variations in the metal reduction potentials, limiting current and anodic stripping potential of the individual metals with time. For these scans, a Pt RDE used as working electrode, Pt mesh as counter electrode and silver wire were the reference electrodes. The RDE speed was maintained as 220 rpm similar to deposition experiments at 25 °C. The obtained voltammetry scans for this analysis is shown in fig. 7-13. Variation was observed in terms of limiting current and the stripping steps at potentials -0.2 V and -0.4 V, marked as peak A and B in fig. 7-13. After a period of four weeks a decrease in limiting current of the system and peak height was observed. These peaks A and B is responsible for Cu : Sn in the achieved deposits. Thus with time decrease in reducible species for metal deposition was observed.

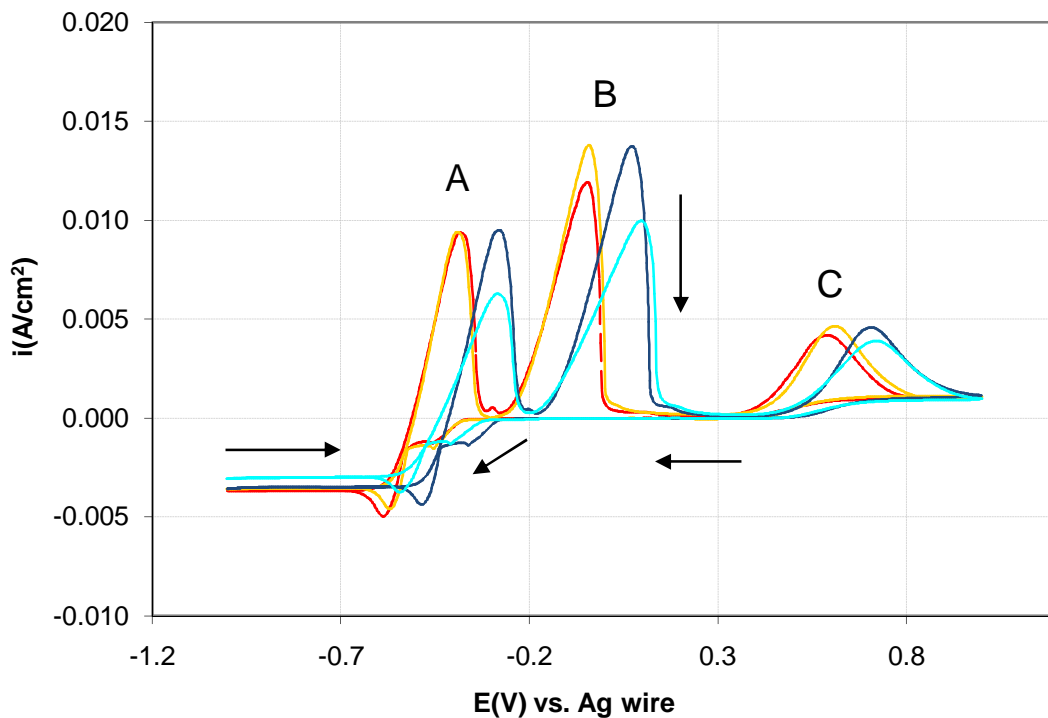


Figure 7-13 : Voltammetry for stability test on ethaline melt containing 0.04 M  $\text{CuCl}_2 \cdot 2\text{H}_2\text{O}$  - 0.1 M  $\text{SnCl}_2 \cdot 2\text{H}_2\text{O}$  at Pt RDE when any deposition experiments was not carried out. The RDE speed was maintained as 220 rpm and the scan rate was 10 mV/s at 25 °C, (—) after one week, (—) after two week, (—) after four week

#### 7.6.2. Bath stability after several deposition process

To examine the stability during long term use when a number of alloy deposition experiments were carried out using the same electrolyte. Plating was carried out by galvanostatic method using the same electrochemical parameters reported in section 7.3.1 and 7.3.2. From all separate experiments, in total 20 hrs of deposition

experiments were carried out. During these experiments 67  $\mu\text{m}$  of equivalent alloy was deposited out from the single electrolyte. The individual metal composition in the alloy deposit for the entire range was determined as 25% Sn - 75% Cu.

It was observed that the current efficiency, deposit morphology or individual metal combination remains relatively unchanged for few deposition processes. After these sets decrease in current efficiency and Sn percentage in the alloy was observed. Smooth and uniform deposits with higher current efficiency and previous alloy composition were obtained again when additional hydrated  $\text{SnCl}_2$  was added in the old solution to increase the metal content of the electrolyte. Thus the irregularity in the deposition process was due to the decrease in metal ion content which can be resolved by direct addition of metal salt to the IL and the stability of the electrolyte can be re-established. However, after three times of refilling, the electrolyte could not be used any more.

To monitor these changes from several deposition involved voltammetry scans were carried out in a defined interval after carrying out a certain number of deposition experiments as shown in fig. 7-14. For these voltammetry scans same electrochemical parameters and electrodes were used as mentioned in section 7.6.1.

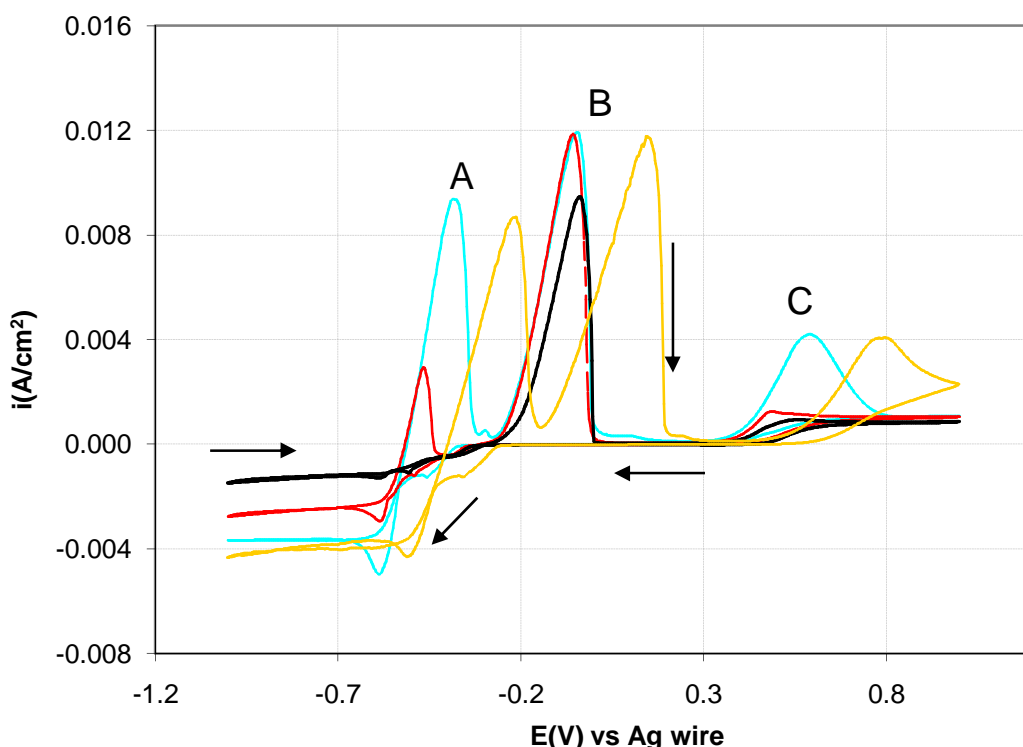


Figure 7-14 : Voltammetry for stability test on ethaline melt containing 0.04 M  $\text{CuCl}_2 \cdot 2\text{H}_2\text{O}$  - 0.1 M  $\text{SnCl}_2 \cdot 2\text{H}_2\text{O}$  at Pt RDE when several deposition experiments was carried out. The RDE speed was maintained as 220 rpm and the scan rate was 10 mV/s at 25 °C, (—) as prepared solution, (---) after few sets of depositions, (—) when alloy deposition was not possible , (—) after  $\text{SnCl}_2$  added in the used electrolyte

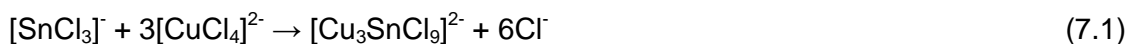
It was observed from the scans shown in fig. 7-14 that the stripping steps started at -0.55 V and +0.4 V, changed with deposition. The change could be noticed in terms of decrease in the peak height of peak A and B as shown in fig. 7-14. Any comparable change in the stripping step at -0.3 V peak with deposition was not observed. As only -0.4 V and +0.6 V peak or peak A and C as shown in fig. 7-2 is related to the achieved Sn content of the deposit, thus with decrease in peak height the Sn content of the deposit also decreases. When alloy deposition was not possible from the present electrolyte, then 0.1 M SnCl<sub>2</sub>.2H<sub>2</sub>O was added in the used electrolyte. From this electrolyte, alloy deposition was possible again and obtained deposits were of the same quality and composition of Cu-Sn. It was also evident in the voltammetry scan that with addition of Sn salt, the stripping peaks A and C regains its previous height.

### 7.7. Discussion

It was observed that the alloy composition in the deposit could not be controlled by the metal content in the electrolyte. Moreover it was not possible to achieve high Sn content in the deposit. It is clear from this observation that the alloy system is not following a normal co-deposition process. This behaviour of the alloy system in the ethaline melt might be explained by abnormal co-deposition process where deposition took place in a mixed potential region.

This could be due to formed complexes other than thermodynamic instability. From the Rota-Hull experiments and anodic stripping voltammetry, it is clear that Cu:Sn ratio in the deposit mostly present as 1:2.5. Moreover, XRD analysis showed a crystalline phase of Cu<sub>3</sub>Sn irrespective of the metal ion concentration in the electrolyte. Thus, it is expected to find Cu<sub>3</sub>Sn complex with chloride and choline in this system. It was reported previously for deposition of NiW alloy from citrate bath that the proposed complex matches the crystalline structure of the deposit [22-24]. Similar to the ternary complex for NiW systems, there is no such direct evidence on the formation of Cu-Sn complex in this mixed system. Due to the influence of the ligand of the system, decrease in Sn content in deposit might took place [22-23]. Again in case of aqueous electrolyte a different ligand for the formed complex is expected depending on the acid or alkali used for deposition along with the type of the metal ions used.

The Cu complex for reduction step Cu<sup>+</sup>/Cu<sup>0</sup> was found to be [CuCl<sub>4</sub>]<sup>2-</sup>. The Sn complexes [SnCl<sub>3</sub>]<sup>-</sup>, [Sn<sub>2</sub>Cl<sub>5</sub>]<sup>-</sup> for reduction step Sn<sup>2+</sup>/Sn<sup>0</sup> was present in the electrolyte as obtained from the individual metal study. Based on the individual metal complexes and the assumed mixed metal complex, the possible reaction in the mixed system is derived from the works of other researchers [24-26] and shown below :



This complex of the mixed system is shown in fig. 7-15.

During the electrolyte stability test for two month long, the ethaline melt containing various concentrations of Cu ions was observed closely which showed variation in the colour of the electrolyte. With variation in concentration, the water content in these electrolytes varies in the range of 8% to 13%. The water content was in the low range, so any effect from water content for complex formation might not be possible. Again when Cu and Sn were mixed in equal concentration, the electrolyte was unable to produce any alloy. The concentration of individual metal ions controls the complex formation and partial current for metal deposition [23-24]. Due to high concentration of Cu ions, very small amount of the above complex might have formed. As an outcome visual variation in the electrolytes was observed.

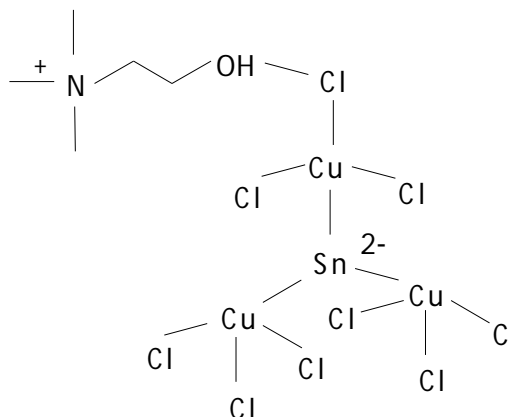


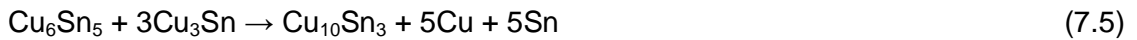
Figure 7-15 : Formed complex in mixed system containing Cu and Sn in ethaline melt

The Cu-Sn deposit from ethaline melt in crystallographic analysis showed mainly  $\text{Cu}_3\text{Sn}$  crystalline structure other than  $\text{Cu}_6\text{Sn}_5$  as observed in case of aqueous electrolytes. It was reported previously that inter-metallic phases in the obtained alloy depends on the applied potential during deposition [1,3]. The applied potential for alloy deposition influences the thermodynamic stability of the formed inter-metallic phases of the alloy. The Gibbs energy of formation for these phases and activity of  $\text{Sn}^{2+}$  varies with the applied potential and as an outcome various inter-metallic phases were formed [3]. These factors are very much influenced by the anion and cation of the electrolyte which leads to the formation of various complexes of different metals. Again variations of these factors are possible due to the dissimilarity in donor ability of the anion and solvation energy of the metal [27-28]. Thus it is expected that values of these factors in aqueous electroplating baths would be different than the IL baths. The proposed reaction for formation of these intermetallic phases are given below [14] :





Moreover with increases in the Sn content the phase change was observed as  $\text{Cu}_6\text{Sn}_5$  phase containing 61 wt% of Sn and  $\text{Cu}_3\text{Sn}$  containing 38 wt% of Sn [1]. With variation in temperature the inward or outward diffusion of Sn will take place and the diffusion rate controlled the inter-metallic phases. After annealing the crystalline structure was appeared to be of  $\text{Cu}_{10}\text{Sn}_3$  phase containing 36 wt% of Sn [1]. Based on the equation (7.3) and (7.4), the possible reaction for formation of this intermetallic phase is shown by eqn. 7.5 and 7.6.



In the above reactions there was reasonable outer diffusion of both Cu and Sn according to the solid state reactions. Though, the XRD pattern of the annealed sample did not show any Cu, Sn or CuSn crystalline phase in the alloy. These phases might remain in deposit as amorphous form. These reactions indicated about the process optimization in fabrication of appropriate Cu-Sn alloy phase.

The scanning electron micrographs showed with increase in deposit thickness favours the increase in grain size with some voids along the length. This indicates that new nuclei did not generated continuously as the deposition thickness increases. Now with increase in deposit thickness, the grain boundary energy increases as an outcome the grain size increases rapidly [29]. Moreover, the nature of the deposit is a function of current strength driven into the plating solution. Formation of voids may be due to the trapping of any air or gas bubble those driven along with cations under the influence of externally applied potential. These deposits also showed poor adhesion to the substrate surface. This might be due to the amalgamation of the cations. The amalgamation of cations developed cohesive forces among themselves and reduced their adhesive force to the substrate surface [30]. As a result poor adhesion of the deposit on the substrate was observed.

To analysis the alloy properties in more detail, the properties of the individual metals should be presented. Comparison between different electrochemical, deposition parameters and deposit morphology of the individual metals and alloy is shown in table 7.2.

Table 7.2 : Comparative study of various parameters of individual metal and alloy deposition process

Parameters	Cu	Sn	Cu-Sn co-deposition
Metal ion concentration in ethaline melt	0.2 M CuCl <sub>2</sub> .2H <sub>2</sub> O	0.05 M SnCl <sub>2</sub> .2H <sub>2</sub> O	0.04 M CuCl <sub>2</sub> .2H <sub>2</sub> O – 0.1 M SnCl <sub>2</sub> .2H <sub>2</sub> O
Deposition potential	-0.6 V	-0.6 V	-0.36 V
Deposition current	4.7x10 <sup>-3</sup> A/cm <sup>2</sup>	1.57x10 <sup>-3</sup> A/cm <sup>2</sup>	0.87x10 <sup>-3</sup> A/cm <sup>2</sup>
Deposit nature	Dense and compact for any deposit thickness	Formation of dendrites with increase in deposit thickness	Non uniform grains with increase in deposit thickness with voids
Growth rate	0.1±10% µm/min	0.1±10% µm/min	0.03±10% µm/min
EDAX analysis	Cu along with C and Cl	Sn along with Cl	Cu-Sn only (75 wt% - 25 wt%)
Crystallite size	66±10 nm	62±10 nm	21±10 nm
Strain	0.0022±0.0007	0.0031±0.0007	0.0122±0.005
Cathode current efficiency	96±4 %	84±4 %	92±4 %

With compared to individual metals the deposition potential and applied current was much lower in case of alloys, as an outcome lower growth rate was obtained. The variations in the deposition parameters also have affected the crystallite size. As a result the strain within the deposit is 10 times higher than individual metals. Moreover from EDAX analysis it was observed that, in case of alloy deposition no other impurity other than Cu and Sn was found. With respect to individual metal this variation might be due to the applied current value which is around 2-5 times smaller than the individual metal. Thus the electrolyte did not decompose and the other side reactions were avoided. Although this low current range applied for alloy deposition had not affected the cathode current efficiency. Even the efficiency value of alloy deposition was the average value of the two individual metals efficiency values.

## 7.8. Conclusion

From the above discussion it is concluded that,

- For alloy deposition, the proportion of metal salts in the ethaline melt need to be chosen very carefully. The proportion of the individual metal in the electrolyte do not corresponds to the metal proportion in the obtained alloy deposit.
- The Sn content in the obtained alloy layers was found in the range of 8 to 30 wt%, with increase in Sn content >30 wt% the deposits turned to be powdery. Homogenous deposit was achieved on stainless steel substrate by potentiostatic method and galvanstatic method. The deposit was achieved by applying potential range of 350 to 360 mV vs. Ag wire or  $0.8$  to  $0.9 \times 10^{-3}$  A/cm<sup>2</sup>. The RDE speed was kept constant as 220 rpm at bath temperature of 25 °C. The concentration of SnCl<sub>2</sub>.2H<sub>2</sub>O was maintained as 0.1 M and CuCl<sub>2</sub>.2H<sub>2</sub>O as 0.04 M. Similar deposit characteristics was obtained from ethaline melt containing 0.1 M SnCl<sub>2</sub>.2H<sub>2</sub>O – 0.02 M CuCl<sub>2</sub>.2H<sub>2</sub>O by maintaining similar deposition currents and potentials. At higher potential or applied current deposited alloy suffer from carbon, oxygen or chlorine content. The growth rate was  $0.04 \pm 10\%$  μm/min with a current efficiency of  $90 \pm 5\%$ .
- The XRD pattern corresponding to orthorhombic Cu<sub>3</sub>Sn crystalline structure for as deposited sample. The crystalline size was determined in order of  $21 \pm 10$  nm. After heat treatment, the crystalline structure changed to hexagonal Cu<sub>10</sub>Sn<sub>3</sub> crystalline structure with crystalline size of  $77 \pm 50$  nm. The strain value in the deposit decreases with annealing process as expected.
- During the bath stability experiment, 67 μm of alloy containing 25 wt% Sn – 75 wt% Cu was obtained from the melt without adding any metal salts. When obtained deposits lacks in current efficiency and metal proportion combination then the stability of the electrolyte can be re-established by adding additional Sn salts. Additionally variation in electrolyte property was observed even when the melt was kept for storage.

## References :

1. K. Murase, R. Kurosaki, T. Katase, H. Sugimura, T. Hirato and Y. Awakura (2007) *Journal of The Electrochemical Society*, 154 (11) : D612-D616.
2. T. Katase, R. Kurosaki, K. Murase, T. Hirato and Y. Awakura (2006) *Electrochemistry and Solid-State Letters*, 9 (4) : C69-C72.
3. K. Murase, A. Ito, T. Ichii and H. Sugimura (2011) *Journal of the Electrochemical Society*, 158 (6) : D335-D341.
4. A. Alhaji (2011) "Electrodeposition of Alloys from Deep Eutectic Solvents", PhD, University of Leicester, Leicester.
5. S. Ghosh (2011) "Electrodeposition of Copper, Tin and their alloys using a Rota Hull system", MPhil, Newcastle University, Newcastle.
6. Q. Zhu and C. L. Hussey (2002) *Journal of the Electrochemical Society*, 149 (5) : C268-C273.
7. Q. Zhu and C. L. Hussey (2001) *Journal of the Electrochemical Society*, 148 (5) : C395-C402.
8. G.A. Finazzi, E.M. de Oliveira and I.A. Carlos (2004) *Surface and Coating Technology*, 187 : 377-387.
9. C.T.J. Low and F.C. Walsh (2008) *Surface and Coating Technology*, 202 : 1339-1349.
10. Y. Sürme, A. Ali Gürten, E. Bayol and E. Ersoy (2009) *Journal of Alloys and Compounds*, 485 : 98-103.
11. A. Brenner (1963) *Electrodeposition of alloys principles and Practice*, vol.1, New York, Academic Press. : 75-78, 497-498.
12. [ICDD reference code 00-006-0621], I. Isajcev (1947) *Zh. Tekh. Fiz.*, 17, 829.
13. [ICDD reference code 00-047-1575], B. Peplinski (1995) *Federal Inst. for Material Research and Testing*, Berlin, Germany., Private Communication.
14. T. Wen-ming, H. An-qiang, L. Qi and D. G. Ivey (2010) *Trans. Nonferrous Met. Soc. China*, 20 : 90-96.
15. H. -C. Shin and M. Liu (2005) *Adv. Funct. Mater.*, 15(4) : 582.
16. J. Park, S. Rajendran and H. Kwon (2006) *Journal of Power Sources*, 159 : 1409-1415.
17. C. Han, Q. Liu and D. G. Ivey (2009) *Electrochimica Acta*, 3419-3427.
18. V. K. Pecharsky and P. Y. Zavalij (eds.) *Fundamentals of Powder Diffraction and Structural Characterization of Materials*, 2<sup>nd</sup> ed. Springer (2008), pp. 266, 352-354.
19. G. K. Williamson and W. H. Hall 1953 *Acta Metallurgica*, 1: 22-31.

20. [ICDD reference code 00-026-0564], S. Lenz (1971) *Monatsh. Chem.*, 102, 1689.
21. P. D. Vreese, N. R. Brooks, K. V. Hecke, L. V. Meervelt, E. Matthijs, K. Binnemans and R. V. Deun (2012) *Inorganic Chemistry*, 51 : 4972-4981.
22. O. Younes and E. Gileadi (2000) *Electrochemical and Solid-State Letters*, 3 (12) : 543-545.
23. O. Younes, L. Zhu and E. Gileadi (2003) *Electrochimica Acta*, 48 : 2551-2562.
24. O. Younes and E. Gileadi (2002) *Journal of The Electrochemical Society*, 149 (2) : C100-C111.
25. P. G. Daniele, G. Ostacoli and O. Zerbini (1988) *Transition Met. Chem.* 13 : 87-91.
26. E. B. Lehman and P. Ozga (1998) *Electrochimica Acta*, 43 (5-6) : 617-629.
27. X. -H. Xu and C. L. Hussey (1993) *Journal of The Electrochemical Society*, 140(3) : 618-626.
28. J. -F. Huang and I. -W. Sun (2003) *Journal of The Electrochemical Society*, 150(6) : E299-E306.
29. Z. Xin, S. Xiao-Hui and Z. Dian-Lin (2010) *Chin. Phys. B*, 19 (8) : 086802.
30. T. N. Vorobyova, V. P. Bobrovskaya and V. V. Sviridov (1997) *Metal Finishing*, November issue, 14-20.

## **Chapter 8 : CONCLUSION**

In the previous chapters several experiments were carried out to deposit individual metallic films like Cu and Sn and their alloy film from ethaline melt a  $\text{ChCl}$  based IL. Physical and electrochemical characteristics of the electrolyte with and without metal salts were studied and the deposition parameters were optimized. The results obtained so far from those measurements some speculations have been made on the deposition parameters and also on the electrolyte characteristics. The conclusion was drawn on the basis of the experimental results and presented as follows.

- The density and viscosity value decreases and conductivity value increases with the increase in operation temperature for ethaline melt with and without metal salt. With addition of metal salt any noticeable variation on the density, conductivity and viscosity value was not observed. The Arrhenius model fits very well for viscosity and conductivity change with variation in temperature change for all ethaline melt with and without metal salt.
- The voltammetry studies on ethaline melt with and without metal salt showed different electrochemical properties of these electrolytes. The Formal potential measurements on the individual metal indicated about the formation of  $\text{CuCl}^{4-}$  complex  $\text{SnCl}^{3-}$  complex, during metal reduction which did not changed over the concentration range. The voltammetry studies on individual metals at static condition showed reduction of  $\text{Cu}^{2+}$  to  $\text{Cu}^+$  is only a reversible couple. The diffusion co-efficient values of  $\text{Cu}^{2+}$  and  $\text{Sn}^{2+}$  were determined as  $1.22 \times 10^{-7} \text{ cm}^2/\text{s}$  and  $1.96 \times 10^{-7} \text{ cm}^2/\text{s}$ , respectively. Limiting current for individual metal reduction was determined from the mass transfer controlled region, this limiting current value was used for metal deposition.
- The deposition by potentiostatic method showed rough deposits for both metals. Smooth and uniform Cu deposits were obtained at  $4.71 \times 10^{-3} \text{ A/cm}^2$  (78% $i_L$ ) using 0.2 M  $\text{CuCl}_2 \cdot 2\text{H}_2\text{O}$  and Sn deposits were obtained at  $1.57 \times 10^{-3} \text{ A/cm}^2$  (76% $i_L$ ) using 0.05 M  $\text{SnCl}_2 \cdot 2\text{H}_2\text{O}$ . These deposits were obtained at 25 °C using RDE speed of 700 rpm for both metals. The growth rate for Cu deposition was  $0.15 \pm 0.01 \text{ } \mu\text{m}/\text{min}$  and for Sn deposition was  $0.1 \pm 0.01 \text{ } \mu\text{m}/\text{min}$ . The cathode current efficiency for Cu process was evaluated as  $95 \pm 5\%$  and for Sn

deposition was  $84\pm 3\%$ . The XRD analysis confirmed the pattern of the Cu deposit corresponds to the face centred cubic structure with crystalline size of  $66\pm 10$  nm. For Sn the crystalline pattern matched to tetragonal structure with crystallite size of  $62\pm 10$  nm.

- Several deposition processes were carried out for one month long from a single electrolyte bath to investigate the maximum deposition limit of this bath. For these measurements, the deposition of individual metal Cu and Sn was carried out at  $25\text{ }^\circ\text{C}$ . The equivalent metal deposited out from one electrolyte bath was in the range of 200 to 250  $\mu\text{m}$  with high cathode current efficiency and quality film obtained from each deposition experiments. So these baths are stable for several metal deposition processes.
- For alloy deposition, the proportion of metal salt in the electrolyte needs to be chosen very carefully. The Sn content in the alloy was achieved in the range of 8 to 30 wt% by potentiostatic method. The smooth and bright deposit was obtained by applying potential in the range of 0.35 to 0.36 V vs. Ag wire or 0.8 to  $0.9\times 10^{-3}$  A/cm<sup>2</sup> when the RDE speed is 220 rpm at  $25\text{ }^\circ\text{C}$ . The concentration of SnCl<sub>2</sub>.2H<sub>2</sub>O was maintained as 0.1 M and CuCl<sub>2</sub>.2H<sub>2</sub>O as 0.04 M. At higher potential or applied current deposited alloy suffered from C, O or Cl content. The growth rate was  $0.04\pm 0.004$   $\mu\text{m}/\text{min}$  with current efficiency of  $90\pm 5\%$ . The XRD pattern corresponding to orthorhombic Cu<sub>3</sub>Sn crystalline structure for as deposited sample. The crystalline size was determined to be in order of  $21\pm 10$  nm. After heat treatment, the crystalline structure changed to hexagonal Cu<sub>10</sub>Sn<sub>3</sub> crystalline structure and the crystalline size was obtained as  $77\pm 50$  nm.

## **AVENUE FOR THE FUTURE WORK**

In the present thesis studies on the electrodeposition of Cu , Sn and Cu-Sn alloy were carried out using ethaline melt a ChCl based IL. Hydrated Cu and Sn salts were added in the ethaline melt as the sources for supplying Cu and the Sn ions into the deposit. Processes were optimized and phenomenon occurred during experimentations were analyzed with the help of existing state of art. The obtained deposits were characterized and the results obtained thereof were used in finding out the optimization of the process for obtaining a quality deposit. Nevertheless a number of studies were remained unexplored in the context of the present studies.

It was observed that at higher concentration the reduction of Sn reaction was kinetically controlled. Thus a full kinetic study on Sn at various concentrations is required to understand the reaction behavior. Again a speciation study on Sn at various concentrations might explain the variations with concentration. Moreover a full speciation study on Cu-Sn system is required for various concentrations. This will explain the role of Sn on alloy deposition.

ChCl based IL electrolyte was chosen for electrodeposition as this electrolyte can be recycled after use. However, during electrodeposition this electrolyte decomposes and forms many harmful chlorinated products. It showed during deposition that with increase in applied current, the amount of unwanted products get increased. So a series of deposition experiments with varying current density should be carried out to determine the suitable current density to eliminate these unwanted products.

The obtained electrodeposited alloy was only characterized from its structural points but for various industrial applications, different properties of the deposit should be studied. The Cu-Sn alloy has several uses in electrical, electronic and mechanical component fabrication. Thus mechanical, electrical and electronic properties of the deposit should be studied for its successful applications.

It was reported that Cu-Sn alloy has successful applications like a component for printing circuit board, the electrode material for rechargeable batteries, and smart materials for shape memory applications. The researchers further reported that the alloy used for the above purposes fabricated from aqueous electrolytes. Thus, to replace the aqueous electrolyte with IL electrolyte, in depth studies are required on the



deposits obtained from IL electrolytes. Moreover, deposition optimization for a particular component from IL electrolyte needs special care for commercial operations.

Although the Cu-Sn alloy was successfully deposited in the present studies still many avenues were opened up in the contexts of applications of green chemistry. It is hoped that the future researchers will filled up these gaps and explored the successful applications of ChCl based ILs in various industrial applications.

## APPENDIX

### A.1. Voltammetry with $\text{CuCl}_2 \cdot 2\text{H}_2\text{O}$ in ethaline melt

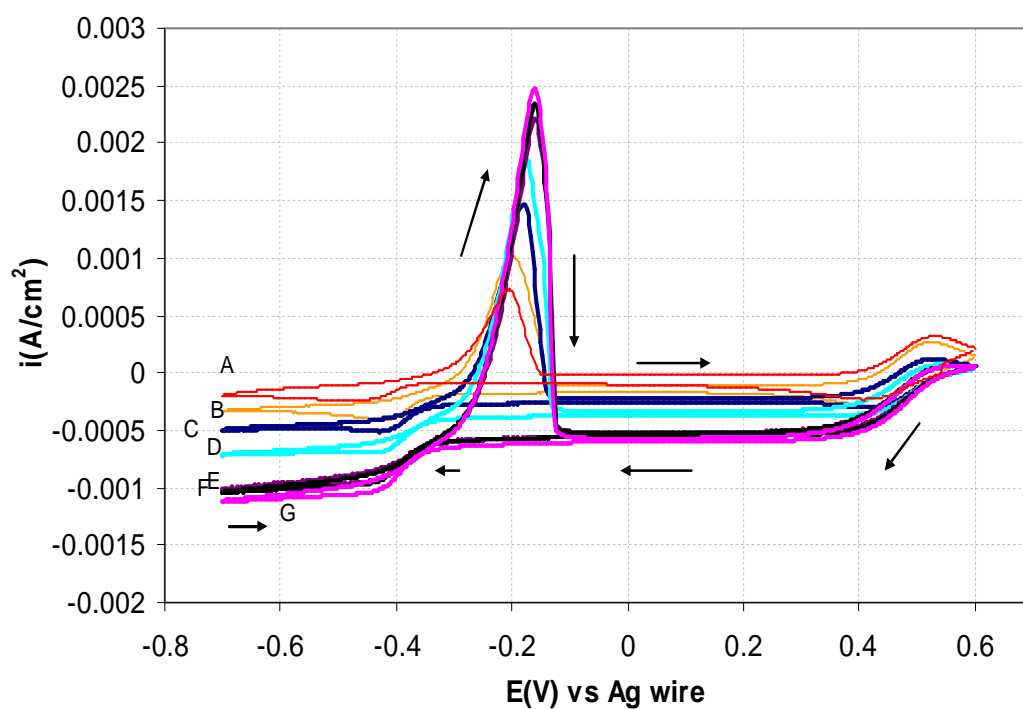


Figure A-1: Voltammetry on ethaline melt containing 0.01 M  $\text{CuCl}_2 \cdot 2\text{H}_2\text{O}$  at 25 °C, scan rate 30 mV/s, (A) 0 rpm, (B) 300 rpm, (C) 700 rpm, (D) 1000 rpm, (E) 1700 rpm, (F) 2500 rpm, (G) 3000 rpm

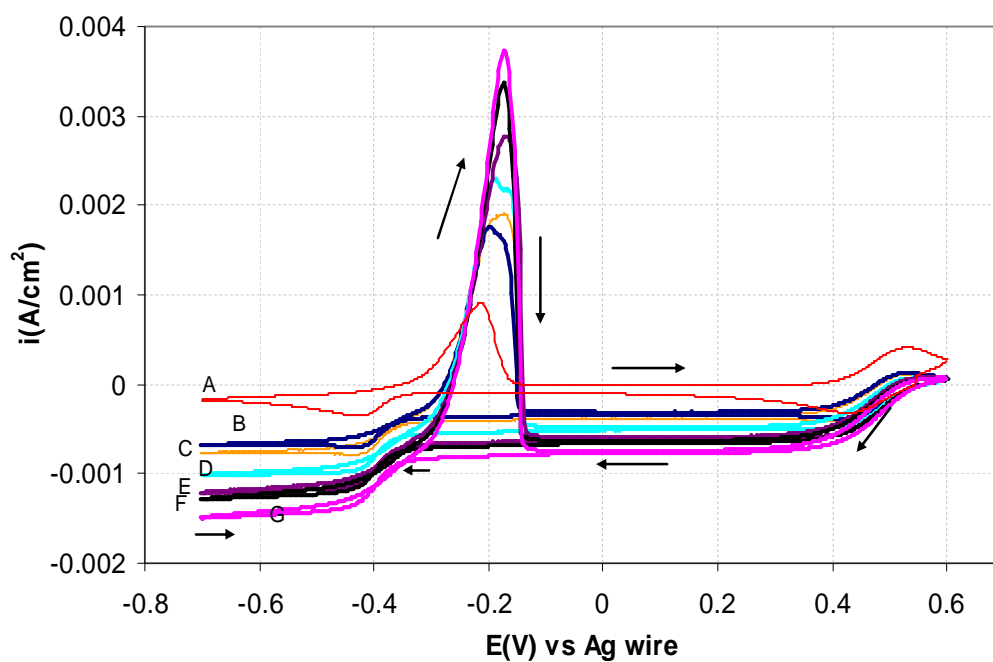


Figure A-2: Voltammetry on ethaline melt containing 0.01 M  $\text{CuCl}_2 \cdot 2\text{H}_2\text{O}$  at 35 °C, scan rate 30 mV/s, (A) 0 rpm, (B) 300 rpm, (C) 700 rpm, (D) 1000 rpm, (E) 1700 rpm, (F) 2500 rpm, (G) 3000 rpm

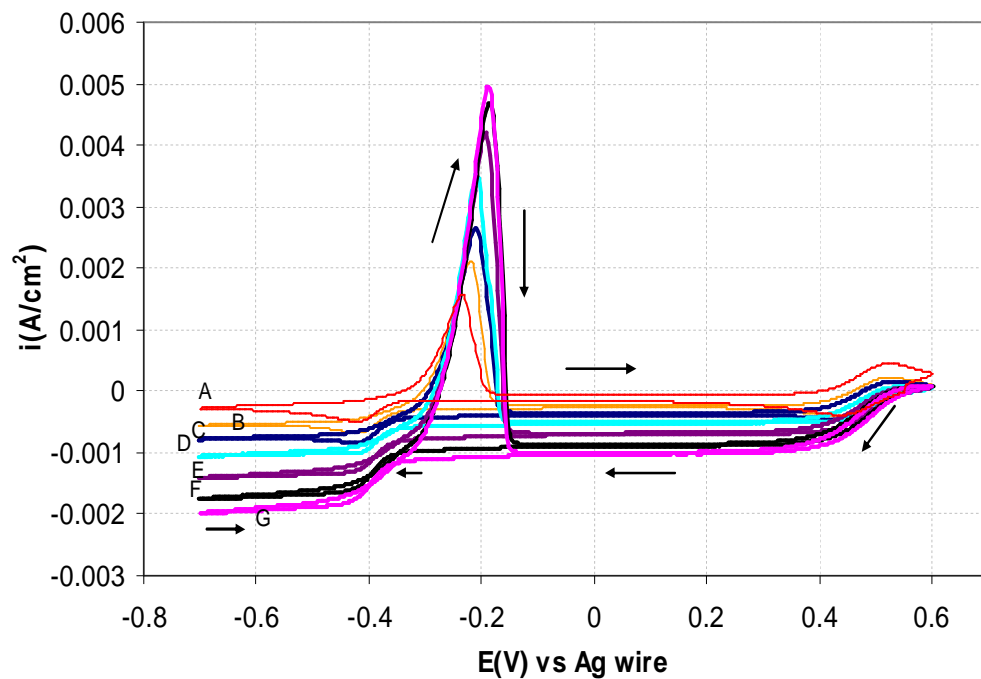


Figure A-3: Voltammetry on ethaline melt containing 0.01 M  $\text{CuCl}_2 \cdot 2\text{H}_2\text{O}$  at 45 °C, scan rate 30 mV/s, (A) 0 rpm, (B) 300 rpm, (C) 700 rpm, (D) 1000 rpm, (E) 1700 rpm, (F) 2500 rpm, (G) 3000 rpm

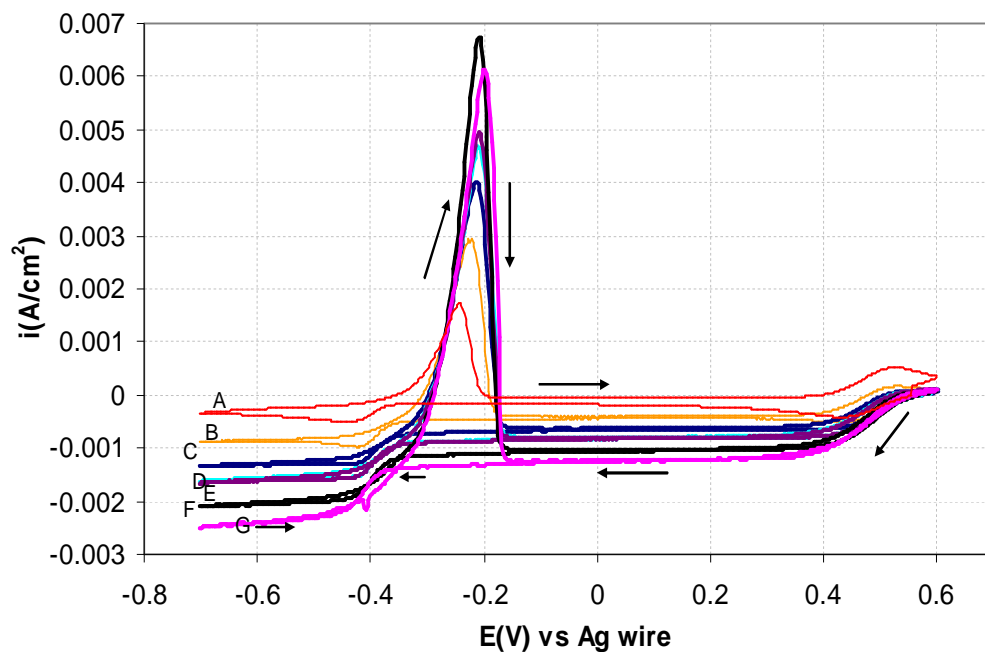


Figure A-4: Voltammetry on ethaline melt containing 0.01 M  $\text{CuCl}_2 \cdot 2\text{H}_2\text{O}$  at 55 °C, scan rate 30 mV/s, (A) 0 rpm, (B) 300 rpm, (C) 700 rpm, (D) 1000 rpm, (E) 1700 rpm, (F) 2500 rpm, (G) 3000 rpm

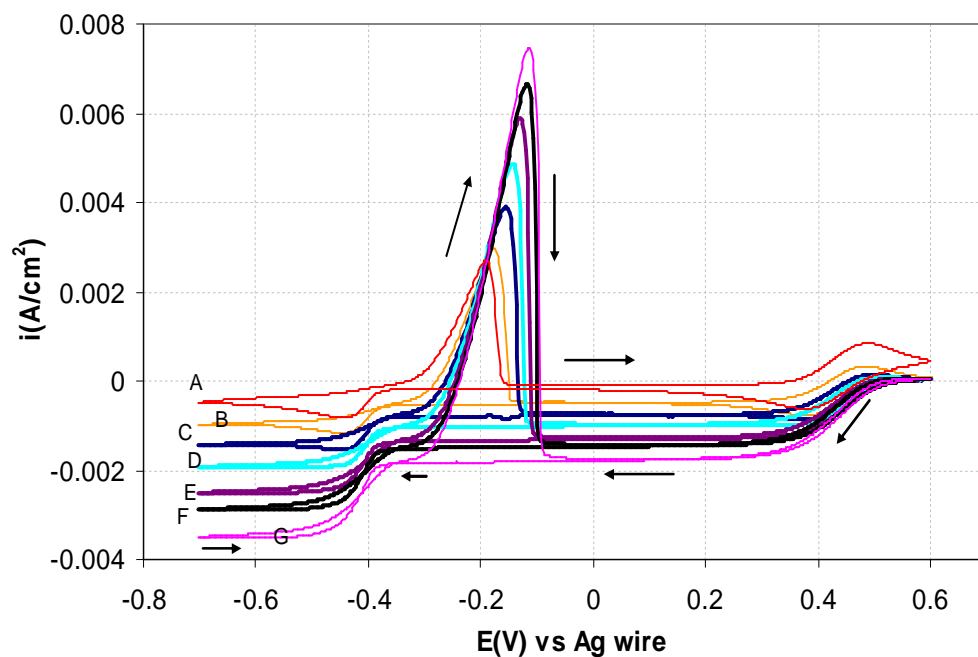


Figure A-5: Voltammetry on ethaline melt containing 0.05 M  $\text{CuCl}_2 \cdot 2\text{H}_2\text{O}$  at 25 °C, scan rate 30 mV/s, (A) 0 rpm, (B) 300 rpm, (C) 700 rpm, (D) 1000 rpm, (E) 1700 rpm, (F) 2500 rpm, (G) 3000 rpm

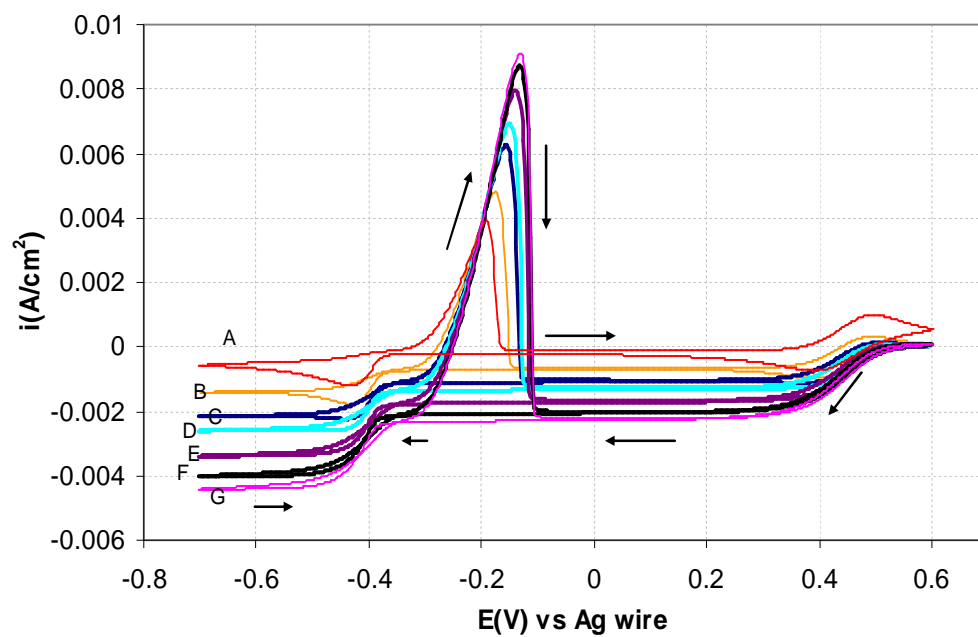


Figure A-6: Voltammetry on ethaline melt containing 0.05 M  $\text{CuCl}_2 \cdot 2\text{H}_2\text{O}$  at 35 °C, scan rate 30 mV/s, (A) 0 rpm, (B) 300 rpm, (C) 700 rpm, (D) 1000 rpm, (E) 1700 rpm, (F) 2500 rpm, (G) 3000 rpm

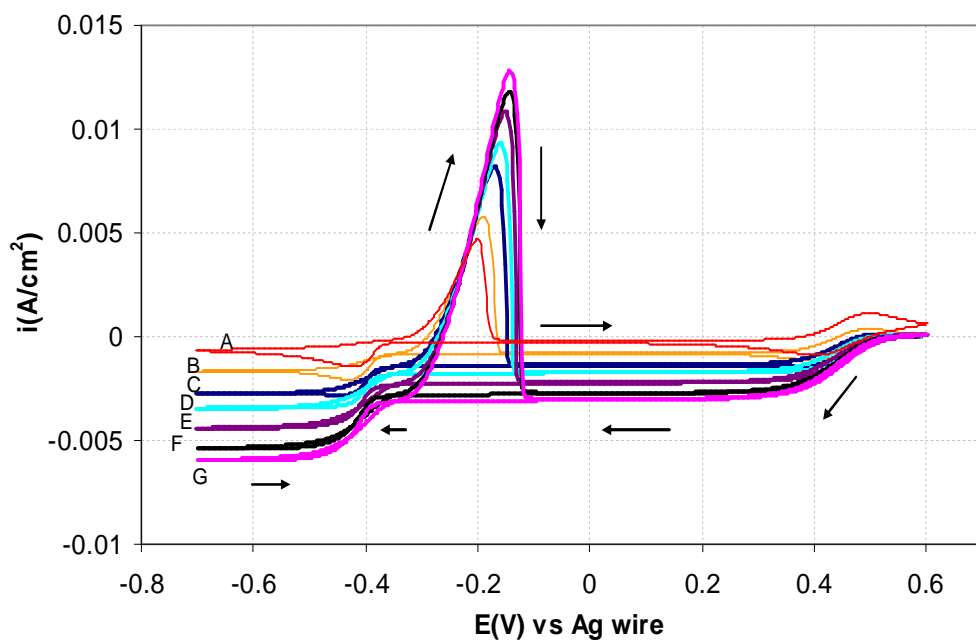


Figure A-7: Voltammetry on ethaline melt containing 0.05 M  $\text{CuCl}_2 \cdot 2\text{H}_2\text{O}$  at 45 °C, scan rate 30 mV/s, (A) 0 rpm, (B) 300 rpm, (C) 700 rpm, (D) 1000 rpm, (E) 1700 rpm, (F) 2500 rpm, (G) 3000 rpm

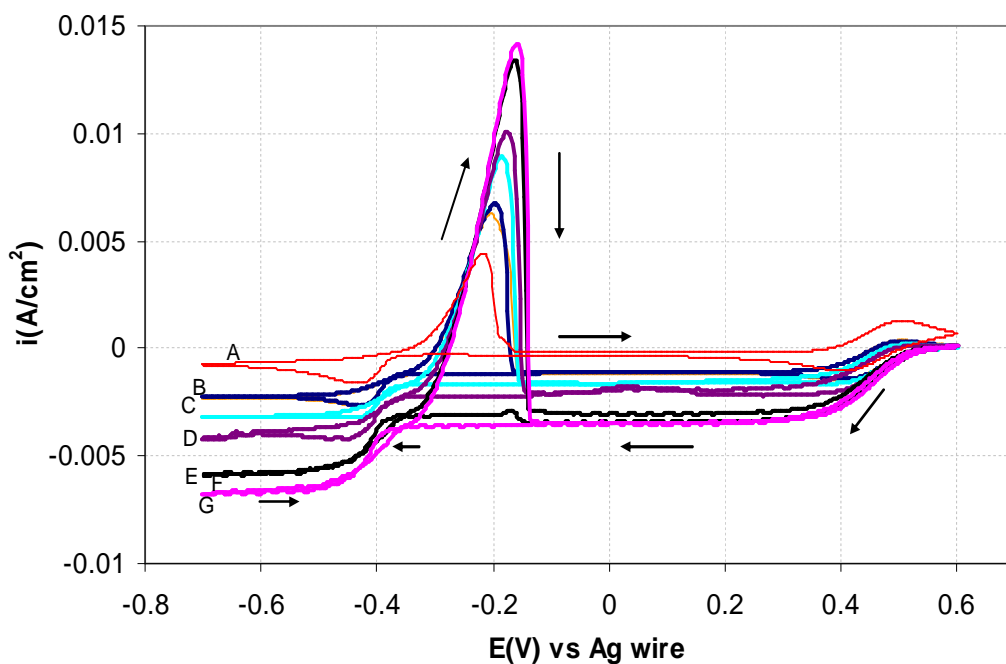


Figure A-8: Voltammetry on ethaline melt containing 0.05 M  $\text{CuCl}_2 \cdot 2\text{H}_2\text{O}$  at 55 °C, scan rate 30 mV/s, (A) 0 rpm, (B) 300 rpm, (C) 700 rpm, (D) 1000 rpm, (E) 1700 rpm, (F) 2500 rpm, (G) 3000 rpm

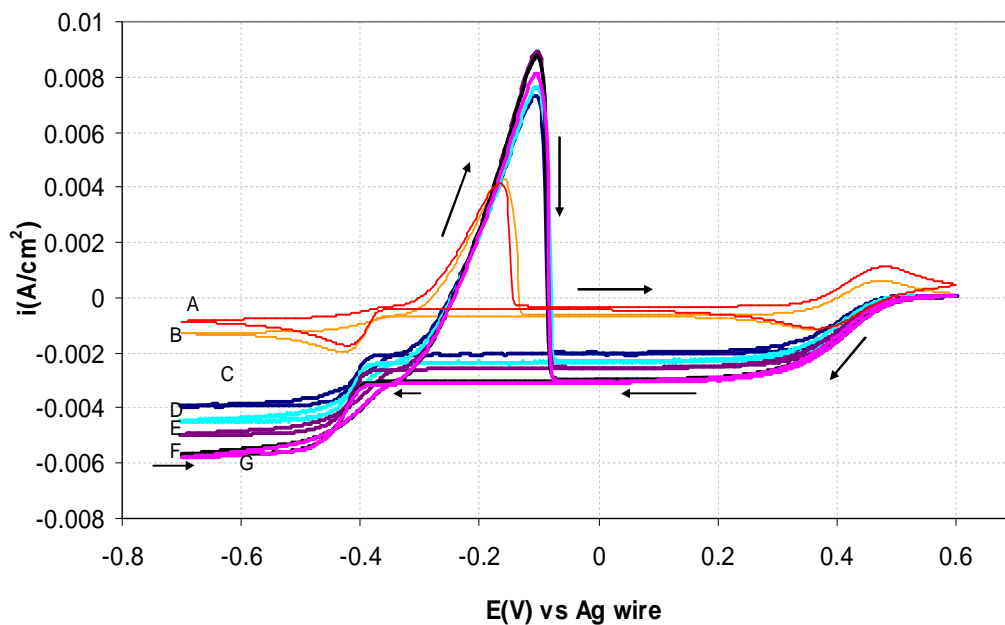


Figure A-9: Voltammetry on ethaline melt containing 0.1 M  $\text{CuCl}_2 \cdot 2\text{H}_2\text{O}$  at 35 °C, scan rate 30 mV/s, (A) 0 rpm, (B) 300 rpm, (C) 700 rpm, (D) 1000 rpm, (E) 1700 rpm, (F) 2500 rpm, (G) 3000 rpm

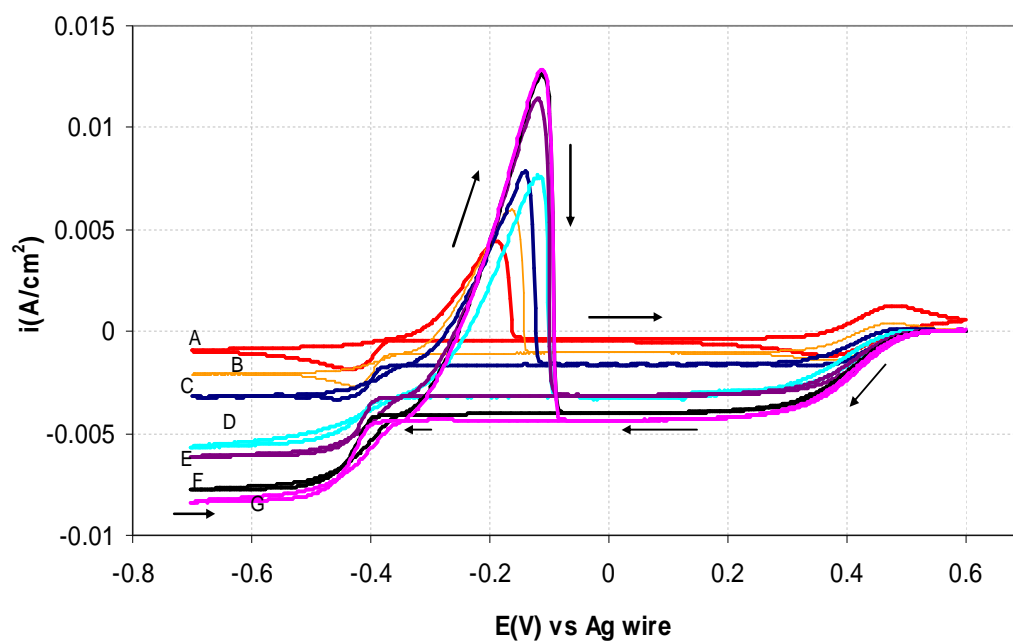


Figure A-10: Voltammetry on ethaline melt containing 0.1 M  $\text{CuCl}_2 \cdot 2\text{H}_2\text{O}$  at 45 °C, scan rate 30 mV/s, (A) 0 rpm, (B) 300 rpm, (C) 700 rpm, (D) 1000 rpm, (E) 1700 rpm, (F) 2500 rpm, (G) 3000 rpm

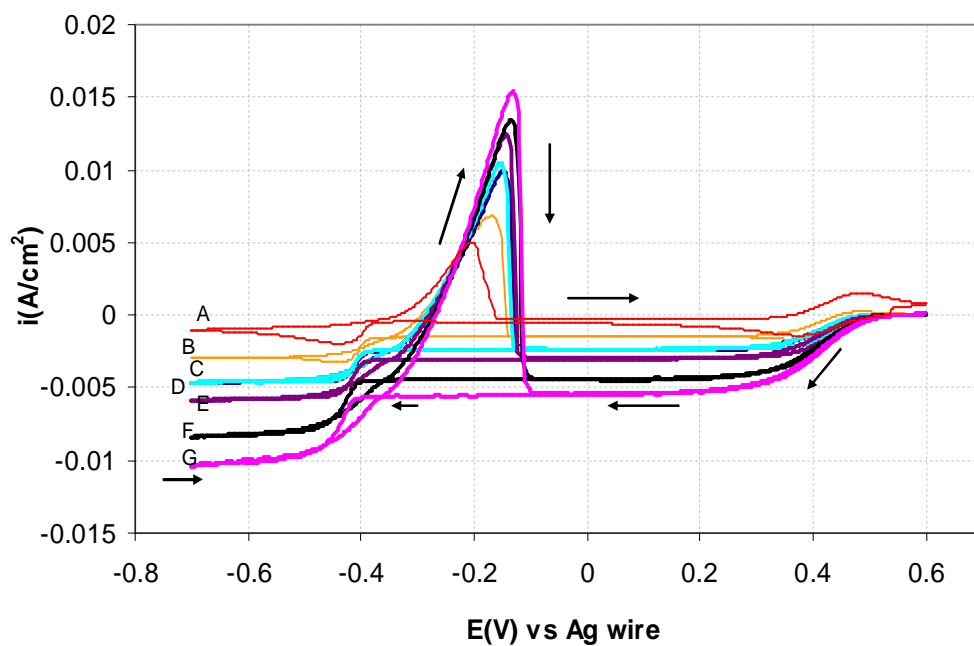


Figure A-11: Voltammetry on ethaline melt containing 0.1 M  $\text{CuCl}_2 \cdot 2\text{H}_2\text{O}$  at 55 °C, scan rate 30 mV/s, (A) 0 rpm, (B) 300 rpm, (C) 700 rpm, (D) 1000 rpm, (E) 1700 rpm, (F) 2500 rpm, (G) 3000 rpm

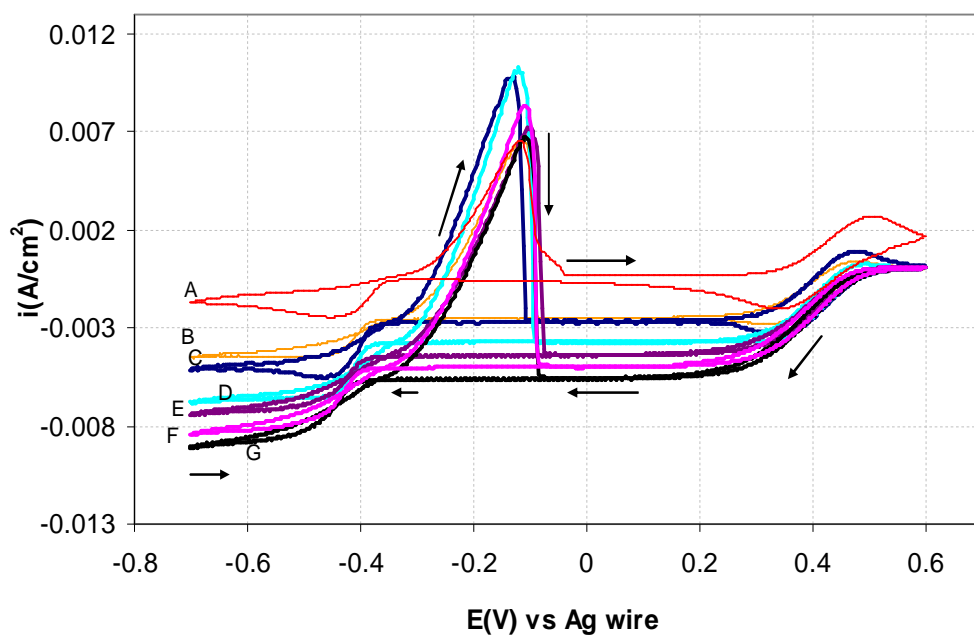


Figure A-12: Voltammetry on ethaline melt containing 0.2 M  $\text{CuCl}_2 \cdot 2\text{H}_2\text{O}$  at 25 °C, scan rate 30 mV/s, (A) 0 rpm, (B) 300 rpm, (C) 700 rpm, (D) 1000 rpm, (E) 1700 rpm, (F) 2500 rpm, (G) 3000 rpm

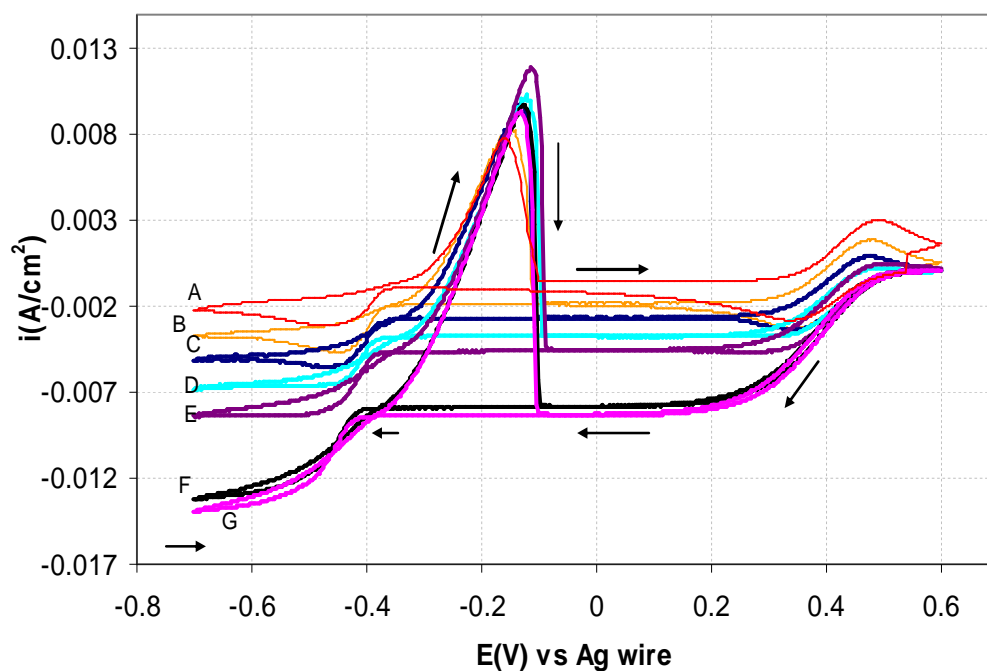


Figure A-13: Voltammetry on ethaline melt containing 0.2 M  $\text{CuCl}_2 \cdot 2\text{H}_2\text{O}$  at 35 °C, scan rate 30 mV/s, (A) 0 rpm, (B) 300 rpm, (C) 700 rpm, (D) 1000 rpm, (E) 1700 rpm, (F) 2500 rpm, (G) 3000 rpm

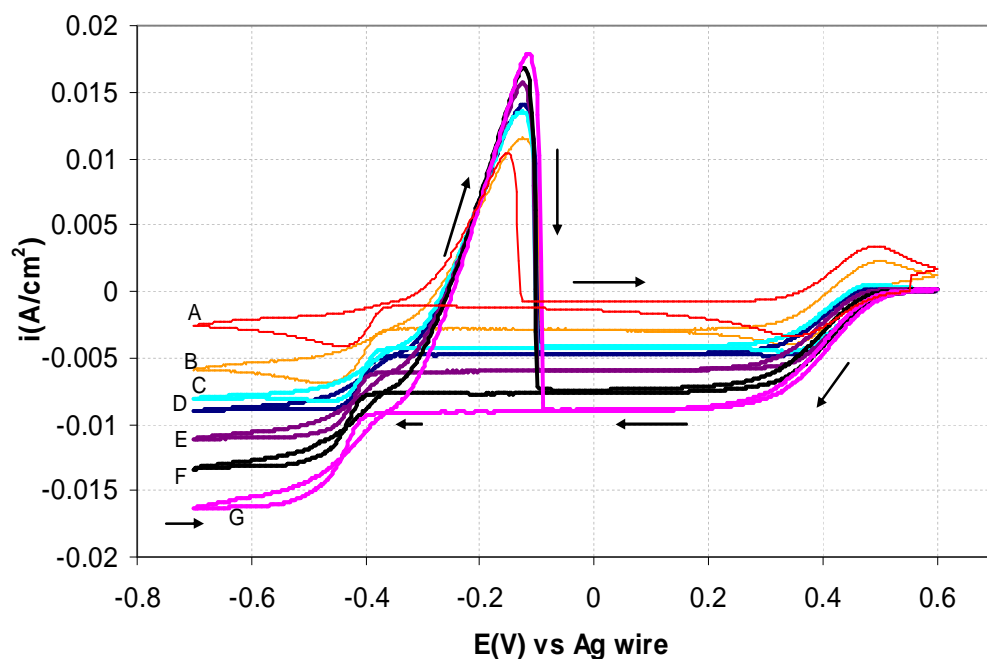


Figure A-14: Voltammetry on ethaline melt containing 0.2 M  $\text{CuCl}_2 \cdot 2\text{H}_2\text{O}$  at 45 °C, scan rate 30 mV/s, (A) 0 rpm, (B) 300 rpm, (C) 700 rpm, (D) 1000 rpm, (E) 1700 rpm, (F) 2500 rpm, (G) 3000 rpm



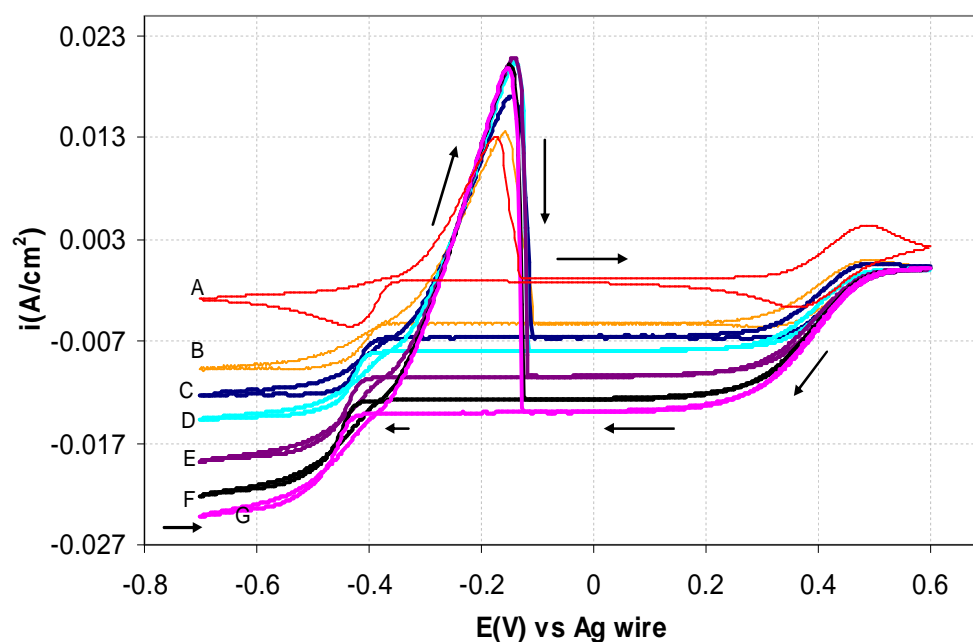


Figure A-15: Voltammetry on ethaline melt containing 0.2 M  $\text{CuCl}_2 \cdot 2\text{H}_2\text{O}$  at 55 °C, scan rate 30 mV/s, (A) 0 rpm, (B) 300 rpm, (C) 700 rpm, (D) 1000 rpm, (E) 1700 rpm, (F) 2500 rpm, (G) 3000 rpm

## A.2. Error calculation

To resolve the issues with the  $R^2$  value in the above plot a systematic error analysis was carried out. The systematic errors are associated with different parameters involved in the system and the error range of these each parameter is listed below.

- Experimental error during limiting current density ( $i_L$ ) measurements =  $\pm 1.6\%$
- Experimental error during viscosity ( $\mu$ ) measurements =  $\pm 8\%$
- Experimental error during density ( $\rho$ ) measurements =  $\pm 1\%$
- Experimental error in temperature (T) measurements =  $\pm 7\%$

The above errors were calculated based on 3 measurements taken for each experiment during limiting current calculation, physical property calculation and temperature measured during these experiments. The error calculation is shown below.

From the Levich equation:

$$\frac{i_L}{C} = 0.623nF \times D^{\frac{2}{3}} \times \omega^{\frac{1}{2}} \times \nu^{-\frac{1}{6}}, \text{ for error calculation on } D \text{ value, the error contributions}$$

are from the parameter  $\nu$  and  $(i_L/C)$ , as other parameters are constant and  $\omega$  doesn't contribute to overall error measurement value.

So for error measurement only considering the influencing parameters,

$$D = \left(\frac{i_L}{C}\right)^{\frac{3}{2}} \times (\nu)^{\frac{1}{4}}$$

According to the definition of kinetic viscosity,  $\nu = \mu/\rho$

Due to the involvement of four different temperatures in the experiments, the systematic error on  $\nu$  for temperature change needed to determine.

Lets assume the error component is  $\delta\nu$ ,

$$\delta\nu = \nu \sqrt{\left(\frac{\delta\mu}{\mu}\right)^2 + \left(\frac{\delta\rho}{\rho}\right)^2}, \text{ using this equation } \delta\nu \text{ for four different temperatures were}$$

determined.

$$\text{So, } \delta\nu_{\text{overall}} = \sqrt{(\delta\nu_1)^2 + (\delta\nu_2)^2 + (\delta\nu_3)^2 + (\delta\nu_4)^2}$$

The overall error on kinetic viscosity was determined as 13%.

In the current analysis, 156 data points are present for  $i_L$  measurement due to the variation of concentration, temperature and rotation speed of the RDE.

$$\text{So, } \delta\left(\frac{i_L}{C}\right)_{\text{overall}} = \sqrt{\left(\delta\frac{i_L}{C}\right)_1^2 + \left(\delta\frac{i_L}{C}\right)_2^2 + \left(\delta\frac{i_L}{C}\right)_3^2 + \dots + \left(\delta\frac{i_L}{C}\right)_{156}^2}$$

The overall error on  $i_L/C$  value was determined as 17.6%.

Now the overall error value on diffusion co-efficient value (D), can be determined as,

$$\therefore \frac{\delta D}{D} = \sqrt{\left(\frac{3}{2} \times \frac{\delta(i_L/C)}{(i_L/C)}\right)^2 + \left(\frac{1}{4} \times \frac{\delta\nu}{\nu}\right)^2}$$

$$\text{Or, } \frac{\delta D}{D} = \sqrt{(1.5 \times 17.6)^2 + (0.25 \times 13.3)^2} = 26$$

So the fractional uncertainty on the D value or overall error on D value was 26%

Or,  $D = 4.26 \times 10^{-7} \pm 1.13 \times 10^{-7} \text{ cm}^2/\text{s}$ .

To determine the zone in the log-log plot, the intercept value was determined,

So  $\log [K_c \times D^{2/3} \times \nu^{-1/6}] = \log [1.686]$  and the determined spread area is  $\pm 0.227$ .

All the data points for limiting current density were included in one plot, where the data points were gathered by varying rotation speed, concentration and temperature. The data points were normalised by dividing them by suitable concentration and the limiting current step relationship value as required. Then these data points were plotted against varying rotation speed of the RDE in a log-log scale. The error range was then included. The plot is shown in fig. A-16.

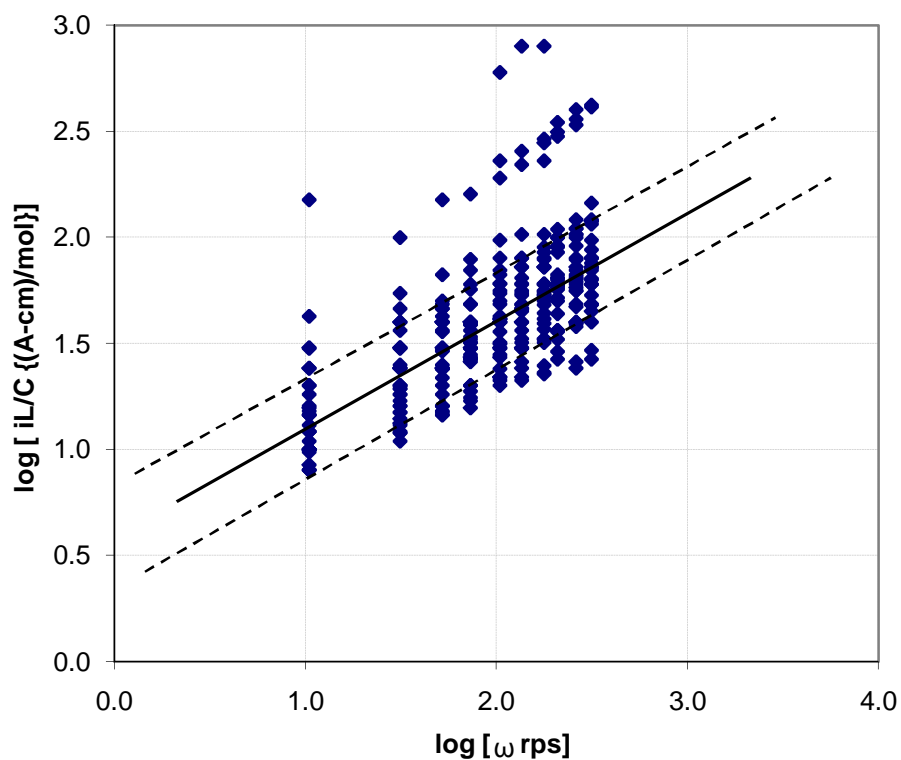


Figure A-16 : Verification of Levich equation by limiting current/concentration verses rotation speed of RDE log- log plot along with error range, regression equation is  $y=0.49x+0.62$  with  $R^2$  value of 0.6

The dashed line above and below the regression line was inserted according to the  $\pm$ error calculated and converted in terms of intercept, so the region within the dashed line in fig. A-16 is showing the region for accepted data points of these experiments.

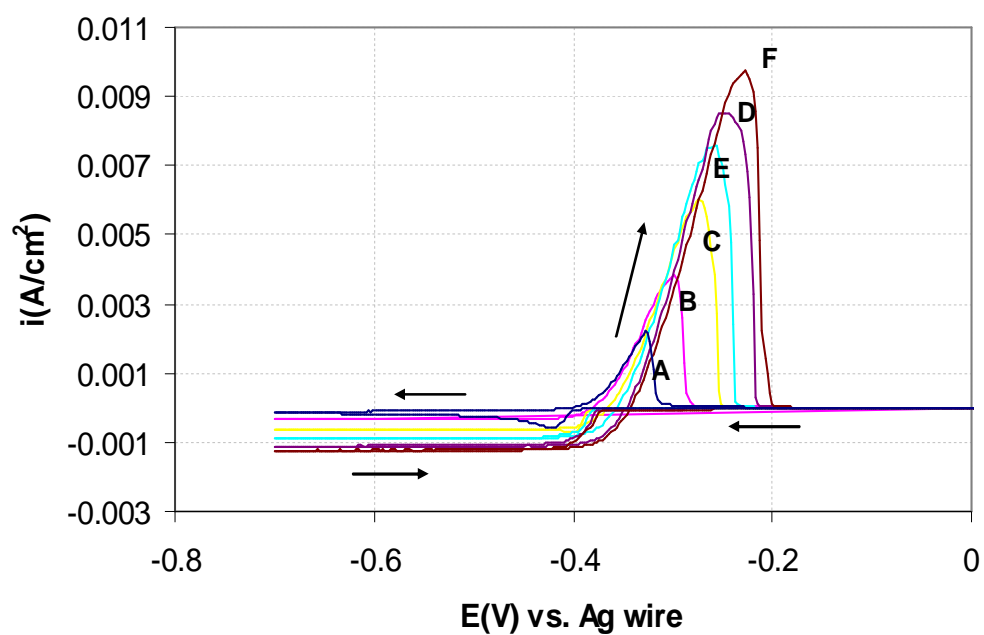
A.3. Voltammetry with  $\text{SnCl}_2 \cdot 2\text{H}_2\text{O}$  in ethaline melt

Figure A-17: Voltammetry on ethaline melt containing 0.01 M  $\text{SnCl}_2 \cdot 2\text{H}_2\text{O}$  at 25 °C, scan rate 10 mV/s, (A) 0 rpm, (B) 300 rpm, (C) 700 rpm, (D) 1000 rpm, (E) 1700 rpm, (F) 2000 rpm

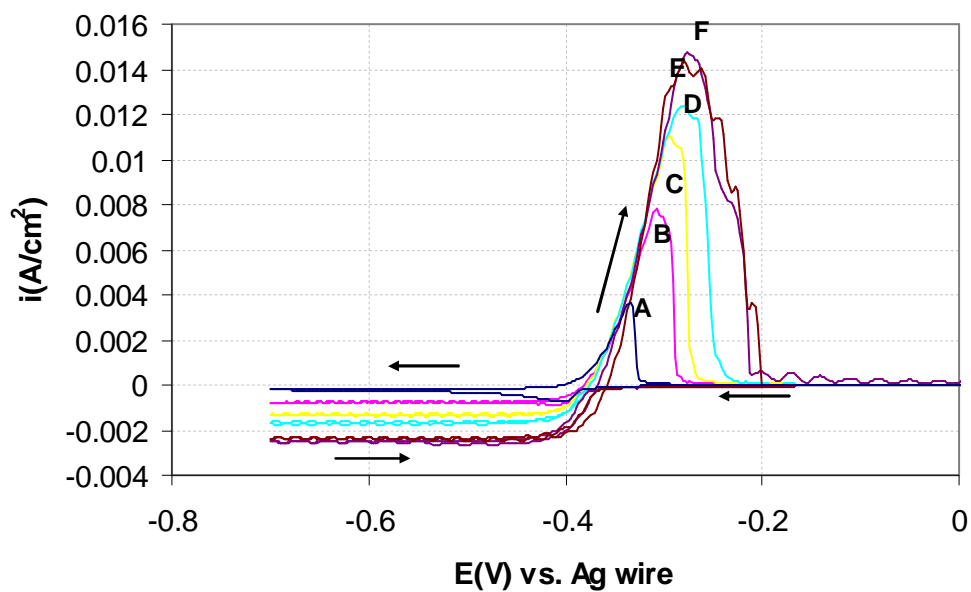
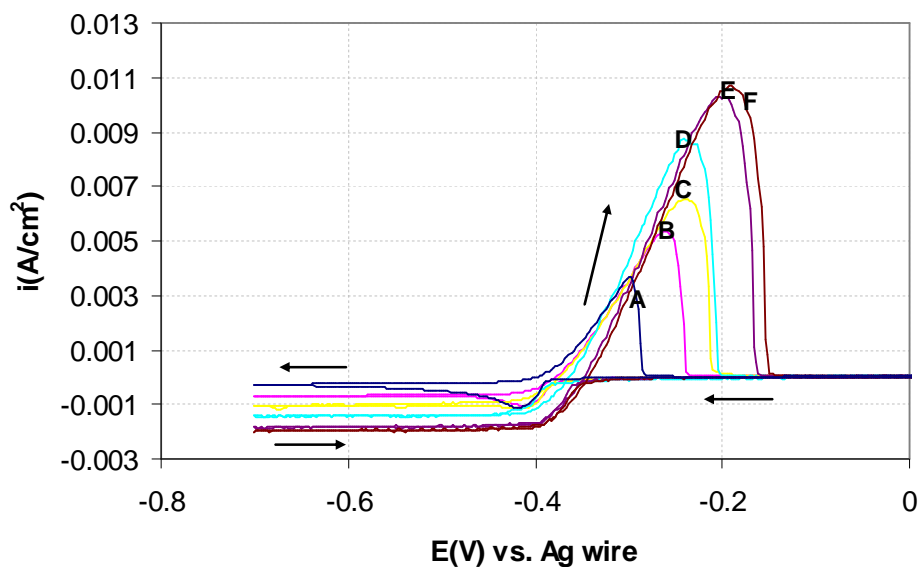
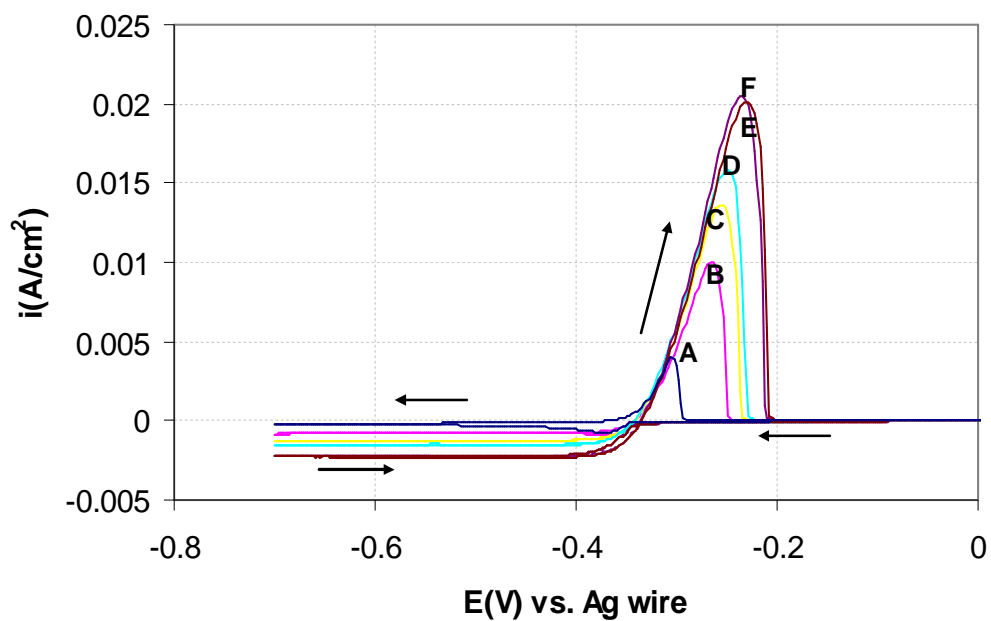


Figure A-18: Voltammetry on ethaline melt containing 0.01 M  $\text{SnCl}_2 \cdot 2\text{H}_2\text{O}$  at 45 °C, scan rate 10 mV/s, (A) 0 rpm, (B) 300 rpm, (C) 700 rpm, (D) 1000 rpm, (E) 1700 rpm, (F) 2000 rpm



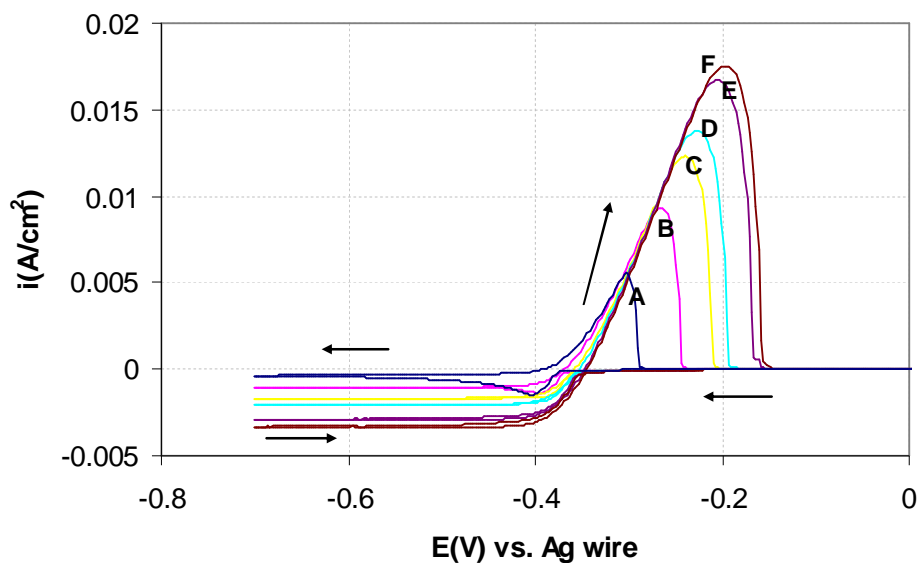


Figure A-21: Voltammetry on ethaline melt containing 0.025 M  $\text{SnCl}_2 \cdot 2\text{H}_2\text{O}$  at 35 °C, scan rate 10 mV/s, (A) 0 rpm, (B) 300 rpm, (C) 700 rpm, (D) 1000 rpm, (E) 1700 rpm, (F) 2000 rpm

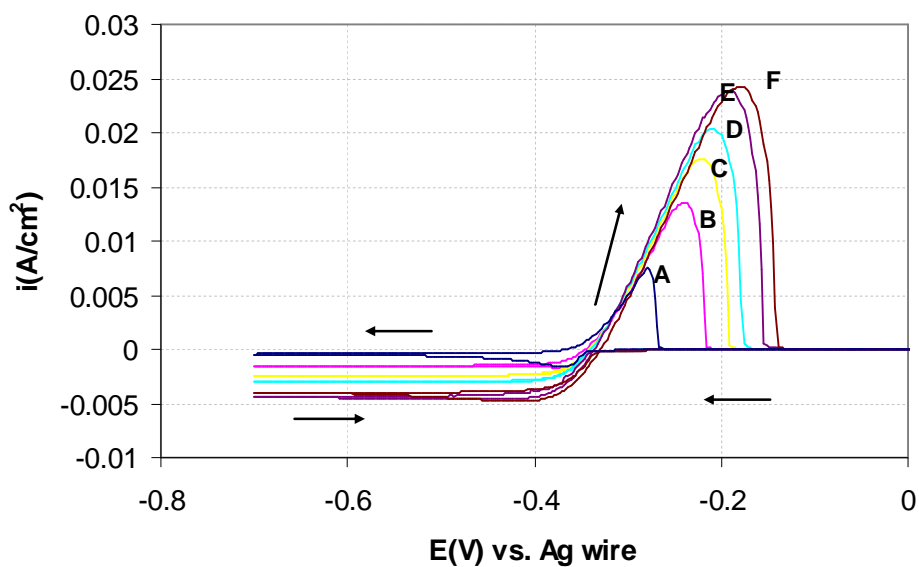


Figure A-22: Voltammetry on ethaline melt containing 0.025 M  $\text{SnCl}_2 \cdot 2\text{H}_2\text{O}$  at 45 °C, scan rate 10 mV/s, (A) 0 rpm, (B) 300 rpm, (C) 700 rpm, (D) 1000 rpm, (E) 1700 rpm, (F) 2000 rpm

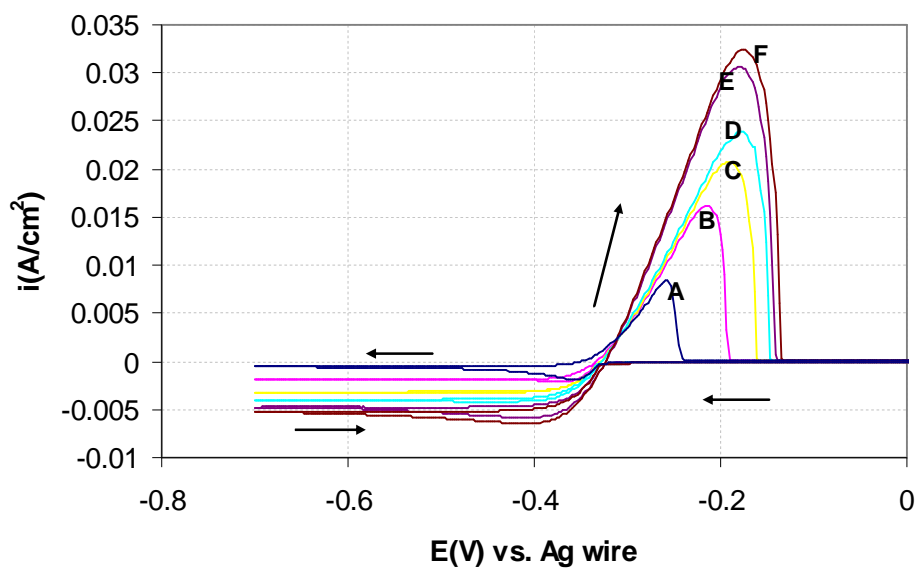


Figure A-23: Voltammetry on ethaline melt containing 0.025 M  $\text{SnCl}_2 \cdot 2\text{H}_2\text{O}$  at 55 °C, scan rate 10 mV/s, (A) 0 rpm, (B) 300 rpm, (C) 700 rpm, (D) 1000 rpm, (E) 1700 rpm, (F) 2000 rpm

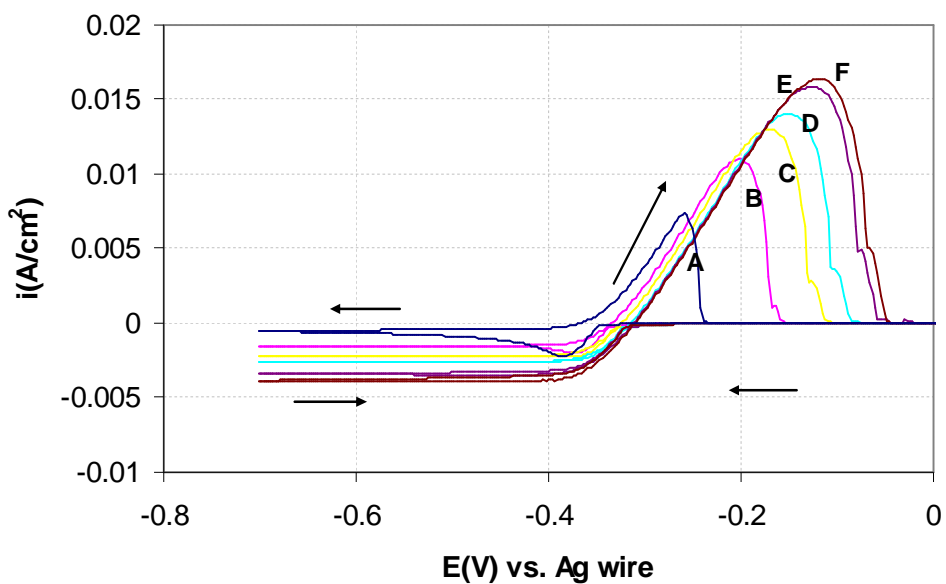


Figure A-24: Voltammetry on ethaline melt containing 0.04 M  $\text{SnCl}_2 \cdot 2\text{H}_2\text{O}$  at 25 °C, scan rate 10 mV/s, (A) 0 rpm, (B) 300 rpm, (C) 700 rpm, (D) 1000 rpm, (E) 1700 rpm, (F) 2000 rpm

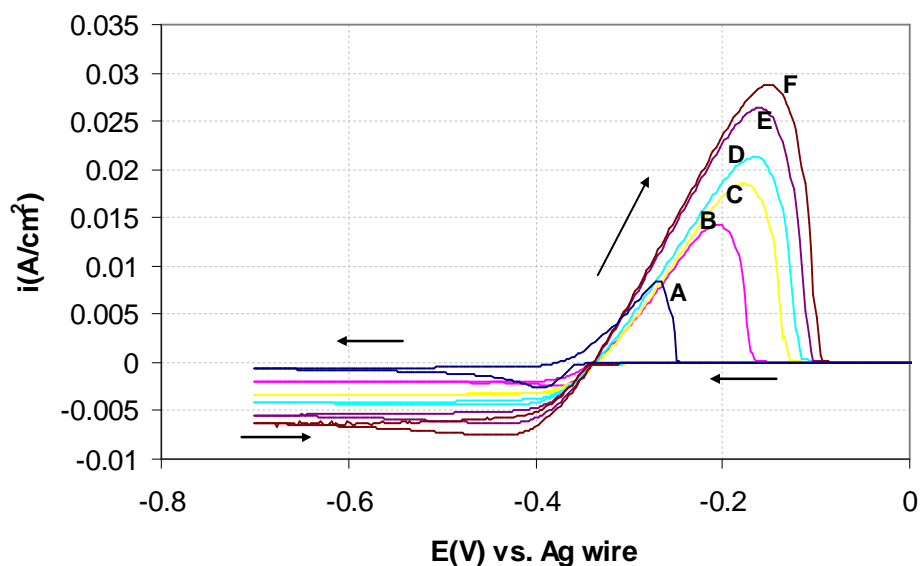


Figure A-25: Voltammetry on ethaline melt containing 0.04 M  $\text{SnCl}_2 \cdot 2\text{H}_2\text{O}$  at 35 °C, scan rate 10 mV/s, (A) 0 rpm, (B) 300 rpm, (C) 700 rpm, (D) 1000 rpm, (E) 1700 rpm, (F) 2000 rpm

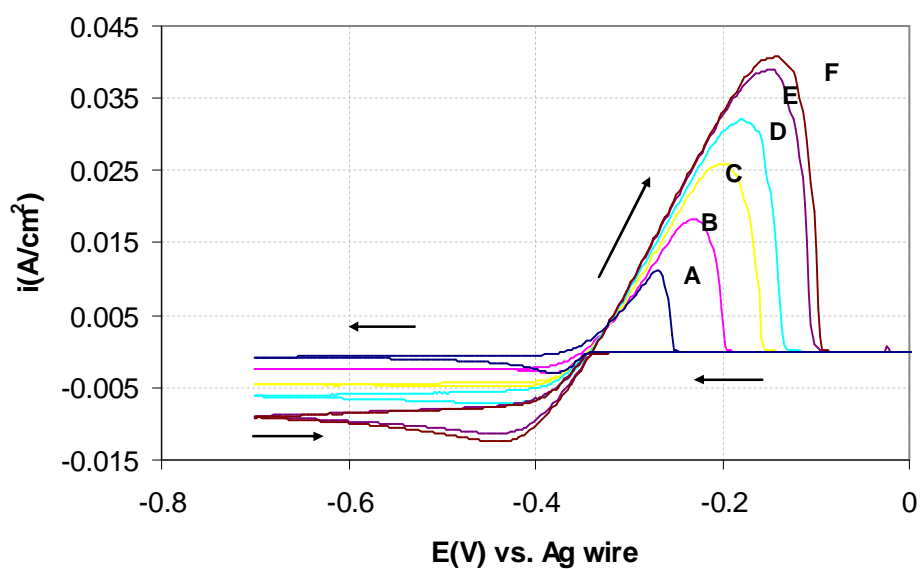


Figure A-26: Voltammetry on ethaline melt containing 0.04 M  $\text{SnCl}_2 \cdot 2\text{H}_2\text{O}$  at 45 °C, scan rate 10 mV/s, (A) 0 rpm, (B) 300 rpm, (C) 700 rpm, (D) 1000 rpm, (E) 1700 rpm, (F) 2000 rpm



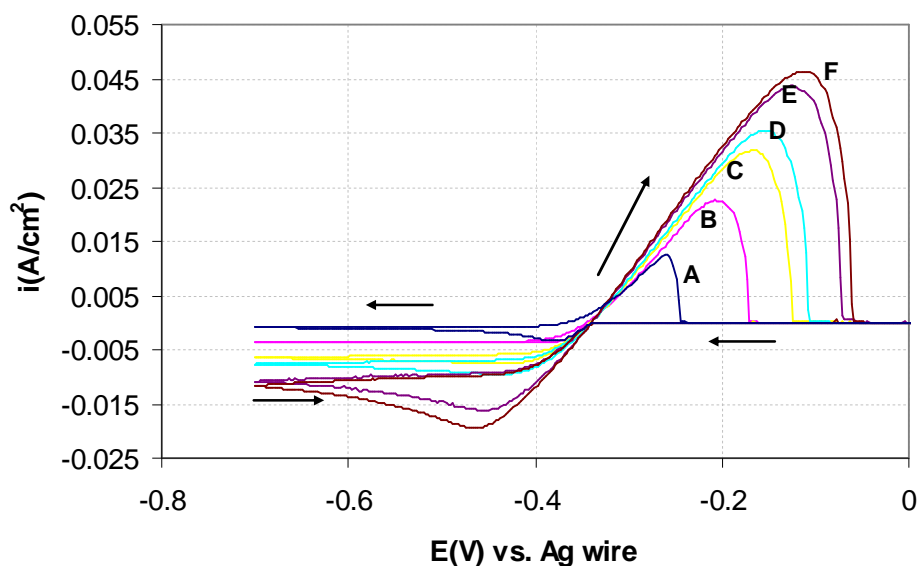


Figure A-27: Voltammetry on ethaline melt containing 0.04 M  $\text{SnCl}_2 \cdot 2\text{H}_2\text{O}$  at 55 °C, scan rate 10 mV/s, (A) 0 rpm, (B) 300 rpm, (C) 700 rpm, (D) 1000 rpm, (E) 1700 rpm, (F) 2000 rpm

#### A.4. Relationship between the parameters of Levich equation for tin system

To determine the effect of concentration on the process, a plot on limiting currents vs. the various concentrations of the electrolyte was carried out. A log-log plot of limiting current vs. concentration of the electrolyte was carried out with entire range of experimental parameters. The best fit line was drawn for each set of data and calculated slope value for each of those lines was estimated as 0.9. The expected value for these slopes was 1 according to Levich equation, this variation from Levich equation might be due to error in the data points.

To remove the effect of concentration on the limiting current data, the limiting current values were normalised. The entire range of data points was divided by the particular concentration value and the co-relation with rotation speed of the RDE is shown in fig. A-31. The slope for the obtained relationship was 0.49, according to levich equation the expected value is 0.5. Thus, it is appeared as the system is following Levich equation. The diffusion co-efficient value was calculated from the intercept of the relationship and the obtained value is  $8.55 \times 10^{-7} \text{ cm}^2/\text{s}$ , irrespective of the temperature. The  $R^2$  value is obtained as 0.3 which is far away from the expected value, so the temperature effect on these data points needed to be analysed.

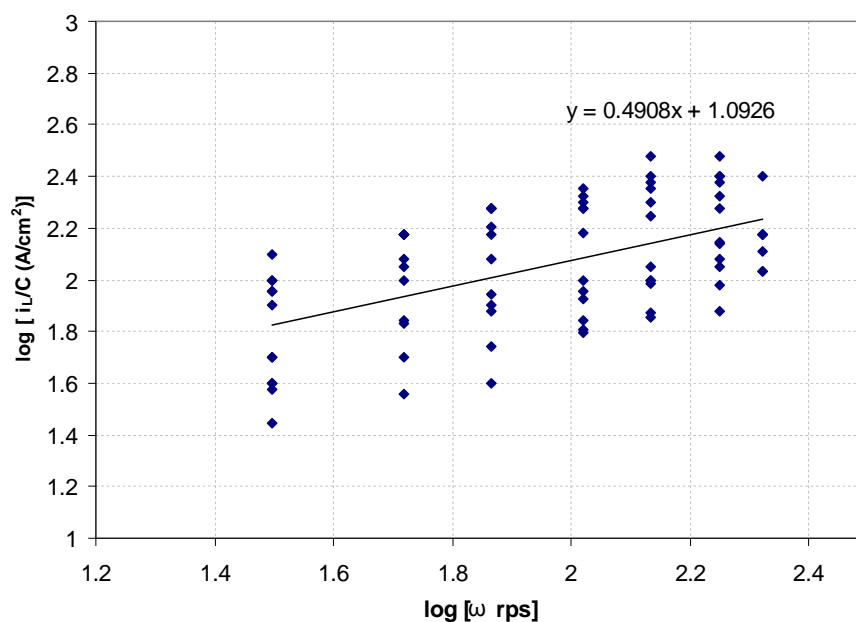


Figure A-28 : Verification of Levich equation by normalised limiting current verses rotation speed of RDE log- log plot

As the viscosity of the electrolyte is an important parameter, which varies with temperature, so a temperature effect on this process was examined. To establish the relationship a log-log plot of (limiting current/concentration) vs. rotation speed of the RDE for each temperature was carried out. Using standard regression techniques the slope value was estimated as  $0.52 \pm 7\%$ . The diffusion co-efficient value was calculated in each case using the Levich equation and the determined values were  $1.4 \times 10^{-7} \text{ cm}^2/\text{s}$  at  $25^\circ\text{C}$ . The  $R^2$  value in each case was 0.82, 0.94, 0.88 and 0.91 respectively.

The  $R^2$  values determined during overall analysis becomes closer to aimed values when the analysis was carried out after eliminating the influencing parameters. Another approach to revolve the co-relation between dependent and independent variables could be systematic error calculation using similar assumptions and approach as used in the Cu study. As the Sn experiments were carried out using the same equipment and electrolyte and the physical properties were similar in values. It could be assumed that the error % would be similar for the Sn study. The error for the Sn system was accepted as 26% as obtained during the Cu study.

Or,  $D = 8.55 \times 10^{-7} \pm 2.27 \times 10^{-7} \text{ cm}^2/\text{s}$ .

To determine the zone in the log-log plot, the intercept value was determined,

So  $\log [K_c \times D^{2/3} \times \nu^{-1/6}] = \log [5.1]$

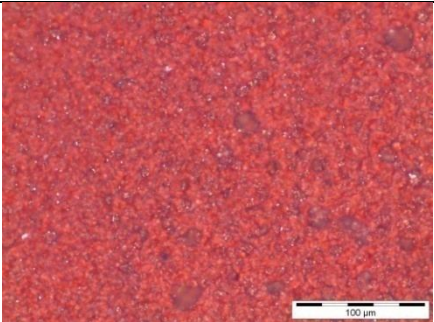
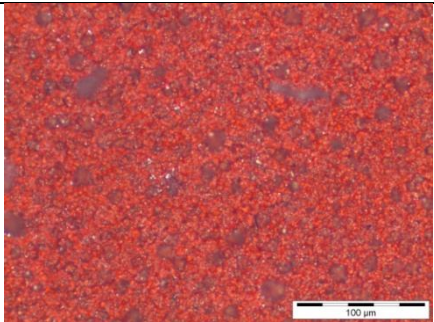
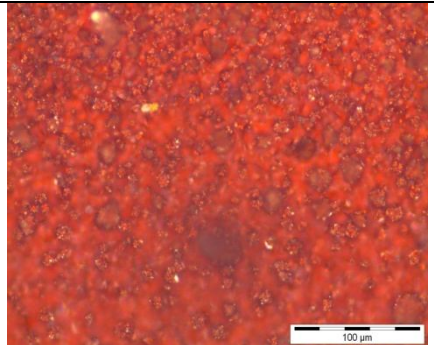
The spread area was  $\pm 0.7$

All the data points for limiting current density were included in one plot, where the data points were gathered by varying rotation speed, concentration and temperature. It was observed that all the data points gathered from all sets of

experiments remained in the spread range of  $\pm 0.5$ , so all data points lied with in error range.

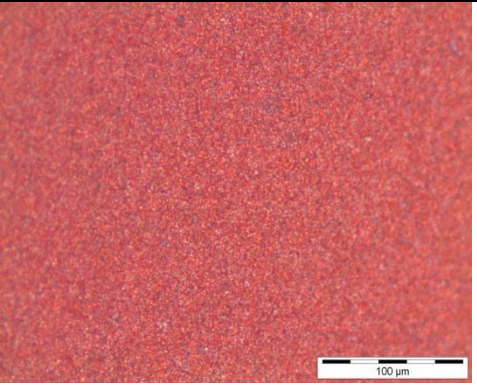
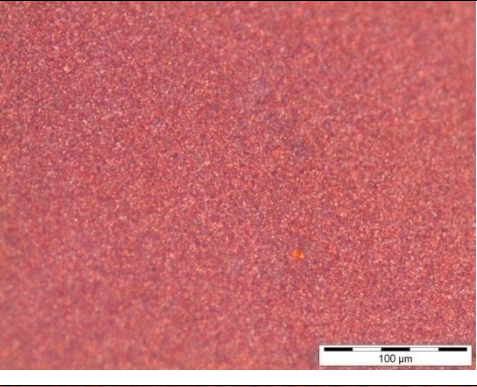
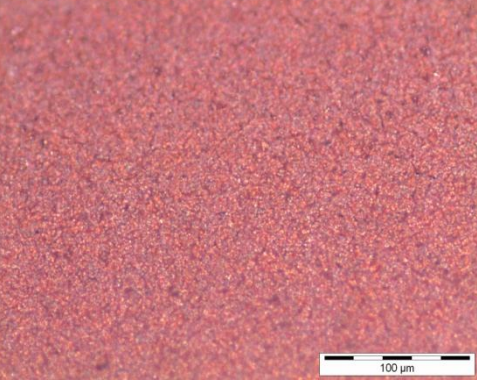
#### A.5. Deposit morphology of Cu by potentiostatic deposition for a range of durations

Table A.1 : Deposition as obtained by varying duration for potentiostatic Cu deposition, scale in the deposit showing 100  $\mu\text{m}$

Other parameters	Varying parameter		Obtained deposit
0.2 M <chem>CuCl2.H2O</chem> using 700 rpm at 25 °C [potentistatic deposition]	Duration (s)	1800	
		2700	
		3600	

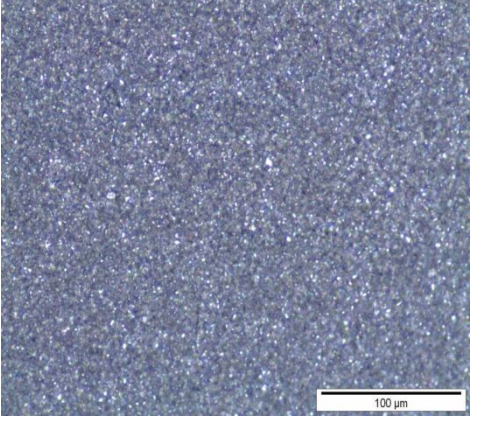
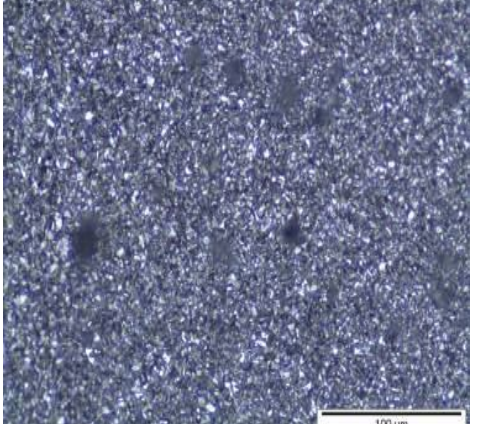
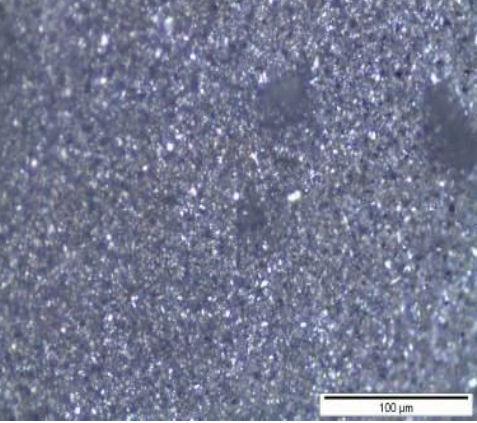
## A.6. Deposit morphology of Cu by galvanostatic deposition for a range of durations

Table A.2 : Deposition as obtained by varying duration for galvanostatic Cu deposition, scale in the deposit showing 100  $\mu\text{m}$ 

Other parameters	Varying parameter		Obtained deposit
0.2 M $\text{CuCl}_2 \cdot \text{H}_2\text{O}$ using 700 rpm at 25 °C [galvanostatic deposition]	Duration (s)	1800	 Micrograph showing a dense, granular red deposit. A scale bar in the bottom right corner indicates 100 $\mu\text{m}$ .
		2700	 Micrograph showing a dense, granular red deposit. A scale bar in the bottom right corner indicates 100 $\mu\text{m}$ .
		3600	 Micrograph showing a dense, granular red deposit. A scale bar in the bottom right corner indicates 100 $\mu\text{m}$ .

## A.7. Deposit morphology of Sn by galvanostatic deposition for a range of durations

Table A.3 : Deposition as obtained by varying duration for galvanostatic Sn deposition, scale in the deposit showing 100  $\mu\text{m}$ 

Other parameters	Varying parameter		Obtained deposit
0.05 M SnCl <sub>2</sub> .H <sub>2</sub> O using 700 rpm at 25 °C [galvanostatic deposition]	Duration (s)	1800	
		3600	
		7200	

## A.8. Cu voltammetry scan at different scan rate

The voltammetry scans on 0.04 M  $\text{CuCl}_2 \cdot 2\text{H}_2\text{O}$  using a range of RDE speeds at 10 mV/s.

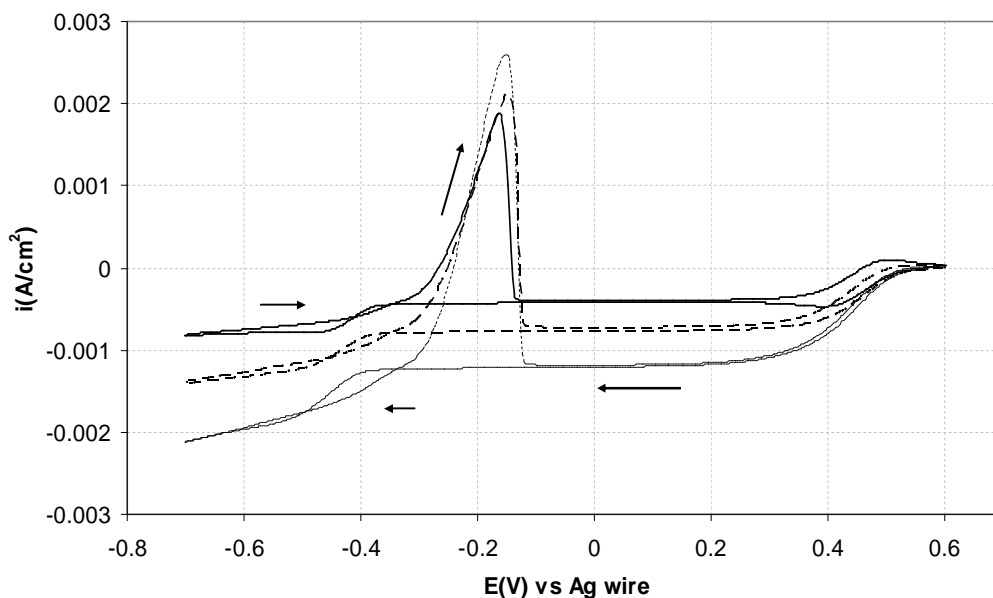


Figure A-29 : The current-potential behaviour in 0.04 M Cu ion electrolyte at agitated condition, (—)220 rpm, (---)700 rpm, (...)1800 rpm

## A.9. XRD pattern of different annealed Cu-Sn alloy deposits

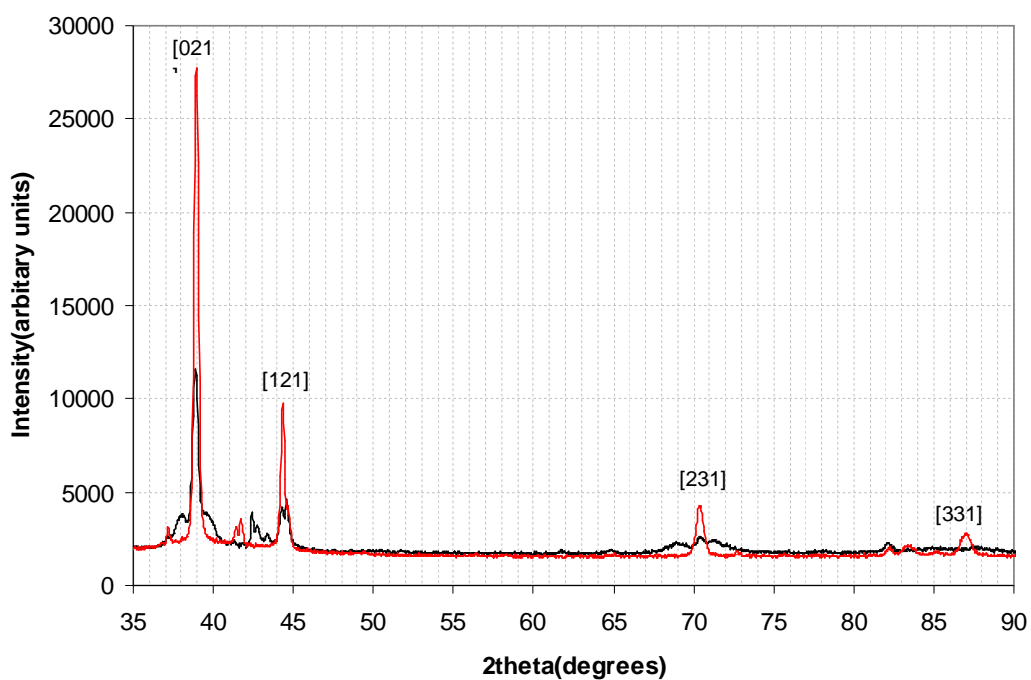


Figure A-30 : XRD pattern of the Cu-Sn deposit from ethaline melt containing 0.04 M  $\text{CuCl}_2 \cdot 2\text{H}_2\text{O}$  -0.1 M  $\text{SnCl}_2 \cdot 2\text{H}_2\text{O}$  electrolyte by galvanostatic method at 220 rpm, 25 °C for 14400 s, [—] annealed at 250 °C, [—] as deposited sample

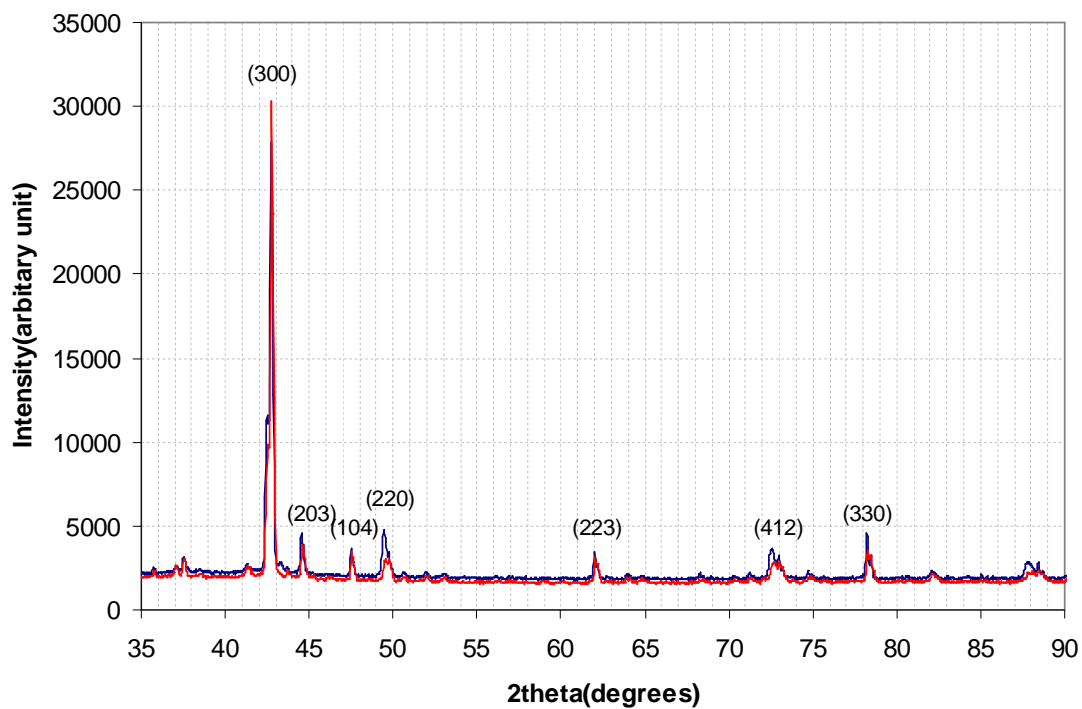


Figure A-31 : XRD pattern of the annealed Cu-Sn deposit at 400 °C from ethaline melt containing 0.04 M  $\text{CuCl}_2 \cdot 2\text{H}_2\text{O}$  -0.1 M  $\text{SnCl}_2 \cdot 2\text{H}_2\text{O}$  electrolyte by galvanostatic method at 220 rpm, 25 °C for 14400s, [—]10 min, [—]30 min